

# THESE POUR OBTENIR LE GRADE DE DOCTEUR DE L'ÉCOLE NATIONALE SUPÉRIEURE DE CHIMIE DE MONTPELLIER

En Chimie et Physico-Chimie des Matériaux

École doctorale Sciences Chimiques Balard (ED459)

Institut Européen des Membranes (IEM)

## Borane compounds for chemical hydrogen storage and carbon dioxide capture

Présentée par **Carlos A. CASTILLA MARTINEZ**  
le 19 Février 2021

Sous la direction de **Umit B. DEMIRCI**

Devant le jury composé de

Mme. Simona BENNICI, Directrice de recherche CNRS, IS2M, Université de Haute-Alsace	<b>Rapporteuse</b>
M. Jean-Louis BOBET, Professeur, ICMCB, Université de Bordeaux	<b>Rapporteur</b>
Mme. Bérange TOURY, Maître de conférences, LMI, Université de Lyon	<b>Examinatrice</b>
M. Ahmad MEHDI, Professeur, ICGM, Université de Montpellier	<b>Président/Examineur</b>
M. Umit B. DEMIRCI, Professeur, IEM, Université de Montpellier	<b>Directeur de thèse</b>





"It's the questions we can't answer that teach us the most.

They teach us how to think.

If you give a man an answer, all he gains is a little fact.

But give him a question and he'll look for his own answers"

-Patrick Rothfuss



## Acknowledgements

---

There are many people that I would like to thank and to mention for their assistance throughout my PhD. First, I want to thank to my thesis director Umit Demirci for all the help that he gave me since that first email that I sent asking for the opportunity to work with him, to the end of this thesis, and even further on. I really consider myself as lucky to have had such a really good advisor during my PhD work. Thanks for all the constructive discussions, either scientific or not, for the encouragement, the support, the guidance, the opportunities to travel and to establish new projects during these three years (and a half) of thesis. I really appreciate it.

Thanks for all the permanent staff of the IEM that kindly helped me and contributed to the realization of this work. A special mention to Christophe Charmette and Jim Cartier for all the help and support to carry out many of my experiments; to Eddy Petit for his disposition to help me with the NMR and Raman techniques; to Nathalie Masquelez for the thermal analyses; and to Didier Cot and Bertrand Rebiere for the SEM-EDX analyses. I would like to mention some other people outside the institute that also participated in my thesis project. Pascal Yot and Guillaume Maurin from the University of Montpellier for their works that contributed to this thesis. Also, for the people from the Platform Balard of the University that assisted me with analyses: Valérie Flaud, Dominique Granier, Amine Geneste, Emmanuel Fernandez, Philippe Gaveau and Erwan Oliviero.

I would like to thank the members of the jury for this dissertation. Thanks to Simona Bennici, Bérangère Toury, Jean-Louis Bobet and Ahmad Mehdi for their valuable comments and their time to read this thesis.

A special thanks for the economic support to the Conacyt for financing my PhD studies. Also, to Campus France for financing one part of my work. For the latter, also thanks to Aysel Kantürk, as the counterpart of the bilateral project that we established with Turkey.

During my stay at the IEM, I had the pleasure to meet really nice people. Starting with the people I worked with in my research team that gave me a hand in some way or another: Damien Alligier

who helped me a lot since the moment that I arrived to the office, Kevin Turani-I-Belloto for all the work and conversations that we had, Rimeh Mighri for all the help in my experiments and the nice conversations, to my internship students Oscar Sonzogni and Lucas Roussignol for the contributions that they did to my project, and for all the other team members with whom I shared nice moments at the lab (or outside): Luc Gimeno, Tetsuo Umegaki, Antigoni Theodoratou and Sebastian Orcel.

I thank all the friends that I made during my stay in Montpellier with whom I shared great moments, "apéros", coffee-breaks and "soirées": Thomas Babut, Habib Belaid, Hana Bouzit, Cyril Oberlin, Pierre Auzan, Sylvain Lamure, Guillaume Seeleuthner, Marleine Tamer, Syreina Al Sayegh, Sara Kawrani, Marcos Díaz, Marianne Benoit, Marine Harguindeguy, Julien Jouannaux, Lucie Ries, Mathieu Lions, Ana Bortolassi, Fanny Duquet, Fida Tanos, Ghady Dakroub... and all the others.

And what it would be of a Mexican in a foreign country without speaking Spanish? I have to mention the wonderful people that I met; those kinds of friends that make your life happier. Thanks for all the moments, the food, the drinks, the travels, the laughs, the talks, the games, the desserts.... I can say that without you, my time in Montpellier wouldn't have been so special. Thanks to my Citadelles group Dánae González, Octavio Graniel, Enrique Folgado and Sofía Domínguez.

I want to mention the most important persons in my life: my family. They are my big support from the distance and they have always been there for me. I have no words to express how much I appreciate all your support and the understanding to my crazy ideas and decisions (like to move to the other side of the ocean). Thanks to my dad Carlos, my mom Lety, my sister Karla, my nephew Ignacio and all the others. I love you so much.

Of course, I don't forget my Mexican friends. Thank you because even in the distance, you have been with me. When we see each other, it is as if no time has passed by. Thank you Perla González, Gina López, Dennise Carrillo, Nancy Cabello and Itzia León.

And last but not least, thank you Ryan McArthur for being with me in all the good and bad moments during this journey. For supporting me and always being there. For all the memories that we have shared in these last years. Thank you, a lot.

# Abstract

---

In the last decade, boron- and nitrogen- based compounds have been considered as potential materials for chemical hydrogen storage due to their unique properties. Ammonia borane ( $\text{NH}_3\text{BH}_3$ , AB, 19.5 wt. % H) and hydrazine borane ( $\text{N}_2\text{H}_4\text{BH}_3$ , HB, 15.4 wt. % H) are two of the most representative examples. However, these materials cannot be used in the pristine state due to different drawbacks (i.e. release of unwanted byproducts during thermolysis, high dehydrogenation temperature...). To overcome these problems, different approaches have been studied. The chemical modification of AB and HB is one of these options, where a protic hydrogen atom of the molecule is substituted by a metal cation. Thereby, the derivatives of AB and HB (amidoboranes and hydrazinidoboranes) have emerged with improved dehydrogenation properties.

In this work, the last two members of the alkali derivatives of hydrazine borane are presented. Rubidium hydrazinidoborane ( $\text{RbN}_2\text{H}_3\text{BH}_3$ , RbHB, 4.6 wt. % H) and cesium hydrazinidoborane ( $\text{CsN}_2\text{H}_3\text{BH}_3$ , CsHB, 3.4 wt. % H) were obtained by a wet synthesis between hydrazine borane and the respective alkali metal. Two new crystalline solids were obtained. The full characterization of RbHB and CsHB was performed in the context of hydrogen storage materials. The successful introduction of the alkali metal cation and the destabilization of the molecule were confirmed. With the family of alkali derivatives of HB complete, we have a better overview of these materials and the findings are discussed.

This thesis also pretends to open new perspectives for amidoboranes. Computational works have shown that boron nitride (BN) can uptake hydrogen or carbon dioxide ( $\text{CO}_2$ ) at room conditions. In this way, we selected the lithium and sodium amidoboranes to be studied as precursors of boron nitride-like structures in order to test their gas sorption properties. The formation of hexagonal BN has been observed when the materials were treated at  $800^\circ\text{C}$ . The capacity of  $\text{CO}_2$  capture of these materials was investigated. The results are presented for the first time in this work.



## Résumé

---

Au cours de la dernière décennie, les composés à base de bore et d'azote ont été considérés comme des matériaux potentiels pour le stockage chimique de l'hydrogène grâce à ses propriétés uniques. L'ammonia borane ( $\text{NH}_3\text{BH}_3$ , AB, 19.5 wt. % H) et l'hydrazine borane ( $\text{N}_2\text{H}_4\text{BH}_3$ , HB, 15.4 wt. % H) sont deux des exemples les plus représentatifs. Malheureusement, ces matériaux ne peuvent pas être utilisés à l'état vierge en raison de différents inconvénients associés à leur déshydrogénation. Pour surmonter ces problèmes, plusieurs stratégies ont été considérées. L'une d'elles est la modification chimique de l'AB et de l'HB, où un des atomes d'hydrogène protique de la molécule est substitué par un cation métallique. Ainsi, les dérivés de l'AB et de l'HB (amidoboranes et hydrazinidoboranes) ont émergé avec des propriétés de déshydrogénation améliorées.

Dans ce travail, les deux derniers membres des dérivés alcalins de l'hydrazine borane sont présentés. L'hydrazinidoborane de rubidium ( $\text{RbN}_2\text{H}_3\text{BH}_3$ , RbHB, 4.6 m % H) et l'hydrazinidoborane de césium ( $\text{CsN}_2\text{H}_3\text{BH}_3$ , CsHB, 3.4 m % H) ont été obtenus par une synthèse par voie humide entre l'HB et le métal alcalin respectif. Deux nouveaux solides cristallins ont été obtenus. La caractérisation complète du RbHB et du CsHB a été réalisée dans le contexte des matériaux par le stockage de l'hydrogène. L'introduction réussie du cation alcalin et la déstabilisation de la molécule ont été confirmées par rapport au précurseur HB. La famille des dérivés alcalins de HB étant complète, nous avons une meilleure vue d'ensemble de ces matériaux et de nouvelles perspectives sont abordées.

Cette thèse a également pour objectif d'ouvrir des nouvelles perspectives pour les amidoboranes. Des études théoriques ont montré que le nitrure de bore (BN) peut absorber l'hydrogène ou le dioxyde de carbone ( $\text{CO}_2$ ) à l'ambiante. Des lors, les amidoboranes de lithium et de sodium ont été étudiés en tant que précurseurs de structures similaires au BN afin d'évaluer leurs propriétés de sorption de gaz. La formation de BN hexagonal a été observée lorsque les matériaux étaient traités à  $800^\circ\text{C}$ . La capacité de captage de  $\text{CO}_2$  de ces matériaux a été estimée. Des résultats intéressants ont été obtenus et ils sont présentés dans ce manuscrit.



# Contents

---

Acknowledgements.....	i
Abstract.....	iii
Résumé .....	v
Contents .....	vii
List of figures and tables.....	xiii
<b>CHAPTER 1. GENERAL INTRODUCTION .....</b>	<b>1</b>
1. The problem of energy and global warming.....	3
2. References .....	7
<b>CHAPTER 2. LITERATURE REVIEW .....</b>	<b>9</b>
1. Hydrogen as energy carrier.....	11
1.1 Properties of hydrogen.....	11
1.2 Production of hydrogen.....	13
1.2.1 Hydrogen from fuels.....	14
1.2.1.1 Hydrocarbon reforming methods.....	14
1.2.1.2 Hydrocarbon pyrolysis.....	15
1.2.1.3 Methane decomposition by plasma arc .....	15
1.2.1.4 Ammonia cracking.....	16
1.2.2 Hydrogen from water .....	16
1.2.2.1 Water electrolysis .....	16
1.2.2.2 Water thermolysis .....	17
1.2.2.3 Water photo-electrolysis.....	17

1.2.3 Hydrogen from renewable sources .....	17
1.2.3.1 Hydrogen from biological sources .....	18
1.2.3.2 Hydrogen from renewable energy .....	19
1.3 Energy from hydrogen .....	19
1.3.1 Fuel cells .....	19
1.3.2 Batteries .....	21
2. Hydrogen storage .....	22
2.1 Compressed hydrogen .....	22
2.2 Liquid hydrogen .....	23
2.3 Hydrogen stored in materials .....	24
2.3.1 Physisorption of hydrogen .....	25
2.3.1.1 Carbon materials .....	25
2.3.1.2 Zeolites .....	27
2.3.1.3 Metal organic frameworks .....	28
2.3.1.4 Clathrate hydrates .....	29
2.3.2 Chemisorption of hydrogen .....	30
2.3.2.1 Metal hydrides .....	32
2.3.2.1.1 Binary metal hydrides .....	32
2.3.2.1.2 Intermetallic hydrides .....	33
2.3.2.1.3 Complex hydrides .....	34
3. Boron- and nitrogen-based materials .....	37
3.1 Ammonia borane and hydrazine borane .....	37
3.1.1 Destabilization strategies of AB .....	39
3.2 Background on amidoboranes .....	40
3.3 Alkali amidoboranes and hydrazinidoboranes .....	41
3.3.1 Synthesis .....	41
3.3.2 Crystalline solids .....	44
3.3.3 Dihydrogen bonding .....	48
3.3.4 Thermolytic dehydrogenation .....	48

3.3.5 Rehydrogenation of thermolytic residues of MAB and MHB.....	51
3.4 Alkaline-earth amidoboranes and hydrazinidoboranes.....	52
3.5 Boron nitride.....	53
4. Conclusion .....	55
5. References .....	56
<b>CHAPTER 3. RUBIDIUM HYDRAZINIDOBORANE.....</b>	<b>79</b>
1. Introduction.....	81
2. Experimental section.....	83
2.1 Reagents.....	83
2.2 Synthesis.....	84
2.2.1 Synthesis of hydrazine borane .....	84
2.2.2 Synthesis of rubidium hydrazinidoborane.....	84
2.3 Characterization.....	85
2.3.1 Structural characterization.....	85
2.3.2 Thermal characterization.....	86
2.4 Dehydrogenation experiments at isothermal conditions.....	86
3. Results and discussion.....	87
3.1 Preliminary comments.....	87
3.2 Molecular structure of RbHB.....	87
3.2.1 Fourier Transformed Infrared Spectroscopy (FTIR).....	87
3.2.2 <sup>11</sup> B Magic Angle Spinning Nuclear Magnetic Resonance (MAS NMR).....	88
3.2.3 Stability of rubidium hydrazinidoborane .....	90
3.2.4 Crystal structure.....	93
3.3 Thermal characterization.....	98
3.3.1 TG-MS and DSC analyses .....	98
3.3.2 Calculation of the apparent activation energy by the Kissinger method ....	101
3.3.3 Dehydrogenation experiments on RbHB.....	102

3.4 Analyses of the solid residues.....	105
3.5 Decomposition mechanism of rubidium hydrazinidoborane .....	108
4. Conclusions .....	109
5. References .....	111
<b>CHAPTER 4. CESIUM HYDRAZINIDOBORANE.....</b>	<b>117</b>
1. Introduction.....	119
2. Experimental section.....	122
2.1 Reagents.....	122
2.2 Synthesis.....	122
2.2.1 Synthesis of hydrazine borane .....	122
2.2.2 Synthesis of cesium hydrazinidoborane.....	123
2.3 Characterization.....	123
2.3.1 Structural characterization.....	123
2.3.2 Thermal characterization.....	124
2.4 Decomposition experiments at isothermal conditions .....	125
3. Results and discussion.....	125
3.1 Synthesis conditions and security issues regarding CsHB.....	125
3.2 Molecular structure of CsHB .....	126
3.2.1 Fourier Transformed Infrared Spectroscopy (FTIR).....	126
3.2.2 <sup>11</sup> B Magic Angle Spinning Nuclear Magnetic Resonance (MAS NMR).....	127
3.2.3 Stability of cesium hydrazinidoborane under inert atmosphere.....	129
3.2.4 Effect of the temperature on the synthesis of CsHB.....	131
3.2.5 Powder X-Ray Diffraction (PXRD) .....	133
3.3 Thermal characterization.....	139
3.3.1 TGA-MS and DSC measurements .....	139
3.3.2 Calculation of apparent activation energy by the Kissinger method.....	141
3.3.3 Decomposition experiments of CsHB.....	142

3.4 Analyses of solid residues.....	149
4. Conclusions.....	151
5. References.....	153
<b>CHAPTER 5. AMIDOBORANE-DERIVED BORON NITRIDE.....</b>	<b>161</b>
1. Introduction.....	163
2. Experimental section.....	165
2.1 Reagents.....	165
2.2 Synthesis.....	165
2.2.1 Synthesis of lithium amidoborane (LiAB).....	165
2.2.2 Synthesis of sodium amidoborane (NaAB).....	166
2.3 Heat treatment.....	166
2.4 Characterization.....	167
2.4.1 Structural characterization.....	167
2.5 Sorption of CO <sub>2</sub> .....	169
2.5.1 Sorption experiments.....	170
3. Results.....	170
3.1 Preliminary commentaries.....	170
3.2 Molecular characterization.....	173
3.2.1 Fourier Transformed Infrared Spectroscopy (FTIR).....	173
3.2.2 Raman Spectroscopy.....	177
3.2.3 Powder X-Ray Diffraction (PXRD).....	180
3.2.4 <sup>11</sup> B Magic Angle Spinning Nuclear Magnetic Resonance (MAS NMR).....	187
3.2.5 X-Ray Photoelectron Spectroscopy (XPS).....	192
3.3 Information about the Li and Na elements.....	195
3.3.1 <sup>7</sup> Li MAS NMR.....	195
3.3.2 <sup>23</sup> Na MAS NMR.....	197
3.3.3 XPS.....	198
3.4 Carbon dioxide sorption properties.....	199

4. Conclusions .....	202
5. References .....	204
<b>CHAPTER 6. GENERAL CONCLUSION &amp; PERSPECTIVES .....</b>	<b>215</b>
1. General conclusion.....	217
2. Future perspectives.....	219
<b>Scientific contributions .....</b>	<b>223</b>
<b>ANNEX I. SUPPLEMENTARY INFORMATION .....</b>	<b>225</b>
Description of Kissinger's method.....	227
Energy Dispersive X-ray Analysis from pyrolyzed samples (LiAB, NaAB).....	228
Powder X-Ray Diffraction comparison from samples (AB, LiAB, NaAB) pyrolyzed at 1000°C.....	232
Evolution of boron species determined by <sup>11</sup> B MAS NMR from the pyrolyzed samples (AB, LiAB, NaAB) .....	233
XPS survey spectra of the samples derived from AB, LiAB and NaAB .....	234
CO <sub>2</sub> uptake by the pyrolyzed samples of AB, LiAB, and NaAB .....	237

# List of Figures and Tables

---

## CHAPTER 1. GENERAL INTRODUCTION

### Figures

<b>Figure 1.</b> Total energy supply by sources in the 1990-2018 period .....	3
<b>Figure 2.</b> Global atmospheric CO <sub>2</sub> concentrations in ppm for the past 800 000 years.....	4
<b>Figure 3.</b> Potential of hydrogen to participate in the energy system.....	5

## CHAPTER 2. LITERATURE CHAPTER

### Figures

<b>Figure 1.</b> Phase diagram of hydrogen .....	11
<b>Figure 2.</b> Specific energy and energy density for different fuels based on heating values.....	12
<b>Figure 3.</b> Main hydrogen production methods. ....	13
<b>Figure 4.</b> Summary of main types of fuel cells describing the feedstock, products, range of working temperature and ions exchanged through the electrolyte.....	20
<b>Figure 5.</b> Materials-based H <sub>2</sub> storage versus compressed and cryogenic storage systems .....	24
<b>Figure 6.</b> Gravimetric vs. volumetric density for different hydrogen storage systems.....	27
<b>Figure 7.</b> Structure I and II of clathrate hydrates.....	30
<b>Figure 8.</b> Plot of hydrogen storage materials as a function of the H <sub>2</sub> release temperature .....	36
<b>Figure 9.</b> Representation of the thermolytic decomposition of AB and HB up to 400°C .....	38
<b>Figure 10.</b> Coordination sphere of: (a) LiAB, (b) NaAB, (c) KAB, (d) RbAB, (e) CsAB.....	45
<b>Figure 11.</b> Coordination sphere of: (a) $\alpha$ -LiHB, (b) $\beta$ -LiHB, (c) NaHB, (d) KHB, (e) RbHB, (f) CsHB .....	47

**Figure 12.** Examples of compounds having tetragonal boron environments and trigonal boron environments, present in the thermolytic residues of MAB and MHB.....50

### Tables

<b>Table 1.</b> Hydrides considered for hydrogen storage .....	31
<b>Table 2.</b> Syntheses of alkali MAB .....	42
<b>Table 3.</b> Syntheses of alkali MHB.....	43
<b>Table 4.</b> Summary of crystallographic properties of MAB and MHB compounds.....	44

## CHAPTER 3. RUBIDIUM HYDRAZINIDOBORANE

### Figures

<b>Figure 1.</b> FTIR spectra of HB and RbHB .....	88
<b>Figure 2.</b> $^{11}\text{B}$ MAS NMR spectra of HB and RbHB.....	89
<b>Figure 3.</b> FTIR spectra of RbHB, RbHB after 1 and 7 months after synthesis (stored at room temperature and under argon atmosphere).....	90
<b>Figure 4.</b> $^{11}\text{B}$ MAS NMR spectra of RbHB, RbHB after 1 and 7 months after synthesis (stored at room temperature and under argon atmosphere) .....	91
<b>Figure 5.</b> Comparison of the PXRD patterns of pure HB and RbHB .....	93
<b>Figure 6.</b> Observed (black line) and calculated (red line) powder XRD profile for the Rietveld refinement of RbHB, differences of the plots (blue line), and calculated angles for Bragg peaks in $2\theta$ (green lines) .....	95
<b>Figure 7.</b> Crystal structure of $\text{RbN}_2\text{H}_3\text{BH}_3$ along the [100], [010], and [001] directions.....	96
<b>Figure 8.</b> Coordination sphere of the cation $\text{Rb}^+$ surrounded by 6 $[\text{N}_2\text{H}_3\text{BH}_3]^-$ anions .....	97
<b>Figure 9.</b> Calculated interatomic distances for rubidium hydrazinidoborane .....	98
<b>Figure 10.</b> TGA-DSC ( $5^\circ \text{C min}^{-1}$ ) and MS results ( $m/z = 2, 17, 28, 32$ for $\text{H}_2, \text{NH}_3, \text{B}_2\text{H}_6$ or $\text{N}_2, \text{N}_2\text{H}_4$ respectively) of RbHB.....	99

<b>Figure 11.</b> Pictures of the evolution of RbHB under heating: a) RbHB at room temperature; b) Foaming starting to occur at c.a. 60 ° C; c) Expansion of the foam due to evolution of volatile products; d) Solidification of the foam resulting in a polymeric residue at c.a. 100°C .....	100
<b>Figure 12.</b> a) DSC curves for RbHB at different heating rates (1, 3, 5, 7, 10 ° C min <sup>-1</sup> ); b) Linear regression for the Kissinger method of the two exothermic events.....	101
<b>Figure 13.</b> a) Time evolution of H <sub>2</sub> release from RbHB under heating at a constant temperature (80, 100, 120 and 140° C); b) Arrhenius plot for the determination of the apparent activation energy .....	103
<b>Figure 14.</b> GC analyses of the gases liberated by RbHB in isothermal conditions (under heating at the constant temperature of 80, 100 and 120° C).....	104
<b>Figure 15.</b> FTIR spectra of RbHB and of the solid residues recovered upon heating a sample of RbHB at 80, 100, 120 and 140° C.....	105
<b>Figure 16.</b> XRD patterns of RbHB and the solid residues recovered upon heating a sample of RbHB at 80 and 140°C .....	106
<b>Figure 17.</b> <sup>11</sup> B MAS NMR spectra of RbHB and of the solid residues recovered upon heating a sample of RbHB at 80, 100, 120 and 140° C.....	107
<b>Figure 18.</b> Proposed mechanism for the decomposition of RbHB .....	109

## Tables

<b>Table 1.</b> Typical chemical shifts assigned to different species formed during the thermal decomposition of BNH compounds.....	92
<b>Table 2.</b> Space group, unit cell parameters, goodness of fit and R values for the refined structure.....	94
<b>Table 3.</b> Experimental structural parameters of RbHB (S.G. <i>P2</i> <sub>1</sub> No.4) at room temperature .....	95
<b>Table 4.</b> Kinetics parameters of RbHB dehydrogenation process calculated by Kissinger method and Arrhenius equation.....	102
<b>Table 5.</b> Equivalentents of H <sub>2</sub> liberated by different alkali hydrazinidoboranes after 1 h of heat treatment at constant temperature .....	104

## CHAPTER 4. CESIUM HYDRAZINIDOBORANE

Figures

<b>Figure 1.</b> FTIR spectra of HB and CsHB with their respective bands .....	127
<b>Figure 2.</b> $^{11}\text{B}$ MAS NMR spectra of HB and CsHB .....	128
<b>Figure 3.</b> FTIR spectra of CsHB and CsHB after 2 months of its synthesis (stored at room temperature and under argon atmosphere).....	129
<b>Figure 4.</b> $^{11}\text{B}$ MAS NMR spectra of a fresh sample of CsHB and one stored for 2 months at room temperature and under argon atmosphere .....	130
<b>Figure 5.</b> FTIR spectra of CsHB synthesized at $-20^{\circ}\text{C}$ and at room temperature.....	131
<b>Figure 6.</b> $^{11}\text{B}$ MAS NMR spectra of CsHB synthesized at $-20^{\circ}\text{C}$ and at room temperature .....	132
<b>Figure 7.</b> Comparison of PXRD patterns of CsHB synthesized at $-20^{\circ}\text{C}$ and at room temperature.....	133
<b>Figure 8.</b> PXRD patterns of HB and CsHB.....	134
<b>Figure 9.</b> Observed (black line) and calculated (red line) PXRD profile for the Rietveld refinement of CsHB, differences of the plots (blue line), calculated angles for Bragg peaks in $2\theta$ (green lines) and omitted peaks (gray peaks) .....	135
<b>Figure 10.</b> Crystal structure of CsHB along the [100], [010] and [001] directions.....	137
<b>Figure 11.</b> Coordination sphere of the Cs cation, surrounded by six $[\text{N}_2\text{H}_3\text{BH}_3]^-$ anions .....	138
<b>Figure 12.</b> Calculated interatomic distances for cesium hydrazinidoborane .....	139
<b>Figure 13.</b> TGA-DSC ( $5^{\circ}\text{C min}^{-1}$ ) and MS results ( $m/z=2, 17, 27, 28, 32$ for $\text{H}_2, \text{NH}_3, \text{B}_2\text{H}_6, \text{N}_2, \text{N}_2\text{H}_4$ or $\text{O}_2$ respectively) of CsHB.....	140
<b>Figure 14.</b> DSC curves for CsHB at different heating rates (1, 3, 5 and $7^{\circ}\text{C min}^{-1}$ ); and linear regression for the Kissinger method of the three exothermic events.....	142
<b>Figure 15.</b> a) Time evolution of $\text{H}_2$ release from CsHB under heating at isothermal conditions (90, 100, 110 and $120^{\circ}\text{C}$ ); b) Arrhenius plot for the determination of the apparent activation energy .....	143
<b>Figure 16.</b> GC analyses of the gases liberated by CsHB at isothermal conditions (under heating at constant temperature of 90, 100, 110 and $120^{\circ}\text{C}$ ).....	145

<b>Figure 17.</b> MS spectra of the gases released by the sample heated isothermally at 100°C.....	146
<b>Figure 18.</b> MS spectra of the gases released by the sample heated isothermally at 120°C.....	147
<b>Figure 19.</b> Formation of the dimer $[(\text{CsN}_2\text{H}_3)_2\text{BH}_2]^+[\text{BH}_4]^-$ , which will release $\text{H}_2$ and $\text{NH}_3$ .....	148
<b>Figure 20.</b> Formation of the dimer $[(\text{CsN}_2\text{H}_3)_2\text{BH}_2]^+[\text{BH}_4]^-$ , which continues reacting to form B- and N-based polymers with the release of $\text{H}_2$ and $\text{B}_2\text{H}_6$ .....	148
<b>Figure 21.</b> Reaction of a polymer chain product of the thermolysis of CsHB and a molecule of CsHB. This leads to a continued growth of the chain, forming CsH and releasing $\text{N}_2\text{H}_4$ .....	149
<b>Figure 22.</b> $^{11}\text{B}$ MAS NMR spectra of CsHB and the solid residues recovered after the isothermal treatment at 90, 100, 110 and 120°C.....	150

### Tables

<b>Table 1.</b> Crystallographic parameters of CsHB.....	134
<b>Table 2.</b> Experimental structural parameters of CsHb (S.G. $P2_1$ No.4) at room temperature....	136
<b>Table 3.</b> Cell parameters of hydrazine borane and alkali hydrazinidoboranes .....	137
<b>Table 4.</b> Kinetic parameters of the thermal decomposition of CsHB obtained by the Kissinger method and Arrhenius equation .....	142
<b>Table 5.</b> Apparent activation energy for different BNH compounds.....	144
<b>Table 6.</b> Equivalentents of $\text{H}_2$ liberated by the alkali hydrazinidoboranes and hydrazine borane after 1 h of heat treatment at isothermal conditions .....	145

## CHAPTER 5. AMIDOBORANE-DERIVED BORON NITRIDE

### Figures

<b>Figure 1.</b> Diagram of the Sieverts system used for the $\text{CO}_2$ sorption experiments.....	169
<b>Figure 2.</b> SEM images of the pyrolyzed samples of LiAB and NaAB at 600, 800 and 1000°C at 10.0 k.....	172
<b>Figure 3.</b> FTIR spectra of AB and the products after pyrolysis at 200, 600, 800 and 1000°C....	173

<b>Figure 4.</b> Species involved in AB thermal decomposition.....	174
<b>Figure 5.</b> FTIR spectra of the alkali amidoboranes and the products after pyrolysis at 200, 600, 800 and 1000°C for a) LiAB and b) NaAB.....	175
<b>Figure 6.</b> Comparison between the spectrum of pure boron nitride and the samples pyrolyzed at 1000°C .....	176
<b>Figure 7.</b> Raman spectra of AB at a) room temperature and pyrolyzed at b) 200°C; c) 600°C; 800°C and 1000°C.....	177
<b>Figure 8.</b> Raman spectra of the alkali amidoboranes and the products after pyrolysis at 200, 600, 800 and 1000°C for a) LiAB and b) NaAB.....	178
<b>Figure 9.</b> PXRD patterns of a) AB and the solid products after pyrolysis at 200, 600, 800 and 1000°C and b) hexagonal boron nitride.....	181
<b>Figure 10.</b> PXRD patterns of the alkali amidoboranes and the solids products treated at 200, 600, 800 and 1000°C for a) LiAB and b) NaAB.....	182
<b>Figure 11.</b> a, b) HRTEM images of LiAB showing the interlayer distance and c) selected area electron diffraction showing a polycrystalline solid.....	185
<b>Figure 12.</b> a) Multiple crystals in a particle of NaAB1000; b, c, d) crystals of different size and interlayer distances; e) selected area electron diffraction of NaAB1000 showing a polycrystalline composition.....	186
<b>Figure 13.</b> $^{11}\text{B}$ MAS NMR spectra of AB and the solid products heated at 200, 600, 800 and 1000°C .....	187
<b>Figure 14.</b> $^{11}\text{B}$ MAS NMR spectra of the alkali amidoboranes and the solid products pyrolyzed at 200, 600, 800 and 1000°C for a) LiAB and b) NaAB .....	189
<b>Figure 15.</b> Possible compounds formed during the decomposition of AB, LiAB and NaAB (M=Li, Na) according to the $^{11}\text{B}$ MAS NMR spectra and reported in the literature .....	191
<b>Figure 16.</b> XPS spectra of AB and the solid products after pyrolysis at 200, 600, 800 and 1000°C for a) B 1s and b) N 1s .....	192
<b>Figure 17.</b> B 1s XPS spectra of the amidoboranes and the solid products after pyrolysis at 200, 600, 800 and 1000°C for a) LiAB and b) NaAB.....	193

**Figure 18.** N 1s XPS spectra of the amidoboranes and the solid products after pyrolysis at 200, 600, 800 and 1000°C for a) LiAB and b) NaAB..... 195

**Figure 19.** <sup>7</sup>Li MAS NMR spectra for LiAB and the solid products recovered after pyrolysis at 200, 600, 800 and 1000° C..... 196

**Figure 20.** <sup>23</sup>Na MAS NMR spectra for NaAB and the solid products recovered after pyrolysis at 200, 600, 800 and 1000° C ..... 197

**Figure 21.** XPS spectra of the amidoboranes and the solid products after pyrolysis at 200, 600, 800 and 1000°C of a) Li 1s for LiAB and b) Na 1s for NaAB..... 198

**Figure 22.** Estimated CO<sub>2</sub> sorption capacity (cm<sup>3</sup> g<sup>-1</sup>) of the pyrolyzed samples of AB, LiAB and NaAB at 1.5 bar and 30°C .....200

Tables

**Table 1.** Yield (wt. %) of the recovered samples after heat treatment..... 167

**Table 2.** Reference of the samples in function of the heat treatment..... 167

**Table 3.** Density and specific surface area of the pyrolyzed samples derived from AB, LiAB and NaAB..... 171

**Table 4.** Position of the E<sub>2g</sub> vibrational mode in the materials, the calculated FWHM and average grain size ..... 180

**Table 5.** Diffractogram data for the (002) peak in LiAB1000 and NaAB1000..... 184

**Table 6.** Estimated CO<sub>2</sub> sorption capacity (cm<sup>3</sup> g<sup>-1</sup>) by the materials studied in this work at 1.5 bar and 30°C ..... 199

**Table 7.** CO<sub>2</sub> uptake by different materials..... 201

**CHAPTER 6. GENERAL CONCLUSION & PERSPECTIVES**

Figures

**Figure 1.** a) FTIR and b) <sup>11</sup>B MAS NMR spectra comparison of pristine HB and Mg(HB)<sub>2</sub>..... 219

<b>Figure 2.</b> MAS NMR spectra of the solid product after the dehydrogenation of AB catalyzed by PdCl <sub>2</sub> in the presence of CO <sub>2</sub> for a) <sup>11</sup> B and b) <sup>13</sup> C .....	220
<b>Figure 3.</b> <sup>11</sup> B MAS NMR spectrum of the solid product after the thermolysis of LiAB under a CO <sub>2</sub> atmosphere.....	221

## ANNEX I. SUPPLEMENTARY INFORMATION

### Figures

<b>Figure A 1.</b> SEM-EDX analysis of LiAB600 in different zones of the compound.....	228
<b>Figure A 2.</b> SEM-EDX analysis of LiAB800 in different zones of the compound .....	228
<b>Figure A 3.</b> SEM-EDX analysis of LiAB1000 in different zones of the compound.....	229
<b>Figure A 4.</b> SEM images and EDX maps of LiAB600, LiAB800 and LiAB1000 .....	229
<b>Figure A 5.</b> SEM-EDX analysis of NaAB600 in different zones of the compound.....	230
<b>Figure A 6.</b> SEM-EDX analysis of NaAB800 in different zones of the compound.....	230
<b>Figure A 7.</b> SEM-EDX analysis of NaAB1000 in different zones of the compound .....	231
<b>Figure A 8.</b> SEM images and EDX maps of NaAB600, NaAB800 and NaAB1000.....	231
<b>Figure A 9.</b> Comparison between the PXRD patterns of the samples treated at 1000° C and h-BN .....	232
<b>Figure A 10.</b> Peak area ratios of boron species (BH <sub>4</sub> , NBH <sub>3</sub> , N <sub>2</sub> BH <sub>2</sub> /N <sub>3</sub> BH and the sp <sup>2</sup> -hybridized B) as a function of the temperature up to 1000° C .....	233
<b>Figure A 11.</b> XPS survey spectra of the AB-derived materials pyrolyzed at 200, 600, 800 and 1000°C .....	234
<b>Figure A 12.</b> XPS survey spectra of LiAB and the LiAB-derived materials pyrolyzed at 200, 600, 800 and 1000°C.....	235
<b>Figure A 13.</b> XPS survey spectra of NaAB and the NaAB-derived materials pyrolyzed at 200, 600, 800 and 1000°C.....	236

### Tables

<b>Table A 1.</b> Density of the pyrolyzed samples of AB, LiAB and NaAB .....	237
---	-----

# Chapter 1

## GENERAL INTRODUCTION

---



# 1 General introduction

## 1. The problem of energy and global warming

Energy is essential for humanity. All the economic, technological and social progresses that we have accomplished are mainly thanks to the use of energy. However, as the population increases, the necessity for energy does it too. Only in 2018 the increase on the energy demand was of 2.3%, which represents twice the 2010-2017 average.<sup>1</sup> At this rate, the energy consumption will rise up more than 25% in 2040 in comparison with this year.<sup>2</sup> At present, the energy is mainly obtained from fossil fuels (oil, gas, coal) and secondarily from alternative sources like solar, wind and nuclear energy (Figure 1).<sup>3</sup>

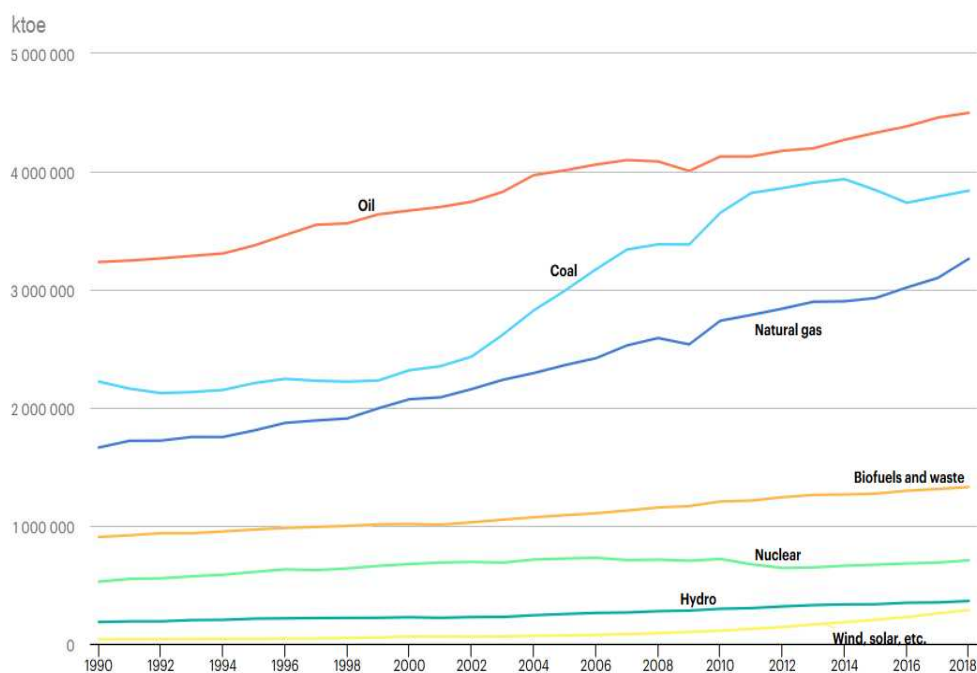
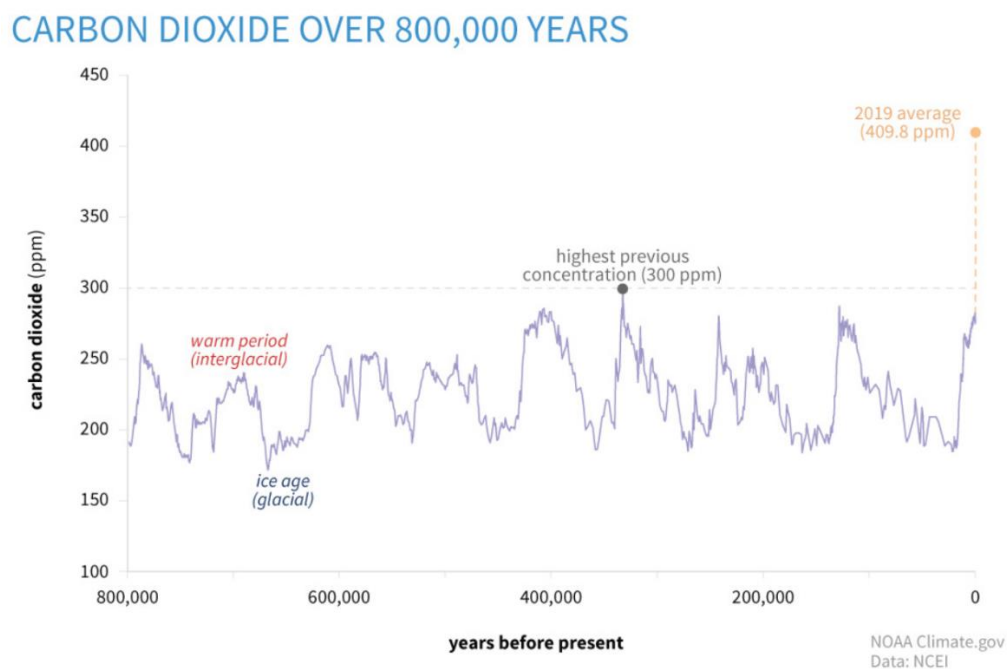


Figure 1. Total energy supply by sources in the 1990-2018 period.<sup>3</sup>

Fossil fuels are limited non-renewable resources that are being depleted. The difficulty to extract such fuels is increasing and it is becoming harder. In addition, the burning of fossil fuels is the main source of the greenhouse gases (carbon dioxide CO<sub>2</sub>, methane CH<sub>4</sub>, nitrous oxide N<sub>2</sub>O, chlorofluorocarbons and hydrofluorocarbons). The release of greenhouse gases into the atmosphere, especially CO<sub>2</sub>, is the main contributor to anthropogenic climate change and global warming.<sup>4-7</sup> The emissions of CO<sub>2</sub> has reached a peak in 2019 (**Figure 2**) and has surpassed by far the highest concentration of this gas in previous years.



**Figure 2.** Global atmospheric CO<sub>2</sub> concentrations in ppm for the past 800 000 years.<sup>7</sup>

Global warming has caused negative effects that affect both humanity and the environment: the acidification of the oceans, more intense and frequently droughts and hurricanes, modifications in ecosystems and melting of glaciers.<sup>8-10</sup> All of these phenomena have a negative impact on society and the economy. For these reasons, efforts have been made to alleviate climate change. Over 100 countries have adopted actions to mitigate global warming to prevent a rise on 2°C in temperature to 2050.<sup>11</sup> But despite the efforts, the global average temperature has increased by 0.8°C. It is

evident that the energy consumption has a direct impact on the generation of greenhouse gases and thus in global warming. That is why decreasing the pollutant emissions while supplying and/or reducing the need for energy has become an urgent matter. Different efforts have been done in order to reduce the energy demand, but it is a challenging task that has not had fruitful results up to now.<sup>12</sup> The only option is to find new ways to provide the required energy with sources that produce zero or near zero noxious emissions.

Hydrogen arises as the best option to substitute fossil fuels due to its high energy density and because it produces zero emission during its combustion. In addition, it can overcome the disadvantages of other renewable sources, like the intermittency of solar and wind energy. Thanks to this potential, the concept of a hydrogen economy was created: it is an alternative economic model where the basic energy needs are supplied by hydrogen. Several reports show that hydrogen can participate in almost every part of the energy system (**Figure 3**), including electricity generation and heat power.<sup>13</sup> This will lead to the decarbonization of the energy chain supply. But different efforts must still be done to achieve a feasible hydrogen economy. There are different challenges that have to be addressed simultaneously which include the production, storage, transportation and distribution of hydrogen. However, hydrogen storage is one of the biggest challenges regarding the hydrogen economy.

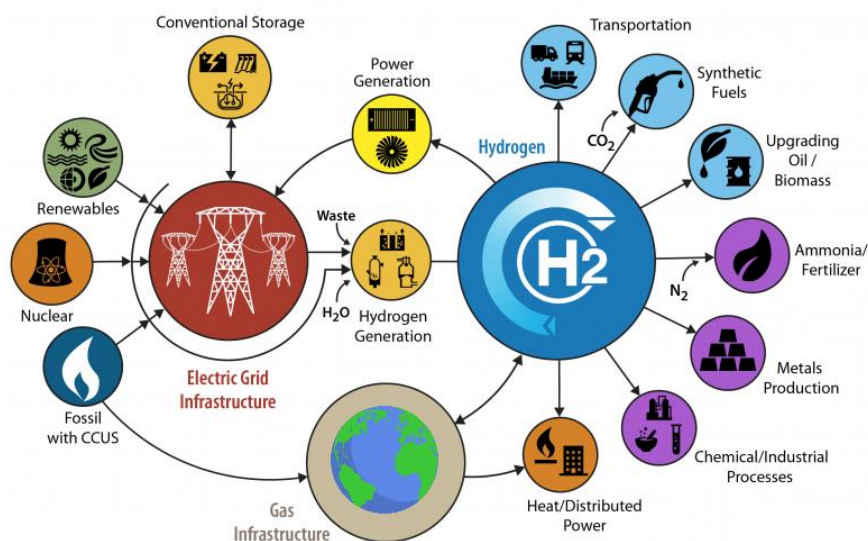


**Figure 3.** Potential of hydrogen to participate in the energy system. Modified from <sup>14</sup>.

On the other hand, the reduction of the CO<sub>2</sub> emissions to the atmosphere is also important. The carbon capture and storage (CCS) technologies can contribute to achieve this. With the implementation of this technologies, the rise in the global average temperature can be avoided in up to 2°C.<sup>15</sup> Some of the CCS technologies are based on the use of a suitable adsorbent to capture CO<sub>2</sub>. Research works are being focused in the development of materials able to capture CO<sub>2</sub> in an efficient way.

The present work intends to contribute and widen the knowledge about boron- and nitrogen-based materials. This thesis presents the results of new materials evaluated in the context of hydrogen storage, and it opens new perspectives regarding CO<sub>2</sub> capture.

The rest of the thesis is organized as follows:

**Chapter 2** follows the literature review by describing hydrogen and summarizing the processes of production and conversion to obtain it. The emphasis of this chapter is on materials for hydrogen storage, especially the boron- and nitrogen-based compounds.

**Chapter 3** presents rubidium hydrazinidoborane, a new alkaline derivative of hydrazine borane and its evaluation in the context of hydrogen storage.

**Chapter 4** introduces cesium hydrazinidoborane, the last alkali derivative of hydrazine borane. The characterization as potential hydrogen storage material is described.

**Chapter 5** features the synthesis of boron nitride derived from ammonia borane and two of its alkali derivatives, lithium and sodium amidoboranes. In addition, the CO<sub>2</sub> sorption properties of these materials were briefly studied.

**Chapter 6** gives the general conclusion of this work and open new perspectives to boron- and nitrogen-based materials.

## 2. References

1. International Energy Agency. Global energy & CO<sub>2</sub> status report. The latest trends in energy and emissions in 2018. *IEA* <https://webstore.iea.org/global-energy-co2-status-report-2018> (2019).
2. International Energy Agency. World energy outlook - executive summary 2018. *IEA* <https://www.iea.org/reports/world-energy-outlook-2018> (2018).
3. International Energy Agency. IEA Data and statistics. [https://www.iea.org/data-and-statistics?country=WORLD&fuel=Energy supply&indicator=TPESbySource](https://www.iea.org/data-and-statistics?country=WORLD&fuel=Energy%20supply&indicator=TPESbySource) (2020).
4. IPCC. Climate change 2014: synthesis report. *Contribution of working groups I, II and III to the fifth assessment report of the Intergovernmental Panel on Climate Change*. <https://www.ipcc.ch/report/ar5/syr/> (2014).
5. Höök, M. & Tang, X. Depletion of fossil fuels and anthropogenic climate change-A review. *Energy Policy* **52**, 797–809 (2013).
6. Abas, N., Kalair, A. & Khan, N. Review of fossil fuels and future energy technologies. *Futures* **69**, 31–49 (2015).
7. Lindsey, R. NOAA Climate. *Climate change: Atmospheric carbon dioxide* <https://www.climate.gov/news-features/understanding-climate/climate-change-atmospheric-carbon-dioxide> (2020).
8. Gattuso, J. P. *et al.* Contrasting futures for ocean and society from different anthropogenic CO<sub>2</sub> emissions scenarios. *Science*. **349**, 1–10 (2015).
9. Dai, A. Drought under global warming: A review. *Wiley Interdiscip. Rev. Clim. Chang.* **2**, 45–65 (2011).
10. Root, T. L. *et al.* Fingerprints of global warming on wild animals and plants. *Nature* **421**, 57–60 (2003).
11. Meinshausen, M. *et al.* Greenhouse-gas emission targets for limiting global warming to 2°C. *Nature* **458**, 1158–1162 (2009).

12. Sorrell, S. Reducing energy demand: A review of issues, challenges and approaches. *Renew. Sustain. Energy Rev.* **47**, 74–82 (2015).
13. Brandon, N. P. & Kurban, Z. Clean energy and the hydrogen economy. *Phil. Trans. R. Soc. A* **375**, 1–17 (2017).
14. DOE-US. Hydrogen and fuel cell technologies office. <https://www.energy.gov/eere/fuelcells/hydrogen-and-fuel-cell-technologies-office> (2020).
15. Anwar, M. N. *et al.* CO<sub>2</sub> capture and storage: A way forward for sustainable environment. *J. Environ. Manage.* **226**, 131–144 (2018).

# Chapter 2

## LITERATURE REVIEW

---



# 2 Literature review

## 1. Hydrogen as energy carrier

### 1.1 Properties of hydrogen

Hydrogen is the lightest element ( $1.0079 \text{ g mol}^{-1}$ ) and is the most abundant in the universe. As an element, it is the third most abundant on Earth, present mainly in water and organic compounds. As a molecule, the concentration of  $\text{H}_2$  is lower than 1 ppm in the atmosphere.  $\text{H}_2$  is a non-toxic, colorless and odorless gas.  $\text{H}_2$  has a density of  $0.08 \text{ g L}^{-1}$  at room temperature and it has melting and boiling points of  $-259.3$  and  $-252.9$  °C, respectively (Figure 1).

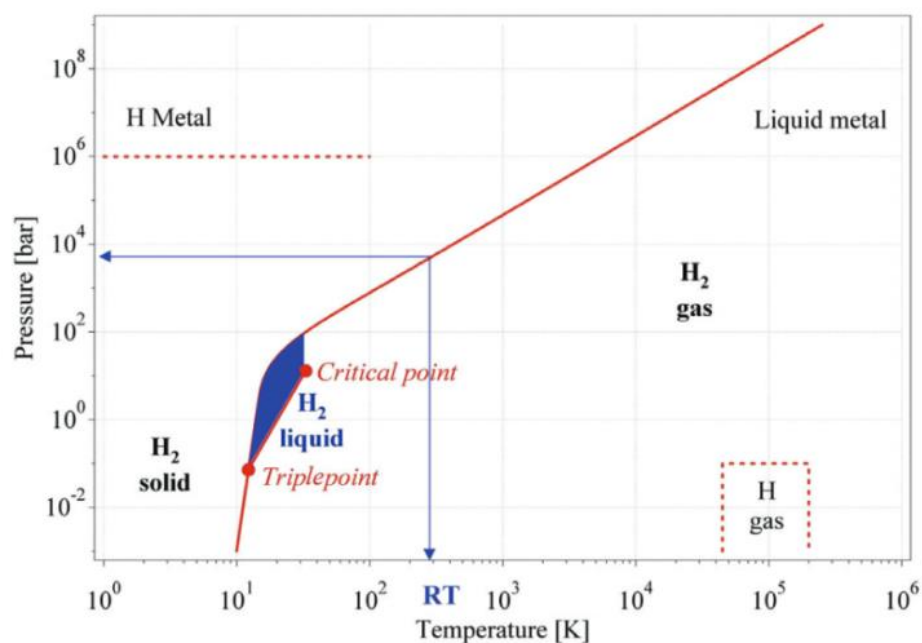


Figure 1. Phase diagram of  $\text{H}_2$ .<sup>1</sup>

H<sub>2</sub> presents two isomeric forms (spin isomers): ortho-hydrogen, when the proton nuclear spins have a parallel alignment; and para-hydrogen, when the proton nuclear spins are aligned antiparallel. At standard conditions, H<sub>2</sub> gas consists of both ortho-hydrogen (75%) and para-hydrogen (25%). H<sub>2</sub> possesses three isotopes: protium (99.985%), deuterium (0.0156%) and tritium (<1 in 10<sup>17</sup> atoms). H<sub>2</sub> can react with different elements. Depending on the element with which it reacts, the H atom can have a partial positive charge H<sup>δ+</sup> (with more electronegative elements) or a partial negative charge H<sup>δ-</sup> (with more electropositive elements). H<sub>2</sub> is a highly flammable gas and it can burn in air. The combustion of H<sub>2</sub> (Equation 1) has an enthalpy of combustion of -286 kJ mol<sup>-1</sup>. The energy released by this reaction allows H<sub>2</sub> to act as a fuel.

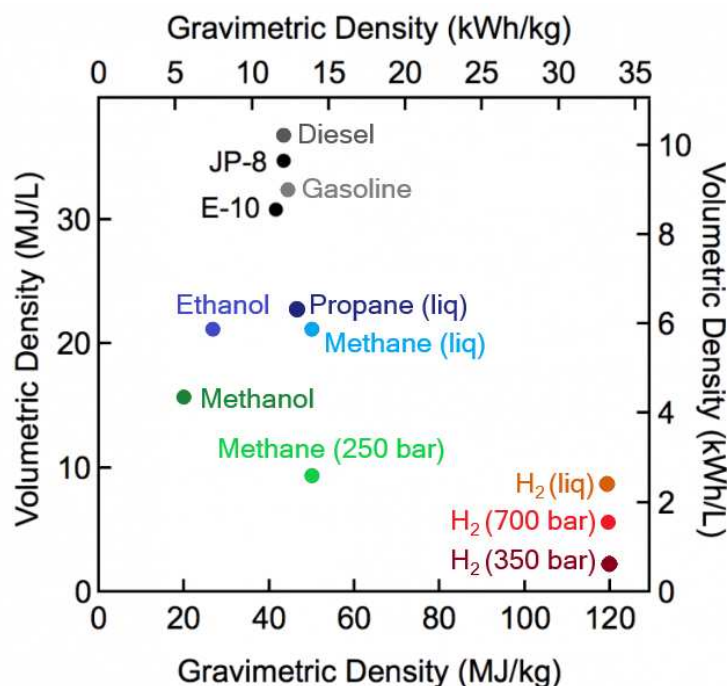


Figure 2. Specific energy and energy density for different fuels based on heating values.<sup>2</sup>

H<sub>2</sub> has a high gravimetric energy density in comparison with other fuels (Figure 2). It has an energy density between 120 and 142 MJ kg<sup>-1</sup>. The lowest value is the lower heating value, and it

assumes that the latent heat of vaporization of water after  $H_2$  combustion is not recovered. The highest value is known as the higher lower heating value and it considers that water is condensed after the combustion of  $H_2$ . This range of energy density is about three times more than fossil fuels. But opposite to fossil fuels,  $H_2$  is a clean and non-toxic fuel, and it has a long-term viability.<sup>3-5</sup> In the concept of an economy based on hydrogen, the fossil fuels will be replaced by  $H_2$ .<sup>6-8</sup> But to reach this goal, some technical issues should be solved: the production, the distribution, the infrastructure, the storage and the conversion technologies.<sup>9,10</sup>

## 1.2 Production of hydrogen

Besides being considered as a fuel,  $H_2$  is also useful for different applications and chemical processes. For example,  $H_2$  is used in the hydrocracking and hydro-processing of hydrocarbons; in the production of organic compounds; in the production of ammonia ( $NH_3$ ) and nitrogen-based fertilizers; in metal refining; as a rocket fuel; and in food preparation.<sup>11-13</sup> In order to obtain  $H_2$ , different chemical processes have been developed. The main processes are presented in Figure 3. The next section briefly describes each one of them.

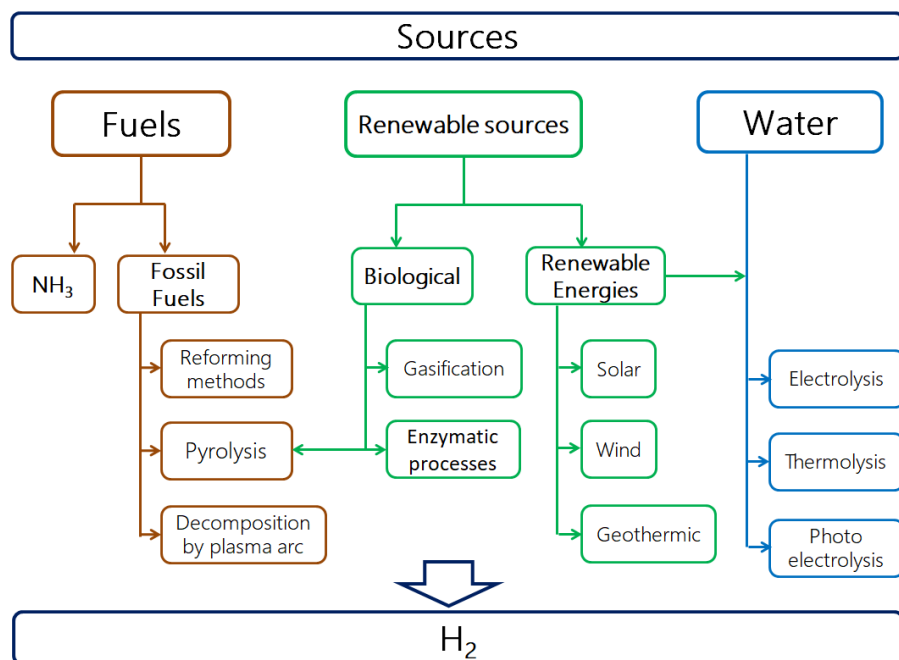


Figure 3. Main  $H_2$  production methods.

## 1.2.1 Hydrogen from fuels

Up to 48% of H<sub>2</sub> is obtained from natural gas, 30% from heavy oils and 18% from coal.<sup>14</sup> Less than 5% is obtained from non-pollutant sources. For a sustainable future, it is indispensable to increase the use of cleaner processes that release less harmful emissions. Nowadays, H<sub>2</sub> is mostly obtained from fossil fuels.

### 1.2.1.1 Hydrocarbon reforming methods

The hydrocarbon reforming is a process in which the hydrocarbon fuel is transformed into H<sub>2</sub> through reforming techniques. The most used reforming technologies are the steam methane reforming (SMR), partial oxidation (POX) and auto-thermal reforming (ATR) processes.<sup>15</sup> SMR is the most used process to produce H<sub>2</sub>,<sup>13</sup> where natural gas or methane reacts with steam (Equation 2) in the presence of a catalyst (usually nickel-based), producing H<sub>2</sub> and carbon oxides. In a further step, additional H<sub>2</sub> is obtained through the reaction of carbon monoxide (CO) and steam (Equation 3). This process requires temperatures between 700-1100°C, pressures up to 3.5 MPa and a ratio steam/carbon of about 3.5. This is a well-known H<sub>2</sub> production process in the industry, but it is the one with the highest emissions of CO<sub>2</sub> to the atmosphere.

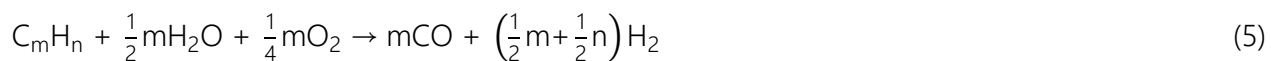


The partial oxidation process is used to convert hydrocarbons into H<sub>2</sub> through the partial oxidation of the hydrocarbon with oxygen (Equation 4). This process can work with any kind of liquid/gaseous fuel and without a catalyst. The main disadvantages of this process are the high temperatures required (1150-1320°C) and that CO is produced.



Finally, the auto-thermal reforming process involves the mixture of the steam methane reforming and the partial oxidation. The principle is to carry out the reforming and oxidation reactions simultaneously, introducing oxygen and steam into the reactor (Equation 5). The advantage of

this method is that it requires lower working temperatures ( $\sim 700^\circ\text{C}$ ). However, it produces CO this process is industrially limited.<sup>15</sup>



### ***1.2.1.2 Hydrocarbon pyrolysis***

The pyrolysis is a process where the hydrocarbon is thermally decomposed in the absence of air and water, obtaining carbon and  $\text{H}_2$  (Equation 6). The nature of the pyrolysis products (gas, liquid and/or solid) can be adjusted modifying variables such as the temperature, heating rate and residence time in the reactor.<sup>16</sup> The advantages of this process include its simplicity, fuel flexibility, the reduction of carbon oxides emissions. However, if oxygen and/or water are present during the pyrolysis, the release of such carbon compounds is not avoided.

In comparison with other processes, the pyrolysis is more energetically efficient. For example, 1 mol of  $\text{H}_2$  obtained from the pyrolysis of methane will require only  $37.8 \text{ kJ mol}^{-1}$  while in the steam reforming process,  $63.3 \text{ kJ mol}^{-1}$  are required.<sup>17</sup>



### ***1.2.1.3 Methane decomposition by plasma arc***

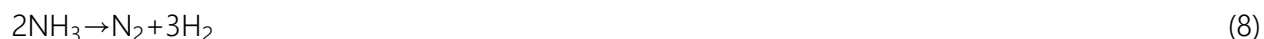
Plasma is the state of matter that consists of a gas of ions and electrons in an excited state. Thanks to the presence of the electrically charged particles, it can release high voltage electric current. For example,  $\text{CH}_4$  can be decomposed by the thermal activity of plasma (Equation 7):<sup>18</sup>



The working temperature of this process is of about  $1700\text{-}1800^\circ\text{C}$ . Conversion of 100% has been achieved with this method, and with zero emissions of carbon oxides.<sup>19</sup> The main challenge for this technology is to reduce the cost of the energy required to produce the plasma.

### **1.2.1.4 Ammonia cracking**

Ammonia has a higher energy density (8.9 kWh kg<sup>-1</sup>) than ethanol and methanol, but lower than diesel or gasoline (Figure 2). It is used in the production of fertilizers, but it also has been considered as a fuel for solid oxide fuel cells (SOFC).<sup>20</sup> The industrial synthesis of ammonia (Haber-Bosch process) comprises the reaction between N<sub>2</sub> and H<sub>2</sub> in the presence of a metal catalyst that will determine the temperature of the process.<sup>21</sup> Normally, the reaction takes place at 15-25 MPa and between 400 and 500°C. The most used catalysts in the Haber-Bosch process are based on iron oxide, ruthenium, nickel and molybdenum.<sup>15</sup> H<sub>2</sub> can be obtained by the inverse synthesis reaction, called ammonia cracking (Equation 8), that is an endothermic process (383 kJ mol<sup>-1</sup>) which requires operating temperatures between 850 and 950°C.



## **1.2.2 Hydrogen from water**

Water is one of the most abundant compounds on Earth and it can be used in the production of H<sub>2</sub>. The commercial use of this process started at the end of the XIX century,<sup>15</sup> but an intense research on an efficient splitting of water into H<sub>2</sub> and O<sub>2</sub> started in recent decades. This research has focused in three main splitting processes: water electrolysis, water thermolysis and water photo-electrolysis.

### **1.2.2.1 Water electrolysis**

Among the water splitting methods, water electrolysis is the most basic industrial process and it produces highly pure H<sub>2</sub> (>99.999%).<sup>22</sup> Water electrolysis is an electrochemical reaction that splits water into H<sub>2</sub> and O<sub>2</sub> with the help of an electrolyzer. This device consists on a cathode and an anode immersed in an electrolyte. When an electrical current with a potential of 1.23 V is applied in the system, water is separated into its components (Equation 9).



Different types of electrolytes can be used. For example, soluble salts based on Na or Li, acid electrolytes or solid polymer electrolyte in proton-exchange membrane fuel cells. The use of a catalyst can also be considered to increase the rate of the reaction and current density. Platinum-based catalysts are the most used for water splitting.<sup>18</sup> Despite the extremely pure H<sub>2</sub> that can be obtained with this method, the high costs related to the electricity has prevented a feasible implementation at large-scale yet.<sup>23</sup>

### **1.2.2.2 Water thermolysis**

Water thermolysis is the decomposition of water into H<sub>2</sub> and oxygen by action of the temperature. However, this reaction has a thermodynamic limitation: the Gibbs free energy of the reaction needs to be near zero and for this, temperatures above 2500°C are required.<sup>24</sup> The difficulties that represent to work at such conditions have complicated the implementation of this technology. In order to overcome this limitation, different thermochemical processes (i.e. Ispra Mark 9 or Shell process) have been proposed to increase the global efficiency of the reaction.<sup>25</sup>

### **1.2.2.3 Water photo-electrolysis**

In water photo-electrolysis, visible light is used to decompose the water into H<sub>2</sub> and oxygen. In principle, it is similar to electrolysis but this technology uses a semiconductor and photo-electrodes to split H<sub>2</sub>O. Different materials with photoelectrocatalytic effect have been tested as electrodes, such as Sb<sub>2</sub>S<sub>3</sub>, ZnS, p-SiC/Pt or TiO<sub>2</sub>.<sup>26-29</sup> The materials used as electrodes and semiconductors determine the efficiency of the system. This technology is still in an early stage, so the H<sub>2</sub> production cost is estimated on 10.36 \$ kg<sup>-1</sup>, which is high in comparison with fossil fuel reforming (0.75 \$ kg<sup>-1</sup>) and plasma arc decomposition (0.85 \$ kg<sup>-1</sup>).<sup>18</sup> The expected price for H<sub>2</sub> obtained by photo-electrolysis is 2.3 \$ kg<sup>-1</sup> for 2020.<sup>30</sup>

## **1.2.3 Hydrogen from renewable sources**

The production of H<sub>2</sub> from fossil fuels has reached the maturity in the industry, but the main problem with those processes is the release of hazardous gases to the atmosphere. In addition, the extraction of fossil fuels represents an environmental risk. The only alternative is the

development and implementation of H<sub>2</sub> production technologies from cleaner sources, such as the renewables ones. The following are examples of technologies that can produce H<sub>2</sub> with a lower environmental impact.

### ***1.2.3.1 Hydrogen from biological sources***

The biological production of H<sub>2</sub> can be performed at room conditions, which represents a big advantage over other processes. Other advantage is that different waste materials can be used to produce H<sub>2</sub>, contributing to the recycling of waste products from other industries. For example, biomass is the most viable organic substitute to petroleum, and it can be obtained from different sources like agricultural/livestock waste, municipal solid wastes, and aquatic plants.<sup>15</sup> Thermochemical processes are widely used in the conversion of biomass into H<sub>2</sub>. For example, biomass gasification uses oxygen, steam or air (or a mixture of all of them) in a temperature range of 700-1200°C to produce a gas consisting mainly of H<sub>2</sub>, CO, CO<sub>2</sub> and CH<sub>4</sub>.<sup>31,32</sup> From a typical biomass, the stoichiometric yield of H<sub>2</sub> expected is 14.3 wt. % (Equation 10). In real processes, this yield tends to be lower as by-products like char, tar and CO<sub>2</sub> are formed.<sup>22</sup> The gasification process depends on different parameters such as the type of biomass used, the reactor design and the gasification medium. Other important aspect of the process is the catalyst, since it has a key role on the reaction: the correct selection of an appropriate catalyst will lead to an increase on the gas production and its quality while lowering the costs. Different catalysts such as ZnO<sub>2</sub>, Ca(OH)<sub>2</sub>, clay or cement kiln can be used.<sup>33</sup>



Pyrolysis of biomass is another attractive thermochemical conversion process for H<sub>2</sub> production. After the biomass pyrolysis, a catalytic steam reforming process can be done in order to obtain bio-oil. These two steps can be carried out at two different places, which benefit small-scale applications and benefits the economic efficiency of the process. The potential yield of H<sub>2</sub> from pyrolysis is 13 wt. %.<sup>22</sup>

A third option are the enzymatic processes. Enzymatic processes for H<sub>2</sub> production are classified as follows: (i) biophotolysis of water using algae and cyanobacteria, (ii) photodecomposition of

organic compounds by photosynthetic bacteria, (iii) fermentation from organic compounds; and (iv) hybrid systems.<sup>34</sup> The processes are controlled by H<sub>2</sub>-producing enzymes (hydrogenase, nitrogenase).<sup>35</sup> However, these methods have not been proved at large-scale yet.

### ***1.2.3.2 Hydrogen from renewable energy***

The use of renewable energies for H<sub>2</sub> production is one of the most sustainable options. The energy required to perform some of the processes aforementioned can be supplied from renewable sources. For example, solar energy has been used to perform water electrolysis by two different ways: (i) photo-electrochemical water splitting, which uses the sunlight to convert water into oxygen and H<sub>2</sub> and (ii) photovoltaic electrolysis, which consists of photovoltaic modules that use electrolyzer units.<sup>36</sup> Wind energy can also be used to provide the required energy for the water electrolysis. Another option is the harness of the thermal and electric energy obtained by geothermal sources that can be used in thermal cycles or electrolysis, to produce H<sub>2</sub>.<sup>37</sup>

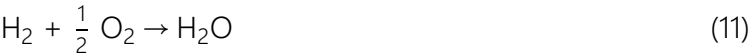
As discussed before, fossil fuels are still the main source for H<sub>2</sub> but, there are other options with the potential to produce H<sub>2</sub> without releasing hazardous emissions to the atmosphere. However, to have a feasible and competitive sustainable technology, different factors have to be considered and evaluated, such as the life cycle, costs, impact on the environment and sustainability of each one of the processes.<sup>38</sup>

## **1.3 Energy from hydrogen**

### **1.3.1 Fuel cells**

One of the most promising technologies that can provide energy and even compete with internal combustion engines and batteries are fuel cells.<sup>39</sup> A fuel cell is an electrochemical device that converts chemical energy directly into electrical energy, using a fuel and an oxidant.<sup>40</sup> Fuel cells consist of an electrolyte between two porous electrodes (anode and cathode) containing a catalyst. The electrolyte allows the ions to move between the electrodes. The chemical reactions take place at the surface of the electrodes: H<sub>2</sub> and O<sub>2</sub> are feed to the fuel cell and they react to produce electricity. Ethanol, methanol, ammonia and hydrazine are examples of fuels that can be

used.<sup>41</sup> The overall reaction in fuel cells is the inverse of the water electrolysis (Equation 11). Fuel cells have the potential to be used in both portable or stationary applications.



Different types of fuel cells exist (Figure 4), but the most common are the polymer electrolyte membrane fuel cells (PEMFCs), alkaline fuel cells (AFCs), phosphoric acid fuel cells (PAFCs), molten carbonate fuel cells (MCFCs) and solid oxide fuel cells (SOFCs).<sup>40,42</sup> The classification is based on the type of electrolyte of each fuel cell. Depending on the chosen electrolyte, other parameters change, like the type of fuel, the catalyst or the operating temperature.

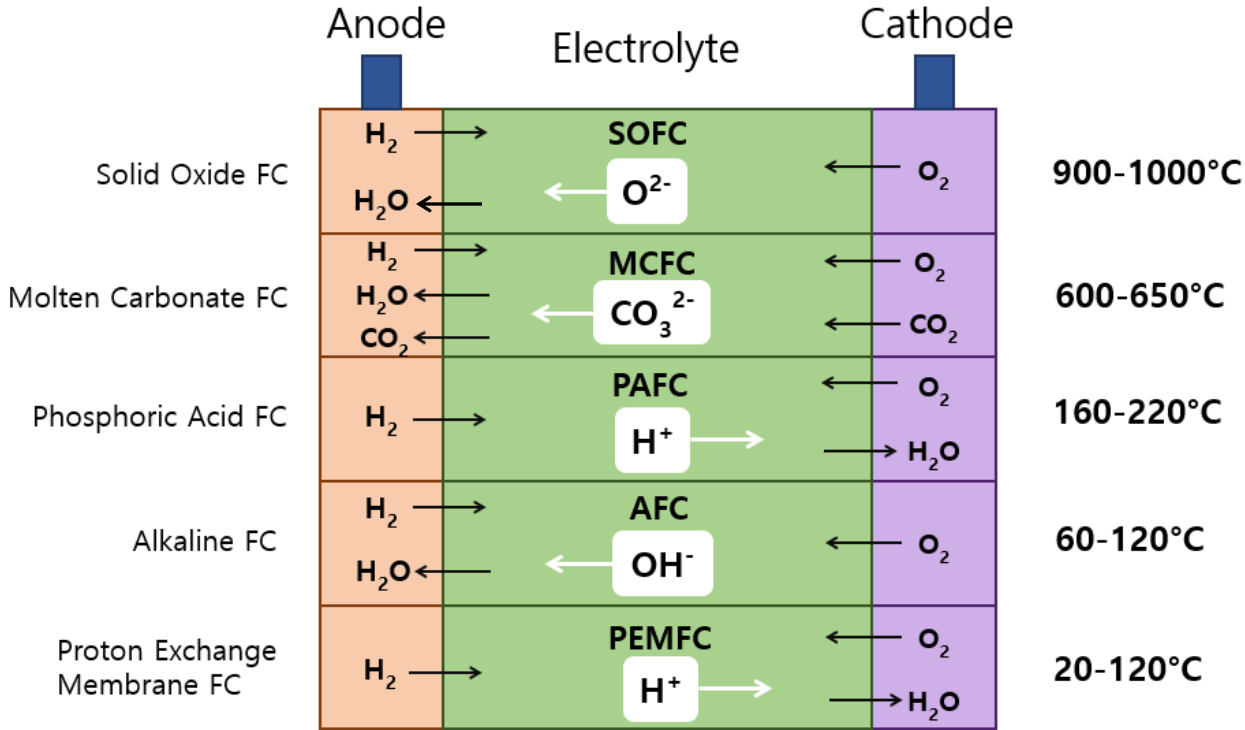


**Figure 4.** Summary of main types of fuel cells describing the feedstock, products, range of working temperature and ions exchanged through the electrolyte. Adapted and modified from <sup>42</sup>.

However, there are other types of fuel cells in development. In recent years, the anionic alkaline exchange membrane fuel cells (AAEMFCs) have bloomed.<sup>43-45</sup> In the case of the AAEMFCs the ion

(OH<sup>-</sup>) is transported from the cathode to the anode. At difference of the PEMFCs, the AAEMFCs create an alkaline pH environment in the cell which have some advantages:<sup>46</sup> (i) the use of Pt-free or precious group metal free catalysts is possible; (ii) different fuels, like nitrogen-based fuels such as hydrazine or ammonia, can be used as feedstock; and (iii) the materials for these fuel cells are cheaper. However, AAEMFCs still have some challenges ahead, like the compatibility of the polyhydrocarbon-based membranes with the electrodes, the stability of the hydroxide ion and the scale-up of the cell.<sup>47</sup>

As mentioned before, fuel cells can provide energy for portable applications. In the last years, portable electronic devices have received attention and market demand, due to its simplicity and convenience for our lives. However, these applications demand compact and long-life power sources, low weight and a long operation.<sup>48</sup> Some fuel cells have been adapted to fulfill these requirements. One example is the direct borohydride fuel cell (DBFC), which uses the chemical energy stored in the borohydride ion (BH<sub>4</sub><sup>-</sup>) as fuel and O<sub>2</sub> as oxidant, according to the reactions at the anode (Equation 12) and the cathode (Equation 13).<sup>49</sup> Usually, a DBFC uses an alkaline solution of sodium borohydride NaBH<sub>4</sub>.



The DBFC presents some advantageous features. For example, NaBH<sub>4</sub> solutions are safely to handle: they are stable under air and they are nonflammable; besides, the products of the reaction in the fuel cell are environmentally safe and can be recycled back to NaBH<sub>4</sub>.<sup>50</sup> However, DBFC also present drawbacks: the fuel undergo through side reactions, the poisoning of the catalyst at the electrodes, the durability, and the cost and operation at long term.<sup>51</sup>

### 1.3.2 Batteries

Even if the metal ion batteries dominate the energy storage field, there have been some attempts to develop batteries that operate with H<sub>2</sub>. Dargily *et al.*<sup>52</sup> worked on a device that has a Pt-electrocatalyst supported on carbon as anode and a benzoquinone-based cathode, separated by

an  $H^+$  ion conducting membrane. In their configuration, the electrons generated from the oxidation of  $H_2$  migrate from the anode to the cathode through the membrane, prompting the conversion of benzoquinone to hydroquinone. This mechanism allows a rechargeable system. Hsu *et al.*<sup>53</sup> and Boddien *et al.*<sup>54</sup> worked in a rechargeable  $H_2$  battery based on the hydrogenation of  $CO_2$  to formic acid (charging process) and the decomposition of formic acid to  $CO_2$  (discharging process), mediated by a ruthenium catalyst. At difference from normal electron-based batteries, in these devices  $H_2$  is used as the energy carrier. This system has a limitation of 4.4 wt. %  $H_2$  content, but is fully reversible. Such devices were able to perform five cycles of charging-discharging without loses in storage capacity. However, these batteries still have some technical issues like the necessity of solid  $CO_2$ .

## 2. Hydrogen storage

Even if some of the  $H_2$ -based technologies are already available in the market, there is still a big issue in order to supply  $H_2$ : its storage. The U.S. Department of Energy (DOE) recognized  $H_2$  storage as the most challenging problem for the hydrogen economy.<sup>55</sup> The targets established by the DOE for 2025 for light-duty vehicles include: specific energy of  $1.8 \text{ kg } H_2 \text{ kg}^{-1}$ , energy density of  $1.3 \text{ kg } H_2 \text{ L}^{-1}$ , cost of  $9 \text{ \$ } \text{kg}^{-1}$  and an operating temperature between  $-40$  and  $85^\circ\text{C}$ .<sup>56</sup> Unfortunately, no existing systems meet these conditions. The remaining challenges for  $H_2$  storage technologies comprise the weight, volume, efficiency, safety and cost of the system. At present,  $H_2$  storage technologies consist of high-pressure tanks, liquefaction at cryogenic conditions and the storage into a host material.

### 2.1 Compressed hydrogen

$H_2$  can be stored in suitable tanks, cylinders or containers at high pressure, up to 700 bar. Three main applications for high pressure vessels can be identified: stationary, vehicular and bulk transportation.<sup>57</sup> The stationary storage is used in  $H_2$  refueling stations because of the low cost. Storage in vehicles should meet three characteristics: high density, light weight of the vessel and

low cost. The bulk transportation of  $H_2$  is used to deliver it from its production to the end user, and it requires of a high capacity and a lightweight to optimize the costs.

$H_2$  storage at high pressure presents advantages: the concept of the technology is simple, the fast release rate of the gas and the reversibility of the process. However, this technology also possesses disadvantages:<sup>58</sup> for transportation and for portable applications, the constraints are the high weight of the vessels, the volume savings and the cost. For stationary applications, the main restriction is the pressure cycle life of the tank. In any case, the safety requirements must be considered. Another problem includes the compatibility of the tank materials and the gas. Finally, there is an additional issue regarding the thermodynamic aspect of the compression: as the process is adiabatic and isentropic, the vessel heats in the inside leading to a loss of exergy. When the vessel cools down to normal storage temperature, there is a loss of pressure and thus of the total  $H_2$  stored.<sup>59</sup> Despite the simplicity and the convenience of the technology for some applications, different storage options with better characteristics are required.

## 2.2 Liquid hydrogen

$H_2$  is a liquid at  $-253^\circ\text{C}$  and atmospheric pressure. It is an attractive option due to the potential to store a large amount of hydrogen that can be easily transported.<sup>60</sup> The vessels to store gases at cryogenic conditions have been used for more than 40 years, and they are composed of an inner pressure vessel with an external jacket to protect it, with an insulator between them.<sup>61</sup> These tanks can store up to  $70 \text{ g L}^{-1}$  of liquid  $H_2$ , which is a higher value compared to the capacity of high pressure tanks ( $30 \text{ g L}^{-1}$ ).<sup>62</sup>

The conventional process to liquefy  $H_2$  follows three steps:<sup>59</sup>

- 1) Compression. Pure and dry  $H_2$  is compressed above its critical point.
- 2) Cooling. This is a double-step process: first,  $H_2$  is cooled down to  $-193 \pm 15^\circ\text{C}$ ; after, the gas is cooled down between  $-251$  and  $-228^\circ\text{C}$ . Heat is removed from the system in each step.
- 3) Expansion.  $H_2$  is depressurized and partially liquefied. Liquid hydrogen is collected in a vessel and the remaining gaseous  $H_2$  is then reinjected to the first compression step.

The storage of liquid H<sub>2</sub> is a good alternative in terms of mass and volume, but it presents some disadvantages. First, the necessary energy to liquefy H<sub>2</sub> represents 30% of the total stored energy of the system.<sup>63</sup> Second, the insulation of the tank is not highly efficient: each day 2-3% of the stored H<sub>2</sub> is lost due to the heating of the vessel.<sup>64</sup> Third, the cost of the tank. Although this technology is very promising, the problems must be overcome in order to assure the feasibility of liquid H<sub>2</sub>.

### 2.3 Hydrogen stored in materials

H<sub>2</sub> stored in a material might be the most promising technology of storage, due to the high H<sub>2</sub> density of different materials. The ultimate targets established by the DOE for H<sub>2</sub> storage materials are a gravimetric density of 0.065 kg-H<sub>2</sub> kg<sup>-1</sup>, a volumetric density of 50 g H<sub>2</sub> L<sup>-1</sup>, a cost of 266 \$ kg<sup>-1</sup> H<sub>2</sub> and a performance near ambient conditions.<sup>65</sup> H<sub>2</sub> can be stored by physical or chemical interactions into a material, and this allows a higher storage capacity compared with the other technologies (Figure 5). In the next section, some of the materials used for chemical or physical H<sub>2</sub> storage in the solid state are described.

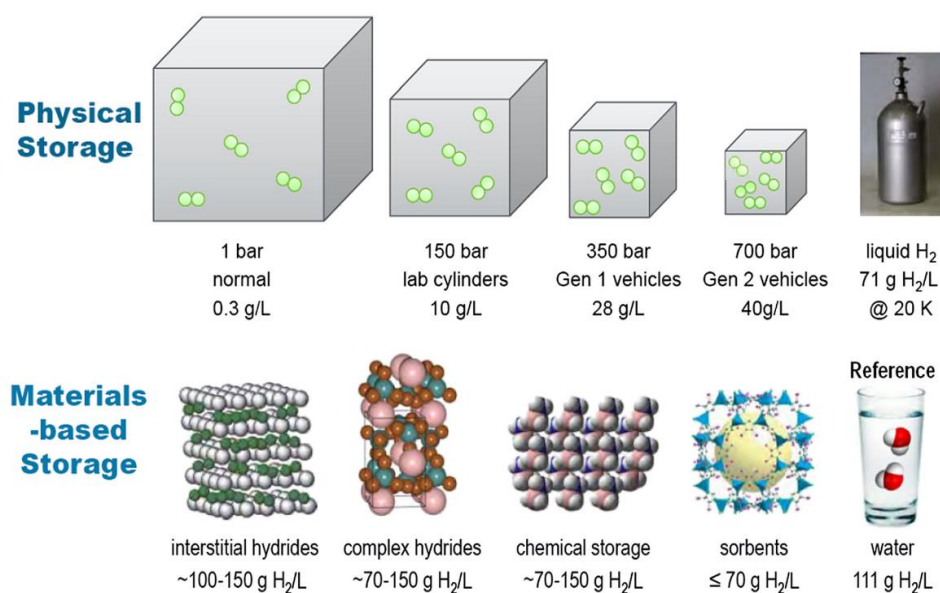


Figure 5. Materials-based H<sub>2</sub> storage versus compressed and cryogenic storage systems.<sup>66</sup>

### 2.3.1 Physisorption of hydrogen

H<sub>2</sub> can be stored as a molecule by physical adsorption on the surface of a porous solid material. According to the IUPAC, there are three types of porous materials: macroporous (pore size >50 nm), mesoporous (pore size between 2 and 50 nm), and microporous materials (pore size <2 nm). The physisorption of a gas is a cyclic reversible process of adsorption/desorption in the surface of a porous solid, where the involved species do not experiment any change or decomposition. The physical adsorption of H<sub>2</sub> on an adsorbent surface is caused by weak interactions (van der Waals or London dispersion forces). This relatively low binding energy allows an 'easy' release of H<sub>2</sub> from the material. For example, for metal organic frameworks, low binding enthalpies in the range of 4-10 kJ mol<sup>-1</sup> are insufficient to hold H<sub>2</sub> molecules on the surface of the material, causing a low storage capacity at room temperature. Some reports have suggested that the ideal heat of adsorption for a determined material is 20-30 kJ mol<sup>-1</sup> to operate at room temperature.<sup>67</sup> In contrast, high enthalpies in the range of 40-100 kJ mol<sup>-1</sup> will favor the chemisorption of H<sub>2</sub>, leading to a 'harder' release of the molecule, poor reversibility and slow kinetics.

A good candidate to store H<sub>2</sub> by physisorption should consider different parameters like the binding energy between H<sub>2</sub> and the selected material, the pore size, the bulky density of the solid and especially, the specific surface area.<sup>68,69</sup> The advantages of physisorption over chemisorption are fast kinetics, reversibility of the process and low heat produced while refueling; while the main disadvantage is that high storage capacities are obtained at low temperatures (-196°C).<sup>70</sup> Different porous materials have been studied as hosts for H<sub>2</sub>. Some of them are briefly discussed in the following section.

#### *2.3.1.1 Carbon materials*

Different structures based on carbon exist due to the partially filled sp<sup>2</sup> orbitals of the carbon atom. Each atom can bind with up to seven neighboring carbon atoms, leading to the formation of different structures such as activated carbon, diamond, fullerenes, graphene, and nanotubes. These compounds have pores of different sizes which are good places for gas physisorption.

Carbon atoms also have the propensity to bind to other atoms or molecules, making it suitable as a H<sub>2</sub> storage material. It has been reported that these materials can adsorb up to 5.5 wt. % H<sub>2</sub>.<sup>71</sup> However, carbon-based materials adsorb H<sub>2</sub> at high pressure or cryogenic temperatures (or both).

Activated carbons are materials with specific surface areas up to 3000 m<sup>2</sup> g<sup>-1</sup>. They have been widely studied as H<sub>2</sub> storage materials. However, the adsorption of H<sub>2</sub> must be done at cryogenic conditions and at high pressure: it has been reported that only 1 wt. % H<sub>2</sub> is adsorbed by activated carbons at room temperature and at 100 bar.<sup>72</sup> There are some approaches to increase the uptake of H<sub>2</sub> in activated carbons. One is to control the pore size of the material. Zhao *et al.*<sup>73</sup> found that uptakes higher than 3 wt. % H<sub>2</sub> are due to the presence of pores with a diameter above 0.7 nm. Another approach is to dope the carbon atoms with other elements. Wang *et al.*<sup>74</sup> worked with activated carbon doped with nitrogen atoms with different pore widths. They obtained an uptake of 2.96 wt. % H<sub>2</sub> at 1 bar and -196°C. Sethia and Sayari<sup>75</sup> achieved an uptake between 4.23-6.77 wt. % H<sub>2</sub> at -196°C and 20 bar from an activated carbon doped with nitrogen; the content of H<sub>2</sub> differs in relation with the surface area of the carbon.

Carbon nanotubes are one of the most investigated materials for H<sub>2</sub> storage based on carbon. The nanotubes are obtained in two different types: single-walled carbon nanotubes (SWCNT) and multi-walled carbon nanotubes (MWCNT). Basically, SWCNT consist of a graphene sheet rolled up into a cylinder with nanometer diameter and microns length. Dillon *et al.*<sup>76</sup> were the first to report experimental data of H<sub>2</sub> adsorption in SWCNT, and estimated a gravimetric storage density from 5 to 10%. More recently, the surface of carbon nanotubes has been modified to enhance H<sub>2</sub> sorption. Rajaura *et al.*<sup>77</sup> worked on the functionalization of carbon nanotubes with an acidic treatment. They increased the gravimetric H<sub>2</sub> storage capacity from 0.65 wt. % to 0.89 wt. % with the functionalized nanotubes at room temperature and high pressure. Other approach to improve the uptake of H<sub>2</sub> is to incorporate precious metals, such as palladium, to the surface of the carbon nanotubes.<sup>78,79</sup> Pd allows a high adsorption of H<sub>2</sub> at room conditions. This is because at the surface of the Pd, the dissociative adsorption of H<sub>2</sub> molecules presents a negligible activation energy barrier.<sup>80</sup>

Graphene is a 2D carbon material which theoretically can store up to 8.3 wt. %  $H_2$ .<sup>81</sup> Klechikov *et al.*<sup>82</sup> reported a high  $H_2$  uptake of ~5 wt. %, at  $-196^\circ C$  and 10 bar working with a bulk graphene with a surface area of  $2300 \text{ m}^2 \text{ g}^{-1}$ . Nevertheless, they conclude that bulk-graphene materials do not exhibit superior  $H_2$  storage parameters in comparison with other carbon-based materials, as experimentally they present a similar uptake as activated carbon, carbon nanotubes or nanofibers. As determined for other carbon materials, the functionalization of graphene with different atoms can enhance  $H_2$  adsorption.<sup>83</sup> A comparison between different  $H_2$  storage systems including graphene systems is shown in Figure 6.

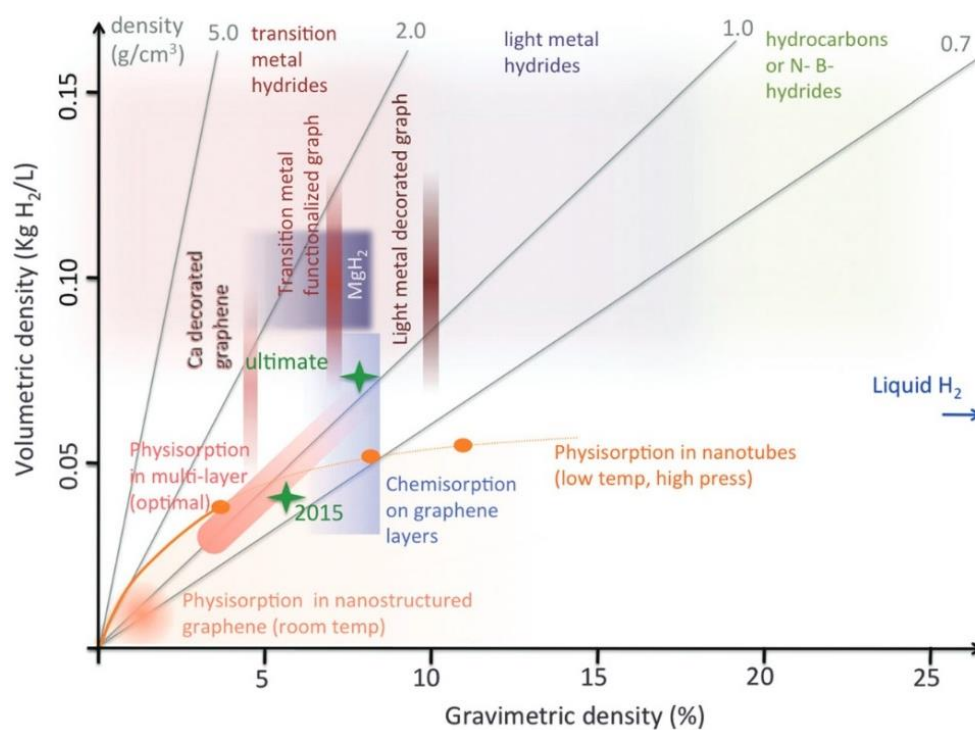


Figure 6. Gravimetric vs. volumetric density for different  $H_2$  storage systems.<sup>81</sup>

### 2.3.1.2 Zeolites

Zeolites are materials with the general formula  $M_{n/x}(Al_nSi_mO_{2(n+m)}) \cdot yH_2O$  where  $M$  is the counterbalancing cation. Zeolites are usually used as molecular sieves, ion exchangers or catalysts.<sup>84</sup> These materials have a regular open pore microstructure with different frameworks

and have been tested as H<sub>2</sub> storage materials, due to some advantageous characteristics: they are inexpensive, environmentally friendly, thermally stable and their ion-exchange property can be easily exploited.<sup>85</sup> It has been reported that the H<sub>2</sub> uptake in these materials depends on factors such as the framework structure and the radius and density of the cation.<sup>86,87</sup> Several types of zeolites have been tested, reaching a H<sub>2</sub> uptake between 0.08-2 wt. %.<sup>88</sup> In a recent computational work, Martin-Calvo *et al.*<sup>89</sup> analyzed 219 zeolites and evaluated parameters like the saturation capacity, the pore size distribution and the curves of H<sub>2</sub> adsorption. They determined that at extreme conditions (100 MPa and -248°C) only six of the analyzed zeolites have the potential of store 7 wt. % H<sub>2</sub>.

Like for other porous materials, computational studies have suggested that doping a zeolite with metal atoms can improve the uptake of H<sub>2</sub>. Ozturk found that dispersed lithium in a pure silica zeolite (CHA-type) can increase the H<sub>2</sub> storage capacity between 3 and 6 times in comparison with the pristine zeolite.<sup>90</sup> Sun *et al.*<sup>91</sup> also analyzed a zeolite (FAU type) by computational methods, finding that the adsorption of H<sub>2</sub> can be enhanced with the introduction of silver atoms in the framework. At -196°C and 5 bar of pressure, the zeolites can store 16.4 g L<sup>-1</sup> of H<sub>2</sub>, in comparison with the 9.2 g L<sup>-1</sup> of the pure zeolite.

### **2.3.1.3 Metal organic frameworks**

Metal organic frameworks (MOFs) are structures composed of inorganic and organic units linked by strong bonds. MOFs have a high crystallinity and their surface area range between 1000 and 10 000 m<sup>2</sup> g<sup>-1</sup>, surpassing those of other porous materials like zeolites and carbon-based materials.<sup>92</sup> These microporous structures have been considered as H<sub>2</sub> storage materials due to their high crystallinity, purity and porosity, in addition to their controllable structural characteristics. The first work that reported H<sub>2</sub> storage in a MOF was done by the group of Yaghi,<sup>93</sup> where they achieved a H<sub>2</sub> uptake of 4.5 wt. % at -195°C and 1 wt. % at room temperature and 20 bar, in the MOF-5. In a further work, the same research group concluded that the interaction between H<sub>2</sub> and the framework of the MOFs can be improved by changing the chemical nature of the organic linker.<sup>94</sup> After these works, it was reported that the adsorption of a gas into a MOF is also strongly dependent on the metal atom.<sup>95</sup> Other relevant approach to

improve the adsorption of H<sub>2</sub> on the MOFs is to dope them with electropositive metals, such as lithium, sodium or magnesium.<sup>96–99</sup>

Due to the huge number of MOFs that can be used for H<sub>2</sub> storage applications, it is difficult to determine the right material with the optimal characteristics. Ahmed *et al.*<sup>100,101</sup> did a systematic assessment of 500 000 MOFs to evaluate their storage capacity. Three of them were selected: SNU-70 (Metal: Zn; linker: 4-(2-carboxyvinyl)-benzoic acid), UMCM-9 (Metal: Zn; linker: H<sub>2</sub>BDC and H<sub>2</sub>NDC) and PCN-610/NU-100 (Metal: Cu; linker: hexatopic carboxylate LH<sub>6</sub>), having a usable gravimetric capacity between 10.6 and 13.9 wt. %. This group also established a volumetric ceiling of 40 g H<sub>2</sub> L<sup>-1</sup> as H<sub>2</sub> adsorbents. However, on a recent study Chen *et al.*<sup>102</sup> reported the synthesis of two highly porous materials, NU-1501-M (Metal: Al or Fe; linker: triptycene-based). The aluminum-based material has a H<sub>2</sub> storage capacity of 14.5 wt. % (47.9 g L<sup>-1</sup>) at 100 bar and -196°C while the iron-based showed 13.2 wt. % (45.4 g L<sup>-1</sup>) under the same conditions. Based on these results, it is evident that MOFs are good candidates for H<sub>2</sub> storage, but further work is still required to achieve a high H<sub>2</sub> uptake at near ambient conditions.

### 2.3.1.4 Clathrate hydrates

A clathrate hydrate is a crystalline compound formed by solid water, which resembles ice, in which a gas molecule is trapped inside. These H<sub>2</sub>-bonded water frameworks can build cages around H<sub>2</sub> molecules. During its formation, the gaseous molecules are hosted in the solid cavities, which increase the density of the guest gas.<sup>103</sup> Two common structures for clathrate hydrates have been identified: (i) hydrates with structure I (sI), consisting of two pentagonal dodecahedron (5<sup>12</sup>) and six tetrakaidecahedron (5<sup>12</sup>6<sup>2</sup>) cages per unit cell; and (ii) hydrates with structure II (sII), consisting of sixteen 5<sup>12</sup> and eight 5<sup>12</sup>6<sup>4</sup> cages per unit cell (Figure 7).

In 2004,<sup>104</sup> Mao and Mao reported a sII clathrate synthesized (5.3 wt. % H<sub>2</sub>) at 200–300 MPa and between -33 and -24°C that could release H<sub>2</sub> at ambient pressure and -133°C. The same year, Florusse *et al.*<sup>105</sup> suggested the use of a promoter, like THF, to improve the storage of H<sub>2</sub> in the clathrate. In this way, the THF molecules would fill the bigger cavities of the clathrate, leaving the smaller cavities for H<sub>2</sub>. They estimated a theoretical value of 4 wt. % H<sub>2</sub>.

In fact, Lee *et al.*<sup>106</sup> achieved the 4 wt. % H<sub>2</sub> in a clathrate synthesized at 12 MPa and 4°C, adding 0.15 mol % of THF. However, they realized that the H<sub>2</sub> occupied both larger and smaller cavities of the clathrate. Clathrate hydrates are safe and environmentally friendly materials. Nevertheless, they present important disadvantages: (i) to synthesize them, high pressures are needed, (ii) slow kinetics of formation and (iii) they are stable only under cold conditions.<sup>107</sup>

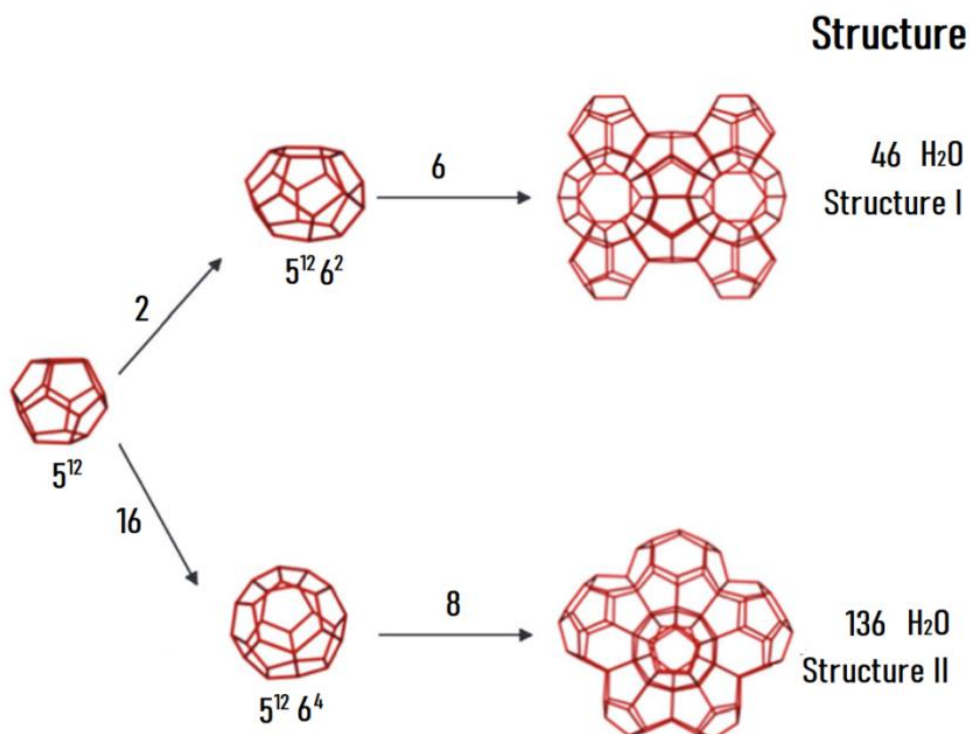


Figure 7. Structure I and II of clathrate hydrates.<sup>108</sup>

### 2.3.2 Chemisorption of hydrogen

In the chemical H<sub>2</sub> storage, a H<sub>2</sub> atom is chemically bonded or complexed into a material. This means that the H<sub>2</sub> uptake/release process implicates the formation and rupture of chemical bonds. The stability of these materials depends on the pressure and temperature. H<sub>2</sub> is released from the compound when it is subjected to thermal or catalytic decomposition. The principal challenges of chemical adsorption are the reversibility of the process, the storage capacity and the stability of

the material.<sup>70</sup> Table 1 presents the most investigated compounds considered for H<sub>2</sub> storage with their respective H<sub>2</sub> storage capacity, the starting decomposition temperature and other properties. Binary, intermetallic and complex hydrides are typical examples of materials that chemically store H<sub>2</sub>.

**Table 1.** Hydrides considered for H<sub>2</sub> storage. Adapted from references <sup>109–111</sup>.

Hydride	Molecular weight (g mol <sup>-1</sup> )	Density (g cm <sup>-3</sup> )	H <sub>2</sub> content		T <sub>dec</sub> (°C)
			wt. %	g L <sup>-1</sup>	
LiH	7.95	0.77	12.70	102	720
NaH	24.00	1.36	4.20	58	420
MgH <sub>2</sub>	26.32	1.45	7.70	109	330
CaH <sub>2</sub>	42.10	1.7	4.80	81	600
LiBH <sub>4</sub>	21.78	0.67	18.40	122.5	400
NaBH <sub>4</sub>	37.83	1.07	10.80	115.6	505
KBH <sub>4</sub>	53.94	1.17	7.42	87.1	585
Mg(BH <sub>4</sub> ) <sub>2</sub>	53.99	0.78	7.20	100	320
Ca(BH <sub>4</sub> ) <sub>2</sub>	69.76	1.07	5.60	97	260
Al(BH <sub>4</sub> ) <sub>3</sub>	71.51	0.78	16.78	132	480
LiAlH <sub>4</sub>	37.95	0.92	10.6	9750	190
Li <sub>3</sub> AlH <sub>6</sub>	53.85	1.02	11.2	114.20	200
NaAlH <sub>4</sub>	54.00	1.28	7.30	93.40	230
Na <sub>3</sub> AlH <sub>6</sub>	102.00	1.45	5.90	85.60	275
KAlH <sub>4</sub>	70.11	-	5.71	53.20	-
Mg(AlH <sub>4</sub> ) <sub>2</sub>	86.33	-	9.27	72.30	-
Ca(AlH <sub>4</sub> ) <sub>2</sub>	102.10	-	7.84	70.4	230
LiNH <sub>2</sub>	22.96	1.18	8.8	104	200
NaNH <sub>2</sub>	39.01	1.39	5.2	72	280
KNH <sub>2</sub>	55.12	1.62	3.66	59.3	338
Mg(NH <sub>2</sub> ) <sub>2</sub>	56.37	1.39	7.15	99.4	360
Ca(NH <sub>2</sub> ) <sub>2</sub>	72.13	1.74	5.59	97.3	-

### 2.3.2.1 Metal hydrides

Back at the 1960s, it was observed that some intermetallic compounds such as  $\text{LaNi}_5$ ,  $\text{Mg}_2\text{Ni}$  and  $\text{TiFe}$  could reversibly adsorb and desorb  $\text{H}_2$  at reasonable conditions (between  $-23$  and  $377^\circ\text{C}$ ), which started different research works on metal hydrides for energy applications.<sup>112</sup> Since then, an extensive investigation on different hydrides has been performed. Metal hydrides are usually classified in three groups:<sup>113</sup> (i) binary hydrides  $\text{MH}_x$  (such as  $\text{MgH}_2$ ,  $\text{NaH}$ ,  $\text{AlH}_3$ ,  $\text{PdH}_{0.6}$ ); (ii) intermetallic hydrides  $\text{A}_x\text{B}_y\text{H}_z$  (where A is the hydriding metal and B the non-hydriding metal, like  $\text{CeNi}_3\text{H}_4$ ,  $\text{ZrV}_2\text{H}_{5.5}$  or  $\text{Mg}_2\text{NiH}_4$ ); and (iii) complex metal hydrides  $\text{MEH}_x$ , where E is a boron atom in borohydrides, a nitrogen atom in amides, or an aluminum atom in alanates (e.g.  $\text{NaBH}_4$ ,  $\text{LiNH}_2$ ,  $\text{Mg}(\text{AlH}_4)_2$  respectively). Interestingly,  $\text{H}_2$  exists as the negative hydride ion  $\text{H}^-$  in binary hydrides, as dissolved atoms in intermetallic hydrides, and with  $\delta^+$  or  $\delta^-$  polarity in complex hydrides. This is due to the different types of bonding that  $\text{H}_2$  can present: metallic, ionic or covalent bonding, depending on the nature of the hydride.<sup>111</sup>

#### 2.3.2.1.1 Binary metal hydrides

Most of the elements can form stable binary metal hydrides, but just a few have been considered as  $\text{H}_2$  storage materials. Despite a considerable  $\text{H}_2$  storage capacity of the lightest metal hydrides such as  $\text{LiH}$  (12.5 wt. %),  $\text{NaH}$  (4.2 wt. %) and  $\text{CaH}_2$  (4.7 wt. %), they present a high temperature of decomposition ( $\sim 700$ ,  $\sim 400$  and  $\sim 600^\circ\text{C}$ , respectively),<sup>114</sup> which exceeds the desired working conditions expected by the DOE. Other applications can be envisaged for this type of hydrides, like as thermal energy storage materials.<sup>115,116</sup>

On the other side,  $\text{MgH}_2$  is a widely investigated material for  $\text{H}_2$  storage because it has the highest energy density ( $9 \text{ MJ kg}^{-1}$ ) of all reversible hydrides, it has a high gravimetric and volumetric  $\text{H}_2$  storage capacities (7.6 wt. % and  $109 \text{ g H}_2 \text{ L}^{-1}$ ), and Mg is an abundant metal.<sup>117</sup> However,  $\text{MgH}_2$  presents a high decomposition temperature ( $\sim 300^\circ\text{C}$ ), shows slow kinetics and high reactivity in the presence of oxygen. Different approaches to enhance the kinetics and/or thermodynamics of the dehydrogenation of  $\text{MgH}_2$  have been proposed. The nanosizing of  $\text{MgH}_2$  is one of them, where it has been observed that kinetic enhancement occurs even at particle size up to 50 nm,

but the thermodynamic improvements only occur for particle sizes <10 nm.<sup>113</sup> Other approaches include the confinement of the hydride, the use of catalysts, to dope with transition metals or form composites with Mg-based alloys.<sup>118</sup>

### *2.3.2.1.2 Intermetallic hydrides*

Ideally, an intermetallic hydride  $A_xB_yH_z$  is formed from an  $A_xB_y$  compound that will absorb  $H_2$  while releasing heat (Equation 14).



Metal A can form stable binary hydrides (alkaline/alkaline-earth metals, transition metals, and rare-earth metals). Metal B does not form a stable hydride (like Ni, Co, Fe, Mn, Al) but it takes part in the dissociation of  $H_2$ .<sup>112</sup> The properties of these hydrides are largely dependent on their crystalline structure.<sup>119</sup> There are different metal hydride families, but the  $A_2B$ ,  $AB_2$  and  $AB_5$  alloys have showed better  $H_2$  storage properties.<sup>120</sup> Intermetallic hydrides have been used not only for  $H_2$  storage, but also as battery electrodes, catalysts,  $H_2$  purification and cooling systems.<sup>121</sup>

One example is the alloy  $LaNi_5$ , that can absorb up to ~1.5 wt. %  $H_2$ . This compound can form hydrides at a low  $H_2$  pressure and ambient temperature and it can be easily activated.<sup>122</sup> However, one of the disadvantages presented by  $LaNi_5$  is the long-term hydrogen absorption/desorption cycling and the limited hydrogen storage capacity. Research has been done in order to introduce other elements into the alloy (such as Al, Cu or Mg) to reduce the  $H_2$  capacity loss because of the cycling.<sup>123–125</sup> Another example of intermetallic compounds is the iron titanium hydride (storage capacity ~1.9 wt. %  $H_2$ ). The reversible absorption and release of hydrogen of the TiFe alloy at near ambient temperature and low pressures (10–20 bar) was reported for the first time in 1974.<sup>126</sup> In addition, the TiFe hydride is non-toxic, cheap and the abundance of the raw elements is high. Most of the research focused on this compound is about enhancing its activation kinetics and the nanosizing of the material.<sup>127</sup>

However, one of the major drawbacks of intermetallic hydrides is that in the practice it is not possible to obtain more than 2 wt. %  $H_2$  from these materials, due to their high stability.<sup>128,129</sup> For this reason, different efforts have been done in order to improve the storage capacity of

intermetallic hydrides, like to optimize the composition and morphology of the hydrides or the nanoconfinement.<sup>130,131</sup> However, the use of intermetallic hydrides is still limited for on-board applications due to the low storage capacity, slow kinetics and complicated activation procedure.<sup>119</sup>

### 2.3.2.1.3 Complex hydrides

Complex hydrides are composed of light metal cations (such as Na, Li, Mg, Ca) and complex anions in which the hydrogen atoms are covalently bonded to the central atom (like B, Al or N). These hydrides have received attention for solid-state H<sub>2</sub> storage due to their high gravimetric and volumetric H<sub>2</sub> contents.<sup>110</sup> Among the drawbacks of complex hydrides, we can mention a highly endothermic dehydrogenation process and the lack of reversibility.<sup>113</sup>

Borohydrides are compounds that fall in this category. For example, LiBH<sub>4</sub> has a high gravimetric H<sub>2</sub> capacity (18.3 wt. %). It starts to decompose above 320°C, but the major decomposition step takes place between 400 and 600°C.<sup>132</sup> Zuttel *et al.*<sup>133</sup> found that if SiO<sub>2</sub> is added as a catalyst, LiBH<sub>4</sub> can release up to 9 wt. % H<sub>2</sub> below 400°C. However, this is still a high dehydrogenation temperature for on-board applications. Another example is NaBH<sub>4</sub> (10.6 wt. % H<sub>2</sub>), that suffers the same problem: it presents sluggish kinetics and it starts to release H<sub>2</sub> above 500°C.<sup>134</sup> However, NaBH<sub>4</sub> can be hydrolyzed at ambient conditions, due to the spontaneous reaction between the hydridic hydrogens H<sup>δ-</sup> of the BH<sub>4</sub><sup>-</sup> anion and the protic hydrogens H<sup>δ+</sup> of water (Equation 15).<sup>135</sup> In this way, NaBH<sub>4</sub> can release up to 4 equivalents of H<sub>2</sub>.



A last interesting case is Mg(BH<sub>4</sub>)<sub>2</sub> (14.9 wt. %). It has different crystalline phases, but the polymorph γ-Mg(BH<sub>4</sub>)<sub>2</sub> presents a 3D net of channels with a pore size of ~8.8 Å and it is the first metal hydride reported to reversibly adsorb H<sub>2</sub>.<sup>136</sup> This compound opened the research for new metal borohydride frameworks materials.

The alumino-hydrides, or alanates, refer to a family of complex hydrides where a central Al atom is ionically bonded to metal cation and covalently bonded to four hydrogens. After the work

published by Bogdanovic and Schwickardi in 1997, alanates started to receive attention.<sup>137</sup> The main disadvantages of these complex hydrides are their poor kinetics and multistep decomposition.<sup>117</sup> One example is NaAlH<sub>4</sub> (5.5 wt. % H<sub>2</sub>), a widely studied material with a high theoretical H<sub>2</sub> capacity. However, experimentally only a 5 wt. % H<sub>2</sub> has been released. The dehydrogenation takes place in two steps, releasing 3.7 wt. % H<sub>2</sub> in the first step, and 1.8 wt. % H<sub>2</sub> in the second (Equations 16 and 17). However, it has been evidenced that NaAlH<sub>4</sub> is not suitable for on-board applications, but rather it can be used in portable applications as the source of H<sub>2</sub>.<sup>138</sup>



A last example is LiAlH<sub>4</sub> (10.5 wt. % H<sub>2</sub>), which dehydrogenates in three steps. In the first two steps, it can release 7.9 wt. % H<sub>2</sub>, but the onset dehydrogenation temperature and the kinetics are not practical. Different options have been presented to improve the dehydrogenation properties of LiAlH<sub>4</sub> like the using Ti-based catalysts or the destabilization of the hydride with metal halides.<sup>139,140</sup>

Metal amides and metal imides are another type of complex hydrides. Alkali metal amides have been used in the synthesis of organic compounds, but also they have been tested for H<sub>2</sub> storage applications. One example is the LiNH<sub>2</sub>+LiH system, that has been widely investigated.<sup>141</sup> When mixed with LiH, LiNH<sub>2</sub> presents a reversible hydrogen storage capacity of 6.5 wt. % H<sub>2</sub> and with an onset dehydrogenation temperature of 285°C. The mechanism of dehydrogenation has been described in the literature: H<sub>2</sub> is produced in a first step due to the interaction between the H<sup>δ+</sup> of the LiNH<sub>2</sub> and the H<sup>δ-</sup> of LiH, with the release of NH<sub>3</sub>.<sup>142,143</sup> A second desorbing mechanism takes place after (Equations 18 and 19).



The main problem with this system is the production of NH<sub>3</sub>, because it poisons the catalysts in a fuel cell. Besides, Ikeda *et al.*<sup>144</sup> determined that the decay in H<sub>2</sub> capacity of the system is

explained by the emission of  $\text{NH}_3$ . Further works are needed in order to suppress the release of  $\text{NH}_3$  and the kinetic constraints to dehydrogenate the intermediate species formed during the reactions.<sup>145</sup>

In resume, different types of materials have been considered as potential candidates for both physical and chemical  $\text{H}_2$  storage. An overview of the most promising materials is presented in Figure 8. Several of these materials can meet the requirements established by the DOE. However, the main objective of the research on these compounds needs to focus in overcome the drawbacks to obtain a feasible technology. Thus,  $\text{H}_2$  needs to be obtained in an easy way at near ambient temperature, the technology must be efficient and at an affordable cost.

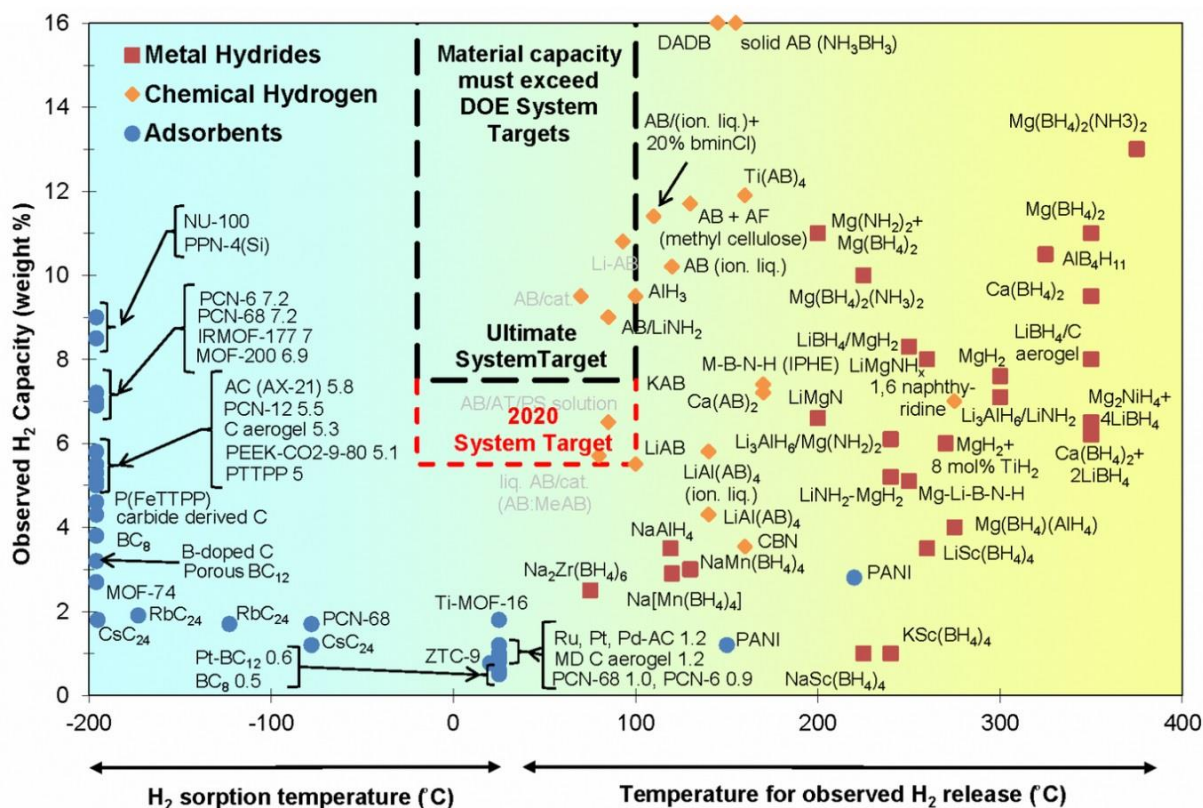


Figure 8. Plot of the observed capacity ( wt. %  $\text{H}_2$ ) of different storage materials as a function of the  $\text{H}_2$  release temperature.<sup>65</sup>

### 3. Boron- and nitrogen-based materials

Reports on the first boron-, nitrogen- and hydrogen-based compounds (BNH) started to be published in the 1950s; but there was no greater interest on these compounds, and the research stopped for 50 years. After this, in the 2000s, BNH materials regained attention due to their potential use as H<sub>2</sub> storage materials.<sup>146–154</sup> BNH compounds have two main advantages over other materials for H<sub>2</sub> storage: (i) both B and N are lightweight elements capable of bonding with multiple hydrogens; and (ii) the interaction between the hydridic hydrogens H<sup>δ-</sup> from the B atom and the protic hydrogens H<sup>δ+</sup> from the N atom results in an easier release of H<sub>2</sub>.<sup>146</sup> Several BNH materials meet the requirements established by the DOE. The next section will describe in detail two of the most investigated materials, and their derivatives, considered for H<sub>2</sub> storage: ammonia borane and hydrazine borane.

#### 3.1 Ammonia borane and hydrazine borane

Ammonia borane NH<sub>3</sub>BH<sub>3</sub> (AB; tetragonal, s.g. *I4mm*) and hydrazine borane N<sub>2</sub>H<sub>4</sub>BH<sub>3</sub> (HB; orthorhombic, s.g. *Pbcn*) have several features in common. First, they are synthesized in a similar way (metathesis followed by dehydrogenation) using NaBH<sub>4</sub> and an ammonium/hydrazine salt in an organic solvent like THF at 30–40°C (Equation 20 and Equation 21).<sup>155,156</sup> Second, AB and HB are solid at ambient conditions. And third, they show comparable stability under argon atmosphere, under air and in an organic/protic solution.<sup>146,157–159</sup>



AB is isoelectronic with ethane C<sub>2</sub>H<sub>6</sub>, and carries 6 hydrogen atoms, giving it a gravimetric H<sub>2</sub> density of 19.6 wt. %.<sup>160</sup> It carries three protic hydrogens H<sup>δ+</sup> in the NH<sub>3</sub> moiety and three hydridic hydrogens H<sup>δ-</sup> in the BH<sub>3</sub> group. The presence of these two types of H atoms implies intermolecular dihydrogen interactions H<sup>δ+</sup>...H<sup>δ-</sup> which allow the solid state of the compound and the possibility of start the dehydrogenation under heating at ca. 100°C.<sup>157,161,162</sup> In fact, the thermolysis of AB has been widely investigated,<sup>158</sup> but unfortunately AB does not only release H<sub>2</sub>:

it decomposes into gaseous species (ammonia  $\text{NH}_3$ , diborane  $\text{B}_2\text{H}_6$  and borazine  $\text{B}_3\text{N}_3\text{H}_6$ ) and into a solid residue of complex composition.  $\text{H}_2$  release by AB hydrolysis also has been investigated, despite the drawbacks associated with the  $\text{NH}_3$  group (like the pollution of the  $\text{H}_2$  stream by evolution of some  $\text{NH}_3$ , and impossible dehydrogenation of  $\text{NH}_3$  in hydrolysis conditions).<sup>163,164</sup>

HB (15.4 wt. %  $\text{H}_2$ ), a derivative of AB where the  $\text{N}_2\text{H}_4$  moiety replaces  $\text{NH}_3$ , also has been studied as potential candidate for  $\text{H}_2$  storage.<sup>165</sup> The hydrolysis of HB is more attractive than AB due to the possibility to dehydrogenate not only the  $\text{BH}_3$  moiety, but also the  $\text{N}_2\text{H}_4$  group (Equation 22).<sup>166,167</sup> For example, in the presence of a selective nickel-based catalyst, a total dehydrogenation of aqueous HB (with the formation of  $\text{N}_2$  and  $\text{B}(\text{OH})_3$ ) is achieved.<sup>168</sup>



HB also has been investigated for dehydrocoupling in thermolytic conditions,<sup>165</sup> even though it is not suitable: it decomposes mainly into the unwanted  $\text{N}_2\text{H}_4$  and generates a shock-sensitive solid when the temperature exceeds  $300^\circ\text{C}$ . A schematic representation of the thermal decomposition of AB and HB is presented in **Figure 9**.

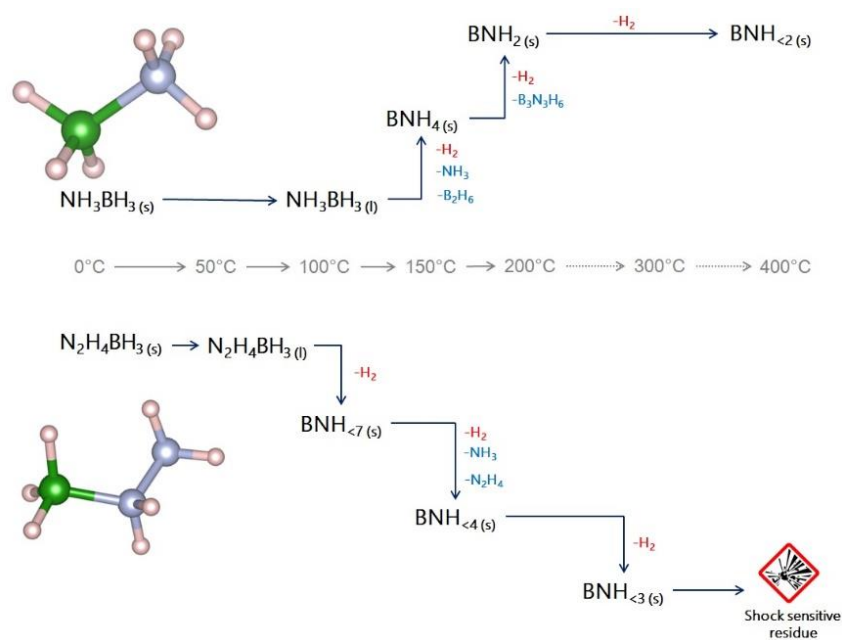


**Figure 9.** Representation of the thermolytic decomposition of AB and HB up to  $400^\circ\text{C}$ . The thermolytic residues are of complex composition and they are represented by  $\text{BNH}_x$  ( $x \leq 7$ ).

### 3.1.1 Destabilization strategies of AB

AB and HB are unsuitable for solid-state H<sub>2</sub> storage in pristine state because of inappropriate thermolytic dehydrogenation properties. This drawback promoted strategies to destabilize these molecules to obtain a purer H<sub>2</sub>.<sup>146</sup> For example, there have been several approaches to destabilize AB: the use of catalysts, the nanoconfinement, the nanosizing or the chemical modification.

The kinetics of AB can be enhanced using a catalyst. Different homogeneous catalysts have been tested for the dehydrogenation of AB in solution. It was reported that in the presence of an iridium-based catalyst ( $[\eta^3\text{-1,3-(OP}^t\text{Bu}_2)_2\text{C}_6\text{H}_3]\text{Ir(H)}_2$ ), a THF solution of AB can liberate 1 equiv H<sub>2</sub> in 14 min.<sup>169</sup> Ruthenium-based catalysts have also been tested in the dehydrogenation of AB. For example, different derivatives of the Shvo catalyst (organoruthenium compound) were developed in order to suppress the formation of borazine, to enhance H<sub>2</sub> release from AB and to avoid the deactivation of the catalyst by hydroboration.<sup>170</sup> The use of heterogeneous catalysts for the dehydrogenation of AB also has been widely reported in the literature based on different metals:<sup>171</sup> Rh/CNT, Pt/CNT, Pd/CeO<sub>2</sub>, AuCo/CNT, PtAuNi are some examples. The use of catalysts with a low content of noble metals is also of interest. Other materials like metal ruthenate perovskites (CaRuO<sub>3</sub>, Ca<sub>2</sub>CoRuO<sub>6</sub>, SrRuO<sub>3</sub>, Sr<sub>2</sub>LaRuO<sub>6</sub>) work as an active and durable catalysts for the dehydrogenation of AB.<sup>172</sup> These compounds achieve a comparable H<sub>2</sub> release rate than other metal noble-based heterogeneous catalysts.

Nanoconfinement of AB has been suggested as a strategy to improve the kinetics and the thermodynamics of the dehydrogenation of AB, as well to reduce undesired by-products.<sup>173</sup> Different materials have been proposed to host ammonia borane: carbon,<sup>174–176</sup> metal organic frameworks,<sup>177–179</sup> or porous silica supports.<sup>180–182</sup> The results indicate the success in destabilizing AB: the dehydrogenation takes places at lower temperatures, the thermodynamics and kinetic parameters were improved and the emission of gaseous by-products was reduced or even suppressed. However, there are many challenges ahead for nanoconfined AB: to find suitable scaffolds with smaller pores and higher pore volume, and to understand the mechanism of decomposition of confined AB.<sup>173</sup> Recently, the encapsulation of AB in halloysite nanotubes embedded with Pd was reported.<sup>183</sup> H<sub>2</sub> evolution started from 60°C and the activation energy of

AB@Pd/HNTs was estimated as  $46 \text{ kJ mol}^{-1}$  (vs  $183 \text{ kJ mol}^{-1}$  for neat AB). But the nanosizing of ammonia borane is possible even without a scaffold.<sup>184</sup> AB nanospheres were obtained in an aqueous solution using a surfactant. The nanostructures showed a lower dehydrogenation temperature and reduced by-product emissions. Such nanostructures open new opportunities in the development of  $\text{H}_2$  storage materials.

A last option for destabilizing AB and HB is the chemical modification to obtain derivatives via substitution of one of the  $\text{H}^{\delta+}$  by a metal cation. This approach improves the dehydrogenation properties of the compounds. The derivatives, namely amidoboranes (MAB) and hydrazinidoboranes (MHB), have shown better dehydrogenation properties than the parent boranes. MAB and MHB will be further discussed in the next sections.

### 3.2 Background on amidoboranes

The first report of an amidoborane dates from the 1940s: sodium amidoborane  $\text{NaNH}_2\text{BH}_3$  (NaAB), synthesized through a two-step process.<sup>185,186</sup> About 60 years later, the lithium amidoborane  $\text{LiNH}_2\text{BH}_3$  (LiAB) was reported.<sup>187</sup> LiAB was found to be a highly nucleophilic reducing agent for transformation of tertiary amides into primary alcohols.

Ten years later, the amidoboranes began to flourish. The first amidoborane to be presented as a potential  $\text{H}_2$  storage material is calcium amidoborane  $\text{Ca}(\text{NH}_2\text{BH}_3)_2$  (CaAB). It was synthesized according to a two-step process.<sup>188</sup> Like the parent AB, CaAB dehydrogenates above  $100^\circ\text{C}$ , but it offers some advantages. The amidoborane releases cleaner  $\text{H}_2$  (polluted by less than 0.1 wt. % of  $\text{NH}_3$  and  $\text{B}_3\text{N}_3\text{H}_6$ ); it does not show an induction period in isothermal conditions; it does not foam; its dehydrogenation extent is higher than 2 equiv  $\text{H}_2$ ; and the dehydrogenation process is less exothermic.<sup>188,189</sup>

The potential of amidoboranes for  $\text{H}_2$  storage was primarily confirmed with the re-discovery of both LiAB and NaAB,<sup>190</sup> and this gave new opportunities towards new amidoboranes: amidoboranes with heavy cations like  $\text{Y}^{3+}$  or  $\text{Al}^{3+}$ ;<sup>191,192</sup> mixed-cation amidoboranes like  $\text{LiAl}(\text{NH}_2\text{BH}_3)_4$ ,  $\text{NaLi}(\text{NH}_2\text{BH}_3)_2$ ,  $\text{NaMg}(\text{NH}_2\text{BH}_3)_3$ ,  $\text{KMg}(\text{NH}_2\text{BH}_3)_3$  and  $\text{RbMg}(\text{NH}_2\text{BH}_3)_3$ ;<sup>193–199</sup> methyl-substituted amidoboranes like  $\text{LiN}(\text{CH}_3)_2\text{BH}_3$ ;<sup>200</sup> and organometallic-complexed amidoboranes.<sup>201</sup>

### 3.3 Alkali amidoboranes and hydrazinidoboranes

Alkali and alkaline-earth derivatives of AB and HB have emerged due to the dehydrogenation at temperatures above 100°C, the emissions of unwanted by-products over the temperature range 100-200°C and the formation of polymeric residues of complex composition by the parent boranes.<sup>202–204</sup>

#### 3.3.1 Synthesis

The substitution of one of the H<sup>δ+</sup> of NH<sub>3</sub> or N<sub>2</sub>H<sub>4</sub> by M<sup>+</sup> is relatively easy. In HB, the substituted H<sup>δ+</sup> is one on the central N atom, giving then the formula NH<sub>2</sub>NH(M)BH<sub>3</sub>; the middle N retains a tetrahedral sp<sup>3</sup> hybridization. Two main routes have been developed for the syntheses of MAB and MHB (Table 2 and Table 3).<sup>190,205,214–222,206–213</sup>

Syntheses of MAB and MHB must be performed under inert atmosphere (He, Ar, N<sub>2</sub>). The reactants (MH, M, AB or HB) as well as the products (MAB and MHB) are not stable under air, especially when it is humid, due to the spontaneous hydrolysis of these compounds. For instance, NaAB evolves under air (mass increase of 48.7%) towards the formation of e.g. sodium carbonate Na<sub>2</sub>CO<sub>3</sub>,<sup>211</sup> and generates H<sub>2</sub> by solvolysis when put into contact with water or methanol.<sup>213</sup> Two other examples are RbAB and CsAB that decompose in air within minutes and are moisture sensitive.<sup>215,216</sup>

The light MAB and MHB compounds (M=Li, Na) are principally prepared by ball- or disc-milling AB or HB with the alkali hydride MH (Equation 23 and Equation 24).



The milling conditions for LiAB and LiHB are mild, because harsh conditions (e.g. >200 rpm or > 1 h) leads to the decomposition into other phases.<sup>206</sup> With respect to NaAB, the milling conditions are softer because NaH is more reactive than LiH.<sup>223</sup> Mixing an equimolar quantity of NaH and AB with a spatula in a mortar under argon atmosphere for 15 min are enough to obtain pure

NaAB.<sup>213</sup> The trend is similar for MHB. Because LiH is relatively inert towards HB (enthalpy of reaction  $<0.1 \text{ kJ mol}^{-1}$ ),<sup>224</sup> LiHB is formed by ball milling only.<sup>217,218,221</sup> NaHB has to be synthesized at  $-30^\circ\text{C}$ ,<sup>220</sup> otherwise the reactivity is too high (enthalpy of reaction  $-27.8 \text{ kJ mol}^{-1}$ ),<sup>224</sup> leading to an explosive reaction. Other approaches to synthesize LiAB, NaAB and NaHB includes using  $\text{LiNH}_2$ ,  $\text{NaNH}_2$  and  $\text{Li}_3\text{N}$  as source of the metal cation,<sup>207–209</sup> or using a wet method with THF as anhydrous solvent.<sup>208,212,221</sup> However, the reaction of  $\text{NaNH}_2$  and AB in THF is less efficient than the synthesis with NaH, because it presents slow kinetics.<sup>212</sup>

**Table 2.** Syntheses of alkali MAB. Details about the nature of the source of  $\text{M}^+$  (Prec.), molar ratio AB: $\text{M}^+$ , synthesis method, conditions, temperature of reaction and atmosphere are given.

Prec.	AB: $\text{M}^+$	Method	Conditions	Temp.	Atm.	Ref.
LiH	1:1	Ball milling	250 rpm / 3 h / Graphite	Room	Ar	190,205
LiH	1:1	Ball milling	250 rpm / 1 h	Room	He	206
LiH	1:1	Disc milling	3 min milling + 5 min break <sup>a</sup>	Room	Ar	207
LiH	1:1.5	Wet chemistry	THF / Stirring 75 min	Room	-	208
$\text{LiNH}_2$	1:1	Disc milling	3 min milling + 5 min break <sup>a</sup>	Room	Ar	206
$\text{Li}_3\text{N}$	4.2:1	Wet chemistry	THF / Stirring 60 min	$30^\circ\text{C}$	Ar	209
NaH	1:1	Ball milling	250 rpm / 3 h / Graphite	Room	Ar	190
NaH	1:1	Ball milling	1 h	Room	$\text{H}_2$ (10 bar)	210
NaH	1:1	Disc milling	3 min milling + 5 min break <sup>a</sup>	Room	Ar	207
NaH	1:1	Disc milling		Room	-	211
NaH	1:1.2	Wet chemistry	THF / Stirring 10 min	Room	-	208
NaH	1:1	Wet chemistry	THF / Stirring 10 min	$-3^\circ\text{C}$	-	212
NaH	1:1	Simple mixing	15 min	Room	Ar	213
$\text{NaNH}_2$	1:1	Wet chemistry	THF / Stirring 20 min	$25^\circ\text{C}$	-	208
KH	1:1	Wet chemistry	THF / 4 h	Room	$\text{N}_2/\text{Ar}$	214
KH	1:1	Wet chemistry	Benzene / 48 h	Room	$\text{N}_2/\text{Ar}$	214
Rb	1:0.93	Wet chemistry	THF / Overnight	$0^\circ\text{C}$	Ar	215
Rb	1:1	Wet chemistry	THF / 24 h	Room	Ar	216
Cs	1:1.03	Wet chemistry	THF / Overnight	$0^\circ\text{C}$	Ar	215
Cs	1:1	Wet chemistry	THF	Room	Ar	216

<sup>a</sup> The number of cycles has not been mentioned.

**Table 3.** Syntheses of alkali MHB. Details about the nature of the source of M+ (Prec.), molar ratio AB:M+, synthesis method, conditions, temperature of reaction and atmosphere are given.

Prec.	HB:M <sup>+</sup>	Method	Conditions	Temp.	Atm.	Ref.
LiH	1:1	Ball milling	200 rpm / 1-3 h	Room	He (1 bar)	217
LiH	1:1	Ball milling	200 rpm / 10 min + 20 min <sup>a</sup>	Room	Ar	218
LiH	1:1	Ball milling	150 rpm / 16 h <sup>b</sup>	Room	He	221
LiH	1:1	Ball milling	300 rpm / 6 h	Room	Ar	219
NaH	1:1	Wet chemistry	THF / 300 rpm	0°C	Ar	221
NaH	1:1	Ball milling	250 rpm / 10 min	-30°C	Ar	220
KH	1:1	Wet chemistry	THF / 300 rpm	25°C	Ar	221
Rb	1.15:1	Wet chemistry	THF / 30 h	Room	Ar	222
Cs	1.15:1	Wet chemistry	THF / 6 h	-20°C	Ar	225

<sup>a</sup> 10 min milling followed by 20 min break, 18 times  
<sup>b</sup> 1 min milling in one direction + 15 s break + 1 min in the other direction, for 16 h

Wet chemistry is the preferred method for the heavier MAB and MHB compounds (M=K, Rb, Cs). Both KAB and KHB can be prepared from KH in anhydrous THF (Equation 23 and Equation 24).<sup>214,221</sup> The use of an autoclave reactor is recommended in the case of KHB; solid-solid mixtures have to be avoided due to the high reactivity of KH towards the borane (shock-sensitive mixture leading to explosive reaction).<sup>221</sup> KH has a stronger basicity than NaH and LiH and, for example, the enthalpy of reaction between KH and HB is thrice (-70.3 kJ mol<sup>-1</sup>) than the one between NaH and HB.<sup>224</sup>

With respect to the Rb and Cs compounds, syntheses are carried out using the metallic alkali elements in anhydrous THF (Equation 25 and Equation 26), because RbH and CsH are not commercially available and the reactivity of Rb and Cs is lower, which is better from a safety point of view.<sup>215,216,222</sup> As amidoborane and hydrazinidoborane compounds are not soluble in THF, they can be isolated by filtration.



### 3.3.2 Crystalline solids

MAB and MHB are crystalline (Table 4). LiAB has two allotropes:  $\alpha$ -LiAB and  $\beta$ -LiAB.<sup>190,205,206</sup> The  $\alpha$  phase forms first, and it transforms to the  $\beta$  phase as the reaction progresses. Both allotropes crystallize in the orthorhombic space group  $Pbca$ . The unit cell of the  $\beta$  phase is twice that of the  $\alpha$  phase. The  $\beta$  phase is seen as a metastable phase arising from energetic milling. The  $\beta$ -LiAB has two coordination environments for  $\text{Li}^+$ : one is tetra-coordinated (with a distorted environment), and the other is penta-coordinated. The  $\alpha$ -LiAB only displays a tetrahedral coordination. (Figure 10). The penta-coordination of  $\beta$ -LiAB makes this phase less stable in comparison with  $\alpha$ -LiAB.

**Table 4.** Summary of crystallographic properties of MAB and MHB compounds.

Comp.	Unit cell <sup>a</sup>	s.g.	<i>a</i> (Å)	<i>b</i> (Å)	<i>c</i> (Å)	$\beta$ (°)	Z	Ref.
AB	Tetrag.	<i>I4mm</i>	5.263	5.263	5.050	90	2	226
$\alpha$ -LiAB	Orthor.	<i>Pbca</i>	7.113	13.949	5.150	90	8	190
$\alpha$ -LiAB	Orthor.	<i>Pbca</i>	7.105	13.930	5.148	90	8	206
$\beta$ -LiAB	Orthor.	<i>Pbca</i>	15.146	7.721	9.268	90	16	205
NaAB	Orthor.	<i>Pbca</i>	7.469	14.655	5.653	90	8	190
NaAB	Orthor.	<i>Pbca</i>	7.464	14.635	5.648	90	8	212
NaAB	Orthor.	<i>Pbca</i>	7.474	14.645	5.674	90	8	212
KAB	Orthor.	<i>Pbca</i>	9.430	8.261	17.340	90	16	214
$\alpha$ -RbAB	Monocl.	<i>P2<sub>1</sub>/c</i>	6.931	5.015	11.074	101.688	4	216
$\beta$ -RbAB	Cubic	<i>Fm<math>\bar{3}</math>m</i>	7.328	7.328	7.328	90	4	216
$\alpha$ -CsAB	Orthor.	<i>Pnam</i>	9.119	7.345	5.969	90	4	216
$\beta$ -CsAB	Cubic	<i>Fm<math>\bar{3}</math>m</i>	7.596	7.596	7.596	90	4	216
HB	Orthor.	<i>Pbca</i>	13.123	5.100	9.581	90	8	217
$\alpha$ -LiHB	Monocl.	<i>P2<sub>1</sub>/c</i>	5.852	7.466	8.897	122.381	4	217
$\beta$ -LiAB	Orthor.	<i>Pbca</i>	10.252	8.479	7.469	90	4	218
NaHB	Monocl.	<i>P2<sub>1</sub>/n</i>	4.974	7.958	9.292	93.814	4	220
KHB	Monocl.	<i>P2<sub>1</sub></i>	6.709	5.882	5.767	108.268	2	221
RbHB	Monocl.	<i>P2<sub>1</sub></i>	5.813	6.701	5.814	108.915	2	222
CsHB	Monocl.	<i>P2<sub>1</sub></i>	5.916	7.009	6.002	108.389	2	

<sup>a</sup> Tetrag. for tetragonal; Orthor. for orthorhombic; Monocl. for monoclinic.

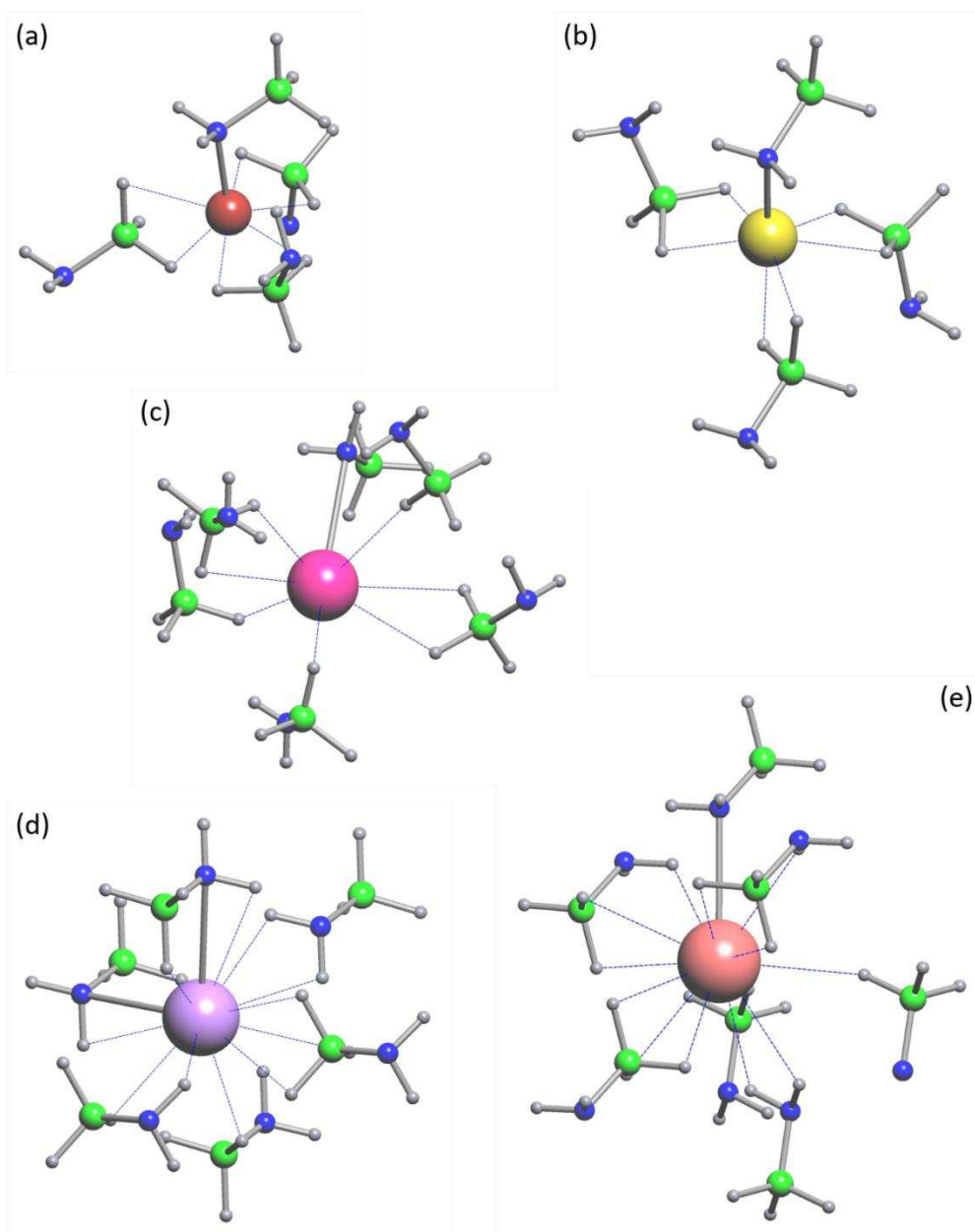


**Figure 10.** Coordination sphere of: (a) LiAB, (b) NaAB, (c) KAB, (d) RbAB, (e) CsAB. The green, blue and grey spheres represent the B, N and H atoms respectively. The other colored spheres show the alkali elements.

LiHB also has two phases, crystallizing, however, in different space groups. The  $\beta$  phase is the low-temperature phase (orthorhombic, s.g. *Pbca*) and is isostructural with LiAB. The high-

temperature phase is  $\alpha$ -LiHB (monoclinic, s.g.  $P2_1/c$ ).<sup>217-219,221,227</sup> The phase transition  $\beta$ -LiHB  $\rightarrow$   $\alpha$ -LiHB occurs when the  $\beta$  phase is heated at 95°C for 2 h or at 90°C while heated at 5°C min<sup>-1</sup> from room temperature.  $\beta$ -LiHB is more stable, as evidenced by a longer distance between two Li<sup>+</sup> (3.49 Å vs 3.31 Å for  $\alpha$ -LiHB). For each phase, the Li<sup>+</sup> cation has a tetrahedral environment, interacting with four [N<sub>2</sub>H<sub>3</sub>BH<sub>3</sub>]<sup>-</sup> anions (**Figure 11**).

NaAB and KAB are isostructural to LiAB.<sup>190,212,214</sup> The Na<sup>+</sup> has a tetrahedral coordination, as Li<sup>+</sup>, via one Na–N bond and three Na $\cdots$ H–BH<sub>2</sub> interactions. The K<sup>+</sup> cation is larger and more diffuse: it is octahedrally coordinated with six [NH<sub>2</sub>BH<sub>3</sub>]<sup>-</sup> anions involving three K–N bonds and three K $\cdots$ H–BH<sub>2</sub> interactions (**Figure 10**). Unlike the aforementioned amidoboranes,  $\beta$ -LiHB, NaHB and KHB crystallize in different monoclinic cells ( $P2_1/c$ ,  $P2_1/n$ ,  $P2_1$  respectively).<sup>217,220,221</sup> NaHB is surrounded by five [N<sub>2</sub>H<sub>3</sub>BH<sub>3</sub>]<sup>-</sup> anions, suggesting a trigonal bipyramid coordination sphere. For KHB, the number of surrounding anions is four. It interacts more intimately with the surrounding anions than Na<sup>+</sup> does (**Figure 11**). The amidoboranes of heavier alkali elements, RbAB and CsAB are not isostructural to the previous MAB.<sup>215,216</sup> RbAB crystallizes in a monoclinic system (s.g.  $P2_1/c$ ) where each Rb<sup>+</sup> coordinates with six [NH<sub>2</sub>BH<sub>3</sub>]<sup>-</sup> anions according to a pseudo-octahedron. CsAB has a primitive orthorhombic structure (s.g.  $Pnam$ ). Each Cs<sup>+</sup> is surrounded by seven [NH<sub>2</sub>BH<sub>3</sub>]<sup>-</sup> anions (**Figure 10**). Both amidoboranes undergo, under heating, a reversible phase transition. These  $\beta$  phases have a cubic  $Fm\bar{3}m$  unit cell. RbHB and CsHB are isostructural to KHB, crystallizing in a monoclinic  $P2_1$  unit cell.<sup>222</sup> The cations Rb<sup>+</sup> and Cs<sup>+</sup> have an octahedral coordination, with six surrounding [N<sub>2</sub>H<sub>3</sub>BH<sub>3</sub>]<sup>-</sup> anions (**Figure 11**).

With MAB, the volume of the unit cell per formula unit increases with the size of the metal cation. However, for MHB the volume of the unit cell per formula unit does not follow a constant evolution. It decreases from LiHB to NaHB, increases from NaHB to KHB, decreases from KHB to RbHB, and increases from RbHB to CsHB. Two factors can explain this behavior. The first one may be the non-linear evolution of the number of coordinating [N<sub>2</sub>H<sub>3</sub>BH<sub>3</sub>]<sup>-</sup> anions, since it is 4 for Li<sup>+</sup>, 5 for Na<sup>+</sup>, 4 for K<sup>+</sup>, and 6 for Rb<sup>+</sup> and Cs<sup>+</sup>. The second might be related to the presence of two N atoms which may enhance the number of interactions resulting in compacter coordination spheres.

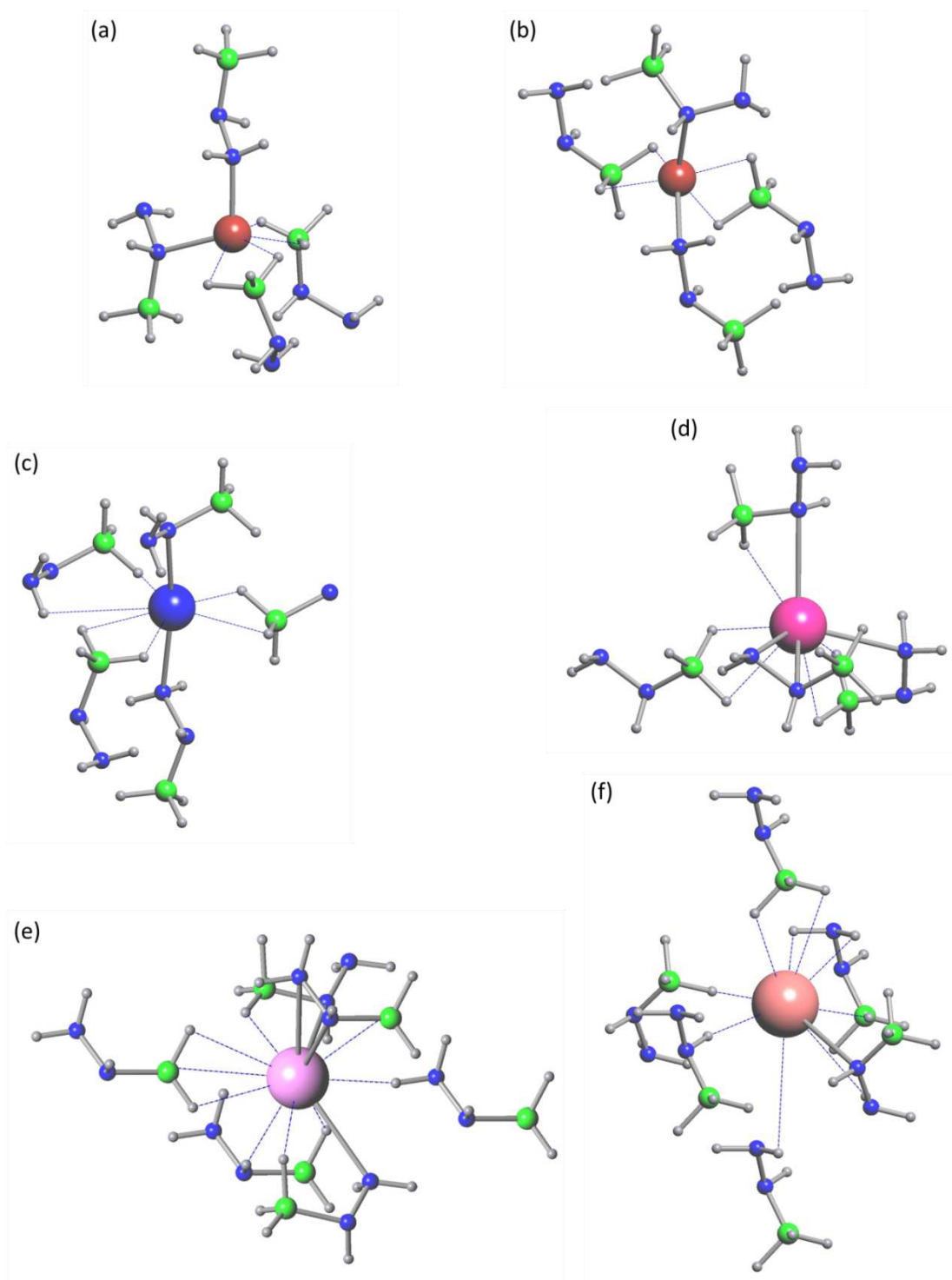


**Figure 11.** Coordination sphere of: (a)  $\alpha$ -LiHB, (b)  $\beta$ -LiHB, (c) NaHB, (d) KHB, (e) RbHB, (f) CsHB. The green, blue and grey spheres represent the B, N and H atoms respectively. The other colored spheres show the alkali elements.

### 3.3.3 Dihydrogen bonding

One of the features of fundamental interest with BNH compounds is the existence of an intermolecular dihydrogen network owing to  $H^{\delta+}\cdots H^{\delta-}$  interactions. With AB, the intermolecular  $H^{\delta+}\cdots H^{\delta-}$  distance is 2.02 Å.<sup>228</sup> With HB, it is 2.01 Å.<sup>156</sup> These distances are shorter than the sum of the van der Waals radii for two H atoms (2.4 Å). This is the characteristic of dihydrogen bonding. Weaker intermolecular dihydrogen bonding characterize MAB and MHB.<sup>214</sup> The  $H^{\delta+}\cdots H^{\delta-}$  is longer than that determined for AB or HB, but it remains lower than the van der Waals distance. For example, the  $H^{\delta+}\cdots H^{\delta-}$  distance is 2.25 Å in the case of  $\alpha$ -LiAB and of  $\beta$ -LiHB.<sup>206,221</sup> Dihydrogen  $H^{\delta+}\cdots H^{\delta-}$  interactions are also present within each  $[NH_2BH_3]^-$  or  $[N_2H_3BH_3]^-$  anion. They have distances of 2.00-2.10 Å in  $[N_2H_3BH_3]^-$  of  $\alpha$ -LiHB for example.<sup>217</sup>

Head-to-tail  $H^{\delta+}\cdots H^{\delta-}$  interactions take part in the stabilization of the solid state, but they are not the only interactions that play a role on this. Homopolar  $H^{\delta+}\cdots H^{\delta+}$  and  $H^{\delta-}\cdots H^{\delta-}$  interactions also contribute to the stability of MAB and MHB.<sup>229</sup> However, the van der Waals interactions between  $M^+$  and the anionic entities predominate: they replace the dihydrogen bonding and are of sufficient energy so that MAB and MHB are solid at ambient conditions.<sup>208,214</sup>

### 3.3.4 Thermolytic dehydrogenation

In comparison to AB and HB, all of the MAB and MHB compounds have shown better dehydrogenation properties with lower temperatures of dehydrogenation and higher purity of the released  $H_2$ .

LiAB dehydrogenates at temperatures below 100°C according to a near thermally neutral event ( $-3 \text{ kJ mol}^{-1}$ ).<sup>190,205</sup> NaAB has slightly better dehydrogenation properties. For example, heated at ca. 80°C, NaAB releases 0.5 equiv  $H_2$  in 92 s, versus 3017 s for LiAB.<sup>208</sup> For both materials, the purity of the released  $H_2$  is contradictory. On the one side, pure  $H_2$  was reported,<sup>190,206,208,212</sup> on the other side,  $H_2$  was found to be polluted by  $NH_3$ .<sup>207,211,230</sup> KAB also has attractive dehydrogenation properties, but the discrepancies in the experimental conditions and devices used make difficult to compare it with LiAB or NaAB. KAB releases 1.5 equiv  $H_2$  up to 100°C, without any pollutant.<sup>214</sup> Both RbAB and CsAB decompose from ca. 65 and 55°C respectively and below 100°C, releasing

H<sub>2</sub> and significant amounts of NH<sub>3</sub>.<sup>215,216</sup> According to theoretical calculations made on the molecular level, the least stable would be LiAB and the most stable would be CsAB.<sup>231,232</sup> This is in contradiction with the experimental observations made on the material level, which suggest a stability ranking of LiAB>NaAB>KAB>RbAB>CsAB. The least stable is CsAB, where the metal cation has the lower electronegativity; the stability of MAB would be driven by the metal electronegativity.<sup>152</sup>

The high-temperature phase  $\alpha$ -LiHB is responsible for a two-step decomposition occurring above 90°C.<sup>217,218,227</sup> Together with H<sub>2</sub>, N<sub>2</sub> and NH<sub>3</sub> are released. The dehydrogenation properties of NaHB are more attractive.<sup>220,221</sup> It releases H<sub>2</sub> from ca. 60°C a total of 2 equiv H<sub>2</sub> up to 100°C. The decomposition mechanism is, however, a bit complex as it is composed of three successive dehydrogenation and one denitrogenation processes. Some traces of N<sub>2</sub>, N<sub>2</sub>H<sub>4</sub> and NH<sub>3</sub> contaminate the H<sub>2</sub> stream. In contrast, when NaHB is "doped" with an excess of NaH, pure H<sub>2</sub> is generated.<sup>233</sup> KHB starts to dehydrogenate at ca. 50°C, releasing small amounts of NH<sub>3</sub> and N<sub>2</sub>.<sup>221</sup> RbHB and CsHB start to decompose at ca. 60 and 75°C, respectively, releasing NH<sub>3</sub> together with H<sub>2</sub>.<sup>222</sup> Though CsHB seems to be slightly more stable than RbHB, there is a rough correlation between the MHB reactivity and the alkali element electronegativity: the lower the electronegativity is, the less stable the MHB is.<sup>152</sup>

The identification of the thermolytic solid residue recovered upon dehydrogenation of MAB and MHB is challenging. A poorly crystalline thermolytic residue systematically forms, which renders powder X-ray diffraction of little assistance. The technique however allows seeing the formation, over 200°C, of crystalline by-products such as NaH, RbH and CsH.<sup>211,212,216</sup> Dehydrogenated NaAB is supposed to transform into a small amount of NaH (detected by <sup>23</sup>Na NMR spectroscopy),<sup>210,211</sup> and mainly into an amorphous solid being either a mixture of boron nitride and polyiminoborane-like structures or boron nitride (**Figure 12**).<sup>210,212</sup> More broadly, the thermolytic residue forming from MAB is considered as being polyborazylene- and polyiminoborane-like compounds.<sup>190,205,214,230,206–213</sup>

With respect to MHB, the nature of the thermolytic residue is as complex. Polymeric compounds having tetragonal boron environments (such as BH<sub>4</sub>, NBH<sub>3</sub>, N<sub>2</sub>BH<sub>2</sub>) as well as trigonal boron

environments (i.e.  $\text{NBH}_2$ ,  $\text{N}_2\text{BH}$ ,  $\text{BN}_3$ ) form. These environments are systematically discussed as polymeric B–N based compounds (Figure 12). Because the thermolytic residues of MAB and MHB have not been well identified yet, the dehydrogenation mechanisms are also not well known. However, there are some elements that may help in better understanding these mechanisms.

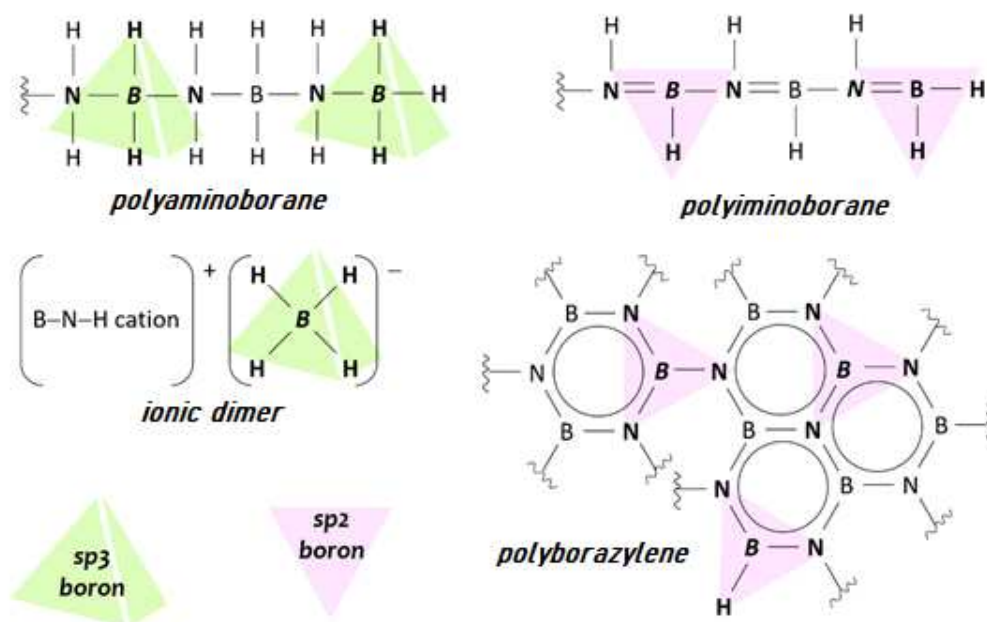


Figure 12. Examples of compounds having tetragonal boron environments and trigonal boron environments, present in the thermolytic residues of MAB and MHB.

With pristine AB, before the release of  $\text{H}_2$ , the compound dimerizes into diammoniate of diborane  $[(\text{NH}_3)_2\text{BH}_2]^+[\text{BH}_4]^-$ .<sup>234</sup> A comparable intermediate was predicted for LiAB:<sup>235</sup>  $[(\text{LiNH}_2)_2\text{BH}_2]^+[\text{BH}_4]^-$ , considered also as a Li–H–Li complex. It would allow thermoneutral  $\text{H}_2$  release via formation of a coiled polymeric product such as  $\text{LiNH}_2\text{BH}_2\text{LiNHBH}_3$ . Another predicted species is the dianion  $[\text{NHBHNHBH}_3]^{2-}$ .<sup>236</sup> For NaAB, the formation of an ionic dimer resembling those mentioned above is, on the one hand, discarded because  $^{11}\text{B}$  NMR analyses did not show signals belonging to  $\text{N}_2\text{BH}_2$  and  $\text{BH}_4$  environments.<sup>210</sup> On the other hand, however, head-to-tail dimerization into the ionic salt  $[\text{NH}_3\text{Na}]^+[\text{BH}_3(\text{NHNa})\text{BH}_3]^-$  would take place at ca.  $55^\circ\text{C}$ .<sup>207,210</sup> This intermediate explains the formation and liberation of  $\text{NH}_3$  at  $>55^\circ\text{C}$  and that of NaH. The as-forming  $\text{BH}_3(\text{NHNa})\text{BH}_2$

liberates H<sub>2</sub> above 55°C. This is a minor mechanism, estimated to have a contribution of 10%. The major mechanism is based on intramolecular dehydrogenation of NaAB. It is based on the key role of the in situ forming metal hydride M–H. In an initial step, it is believed to form by H<sup>δ-</sup> transfer from e.g. [NH<sub>2</sub>BH<sub>3</sub>]<sup>-</sup> to M<sup>+</sup>. The mechanism is called metal ion assisted hydride transfer or metal cation driven hydride-transfer. It takes place involving one MAB compound and the M–H formed induces low temperature dehydrogenation (Equation 27).<sup>237–241</sup>



Regarding to the dehydrogenation of MHB, it is likely that ionic dimer species similar to diammoniate of diborane are involved as transient phases, such as [(LiN<sub>2</sub>H<sub>3</sub>)<sub>2</sub>BH<sub>2</sub>]<sup>+</sup>[BH<sub>4</sub>]<sup>-</sup> and [(NaN<sub>2</sub>H<sub>3</sub>)<sub>2</sub>BH<sub>2</sub>]<sup>+</sup>[BH<sub>4</sub>]<sup>-</sup>.<sup>218,220</sup> Other non-ionic dimer species are NH<sub>2</sub>NH(M)BH<sub>2</sub>NHNNH(M)BH<sub>3</sub> and NH<sub>2</sub>NH(M)BHNNH(M)BH<sub>3</sub> (M=Li, Na, K).<sup>221</sup> Theoretical studies have suggested that dimers of NaHB may play the major role in the dehydrogenation pathway.<sup>242</sup>

Dehydrogenation of BNH compounds also implies counterintuitive homopolar H<sup>δ+</sup>...H<sup>δ+</sup> and H<sup>δ-</sup>...H<sup>δ-</sup> reactions.<sup>243–245</sup> For example, when heated, LiND<sub>2</sub>BH<sub>3</sub> releases significant quantity of H<sub>2</sub> along with HD, and the formation of H<sub>2</sub> is explained by the existence of homopolar H<sup>δ-</sup>...H<sup>δ-</sup> interactions. On the other hand, LiN<sub>2</sub>H<sub>3</sub>BD<sub>3</sub> generates appreciable amounts of HD, H<sub>2</sub> and D<sub>2</sub>. More precisely, initial thermolytic dehydrocoupling at low temperature takes place through homopolar H<sup>δ+</sup>...H<sup>δ+</sup> interactions, and this step is followed by heteropolar H<sup>δ+</sup>...D<sup>δ-</sup> and homopolar D<sup>δ-</sup>...D<sup>δ-</sup> pathways.

### 3.3.5 Rehydrogenation of thermolytic residues of MAB and MHB

The dehydrogenation of MAB and MHB is exothermic, and the rehydrogenation of the thermolytic residues under H<sub>2</sub> is thermodynamically unfavorable. A few unsuccessful attempts were published. For LiBNH<sub>1.32</sub> (a by-product of Li AB heated up to 200°C), no hydrogenation took place at 50 bar H<sub>2</sub> and up to 250°C.<sup>206</sup> Other example is the dehydrogenated form of NaAB, [BN]<sub>n</sub>, which did not rehydrogenated at 120 bar H<sub>2</sub>.<sup>212</sup>

Alternatively, MAB can be regenerated by chemical recycling/reduction of its thermolytic residue. Polyborazylene can be recycled back into AB by reduction using N<sub>2</sub>H<sub>4</sub> in NH<sub>3</sub> medium.<sup>246</sup> The

same path was applied to a thermolytic residue of LiAB identified as being made of cross-linked polyborazylene-based structures.<sup>247</sup> The conversion back to LiAB was found to be 63%. The formation of boron nitride must be avoided because it is chemically stable, excluding then chemical recycling/reduction.<sup>248</sup>

Another regeneration approach was proposed,<sup>247</sup> where a thermolytic residue (denoted MBNH, with M=Li, K) is first digested by methanol, and then, the forming product  $B(OCH_3)_3$  is reduced by  $LiAlH_4$  in the presence of a source of  $NH_3$ . This regeneration approach results in the formation of AB, which finally can be reacted with MH to form MAB back. However, the energy efficiency of this process is not attractive (ca. 46%).

### 3.4 Alkaline-earth amidoboranes and hydrazinidoboranes

Beryllium is highly toxic and carcinogenic, and has not been considered as a possible cation for AB and HB derivatives. Magnesium amidoborane was first tried to be synthesized by ball milling 2 equivalents of AB with  $MgH_2$  or Mg. However, both of them were apparently inert towards AB.<sup>206,249</sup> This could be explained by the low Lewis basicity of  $MgH_2$  compared with LiH, NaH or  $CaH_2$ . However, a later work reported the slow evolution of  $Mg(AB)_2$  from a mixture  $MgH_2$ -2AB and Mg-2AB.<sup>250</sup> Under argon atmosphere and room temperature, this evolution takes place between 45 days and 6 months. The process can be accelerated to 60-90 h by increasing the ageing temperature to 40°C.

The synthesis of  $Mg(HB)_2$  have been tested in several occasions in our research team, but all of them have failed up to now.<sup>224</sup> The attempts include the ball milling of HB with Mg or  $MgH_2$ , or a wet route with di-n-butylmagnesium.

To synthesize a pure phase of  $Ca(AB)_2$  is challenging. Intense milling is required to form mixtures where  $Ca(AB)_2$  is the major phase;  $CaH_2$  and AB are the minor phases.<sup>206,251</sup>  $Ca(AB)_2$  is less stable as  $Mg(AB)_2$  as it is able to release  $H_2$  from ca. 80°C, most of the  $H_2$  being generated at 100 and 140°C. Within the range 80-250°C,  $Ca(AB)_2$  generates ca. 3.8 equiv  $H_2$  and transforms into an amorphous residue suggested to be  $Ca_2B_2N_2H_2$ .<sup>33</sup>

As in the case for  $\text{MgH}_2$ ,  $\text{CaH}_2$  does not react with HB when they are ball milled. The reaction can be however thermally activated.<sup>252</sup> At ca.  $60^\circ\text{C}$ , the temperature at which HB has melted, solid-state  $\text{CaH}_2$  and liquid-state HB reacts and  $\text{Ca}(\text{HB})_2$  forms. The conversion is not total, as it was crystalline  $\text{CaH}_2$  was found together with crystalline  $\text{Ca}(\text{HB})_2$  in relative amounts of 29 and 71 wt. %. Under heating, the  $\text{Ca}(\text{HB})_2$  phase-rich solid decomposes from ca.  $90^\circ\text{C}$ . Up to  $200^\circ\text{C}$ , it releases 5.3 wt. % of gases composed mainly by  $\text{H}_2$  and with traces of  $\text{N}_2$ ,  $\text{NH}_3$  and  $\text{N}_2\text{H}_4$ . The dehydrogenation extent of  $\text{Ca}(\text{HB})_2$  was reported to be lower than any other MABs or MHBs, suggesting that the destabilization effect of  $\text{Ca}^{2+}$  is among the least important.

Strontium amidoborane  $\text{Sr}(\text{AB})_2$  is prepared by the ball milling a mixture of strontium hydride and two equivalents of AB.<sup>253</sup> The reactants have to be first milled at  $0^\circ\text{C}$  to avoid a partial decomposition of  $\text{Sr}(\text{AB})_2$ , and then the mixture is heated at  $45^\circ\text{C}$  for 2 h. The final product is not pure and it is composed of 55 wt. % of crystalline  $\text{Sr}(\text{AB})_2$ , 34 wt. % of an unidentified amorphous phase, 7 wt. % of  $\text{SrH}_2$  and 4 wt. % of AB. This mixture dehydrogenates slowly from  $60^\circ\text{C}$  and violently at  $80\text{--}90^\circ\text{C}$ .  $\text{Sr}(\text{AB})_2$  loses 9.9 wt. %, which ca. 3 wt. % higher than the gravimetric  $\text{H}_2$  density, meaning the generation of volatile by-products.

$\text{Ba}(\text{AB})_2$  is synthesized by wet chemistry in THF, while using metallic Ba.<sup>254</sup> The reaction is exothermic and it should be performed at low temperature (e.g.  $-10^\circ\text{C}$ ) to avoid the decomposition of  $\text{Ba}(\text{AB})_2$ . At this temperature, an amorphous white precipitate forms, confirmed to be pure  $\text{Ba}(\text{AB})_2$  by FTIR and  $^{11}\text{B}$  MAS NMR spectroscopy. This compound loses 5 wt. %  $\text{H}_2$  between 81 and  $161^\circ\text{C}$ .

### 3.5 Boron Nitride

Boron nitride (BN) is likely to belong to the list of reversible  $\text{H}_2$  storage materials. Almost twenty years ago, Wang *et al.*<sup>255</sup> showed that milled hexagonal boron nitride (crystallites of about 3 nm) adsorbs up to 2.6 wt. %  $\text{H}_2$  at 10 bar and room temperature. The uptake of  $\text{H}_2$  is reversible though desorption takes place at high temperature ( $297^\circ\text{C}$ ), because of chemisorption. Ma *et al.*<sup>256</sup> investigated bamboo-like BN nanotubes (BNNTs,  $210\text{ m}^2\text{ g}^{-1}$ ) capable of adsorbing up to 2.6 wt. %  $\text{H}_2$  under 100 bar and  $20^\circ\text{C}$ , with 0.8 wt. %  $\text{H}_2$  being physisorbed. Desorption of the remaining 1.8

wt. % of chemisorbed requires heating up to 300°C. Such interesting H<sub>2</sub> uptake properties were explained in terms of defects in the nanostructured material, specific surface area, polarity and partial ionic character of the B–N bonds. However, boron nitride has been investigated more scarcely than any other material sorbing H<sub>2</sub> reversibly, which can be explained by a lack of easy approaches of boron nitride synthesis and by a preferential occurrence of H<sub>2</sub> chemisorption.<sup>257</sup> Recently, computational calculations have identified strategies for improving the sorption properties of boron nitride, such as: higher specific surface area;<sup>258</sup> substitution of some B and N atoms of boron nitride by C and/or O;<sup>259</sup> surface functionalization (decoration) with e.g. Li or Na;<sup>260,261</sup> 2D boron nitride layers with optimized interlayer spacing.<sup>262</sup> It is reasonable to affirm that boron nitride, boron nitride-based materials or their derivatives have the potential to be considered as a viable H<sub>2</sub> storage material.

Interestingly, besides H<sub>2</sub> sorption properties, boron nitride also has the potential to adsorb carbon dioxide. From computational calculations, strong adsorption of CO<sub>2</sub> was estimated on boron antisite in boron-rich boron nitride nanotubes, where the lone pair of electrons of CO<sub>2</sub> interact with the boron atoms.<sup>263</sup> In another theoretical work, the interaction between pristine and doped boron nitride nanotubes was calculated.<sup>264</sup> It was found that CO<sub>2</sub> molecules interact weakly with pristine BNNTs through van der Waals interactions. In the case of Co-doped BNNTs, the binding energy between the CO<sub>2</sub> and the nanotubes increased, showing stronger interaction in comparison with carbon nanotubes. The capture of CO<sub>2</sub> by BN structures also has been demonstrated experimentally. For example, BN nanosheets were functionalized with polyetherimide, increasing the CO<sub>2</sub> sorption capacity of the nanosheets (3.12 mmol g<sup>-1</sup> for BN functionalized vs. 0.29 mmol g<sup>-1</sup> for pristine BN at 75°).<sup>265</sup> In another work, Cu-loaded porous BN nanofibers were tested for CO<sub>2</sub> capture. The results showed an enhance on the CO<sub>2</sub> sorption capacity of the Cu-doped BN nanofibers from 1.34 to 2.77 mmol g<sup>-1</sup> (at 1 bar and 0°C).<sup>266</sup> As a last example, a work of a functionalized porous BN with a triblock copolymer surfactant (P123) was reported.<sup>267</sup> The results showed that the BN-P123 had better adsorption properties than the pristine BN (2.69 mmol g<sup>-1</sup> vs. 2.00 mmol g<sup>-1</sup>). Therefore, BN has the capacity of capture CO<sub>2</sub>, and this can be improved by the functionalization of the structures, which offers new perspectives for BN.

## 4. Conclusion

The energy demand will rise in the years to come. The fossil fuels, which represent our main source of energy, are becoming scarce and the gases released by their combustion have a negative effect on the environment. The need of cleaner technologies is then imperative.  $H_2$  emerges as the most attractive option to substitute fossil fuels and to reach a more sustainable future. However, to achieve a feasible hydrogen future some challenges need to be overcome, especially the ones regarding  $H_2$  storage. As aforementioned, the current  $H_2$  storage technologies are not efficient enough for most applications. The most promising alternative to attain a high  $H_2$  storage capacity is to store the gas into a material.

Different materials have emerged as candidates for  $H_2$  storage applications, each one with advantages and challenges to overcome. Among the possible choices, boron- and nitrogen-based materials represent a promising option as  $H_2$  storage materials. Boron nitride, ammonia borane, hydrazine borane and their derivatives are good examples. However, fundamental research is still required to better understand the properties, behavior and chemistry of these compounds.

Amidoboranes and hydrazinidoboranes are new materials that have mostly been discovered in the last decade. Accordingly, these compounds have been investigated scarcely and there is a lack of knowledge on their chemistry. Further efforts are required to better understand the behavior and properties of amidoboranes and hydrazinidoboranes in the context of  $H_2$  storage. This is important from a fundamental point of view, as new research will increase the knowledge of such materials in the fields of inorganic and material chemistry. The purpose of this work is to shed more light into the chemistry of alkali hydrazinidoboranes by the synthesis of the last two missing compounds. Besides, the exploration of new applications for amidoboranes is explored. A better overview over these materials is expected and new perspectives could be open.

## 5. References

1. Züttel, A. Materials for hydrogen storage. *Mater. Today* **6**, 24–33 (2003).
2. DOE-US. Hydrogen Storage. <https://www.energy.gov/eere/fuelcells/hydrogen-storage> (2020).
3. Mazloomi, K. and Gomes, C. Hydrogen as an energy carrier: Prospects and challenges. *Renew. Sustain. Energy Rev.* **16**, 3024–3033 (2012).
4. Marchenko, O. V. and Solomin, S. V. The future energy: Hydrogen versus electricity. *Int. J. Hydrogen Energy* **40**, 3801–3805 (2015).
5. Andrews, J. and Shabani, B. Re-envisioning the role of hydrogen in a sustainable energy economy. *Int. J. Hydrogen Energy* **37**, 1184–1203 (2012).
6. Muradov, N. Z. and Veziroğlu, T. N. 'Green' path from fossil-based to hydrogen economy: An overview of carbon-neutral technologies. *Int. J. Hydrogen Energy* **33**, 6804–6839 (2008).
7. Goltsov, V. A. *et al.* Hydrogen civilization of the future - A new conception of the IAHE. *Int. J. Hydrogen Energy* **31**, 153–159 (2006).
8. Dunn, S. Hydrogen futures: Toward a sustainable energy system. *Int. J. Hydrogen Energy* **27**, 235–264 (2002).
9. Edwards, P. P. *et al.* Hydrogen and fuel cells: Towards a sustainable energy future. *Energy Policy* **36**, 4356–4362 (2008).
10. Tollefson, J. Fuel of the future? *Nature* **464**, 1262–1264 (2010).
11. Eliezer, D. *et al.* Positive effects of hydrogen in metals. *Mater. Sci. Eng. A* **280**, 220–224 (2000).
12. Ramachandran, R. and Menon, R. K. An overview of industrial uses of hydrogen. *Int. J. Hydrogen Energy* **23**, 593–598 (1998).
13. Sharma, S. and Ghoshal, S. K. Hydrogen the future transportation fuel: From production to applications. *Renew. Sustain. Energy Rev.* **43**, 1151–1158 (2015).

14. Kothari, R. *et al.* Comparison of environmental and economic aspects of various hydrogen production methods. *Renew. Sustain. Energy Rev.* **12**, 553–563 (2008).
15. Holladay, J. D. *et al.* An overview of hydrogen production technologies. *Catal. Today* **139**, 244–260 (2009).
16. Dickerson, T. and Soria, J. Catalytic fast pyrolysis: A review. *Energies* **6**, 514–538 (2013).
17. Muradov, N. Hydrogen via methane decomposition: An application for decarbonization of fossil fuels. *Int. J. Hydrogen Energy* **26**, 1165–1175 (2001).
18. Dincer, I. and Acar, C. Review and evaluation of hydrogen production methods for better sustainability. *Int. J. Hydrogen Energy* **40**, 11094–11111 (2014).
19. Fulcheri, L. *et al.* Plasma processing: A step towards the production of new grades of carbon black. *Carbon N. Y.* **40**, 169–176 (2002).
20. Wojcik, A. *et al.* Ammonia as a fuel in solid oxide fuel cells. *J. Power Sources* **118**, 342–348 (2003).
21. Thomas, G. and Parks, G. *US-DOE. Potential roles of ammonia in a hydrogen economy: a study of issues related to the use of ammonia for on-board vehicular hydrogen storage* (2006).
22. Turner, J. *et al.* Renewable hydrogen production. *Int. J. Energy Res.* **32**, 379–407 (2008).
23. Nikolaidis, P. and Poullikkas, A. A comparative overview of hydrogen production processes. *Renew. Sustain. Energy Rev.* **67**, 597–611 (2017).
24. Funk, J. E. Thermochemical hydrogen production: Past and present. *Int. J. Hydrogen Energy* **26**, 185–190 (2001).
25. Tolga Balta, M. *et al.* Thermodynamic assessment of geothermal energy use in hydrogen production. *Int. J. Hydrogen Energy* **34**, 2925–2939 (2009).
26. Akikusa, J. and Khan, S. U. M. Photoelectrolysis of water to hydrogen in p-SiC/Pt and p-SiC/n-TiO<sub>2</sub> cells. *Int. J. Hydrogen Energy* **27**, 863–870 (2002).

27. Mor, G. K. *et al.* A review on highly ordered, vertically oriented TiO<sub>2</sub> nanotube arrays: Fabrication, material properties, and solar energy applications. *Sol. Energy Mater. Sol. Cells* **90**, 2011–2075 (2006).
28. DeAngelis, A. D. *et al.* Antimony(III) sulfide thin films as a photoanode material in photocatalytic water splitting. *ACS Appl. Mater. Interfaces* **8**, 8445–8451 (2016).
29. Arriaga, L. G. and Fernández, A. M. Determination of flat band potential and photocurrent response in (Cd,Zn)S used in photoelectrolysis process. *Int. J. Hydrogen Energy* **27**, 27–31 (2002).
30. DOE-US. Technical targets for hydrogen production from electrolysis. <https://www.energy.gov/eere/fuelcells/doe-technical-targets-hydrogen-production-electrolysis> (2020).
31. Arregi, A. *et al.* Evaluation of thermochemical routes for hydrogen production from biomass: A review. *Energy Convers. Manag.* **165**, 696–719 (2018).
32. Li, S. *et al.* Recent advances in hydrogen production by thermo-catalytic conversion of biomass. *Int. J. Hydrogen Energy* **44**, 14266–14278 (2019).
33. Hamad, M. A. *et al.* Hydrogen rich gas production from catalytic gasification of biomass. *Renew. Energy* **85**, 1290–1300 (2016).
34. Das, D. and Veziroğlu, T. N. Hydrogen production by biological processes: A survey of literature. *Int. J. Hydrogen Energy* **26**, 13–28 (2001).
35. Ni, M. *et al.* An overview of hydrogen production from biomass. *Fuel Process. Technol.* **87**, 461–472 (2006).
36. Shaner, M. R. *et al.* A comparative technoeconomic analysis of renewable hydrogen production using solar energy. *Energy Environ. Sci.* **9**, 2354–2371 (2016).
37. Hosseini, S. E. and Wahid, M. A. Hydrogen production from renewable and sustainable energy resources: Promising green energy carrier for clean development. *Renew. Sustain. Energy Rev.* **57**, 850–866 (2016).
38. Miltner, A. *et al.* Renewable hydrogen production: A technical evaluation based on process

- simulation. *J. Clean. Prod.* **18**, S51–S62 (2010).
39. Wilberforce, T. *et al.* Advances in stationary and portable fuel cell applications. *Int. J. Hydrogen Energy* **41**, 16509–16522 (2016).
  40. Zhang, J. *PEM fuel cell electrocatalysts and catalyst layers: Fundamentals and applications.* (Springer, 2008).
  41. Demirci, U. B. How green are the chemicals used as liquid fuels in direct liquid-feed fuel cells? *Environ. Int.* **35**, 626–631 (2009).
  42. Steele, B. C. H. and Heinzel, A. Materials for fuel-cell technologies. *Nature* **414**, 345–352 (2001).
  43. Pan, Z. F. *et al.* Advances and challenges in alkaline anion exchange membrane fuel cells. *Prog. Energy Combust. Sci.* **66**, 141–175 (2018).
  44. Dekel, D. R. Unraveling mysteries of hydrogen electrooxidation in anion exchange membrane fuel cells. *Curr. Opin. Electrochem.* **12**, 182–188 (2018).
  45. Wang, Z. *et al.* Advances in anion exchange membranes for electrochemical energy conversion. *Curr. Opin. Electrochem.* **12**, 240–245 (2018).
  46. Dekel, D. R. Review of cell performance in anion exchange membrane fuel cells. *J. Power Sources* **375**, 158–169 (2018).
  47. Gottesfeld, S. *et al.* Anion exchange membrane fuel cells: Current status and remaining challenges. *J. Power Sources* **375**, 170–184 (2018).
  48. Kundu, P. P. and Dutta, K. *Hydrogen fuel cells for portable applications. Compendium of Hydrogen Energy* (Elsevier Ltd., 2016).
  49. Ma, J. *et al.* A comprehensive review of direct borohydride fuel cells. *Renew. Sustain. Energy Rev.* **14**, 183–199 (2010).
  50. Wee, J. H. A comparison of sodium borohydride as a fuel for proton exchange membrane fuel cells and for direct borohydride fuel cells. *J. Power Sources* **155**, 329–339 (2006).

51. Demirci, U. B. and Miele, P. Sodium borohydride versus ammonia borane, in hydrogen storage and direct fuel cell applications. *Energy Environ. Sci.* **2**, 627–637 (2009).
52. Christudas Dargily, N. *et al.* A rechargeable hydrogen battery. *J. Phys. Chem. Lett.* **9**, 2492–2497 (2018).
53. Hsu, S. F. *et al.* A rechargeable hydrogen battery based on Ru catalysis. *Angew. Chem. Int. Ed.* **53**, 7074–7078 (2014).
54. Boddien, A. *et al.* Towards the development of a hydrogen battery. *Energy Environ. Sci.* **5**, 8907–8911 (2012).
55. DOE-US. *Basic research needs for the hydrogen economy.* (2004).
56. DOE-US. Technical targets for onboard hydrogen storage for light-duty vehicles. <https://www.energy.gov/eere/fuelcells/doe-technical-targets-onboard-hydrogen-storage-light-duty-vehicles> (2019).
57. Zheng, J. *et al.* Development of high pressure gaseous hydrogen storage technologies. *Int. J. Hydrogen Energy* **37**, 1048–1057 (2012).
58. Barthélémy, H. Hydrogen storage - Industrial perspectives. *Int. J. Hydrogen Energy* **37**, 17364–17372 (2012).
59. Preuster, P. *et al.* Hydrogen storage technologies for future energy systems. *Annu. Rev. Chem. Biomol. Eng.* **8**, 445–471 (2017).
60. Mori, D. and Hirose, K. Recent challenges of hydrogen storage technologies for fuel cell vehicles. *Int. J. Hydrogen Energy* **34**, 4569–4574 (2009).
61. Barthélémy, H. *et al.* Hydrogen storage: Recent improvements and industrial perspectives. *Int. J. Hydrogen Energy* **42**, 7254–7262 (2017).
62. Niaz, S. *et al.* Hydrogen storage: Materials, methods and perspectives. *Renew. Sustain. Energy Rev.* **50**, 457–469 (2015).
63. Zhang, Y. H. *et al.* Development and application of hydrogen storage. *J. Iron Steel Res. Int.* **22**, 757–770 (2015).

64. Zhang, F. *et al.* The survey of key technologies in hydrogen energy storage. *Int. J. Hydrogen Energy* **41**, 14535–14552 (2016).
65. DOE-US. Material-based hydrogen storage. <https://www.energy.gov/eere/fuelcells/materials-based-hydrogen-storage> (2019).
66. Ren, J. *et al.* Review on processing of metal-organic framework (MOF) materials towards system integration for hydrogen storage. *Int. J. Energy Res.* **39**, 607–620 (2015).
67. Ren, J. *et al.* Current research trends and perspectives on materials-based hydrogen storage solutions: A critical review. *Int. J. Hydrogen Energy* **42**, 289–311 (2017).
68. Bénard, P. and Chahine, R. Storage of hydrogen by physisorption on carbon and nanostructured materials. *Scr. Mater.* **56**, 803–808 (2007).
69. Xia, Y. *et al.* Porous carbon-based materials for hydrogen storage: Advancement and challenges. *J. Mater. Chem. A* **1**, 9365–9381 (2013).
70. Dalebrook, A. F. *et al.* Hydrogen storage: Beyond conventional methods. *Chem. Commun.* **49**, 8735–8751 (2013).
71. Züttel, A. *et al.* Hydrogen sorption by carbon nanotubes and other carbon nanostructures. *J. Alloys Compd.* **330–332**, 676–682 (2002).
72. De La Casa-Lillo, M. A. *et al.* Hydrogen storage in activated carbons and activated carbon fibers. *J. Phys. Chem. B* **106**, 10930–10934 (2002).
73. Zhao, W. *et al.* Activated carbons with appropriate micropore size distribution for hydrogen adsorption. *Int. J. Hydrogen Energy* **36**, 5431–5434 (2011).
74. Wang, Z. *et al.* Nitrogen-doped porous carbons with high performance for hydrogen storage. *Int. J. Hydrogen Energy* **41**, 8489–8497 (2016).
75. Sethia, G. and Sayari, A. Activated carbon with optimum pore size distribution for hydrogen storage. *Carbon N. Y.* **99**, 289–294 (2016).
76. Dillon, A. C. *et al.* Storage of hydrogen in single-walled carbon nanotubes. *Nature* **386**, 377–379 (1997).

77. Rajaura, R. S. *et al.* Structural and surface modification of carbon nanotubes for enhanced hydrogen storage density. *Nano-Struct. Nano-Objects* **14**, 57–65 (2018).
78. Shiraz, H. G. and Shiraz, M. G. Palladium nanoparticle and decorated carbon nanotube for electrochemical hydrogen storage. *Int. J. Hydrogen Energy* **42**, 11528–11533 (2017).
79. Erünal, E. *et al.* Enhancement of hydrogen storage capacity of multi-walled carbon nanotubes with palladium doping prepared through supercritical CO<sub>2</sub> deposition method. *Int. J. Hydrogen Energy* **43**, 10755–10764 (2018).
80. Adams, B. D. and Chen, A. The role of palladium in a hydrogen economy. *Mater. Today* **14**, 282–289 (2011).
81. Tozzini, V. and Pellegrini, V. Prospects for hydrogen storage in graphene. *Phys. Chem. Chem. Phys.* **15**, 80–89 (2013).
82. Klechikov, A. G. *et al.* Hydrogen storage in bulk graphene-related materials. *Micropor. Mesopor. Mater.* **210**, 46–51 (2015).
83. Nagar, R. *et al.* Recent advances in hydrogen storage using catalytically and chemically modified graphene nanocomposites. *J. Mater. Chem. A* **5**, 22897–22912 (2017).
84. Yang, R. T. *Adsorbents: Fundamentals and Applications*. (John Wiley & Sons, 2003).
85. Dong, J. *et al.* Hydrogen storage in several microporous zeolites. *Int. J. Hydrogen Energy* **32**, 4998–5004 (2007).
86. Li, Y. and Yang, R. T. Hydrogen storage in low silica type X zeolites. *J. Phys. Chem. B* **110**, 17175–17181 (2006).
87. Langmi, H. W. *et al.* Hydrogen storage in ion-exchanged zeolites. *J. Alloys Compd.* **404–406**, 637–642 (2005).
88. Gil, A. and Vicente, M. A. Energy storage materials from clay minerals and zeolite-like structures. in *Modified Clay and Zeolite Nanocomposite Materials* 275–288 (Elsevier Inc., 2019).
89. Martin-Calvo, A. *et al.* Identifying zeolite topologies for storage and release of hydrogen. *J.*

- Phys. Chem. C* **122**, 12485–12493 (2018).
90. Ozturk, Z. Hydrogen storage on lithium modified silica based chabazite type zeolite, a computational study. *Int. J. Hydrogen Energy* **43**, 22365–22376 (2018).
  91. Sun, W. F. *et al.* Hydrogen storage, magnetism and electrochromism of silver doped FAU zeolite: First-principles calculations and molecular simulations. *Polymers*. **11**, 1–17 (2019).
  92. Furukawa, H. *et al.* The chemistry and applications of metal-organic frameworks. *Science*. **341**, 1–12 (2013).
  93. Rosi, N. L. *et al.* Hydrogen storage in microporous metal-organic frameworks. *Science*. **300**, 1127–1129 (2012).
  94. Rowsell, J. L. C. *et al.* Hydrogen sorption in functionalized metal-organic frameworks. *J. Am. Chem. Soc.* **126**, 5666–5667 (2004).
  95. Suh, M. P. *et al.* Hydrogen storage in metal-organic frameworks. *Chem. Rev.* **112**, 782–835 (2012).
  96. Volkova, E. I. *et al.* Improved design of metal-organic frameworks for efficient hydrogen storage at ambient temperature: A multiscale theoretical investigation. *Int. J. Hydrogen Energy* **39**, 8347–8350 (2014).
  97. Chu, C. L. *et al.* Enhancement of hydrogen adsorption by alkali-metal cation doping of metal-organic framework-5. *Int. J. Hydrogen Energy* **37**, 6721–6726 (2012).
  98. Xia, L. *et al.* Li-doped and functionalized metal-organic framework-519 for enhancing hydrogen storage: A computational study. *Comput. Mater. Sci.* **166**, 179–186 (2019).
  99. Wang, Y. *et al.* Study on catalytic effect and mechanism of MOF (MOF = ZIF-8, ZIF-67, MOF-74) on hydrogen storage properties of magnesium. *Int. J. Hydrogen Energy* **44**, 28863–28873 (2019).
  100. Ahmed, A. *et al.* Balancing gravimetric and volumetric hydrogen density in MOFs. *Energy Environ. Sci.* **10**, 2459–2471 (2017).
  101. Ahmed, A. *et al.* Exceptional hydrogen storage achieved by screening nearly half a million

- metal-organic frameworks. *Nat. Commun.* **10**, 1–9 (2019).
102. Chen, Z. *et al.* Balancing volumetric and gravimetric uptake in highly porous materials for clean energy. *Science*. **368**, 297–303 (2020).
  103. Strobel, T. A. *et al.* Hydrogen storage properties of clathrate hydrate materials. *Fluid Phase Equilib.* **261**, 382–389 (2007).
  104. Mao, W. L. and Mao, H. K. Hydrogen storage in molecular compounds. *Proc. Natl. Acad. Sci. U. S. A.* **101**, 708–710 (2004).
  105. Florusse, L. J. *et al.* Stable low-pressure hydrogen clusters stored in a binary clathrate hydrate. *Science*. **306**, 469–471 (2004).
  106. Lee, H. *et al.* Tuning clathrate hydrates for hydrogen storage. *Nature* **434**, 743–746 (2005).
  107. Hu, Y. H. and Ruckenstein, E. Clathrate hydrogen hydrate - A promising material for hydrogen storage. *Angew. Chem. Int. Ed.* **45**, 2011–2013 (2006).
  108. Perrin, A. *et al.* The chemistry of low dosage clathrate hydrate inhibitors. *Chem. Soc. Rev.* **42**, 1996–2015 (2013).
  109. Orimo, S. I. *et al.* Complex hydrides for hydrogen storage. *Chem. Rev.* **107**, 4111–4132 (2007).
  110. Qiu, S. *et al.* Light metal borohydrides/amides combined hydrogen storage systems: Composition, structure and properties. *J. Mater. Chem. A* **5**, 25112–25130 (2017).
  111. Jepsen, L. H. *et al.* Nanostructured and complex hydrides for hydrogen storage. in *Nanotechnology for Energy Sustainability*. 415–432 (Wiley-VCH, 2017).
  112. Bowman Jr., R. C. and Fultz, B. Metallic hydrides I: Hydrogen storage and other gas-phase applications. *MRS Bull.* **27**, 688–693 (2002).
  113. Schneemann, A. *et al.* Nanostructured metal hydrides for hydrogen storage. *Chem. Rev.* **118**, 10775–10839 (2018).
  114. Grochala, W. Thermal decomposition of chemical hydrides. *Pol. J. Chem.* **79**, 1087–1092

- (2005).
115. Javadian, P. *et al.* Destabilization of lithium hydride and the thermodynamic assessment of the Li-Al-H system for solar thermal energy storage. *RSC Adv.* **6**, 94927–94933 (2016).
  116. Sheppard, D. A. *et al.* Metal hydrides for concentrating solar thermal power energy storage. *Appl. Phys. A Mater. Sci. Process.* **122**, (2016).
  117. Sakintuna, B. *et al.* Metal hydride materials for solid hydrogen storage: A review. *Int. J. Hydrogen Energy* **32**, 1121–1140 (2007).
  118. Ley, M. B. *et al.* Complex hydrides for hydrogen storage - New perspectives. *Mater. Today* **17**, 122–128 (2014).
  119. Rusman, N. A. A. and Dahari, M. A review on the current progress of metal hydrides material for solid-state hydrogen storage applications. *Int. J. Hydrogen Energy* **41**, 12108–12126 (2016).
  120. Okada, M. *et al.* Role of intermetallics in hydrogen storage materials. *Mater. Sci. Eng. A* **329–331**, 305–312 (2002).
  121. Falahati, H. and Barz, D. P. J. Evaluation of hydrogen sorption models for AB<sub>5</sub>-type metal alloys by employing a gravimetric technique. *Int. J. Hydrogen Energy* **38**, 8838–8851 (2013).
  122. Łodziana, Z. *et al.* Ternary LaNi<sub>4.75</sub>Mg<sub>0.25</sub> hydrogen storage alloys: Surface segregation, hydrogen sorption and thermodynamic stability. *Int. J. Hydrogen Energy* **44**, 1760–1773 (2019).
  123. Liu, J. *et al.* New insights into the hydrogen storage performance degradation and Al functioning mechanism of LaNi<sub>5-x</sub>Al<sub>x</sub> alloys. *Int. J. Hydrogen Energy* **42**, 24904–24914 (2017).
  124. Kohno, T. *et al.* Hydrogen storage properties of new ternary system alloys: La<sub>2</sub>MgNi<sub>9</sub>, La<sub>5</sub>Mg<sub>2</sub>Ni<sub>23</sub>, La<sub>3</sub>MgNi<sub>14</sub>. *J. Alloys Compd.* **311**, 5–7 (2000).
  125. Spodaryk, M. *et al.* Hydrogen storage and electrochemical properties of LaNi<sub>5-x</sub>Cu<sub>x</sub> hydride-forming alloys. *J. Alloys Compd.* **775**, 175–180 (2019).
  126. Reilly, J. J. and Wiswall, R. H. Formation and properties of iron titanium hydride. *Inorg.*

*Chem.* **13**, 218–222 (1974).

127. Sujan, G. K. *et al.* An overview on TiFe intermetallic for solid-state hydrogen storage: microstructure, hydrogenation and fabrication processes. *Crit. Rev. Solid State Mater. Sci.* **45**, 410–427 (2020).
128. Gasiorowski, A. *et al.* Hydriding properties of nanocrystalline  $Mg_{2-x}M_xNi$  alloys synthesized by mechanical alloying (M = Mn, Al). *J. Alloys Compd.* **364**, 283–288 (2004).
129. Dantzer, P. Properties of intermetallic compounds suitable for hydrogen storage applications. *Mater. Sci. Eng. A* **329–331**, 313–320 (2002).
130. Shahi, R. R. *et al.*  $MgH_2$ - $ZrFe_2H_x$  nanocomposites for improved hydrogen storage characteristics of  $MgH_2$ . *Int. J. Hydrogen Energy* **40**, 11506–11513 (2015).
131. Zhang, J. *et al.* Metal hydride nanoparticles with ultrahigh structural stability and hydrogen storage activity derived from microencapsulated nanoconfinement. *Adv. Mater.* **29**, 1–6 (2017).
132. Schüth, F. *et al.* Light metal hydrides and complex hydrides for hydrogen storage. *Chem. Commun.* **20**, 2249–2258 (2004).
133. Züttel, A. *et al.*  $LiBH_4$  a new hydrogen storage material. *J. Power Sources* **118**, 1–7 (2003).
134. Mao, J. and Gregory, D. H. Recent advances in the use of sodium borohydride as a solid state hydrogen store. *Energies* **8**, 430–453 (2015).
135. Schlesinger, H. I. *et al.* Sodium borohydride, its hydrolysis and its use as a reducing agent and in the generation of hydrogen. *J. Am. Chem. Soc.* **75**, 215–219 (1953).
136. Filinchuk, Y. *et al.* Porous and dense magnesium borohydride frameworks: Synthesis, stability, and reversible absorption of guest species. *Angew. Chem. Int. Ed.* **50**, 11162–11166 (2011).
137. Bogdanović, B. and Schwickardi, M. Ti-doped alkali metal aluminium hydrides as potential novel reversible hydrogen storage materials. *J. Alloys Compd.* **253–254**, 1–9 (1997).
138. Milanese, C. *et al.* Solid state hydrogen storage in alanates and alanate-based compounds:

- A review. *Metals (Basel)*. **8**, 1–15 (2018).
139. Ares Fernandez, J. R. *et al.* Mechanical and thermal decomposition of  $\text{LiAlH}_4$  with metal halides. *Int. J. Hydrogen Energy* **32**, 1033–1040 (2007).
  140. Balema, V. P. *et al.* Titanium catalyzed solid-state transformations in  $\text{LiAlH}_4$  during high-energy ball-milling. *J. Alloys Compd.* **329**, 108–114 (2001).
  141. Garroni, S. *et al.* Recent progress and new perspectives on metal amide and imide systems for solid-state hydrogen storage. *Energies* **11**, 1–28 (2018).
  142. Ichikawa, T. *et al.* Mechanism of novel reaction from  $\text{LiNH}_2$  and  $\text{LiH}$  to  $\text{Li}_2\text{NH}$  and  $\text{H}_2$  as a promising hydrogen storage system. *J. Phys. Chem. B* **108**, 7887–7892 (2004).
  143. Chen, P. *et al.* Interaction between lithium amide and lithium hydride. *J. Phys. Chem. B* **107**, 10967–10970 (2003).
  144. Ikeda, S. *et al.* Simultaneous determination of ammonia emission and hydrogen capacity variation during the cyclic testing for  $\text{LiNH}_2$ - $\text{LiH}$  hydrogen storage system. *Int. J. Hydrogen Energy* **33**, 6201–6204 (2008).
  145. Makepeace, J. W. and David, W. I. F. Structural insights into the lithium amide-imide solid solution. *J. Phys. Chem. C* **121**, 12010–12017 (2017).
  146. Hamilton, C. W. *et al.* B-N compounds for chemical hydrogen storage. *Chem. Soc. Rev.* **38**, 279–293 (2009).
  147. Moussa, G. *et al.* Boron-based hydrides for chemical hydrogen storage. *Int. J. Energy Res.* **37**, 825–842 (2013).
  148. Umegaki, T. *et al.* Boron- and nitrogen-based chemical hydrogen storage materials. *Int. J. Hydrogen Energy* **34**, 2303–2311 (2009).
  149. Huang, Z. and Autrey, T. Boron-nitrogen-hydrogen (BNH) compounds: Recent developments in hydrogen storage, applications in hydrogenation and catalysis, and new syntheses. *Energy Environ. Sci.* **5**, 9257–9268 (2012).
  150. Lu, Z. H. and Xu, Q. Recent progress in boron- and nitrogen-based chemical hydrogen

- storage. *Funct. Mater. Lett.* **5**, 1–9 (2012).
151. Jepsen, L. H. *et al.* Boron-nitrogen based hydrides and reactive composites for hydrogen storage. *Mater. Today* **17**, 129–135 (2014).
  152. Wang, K. *et al.* Metal B-N-H hydrogen-storage compound: Development and perspectives. *J. Alloys Compd.* **794**, 303–324 (2019).
  153. Kumar, S. *et al.* Development of vanadium based hydrogen storage material: A review. *Renew. Sustain. Energy Rev.* **72**, 791–800 (2017).
  154. Kumar, R. *et al.* Solid-state hydrogen rich boron-nitrogen compounds for energy storage. *Chem. Soc. Rev.* **48**, 5350–5380 (2019).
  155. Kantürk Figen, A. *et al.* Synthesis, structural characterization, and hydrolysis of ammonia borane ( $\text{NH}_3\text{BH}_3$ ) as a hydrogen storage carrier. *Int. J. Hydrogen Energy* **38**, 16215–16228 (2013).
  156. Moury, R. *et al.* Hydrazine borane: Synthesis, characterization, and application prospects in chemical hydrogen storage. *Phys. Chem. Chem. Phys.* **14**, 1768–1777 (2012).
  157. Al-Kukhun, A. *et al.* Mechanistic studies of ammonia borane dehydrogenation. *Int. J. Hydrogen Energy* **38**, 169–179 (2013).
  158. Demirci, U. B. Ammonia borane, a material with exceptional properties for chemical hydrogen storage. *Int. J. Hydrogen Energy* **42**, 9978–10013 (2017).
  159. Moury, R. and Demirci, U. B. Hydrazine borane and hydrazinidoboranes as chemical hydrogen storage materials. *Energies* **8**, 3118–3141 (2015).
  160. Li, H. *et al.* Ammonia borane, past as prolog. *J. Organomet. Chem.* **751**, 60–66 (2014).
  161. Chen, X. *et al.* The roles of dihydrogen bonds in amine borane chemistry. *Acc. Chem. Res.* **46**, 2666–2675 (2013).
  162. Kar, T. and Scheiner, S. Comparison between hydrogen and dihydrogen bonds among  $\text{H}_3\text{BNH}_3$ ,  $\text{H}_2\text{BNH}_2$ , and  $\text{NH}_3$ . *J. Chem. Phys.* **119**, 1473–1482 (2003).

163. Akbayrak, S. and Özkar, S. Ammonia borane as hydrogen storage materials. *Int. J. Hydrogen Energy* **43**, 18592–18606 (2018).
164. Liu, C. H. *et al.* Hydrogen generated from hydrolysis of ammonia borane using cobalt and ruthenium based catalysts. *Int. J. Hydrogen Energy* **37**, 2950–2959 (2012).
165. Hügler, T. *et al.* Hydrazine borane: A promising hydrogen storage material. *J. Am. Chem. Soc.* **131**, 7444–7446 (2009).
166. Karahan, S. *et al.* Catalytic hydrolysis of hydrazine borane for chemical hydrogen storage: Highly efficient and fast hydrogen generation system at room temperature. *Int. J. Hydrogen Energy* **36**, 4958–4966 (2011).
167. Hannauer, J. *et al.* High-extent dehydrogenation of hydrazine borane  $N_2H_4BH_3$  by hydrolysis of  $BH_3$  and decomposition of  $N_2H_4$ . *Energy Environ. Sci.* **4**, 3355–3358 (2011).
168. Zhu, Q. L. *et al.* Controlled synthesis of ultrafine surfactant-free NiPt nanocatalysts toward efficient and complete hydrogen generation from hydrazine borane at room temperature. *ACS Catal.* **4**, 4261–4268 (2014).
169. Denney, M. C. *et al.* Efficient catalysis of ammonia borane dehydrogenation. *J. Am. Chem. Soc.* **128**, 12048–12049 (2006).
170. Zhang, X. *et al.* Ruthenium-catalyzed ammonia borane dehydrogenation: Mechanism and utility. *Acc. Chem. Res.* **50**, 86–95 (2017).
171. Zhan, W. W. *et al.* Dehydrogenation of ammonia borane by metal nanoparticle catalysts. *ACS Catal.* **6**, 6892–6905 (2016).
172. Badding, C. K. *et al.* Metal ruthenate perovskites as heterogeneous catalysts for the hydrolysis of ammonia borane. *ACS Omega* **3**, 3501–3506 (2018).
173. Rueda, M. *et al.* Innovative methods to enhance the properties of solid hydrogen storage materials based on hydrides through nanoconfinement: A review. *J. Supercrit. Fluids* **141**, 198–217 (2018).
174. Sepehri, S. *et al.* Influence of surface chemistry on dehydrogenation in carbon cryogel ammonia borane nanocomposites. *Eur. J. Inorg. Chem.* **2009**, 599–603 (2009).

175. Feaver, A. *et al.* Coherent carbon cryogel-ammonia borane nanocomposites for H<sub>2</sub> storage. *J. Phys. Chem. B* **111**, 7469–7472 (2007).
176. Alipour, J. *et al.* Ammonia borane confined by poly(methyl methacrylate)/multiwall carbon nanotube nanofiber composite, as a polymeric hydrogen storage material. *J. Mater. Sci.* **50**, 3110–3117 (2015).
177. Li, Z. *et al.* Ammonia borane confined by a metal-organic framework for chemical hydrogen storage: Enhancing kinetics and eliminating ammonia. *J. Am. Chem. Soc.* **132**, 1490–1491 (2010).
178. Li, Z. *et al.* Improved thermal dehydrogenation of ammonia borane by MOF-5. *RSC Adv.* **5**, 10746–10750 (2015).
179. Chung, J. Y. *et al.* Influence of metal-organic framework porosity on hydrogen generation from nanoconfined ammonia borane. *J. Phys. Chem. C* **121**, 27369–27378 (2017).
180. Rueda, M. *et al.* Improvement of the kinetics of hydrogen release from ammonia borane confined in silica aerogel. *Micropor. Mesopor. Mater.* **237**, 189–200 (2017).
181. Paolone, A. *et al.* Absence of the structural phase transition in ammonia borane dispersed in mesoporous silica: Evidence of novel thermodynamic properties. *J. Phys. Chem. C* **113**, 10319–10321 (2009).
182. Wang, L. Q. *et al.* Hyperpolarized <sup>129</sup>Xe NMR investigation of ammonia borane in mesoporous silica. *J. Phys. Chem. C* **113**, 6485–6490 (2009).
183. Feng, Y. *et al.* Encapsulation of ammonia borane in Pd/Halloysite nanotubes for efficient thermal dehydrogenation. *ACS Sustain. Chem. Eng.* **8**, 2122–2129 (2020).
184. Valero-Pedraza, M.-J. *et al.* Ammonia borane nanospheres for hydrogen storage. *ACS Appl. Nano Mater.* **2**, 1129–1138 (2019).
185. Schlesinger, H. J. and Burg, A. B. Hydrides of boron. VIII. The structure of the diammoniate of diborane and its relation to the structure of diborane. *J. Am. Chem. Soc.* **60**, 290–299 (1938).
186. Schlesinger, H. I. and Burg, A. B. Recent developments in the chemistry of the boron

- hydrides. *Chem. Rev.* **31**, 1–41 (1942).
187. Myers, A. G. *et al.* Lithium amidotrihydroborate, a powerful new reductant. Transformation of tertiary amides to primary alcohols. *Tetrahedron Lett.* **37**, 3623–3626 (1996).
188. Diyabalanage, H. V. K. *et al.* Calcium amidotrihydroborate: A hydrogen storage material. *Angew. Chem. Int. Ed.* **46**, 8995–8997 (2007).
189. Spielmann, J. *et al.* Calcium amidoborane hydrogen storage materials: Crystal structures of decomposition products. *Angew. Chem. Int. Ed.* **47**, 6290–6295 (2008).
190. Xiong, Z. *et al.* High-capacity hydrogen storage in lithium and sodium amidoboranes. *Nat. Mater.* **7**, 138–141 (2008).
191. Genova, R. V. *et al.* Towards  $Y(NH_2BH_3)_3$ : Probing hydrogen storage properties of  $YX_3/MNH_2BH_3$  ( $X=F, Cl$ ;  $M=Li, Na$ ) and  $YH_{x-3}/NH_3BH_3$  composites. *J. Alloys Compd.* **499**, 144–148 (2010).
192. Hawthorne, M.F., Jalisatgi, S.S., Safronov, A.V., Lee, H.B., Wu, J. *Chemical hydrogen storage using polyhedral borane anions and aluminum-ammonia-borane complexes: Final report.* (University of Missouri, 2010).
193. Kang, X. *et al.* Combined formation and decomposition of dual-metal amidoborane  $NaMg(NH_2BH_3)_3$  for high-performance hydrogen storage. *Dalton Trans.* **40**, 3799–3801 (2011).
194. Fijalkowski, K. J. *et al.*  $Na[Li(NH_2BH_3)_2]$  - The first mixed-cation amidoborane with unusual crystal structure. *Dalton Trans.* **40**, 4407–4413 (2011).
195. Wu, H. *et al.* Sodium magnesium amidoborane: The first mixed-metal amidoborane. *Chem. Commun.* **47**, 4102–4104 (2011).
196. Kang, X. D. *et al.* Efficient and highly rapid hydrogen release from ball-milled  $3NH_3BH_3/MMgH_3$  ( $M = Na, K, Rb$ ) mixtures at low temperatures. *Int. J. Hydrogen Energy* **37**, 4259–4266 (2012).
197. Xia, G. *et al.* Mixed-metal (Li, Al) amidoborane: Synthesis and enhanced hydrogen storage properties. *J. Mater. Chem. A* **1**, 1810–1820 (2013).

198. Dovgaliuk, I. *et al.* A composite of complex and chemical hydrides yields the first Al-based amidoborane with improved hydrogen storage properties. *Chem. Eur. J.* **21**, 14562–14570 (2015).
199. Wang, K. *et al.* Electronic structures and dehydrogenation properties of bimetallic amidoboranes. *Int. J. Hydrogen Energy* **40**, 2500–2508 (2015).
200. Wolstenholme, D. J. *et al.* Homopolar dihydrogen bonding in alkali metal amidoboranes: Crystal engineering of low-dimensional molecular materials. *J. Am. Chem. Soc.* **135**, 2439–2442 (2013).
201. Forster, T. D. *et al.* Characterization of  $\beta$ -B-agostic isomers in zirconocene amidoborane complexes. *J. Am. Chem. Soc.* **131**, 6689–6691 (2009).
202. Sit, V. *et al.* The thermal dissociation of  $\text{NH}_3\text{BH}_3$ . *Thermochim. Acta* **113**, 379–382 (1987).
203. Hu, M. G. *et al.* The thermal decomposition of ammonia borane. *Thermochim. Acta* **23**, 249–255 (1978).
204. Baitalow, F. *et al.* Thermal decomposition of B-N-H compounds investigated by using combined thermoanalytical methods. *Thermochim. Acta* **391**, 159–168 (2002).
205. Wu, C. *et al.* Stepwise phase transition in the formation of lithium amidoborane. *Inorg. Chem.* **49**, 4319–4323 (2010).
206. Wu, H. *et al.* Alkali and alkaline-earth metal amidoboranes: Structure, crystal chemistry, and hydrogen storage properties. *J. Am. Chem. Soc.* **130**, 14834–14839 (2008).
207. Fijalkowski, K. J. *et al.* Insights from impedance spectroscopy into the mechanism of thermal decomposition of  $\text{M}(\text{NH}_2\text{BH}_3)$ ,  $\text{M} = \text{H}, \text{Li}, \text{Na}, \text{Li}_{0.5}, \text{Na}_{0.5}$ , hydrogen stores. *Phys. Chem. Chem. Phys.* **14**, 5778–5784 (2012).
208. Luedtke, A. T. and Autrey, T. Hydrogen release studies of alkali metal amidoboranes. *Inorg. Chem.* **49**, 3905–3910 (2010).
209. Xia, G. *et al.* Well-dispersed lithium amidoborane nanoparticles through nanoreactor engineering for improved hydrogen release. *Nanoscale* **6**, 12333–12339 (2014).

210. Shimoda, K. *et al.* Solid state NMR study on the thermal decomposition pathway of sodium amidoborane  $\text{NaNH}_2\text{BH}_3$ . *J. Mater. Chem.* **21**, 2609–2615 (2011).
211. Fijałkowski, K. J. and Grochala, W. Substantial emission of  $\text{NH}_3$  during thermal decomposition of sodium amidoborane,  $\text{NaNH}_2\text{BH}_3$ . *J. Mater. Chem.* **19**, 2043–2050 (2009).
212. Xiong, Z. *et al.* Synthesis of sodium amidoborane ( $\text{NaNH}_2\text{BH}_3$ ) for hydrogen production. *Energy Environ. Sci.* **1**, 360–363 (2008).
213. Sandra, F. P. R. *et al.* A simple preparation method of sodium amidoborane, highly efficient derivative of ammonia borane dehydrogenating at low temperature. *Int. J. Hydrogen Energy* **36**, 7423–7430 (2011).
214. Diyabalanage, H. V. K. *et al.* Potassium(I) amidotrihydroborate: Structure and hydrogen release. *J. Am. Chem. Soc.* **132**, 11836–11837 (2010).
215. Kazakov, I. V. *et al.* Reversible structural transformations of rubidium and cesium amidoboranes. *Polyhedron* **127**, 186–190 (2017).
216. Owarzany, R. *et al.* Amidoboranes of rubidium and caesium: The last missing members of the alkali metal amidoborane family. *Dalton Trans.* **46**, 16315–16320 (2017).
217. Wu, H. *et al.* Metal hydrazinoborane  $\text{LiN}_2\text{H}_3\text{BH}_3$  and  $\text{LiN}_2\text{H}_3\text{BH}_3 \cdot 2\text{N}_2\text{H}_4\text{BH}_3$ : Crystal structures and high-extent dehydrogenation. *Energy Environ. Sci.* **5**, 7531–7535 (2012).
218. Moury, R. *et al.* Lithium hydrazinidoborane: A polymorphic material with potential for chemical hydrogen storage. *Chem. Mater.* **26**, 3249–3255 (2014).
219. Tan, Y. *et al.* The decomposition of  $\alpha\text{-LiN}_2\text{H}_3\text{BH}_3$ : An unexpected hydrogen release from a homopolar proton-proton pathway. *J. Mater. Chem. A* **2**, 15627–15632 (2014).
220. Moury, R. *et al.* Sodium hydrazinidoborane: A chemical hydrogen-storage material. *ChemSusChem* **6**, 667–673 (2013).
221. Chua, Y. S. *et al.* Alkali metal hydride modification on hydrazine borane for improved dehydrogenation. *J. Phys. Chem. C* **118**, 11244–11251 (2014).
222. Castilla-Martinez, C. A. *et al.* Rubidium hydrazinidoborane: Synthesis, characterization and

- hydrogen release properties. *Int. J. Hydrogen Energy* **44**, 28252–28261 (2019).
223. Harder, S. Molecular early main group metal hydrides: Synthetic challenge, structures and applications. *Chem. Commun.* **48**, 11165–11177 (2012).
224. Pylypko, S. *et al.* Metal hydride-hydrazine borane: Towards hydrazinidoboranes or composites as hydrogen carriers. *Int. J. Hydrogen Energy* **40**, 14875–14884 (2015).
225. Castilla-Martinez, C. A. *et al.* Cesium hydrazinidoborane, the last of the alkali hydrazinidoboranes, studied as potential hydrogen storage material. *Int. J. Hydrogen Energy* **45**, 16634–16643 (2020).
226. Bowden, M. E. *et al.* Room-temperature structure of ammonia borane. *Aust. J. Chem.* **60**, 149–153 (2007).
227. Moury, R. *et al.* In situ thermodiffraction to monitor synthesis and thermolysis of hydrazine borane-based materials. *J. Alloys Compd.* **659**, 210–216 (2016).
228. Klooster, W. T. *et al.* Study of the N-H...H-B dihydrogen bond including the crystal structure of  $\text{BH}_3\text{NH}_3$  by neutron diffraction. *J. Am. Chem. Soc.* **121**, 6337–6343 (1999).
229. Wolstenholme, D. J. *et al.* Homopolar dihydrogen bonding in alkali-metal amidoboranes and its implications for hydrogen storage. *J. Am. Chem. Soc.* **133**, 16598–16604 (2011).
230. Shimoda, K. *et al.* Comparative study of structural changes in  $\text{NH}_3\text{BH}_3$ ,  $\text{LiNH}_2\text{BH}_3$ , and  $\text{KNH}_2\text{BH}_3$  during dehydrogenation process. *J. Phys. Chem. C* **116**, 5957–5964 (2012).
231. Wang, K. *et al.* Crystal and electronic structures of solid  $\text{M}(\text{NH}_2\text{BH}_3)_n$  ( $\text{M} = \text{Li}, \text{Na}, \text{K}$ ) and the decomposition mechanisms. *Int. J. Hydrogen Energy* **39**, 21372–21379 (2014).
232. Zhang, Y. and Wolverton, C. Crystal structures, phase stabilities, and hydrogen storage properties of metal amidoboranes. *J. Phys. Chem. C* **116**, 14224–14231 (2012).
233. Moury, R. *et al.* Pure hydrogen-generating ‘doped’ sodium hydrazinidoborane. *Int. J. Hydrogen Energy* **40**, 7475–7482 (2015).
234. Bowden, M. *et al.* The diammoniate of diborane: Crystal structure and hydrogen release. *Chem. Commun.* **46**, 8564–8566 (2010).

235. Shevlin, S. A. *et al.* Dehydrogenation mechanisms and thermodynamics of  $MNH_2BH_3$  ( $M = Li, Na$ ) metal amidoboranes as predicted from first principles. *Phys. Chem. Chem. Phys.* **13**, 7649–7659 (2011).
236. Zhang, Y. *et al.* First-principles prediction of intermediate products in the decomposition of metal amidoboranes. *J. Phys. Chem. C* **116**, 26728–26734 (2012).
237. Kim, D. Y. *et al.* Hydrogen-release mechanisms in lithium amidoboranes. *Chem. Eur. J.* **15**, 5598–5604 (2009).
238. Swinnen, S. *et al.* Potential hydrogen storage of lithium amidoboranes and derivatives. *Chem. Phys. Lett.* **489**, 148–153 (2010).
239. Ryan, K. R. *et al.* A combined experimental inelastic neutron scattering, Raman and ab initio lattice dynamics study of  $\alpha$ -lithium amidoborane. *Phys. Chem. Chem. Phys.* **13**, 12249–12253 (2011).
240. Kim, D. Y. *et al.* Rules and trends of metal cation driven hydride-transfer mechanisms in metal amidoboranes. *Phys. Chem. Chem. Phys.* **12**, 5446–5453 (2010).
241. Li, T. and Zhang, J.-G. Theoretical study of the metal-controlled dehydrogenation mechanism of  $MN_2H_3BH_3$  ( $M = Li, Na, K$ ): A new family of hydrogen storage material. *J. Phys. Chem. A* **122**, 1344–1349 (2018).
242. Li, T. *et al.* Theoretical study of the structure and dehydrogenation mechanism of sodium hydrazinidoborane. *J. Theor. Comput. Chem.* **16**, 1750020 (2017).
243. Wolstenholme, D. J. *et al.* Thermal desorption of hydrogen from ammonia borane: Unexpected role of homopolar B-H $\cdots$ H-B interactions. *Chem. Commun.* **48**, 2597–2599 (2012).
244. Roy, B. *et al.* Supported ammonia borane decomposition through enhanced homopolar B-B coupling. *Dalton Trans.* **47**, 6570–6579 (2018).
245. Petit, J. F. and Demirci, U. B. Mechanistic insights into dehydrogenation of partially deuterated ammonia borane  $NH_3BD_3$  being heating to 200°C. *Inorg. Chem.* **58**, 489–494 (2019).

246. Sutton, A. D. *et al.* Regeneration of ammonia borane spent fuel by direct reaction with hydrazine and liquid ammonia. *Science*. **331**, 1426–1429 (2011).
247. Tang, Z. *et al.* Regenerable hydrogen storage in lithium amidoborane. *Chem. Commun.* **48**, 9296–9298 (2012).
248. Eichler, J. and Lesniak, C. Boron nitride (BN) and BN composites for high-temperature applications. *J. Eur. Ceram. Soc.* **28**, 1105–1109 (2008).
249. Nakagawa, Y. *et al.* AB-MH (Ammonia borane-Metal hydride) composites: Systematic understanding of dehydrogenation properties. *J. Mater. Chem. A* **2**, 3926–3931 (2014).
250. Luo, J. *et al.* Synthesis, formation mechanism, and dehydrogenation properties of the long-sought  $\text{Mg}(\text{NH}_2\text{BH}_3)_2$  compound. *Energy Environ. Sci.* **6**, 1018–1025 (2013).
251. Leardini, F. *et al.* Hydrogen desorption behavior of calcium amidoborane obtained by reactive milling of calcium hydride and ammonia borane. *J. Phys. Chem. C* **116**, 24430–24435 (2012).
252. Ould-Amara, S. *et al.* Calcium hydrazinidoborane: Synthesis, characterization, and promises for hydrogen storage. *Int. J. Hydrogen Energy* **45**, 2022–2033 (2019).
253. Zhang, Q. *et al.* Synthesis, crystal structure, and thermal decomposition of strontium amidoborane. *J. Phys. Chem. C* **114**, 1709–1714 (2010).
254. Shcherbina, N. A. *et al.* Synthesis and characterization of barium amidoborane. *Russ. J. Gen. Chem.* **87**, 2875–2877 (2017).
255. Wang, P. *et al.* Hydrogen in mechanically prepared nanostructured h-BN: A critical comparison with that in nanostructured graphite. *Appl. Phys. Lett.* **80**, 318–320 (2002).
256. Ma, R. *et al.* Hydrogen uptake in boron nitride nanotubes at room temperature. *J. Am. Chem. Soc.* **124**, 7672–7673 (2002).
257. Lale, A. *et al.* Boron nitride for hydrogen storage. *ChemPlusChem* **83**, 893–903 (2018).
258. Dai, J. *et al.* Porous boron nitride with tunable pore size. *J. Phys. Chem. Lett.* **5**, 393–398 (2014).

259. Kumar, E. M. *et al.* First principles guide to tune h-BN nanostructures as superior light-element-based hydrogen storage materials: Role of the bond exchange spillover mechanism. *J. Mater. Chem. A* **3**, 304–313 (2015).
260. Wang, Y. *et al.* Theoretical prediction of hydrogen storage on Li-decorated boron nitride atomic chains. *J. Appl. Phys.* **113**, 064309 (1–6) (2013).
261. Liu, Y. *et al.* Hydrogen storage using Na-decorated graphyne and its boron nitride analog. *Int. J. Hydrogen Energy* **39**, 12757–12764 (2014).
262. Zhao, G. *et al.* Boron nitride substrate-induced reversible hydrogen storage in bilayer solid matrix via interlayer spacing. *Int. J. Hydrogen Energy* **37**, 9677–9687 (2012).
263. Choi, H. *et al.* Ambient carbon dioxide capture by boron-rich boron nitride nanotube. *J. Am. Chem. Soc.* **133**, 2084–2087 (2011).
264. Paura, E. N. C. *et al.* Carbon dioxide adsorption on doped boron nitride nanotubes. *RSC Adv.* **4**, 28249–28258 (2014).
265. Huang, K. *et al.* Aminopolymer functionalization of boron nitride nanosheets for highly efficient capture of carbon dioxide. *J. Mater. Chem. A* **5**, 16241–16248 (2017).
266. Liang, J. *et al.* In situ Cu-loaded porous boron nitride nanofiber as an efficient adsorbent for CO<sub>2</sub> capture. *ACS Sustain. Chem. Eng.* **8**, 7454–7462 (2020).
267. Hojatisaeidi, F. *et al.* Metal-free modified boron nitride for enhanced CO<sub>2</sub> capture. *Energies* **13**, 1–11 (2020).



# Chapter 3

RUBIDIUM

HYDRAZINIDOBORANE

---



# 3 Rubidium hydrazinidoborane

---

## 1. Introduction

Energy is one of the most critical issues for humanity, and it is expected that the energy demand will rise up to 30% by 2040.<sup>1</sup> The primary source of energy nowadays is based on fossil fuels, but the consumption in a large scale has led to the release of pollutants and greenhouse gases directly into the atmosphere contributing to global warming, with all the negative consequences that this implies.<sup>2,3</sup> Besides, fossil fuels are limited resources that are being rapidly depleted. One of the alternatives to circumvent this problem is the use of hydrogen as an energy carrier because this fuel is clean and nontoxic. As an element, hydrogen is the most abundant in the universe and its molecular counterpart  $H_2$  can be produced by a variety of methods (i.e. hydrocarbon and ammonia reforming, biomass gasification or water electrolysis).<sup>4-7</sup> However, one of the major challenges to use hydrogen as a fuel is its storage. Currently, different approaches are under investigation: hydrogen can be stored by compression in high-pressure gas cylinders, as a liquid in cryogenic tanks, or stored in a host material. In addition, there are some requirements that a given technology must have to be considered for hydrogen storage such as high gravimetric/volumetric hydrogen storage capacity, reversibility of storage, stability, safety and its cycle life.<sup>7-9</sup> On this basis, a series of materials have emerged due to high hydrogen storage capacities (e.g. metal hydrides, carbonaceous porous hosts, metal organic frameworks, and inorganic compounds).<sup>10-13</sup>

Among the inorganic materials, boron and nitrogen-based compounds have received particular attention as chemical hydrogen storage materials.<sup>14-17</sup> Ammonia borane  $NH_3BH_3$  (AB) is a typical example. It is a crystalline solid at ambient conditions that was reported for the first time in 1955<sup>18</sup>, and since then it has been widely investigated for hydrogen storage.<sup>19,20</sup> This material shows high

gravimetric hydrogen density (19.6 wt. % H) and is able to release, exothermically and thus irreversibly, 1 equiv.  $H_2$  between 95-110°C; then, it liberates an additional 1.2-1.4 of hydrogen between 120-200°C, and the residual hydrogen above 500°C. However, there are some problems with AB: the thermolysis kinetics are slow; undesired by-products like borazine  $B_3N_3H_6$ , ammonia  $NH_3$ , and diborane  $B_2H_6$  are formed; and the solid polymeric residue product is of complex composition.<sup>21</sup> In other words, pristine AB is not suitable for hydrogen storage in the solid state.

Hydrazine borane  $N_2H_4BH_3$  (HB) is another boron and nitrogen-based compound that has been studied as hydrogen storage material.<sup>22</sup> HB is a derivative of AB where the  $NH_3$  moiety has been substituted by the hydrazine moiety  $N_2H_4$ .<sup>23</sup> HB possesses a gravimetric hydrogen density of 15.4 wt. % H, but differently than AB, it has four protic hydrogens ( $H^{\delta+}$ ) and three hydridic hydrogens ( $H^{\delta-}$ ). The dehydrogenation of HB starts at about 60°C, and the borane loses 2 equivalents of  $H_2$  up to 250°C, together with hazardous and toxic by-products (i.e.  $N_2H_4$ ,  $NH_3$  and  $B_2H_6$ ). Worse, it presents the formation of a shock-sensitive residue when heated above 300°C.<sup>24</sup> There have been attempts to avoid these problems. One method is the chemical modification of HB.

Alkali hydrazinidoboranes  $MN_2H_3BH_3$  (MHB) are obtained by the substitution of one of the protic hydrogens  $H^{\delta+}$  of the middle  $NH_2$  of HB by an alkali cation  $M^+$ , which results in an equivalent number of  $H^{\delta+}$  and  $H^{\delta-}$  in the as-formed ionic compound. Usually, MHB are synthesized by the reaction between HB and a metal hydride MH. The first hydrazinidoborane that was synthesized is lithium hydrazinidoborane  $LiN_2H_3BH_3$  (LiHB, 11.7 wt. % H). Wu *et al.*<sup>25</sup> and Moury *et al.*<sup>26</sup> reported two different phases of LiHB obtained by ball milling, in different conditions, an equimolar mixture of HB and LiH. The former group obtained the high-temperature phase  $\alpha$ -LiHB (monoclinic, s.g.  $P2_1/c$ ), while the latter group obtained the low-temperature phase  $\beta$ -LiHB (orthorhombic, s.g.  $Pbca$ ). The phase transition takes place at ca. 90°C and then  $\alpha$ -LiHB dehydrogenates while liberating 2.6 equivalents of  $H_2$  up to 150°C. Another derivative is sodium hydrazinidoborane  $NaNH_3NH_3$  (NaHB, 8.9 wt. % H; monoclinic, s.g.  $P2_1/n$ ). The synthesis of NaHB was carried out at -30°C due to the high reactivity of NaH towards HB at ambient conditions ( $-27.7 \text{ kJ mol}^{-1}$ ).<sup>27,28</sup> NaHB starts to release  $H_2$  below 60°C, and it can release 2.6 equivalents of  $H_2$  between 60 and 150°C. Despite this performance, NaHB also releases traces of  $N_2$  and  $NH_3$ . The last alkali derivative of HB reported is potassium hydrazinidoborane  $KNH_3NH_3$  (KHB, 7.2 wt. % H;

monoclinic, s.g.  $P2_1$ ).<sup>29</sup> It was prepared in a stainless steel vessel and in THF for safety reasons, as the reaction between KH and HB is highly exothermic ( $70.3 \text{ kJ mol}^{-1}$ ).<sup>27</sup> KHB shows slightly better dehydrogenation properties than NaHB and LiHB, with a first dehydrogenation step at  $52^\circ\text{C}$ .<sup>29</sup>

Computational calculations have shed more light into the behavior of hydrazinidoboranes. The role of the metal cation  $M^+$  was predicted to be crucial, as it is believed to drive the formation of the complex intermediate  $M\text{-H}\cdots\text{H}_3\text{N}_2\text{BH}_2$ .<sup>30,31</sup> This is known as the “metal cation driven hydride-transfer” mechanism that was first reported for alkali amidoboranes  $\text{MNH}_2\text{BH}_3$  (MAB), namely the alkali derivatives of AB.<sup>32,33</sup> However the dehydrogenation mechanism is more complex, as for amidoboranes.<sup>34,35</sup> While studying the isotopomer  $\text{LiN}_2\text{H}_3\text{BD}_3$ , Tan *et al.* brought to light the occurrence of counterintuitive homopolar  $\text{H}^{\delta+}\cdots\text{H}^{\delta+}$  and  $\text{D}^{\delta-}\cdots\text{D}^{\delta-}$  reactions resulting in the formation of  $\text{H}_2$  and  $\text{D}_2$  (together with heteropolar  $\text{H}^{\delta+}\cdots\text{D}^{\delta-}$  reactions forming HD).<sup>36</sup>

No other derivatives of HB have been reported so far. Efforts have been done to obtain  $\text{Mg}(\text{N}_2\text{H}_3\text{BH}_3)_2$  (MgHB, 11.6 wt. % H) or  $\text{Ca}(\text{N}_2\text{H}_3\text{BH}_3)_2$  (CaHB, 9.3 wt. % H) by ball milling  $\text{MgH}_2$  or  $\text{CaH}_2$  with HB, but all the attempts have failed.<sup>27</sup> It is evident that the chemical modification is an efficient strategy in getting derivatives of HB (as well as of AB) with improved dehydrogenation properties in terms of temperature, kinetics, and  $\text{H}_2$  purity. We consider as crucial to obtain and study new derivatives, having 3 main reasons to do that. 1) It is important to increase our knowledge and fundamental understanding of boron and nitrogen-based materials through new compounds. 2) They may widen the prospects for hydrogen storage applications. 3) They might open up new opportunities. According to this, we present a new alkali derivative, namely rubidium hydrazinidoborane  $\text{RbN}_2\text{H}_3\text{BH}_3$  (RbHB, 4.65 wt. % H) and the evaluation of its properties.

## 2. Experimental Section

### 2.1 Reagents

Hydrazine hemisulphate  $\text{N}_2\text{H}_4\cdot\frac{1}{2}\text{H}_2\text{SO}_4$  ( $\geq 98\%$ ), sodium borohydride  $\text{NaBH}_4$  ( $\geq 98\%$ ) and anhydrous 1,4-dioxane ( $\geq 99.8\%$ ) were purchased from Sigma-Aldrich and used for the synthesis of hydrazine borane. Rubidium ingot (99.6%, Sigma-Aldrich) and THF (99.5%, extra dry, Acros

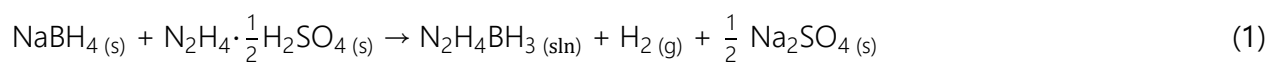
Organics) were used for the synthesis of RbHB. We preferred to use Rb over RbH for three reasons: i) RbH has not been found to be available commercially; ii) using RbH supposes its preparation and the subsequent reaction with HB, increasing the number of steps for the process; and iii) the use of RbH is not convenient for safety reasons, because of its high reactivity.

## 2.2 Synthesis

The boranes used in our works are sensitive to humidity and to oxygen. For this reason all the experiments were done in an argon-filled glovebox (MBraun M200B,  $O_2 < 0.1$  ppm and  $H_2O < 0.1$  ppm) or in a Schlenk line under an argon atmosphere.

### 2.2.1 Synthesis of hydrazine borane

The path to synthesize hydrazine borane was previously developed by our team.<sup>24</sup> For this work, HB was obtained by the same method: 10.1 g (0.267 mol) of  $NaBH_4$  and 21.64 g (0.267 mol) of  $N_2H_4 \cdot \frac{1}{2}H_2SO_4$  were weighted, grounded in a mortar and put into a Schlenk flask and a three-necked round-bottom flask, respectively. 150 mL of 1,4-dioxane was added to the  $NaBH_4$ , and the suspension was then poured into the  $N_2H_4 \cdot \frac{1}{2}H_2SO_4$ . A hydrogen evolution started immediately. The system was left under reflux and vigorous stirring for 48 h at 30°C. The reaction takes place as follows:

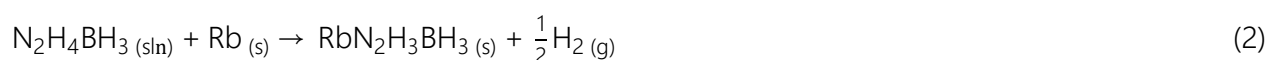


The obtained hydrazine borane was solved in the 1,4-dioxane, and the  $Na_2SO_4$  was in suspension. The suspension is then filtered, the solution was recovered and the solvent was finally removed. The solid product was dried under vacuum for 48 h at room temperature. The obtained hydrazine borane was stored in the glovebox.

### 2.2.2 Synthesis of rubidium hydrazinidoborane

The synthesis of RbHB was carried out in the glovebox at room temperature. Hydrazine borane directly reacts with metallic rubidium, as ammonia borane does.<sup>37,38</sup> HB (246 mg, 5.36 mmol) was solved in 20 mL of THF and poured into one flask that contained the metallic rubidium (400 mg,

4.68 mmol). The release of hydrogen started immediately. The reaction was left under stirring for 30 h. After, the remaining rubidium was collected (90 mg, 1.05 mmol). The solid precipitate was washed two times with THF and two times with 1,4 dioxane, dried under vacuum overnight and recovered. At most, it was possible to recover 393 mg of product (corresponding to a yield of 83% with respect to the reacted alkali metal). The reaction can be written as follows:



## 2.3 Characterization

### 2.3.1 Structural characterization

The obtained RbHB and the dehydrogenated solid products were analyzed by solid state  $^{11}\text{B}$  magic angle spin – nuclear magnetic resonance MAS-NMR (Varian VNMR400, 128.31 MHz) and Fourier Transformed Infrared (FTIR) spectroscopy (NEXUS instrument, ThermoFisher Scientific; equipped with an attenuated total reflection accessory from 600 to 4000  $\text{cm}^{-1}$  wavenumber). The samples analyzed by FTIR were prepared in closed vials inside the glovebox and the analyses were carried out in an air atmosphere. The samples were carried to the FTIR apparatus in the closed vials. The samples were taken out of the vials just before the FTIR analysis, in order to avoid a long time of exposition of the sample to the air atmosphere.

The samples for the MAS-NMR were prepared inside the glovebox, using zirconia rotors of 3.2 mm of diameter. Mr. Philippe Gaveau and Mr. Emmanuel Fernandez, from the Platform Balard of the University of Montpellier, did the sample preparation and the measurements.

The crystalline structure of RbHB was determined by power X-ray diffraction (PXRD) analysis. A PANalytical X'Pert Pro Multipurpose diffractometer equipped with an X'Celerator detector (Cu- $K_{\alpha 1/\alpha 2}$  radiation  $\lambda=1.5418 \text{ \AA}$ , 45 kV, 30 mA) equipped with fixed divergence slits was used for the measurements. The pattern was collected using Bragg-Brentano geometry on a spinning zero background sample holder that was prepared into the glovebox. The powder was protected using a Kapton film stuck onto the sample holder with Apiezon grease (H quality) to prevent any  $\text{O}_2$  and  $\text{H}_2\text{O}$  contamination. The diffraction pattern was recorded in the 15-80° angle range in  $2\theta$  using a

step size of 0.017, and a scan step time of ~450 seconds. The crystallinity of the dehydrogenated solids was analyzed using a Debye-Scherrer configuration (Cu/K $\alpha_1$  radiation  $\lambda=1.5418$  Å). The samples were filled in glass capillary of 0.5 mm diameter in the glovebox, sealed and then analyzed in the equipment. Ms. Dominique Granier, from the Platform Balard of the University of Montpellier, performed all the manipulations of the XRD apparatus.

### 2.3.2 Thermal characterization

The thermal behavior of RbHB was preliminary analyzed by simultaneous thermogravimetric (TG) and differential scanning calorimetry (DSC) analysis (SDT Q600, TA Instruments). A further TG analysis was carried out in a Netzsch STA 449 F1 Jupiter equipment that was coupled to a mass spectrometer (MS; Netzsch QMS 403 D Aëolos Quadro) in order to analyze the gases released by RbHB. The sample preparation was done in the glovebox, where the powder was put into a Tzero hermetic pan to protect it from air. The pan is pierced right before the analysis to allow the produced gases to escape. The manipulation of the TGA-MS equipment was carried out by the technician of the apparatus Ms. Libeth Maldonado, from the Platform Balard of the University of Montpellier.

A gas chromatograph (GC; PerkinElmer Clarus 400 equipped to a ShinCarbon ST column) was used to analyze the purity of H<sub>2</sub> produced in the isothermal experiments. After the reaction finished and the reactor was cooled down to room temperature, a glass syringe was used to take a sample of the gas produced and it is injected in the GC.

### 2.4 Dehydrogenation experiments at isothermal conditions

The thermal behavior of rubidium hydrazinidoborane was analyzed at isothermal conditions (80, 100, 120 and 140°C) in a stainless steel reactor. Inside the glovebox, 100 mg of sample was weighted, placed into a glass vial inside the reactor and then closed tightly. Outside the glovebox, the reactor was connected to a pressure controller and immersed into an oil bath at the designated temperature. The evolution of the sample was followed by measuring the change of pressure inside the reactor. The data were converted into mol H<sub>2</sub> per mol of RbHB (i.e. equivalents of H<sub>2</sub>, denoted equiv H<sub>2</sub>) and were plotted as a function of time. The solid product was recovered for its characterization.

## 3. Results and discussion

### 3.1 Preliminary comments

The first attempt to synthesize rubidium hydrazinidoborane consisted in putting rubidium and hydrazine borane in a round flask and then add extra-dry THF. However, a violent reaction between both reactants occurred. After different attempts, we found that it is of extreme importance to dissolve HB in THF before putting it into contact with Rb. In this way, RbHB can be synthesized in safer conditions.

RbHB is a white powder. We looked for suitable (anhydrous) organic solvents for the compound. It is insoluble in THF, 1,4-dioxane and toluene. We also checked the behavior in the presence of protic solvents. RbHB reacts with water and ethanol (by solvolysis) and the reaction is accompanied by H<sub>2</sub> generation. These observations are consistent with those made for the other alkali hydrazinidoboranes and amidoboranes.<sup>16,25,26,28,39</sup>

### 3.2 Molecular structure of RbHB

#### 3.2.1 Fourier Transformed Infrared Spectroscopy (FTIR)

Rubidium hydrazinidoborane was analyzed by FTIR and the spectrum was compared to the one of HB (**Figure 1**). The N–H stretching region is different in comparison with HB. For RbHB, there are fewer bands of lower intensity. Less intense bands are also observed at the N–H bending region. This observation indicates differences between the N<sub>2</sub>H<sub>4</sub><sup>–</sup> of HB and N<sub>2</sub>H<sub>3</sub>(Rb)<sup>–</sup> of RbHB in terms of electronic structure and binding strength. This is typical of derivatives where weaker interactions of H<sup>δ+</sup> and H<sup>δ–</sup> between molecules exist (because of longer distances due to the big Rb<sup>+</sup> cation)<sup>40,41</sup>.

Regarding the B–H stretching region, RbHB presents the vibrational bands at lower wavenumbers than HB, suggesting a different chemical environment for the B–H bonds and the BH<sub>3</sub> groups. The band of N–N stretching shows a slight change; it is less intense for RbHB. In the B–N region, the peak at 906 cm<sup>–1</sup> for HB has red-shifted to 838 cm<sup>–1</sup> for RbHB, indicating a stronger B–N bond. Shorter B–N bonds are typical of hydrazinidoboranes and amidoboranes.<sup>16,25–28,37,38,42,43</sup> All of the

changes in the spectrum are due to the displacement of one  $\text{H}^{\delta+}$  by the  $\text{Rb}^+$  into the network. Therefore, the modification of the chemical environment is caused by the alkaline cation  $\text{Rb}^+$ .

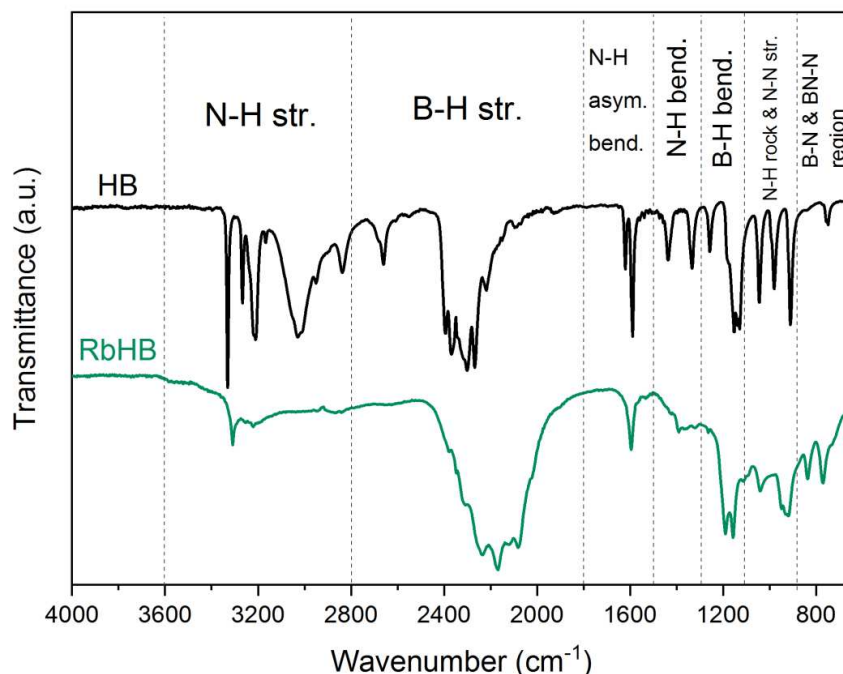


**Figure 1.** FTIR spectra of HB and RbHB. The bands have been assigned.

### 3.2.2 $^{11}\text{B}$ Magic Angle Spinning Nuclear Magnetic Resonance (MAS NMR)

Rubidium hydrazinidoborane was analyzed by solid state  $^{11}\text{B}$  MAS NMR spectroscopy and the spectrum was compared to that of HB (**Figure 2**). The spectrum of HB shows a single signal centered at  $-24$  ppm, with a split shape that is due to the quadrupolar coupling.<sup>44–47</sup> The spectrum of RbHB shows a comparable split signal at lower chemical shift centered at  $-17.5$  ppm, which is consistent with the substitution of one  $\text{H}^{\delta+}$  of the hydrazine moiety by the rubidium cation. This thus indicates a different electronic arrangement in the  $\text{NBH}_3$  environment of RbHB where  $-\text{NH}(\text{Rb})-$  is a stronger donor complex with  $\text{BH}_3$ .<sup>43</sup> This might also suggest shortening of the B–N bond of the anion  $\text{N}_2\text{H}_3\text{BH}_3^-$ , which agrees with the results of the FTIR analysis.<sup>16</sup> It is interesting that the  $\text{NBH}_3$  signal of RbHB is asymmetric and suggests the prevalence of anisotropy around the boron atom. In contrast, the other hydrazinidoborane and amidoborane compounds

presents a symmetric  $\text{NBH}_3$  signal due to isotropy around the boron atom.<sup>16,25,26,28</sup> We may suppose that the molecular degree of freedom is less pronounced for RbHB.

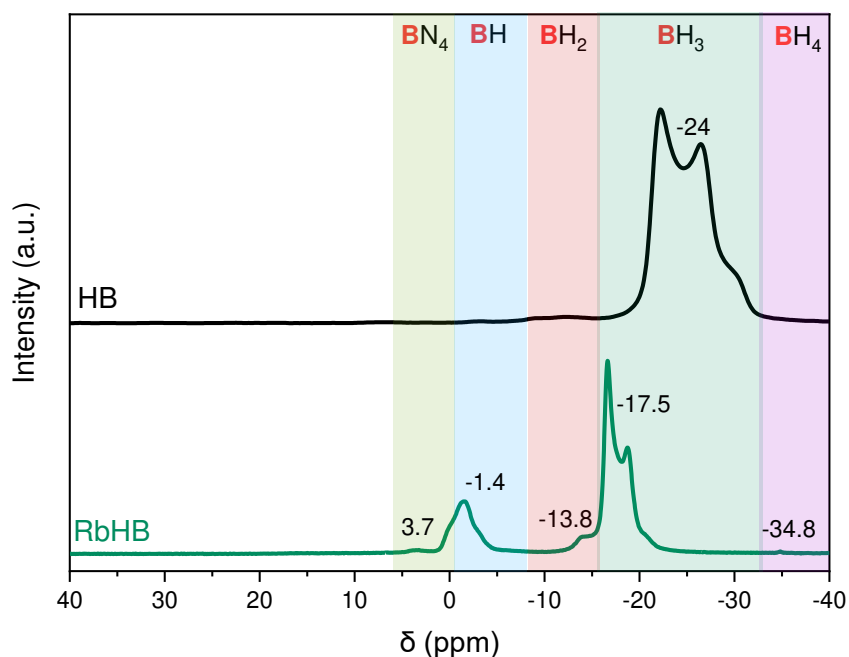


**Figure 2.**  $^{11}\text{B}$  MAS NMR spectra of HB and RbHB. The chemical shifts in ppm and the assigned boron environments are indicated.

The  $^{11}\text{B}$  MAS NMR spectrum of RbHB presents four other signals of different intensities at -34.8, -13.8, -1.4 and 3.7 ppm. The first two signals are ascribed to  $\text{BH}_4$  and  $\text{N}_2\text{BH}_2$  environments respectively.<sup>48</sup> They may occur due to the formation of some dehydrocoupling intermediates like the ionic dimer of formulae  $[(\text{MN}_2\text{H}_3)_2\text{BH}_2]^+[\text{BH}_4]^-$ .<sup>26,28</sup> The  $\text{N}_2\text{BH}_2$  environment could be assigned to the complex  $\text{Rb}-\text{H}\cdots\text{H}_3\text{N}_2\text{BH}_2$  or the dimer  $\text{N}_2\text{H}_3(\text{Rb})\text{BH}_2\text{N}_2\text{H}_2(\text{Rb})\text{BH}_3$ .<sup>30,31,42</sup> The signal at -1.4 ppm is attributed to an  $\text{N}_3\text{BH}$  environment, and that at 3.7 ppm to an  $\text{BN}_4$  environment<sup>49</sup>. The presence of such environments implies the formation of highly dehydrogenated polymeric residues of RbHB. Dehydrocoupling is likely to happen because of a slow evolution of RbHB at room temperature (the MAS NMR analyses are performed one day after the preparation of the sample), which could be aggravated due to the rotor rotation during the NMR analysis (slight decomposition of the sample during the analysis due to a possible increase of temperature).

### 3.2.3 Stability of rubidium hydrazinidoborane

The stability of RbHB in solid state was investigated by  $^{11}\text{B}$  MAS NMR and FTIR spectroscopy. Two RbHB samples were stored in the argon-filled glovebox for one and seven months after synthesis. The FTIR analysis (Figure 3) indicates that the N–H stretching bands broaden with time. The broadening extends beyond  $3400\text{ cm}^{-1}$ , which indicates the presence of polymeric compounds. Consistently, the B–H stretching bands become weaker in intensity.

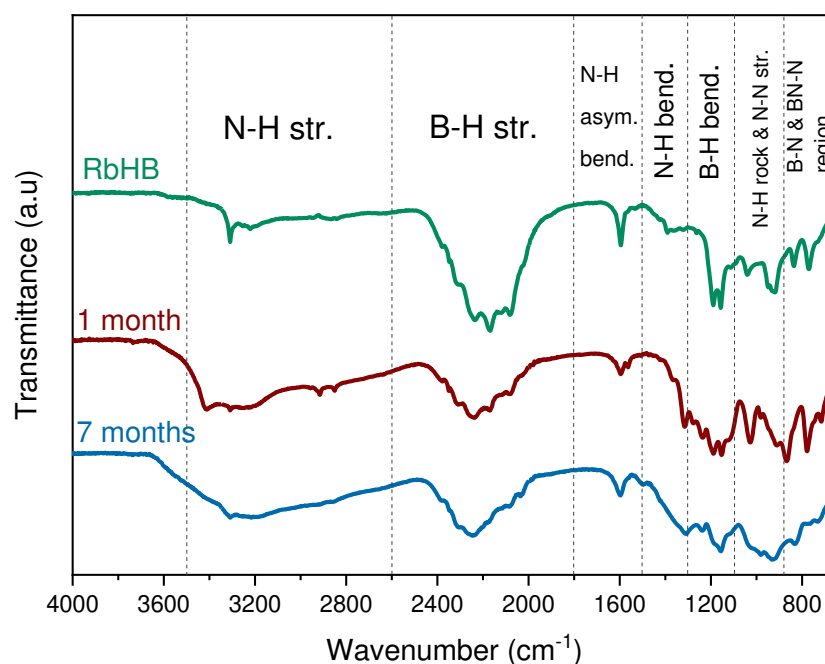
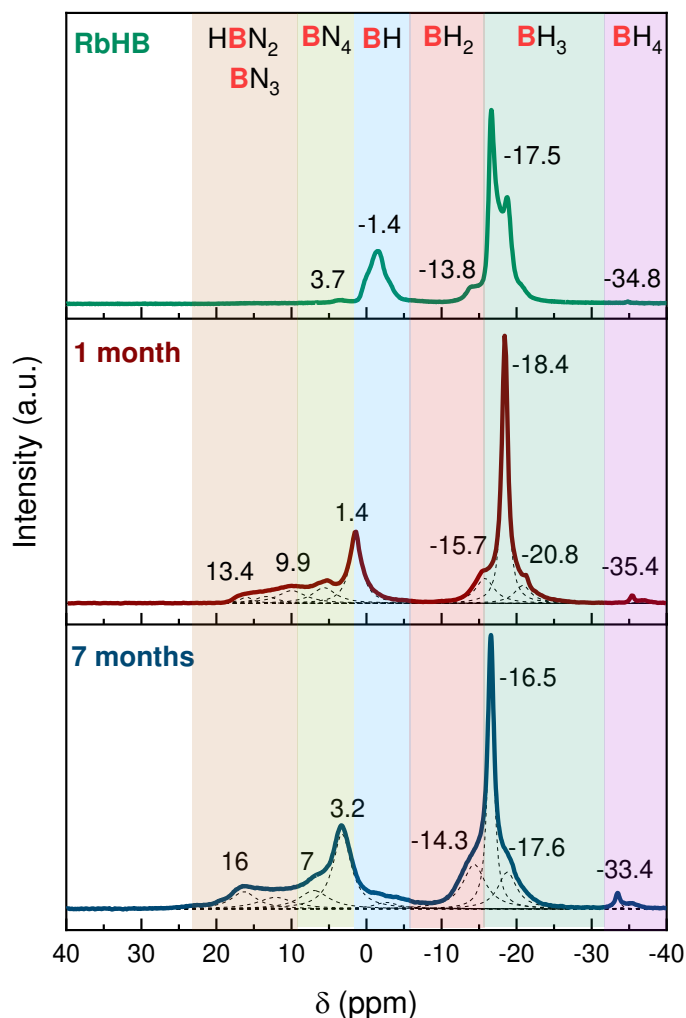


Figure 3. FTIR spectra of RbHB, RbHB after 1 and 7 months after synthesis (stored at room temperature and under argon atmosphere). The bands have been assigned.

The  $^{11}\text{B}$  MAS NMR spectra show several changes (Figure 4). The most prominent one is the change of the signal at  $-17.5\text{ ppm}$ , attributed to the  $\text{NBH}_3$  environment, which loses its initial asymmetric shape. It is symmetric, suggesting much higher isotropy around the boron atom. The intensity of the signal at around  $-35\text{ ppm}$  and that of the hump at around  $-15\text{ ppm}$  are higher. The former signal is characteristic of a  $\text{BH}_4$  environment. The latter one may be ascribed to an  $\text{N}_2\text{BH}_2$  environment<sup>48</sup>. A broad signal of low intensity can be seen between  $0$  and  $-12\text{ ppm}$  and it

can be attributed to  $\text{N}_2\text{BH}$  and  $\text{N}_3\text{BH}$  environments. Another broad signal deconvoluted into 4-5 signals appeared at positive chemical shifts.



**Figure 4.**  $^{11}\text{B}$  MAS NMR spectra of RbHB, RbHB after 1 month and after 7 months of synthesis (stored at room temperature and under an argon atmosphere). The signals for the aged samples were deconvoluted. The chemical shifts in ppm and the boron environments are indicated.

The signals at  $<10$  ppm are typical of tetravalent  $\text{BN}_4$  environments; the others are due to trivalent boron environments generally observed for borazine-linked polymeric species.<sup>48–54</sup> Table 1 presents the chemical shifts of different compounds formed in the thermolysis of BNH compounds. The aged samples revealed that RbHB is not stable at room temperature. It evolves by dehydrocoupling and could form species such as polyiminoborane and/or polyborazylene-like

compounds. This behavior is similar to the one showed by the ammonia borane derivative,  $\text{RbNH}_2\text{BH}_3$ , that also undergoes a slow decomposition at room temperature.<sup>37,38</sup> The reason is the size of the  $\text{Rb}^+$  cation that destabilizes the molecule.<sup>55</sup>

**Table 1.** Typical chemical shifts assigned to different species formed during the thermal decomposition of BNH compounds.

$\delta$ (ppm)	Boron site	Assigned species	Reference
-38	$\text{BH}_4$	$[(\text{NH}_3)_2\text{BH}_2]^+[\text{BH}_4]^-$	48
-37	$\text{BH}_4$	DADB	49
-30	$\text{BNH}_3$	-	56
-24	$\text{BH}_3$	AB, HB, MAB, MHB	48
-22	$\text{BH}_3\text{N}$	MAB, MHB	48,49,52
-20	$\text{BH}_2\text{N}_2$	DADB	48,56
-13	$\text{BH}_2$	$[(\text{NH}_3)_2\text{BH}_2]^+[\text{BH}_4]^-$	48
-12	$\text{BH}_2\text{N}_2$	Linear and/or cyclic dimers	48,52
-10.9	$\text{BH}_2$	Transient species	48
-10	$\text{BH}_2\text{N}_2$	DADB	48,49
-6.1	BH	-	53
-4	$\text{BHN}_3$	-	49
-0.85	BH	-	53
1	$\text{BN}_4$	-	49
1.5	$\text{BN}_4$	-	53
27	$\text{B}_3\text{N}_3$	Polyborazylene	51,52,56,57
31	$\text{BN}_3$	Polyborazylene	51,52,57
35	$\text{BN}_3$	$\text{B}(\text{NBH})_2(\text{NB}_2)$	49
40	$\text{BHN}_2$	$\text{BH}(\text{NBH})_2$	49

### 3.2.4 Crystal structure

The PXRD pattern of RbHB was compared to that of HB (Figure 5). It does not exhibit any diffraction peaks of HB and can be considered as a pure phase. The broad amorphous-like peaks were identified from the Kapton film used to protect the sample. But as suggested by the  $^{11}\text{B}$  MAS NMR results, the presence of some amorphous dehydrogenated products cannot be discarded.

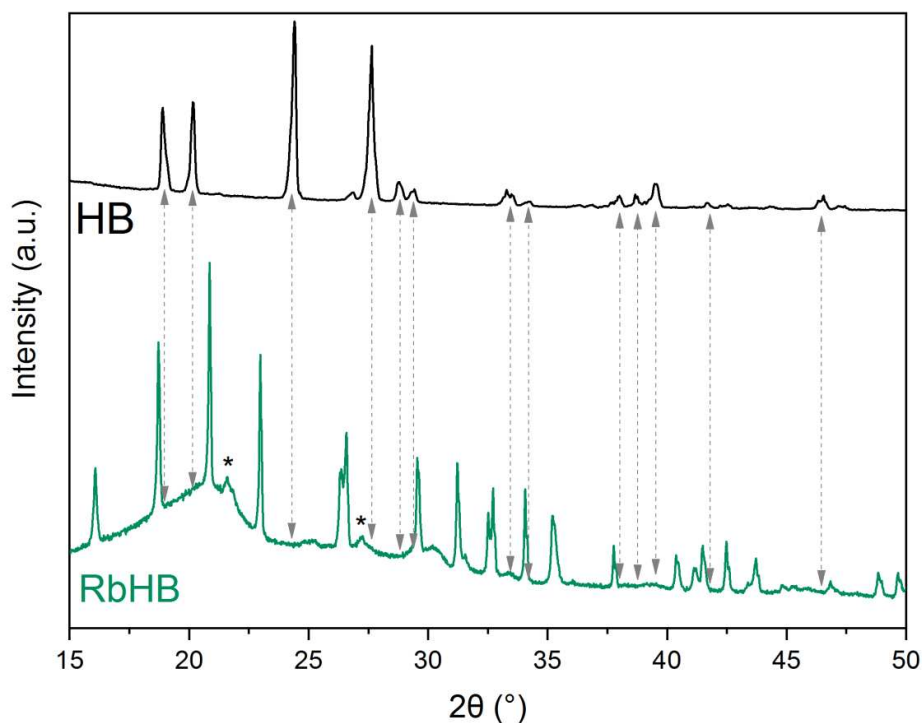


**Figure 5.** Comparison of the PXRD patterns of pure HB and RbHB. The stars indicate the peaks due to the Kapton foil used in the analysis.

The crystallographic data and the Rietveld refinement were obtained thanks to the collaboration with Mr. Pascal Yot (ICGM UMR5253 Montpellier), who performed these works. The PXRD pattern of RbHB was successfully indexed as a single phase using FOX.<sup>58</sup> JANA2006 package was used to refine the structure by the Rietveld method.<sup>59</sup> The position of Rb atoms was first determined by Charge Flipping algorithm 'SuperFlip' included into JANA2006 package, and then used into FOX to reach the position of the  $\text{N}_2\text{H}_3\text{BH}_3^-$  anions.<sup>60</sup> The crystallographic data is presented in Table 2.

**Table 2.** Space group, unit cell parameters, goodness of fit and R values for the refined structure.

Space Group	P2 <sub>1</sub> (No. 4)
Z	2
a (Å)	5.8128(5)
b (Å)	6.7010(5)
c (Å)	5.8143(5)
$\beta$ (°)	108.915(4)
V (Å <sup>3</sup> )	214.25(3)
Crystallographic density	1.7252
Temperature (°C)	20
GoF	2.44
R <sub>p</sub>	1.23
wR <sub>p</sub>	3.01
R <sub>(obs)}/wR<sub>(obs)</sub></sub>	7.85 / 7.91
R <sub>(all)}/wR<sub>(all)</sub></sub>	6.88 / 6.89

The Rietveld refinement of the pattern was carried out using a Lorentzian peak shape with a cut-off of 20. Considering the quality of the diffraction pattern, the atomic displacement parameters were taken equal and isotropic for all atoms of the unit cell. The peaks asymmetry was corrected using Howard model (Boole's rule) and preferred orientation using March-Dollase model following the (010) direction. As shown in Figure 6, the calculated pattern (red line) is comparable to the experimental one (black line). The B–H and N–H distances were constrained to 1.20 Å and 1.04 Å respectively, in accordance with the optimization realized by FoX program. The uncertainties of the atomic coordinates for hydrogen atoms are not reported here because they were not freely refined. The isotropic thermal parameters ( $U_{iso}$ ) were constrained to be identical for all atom types (Table 3).

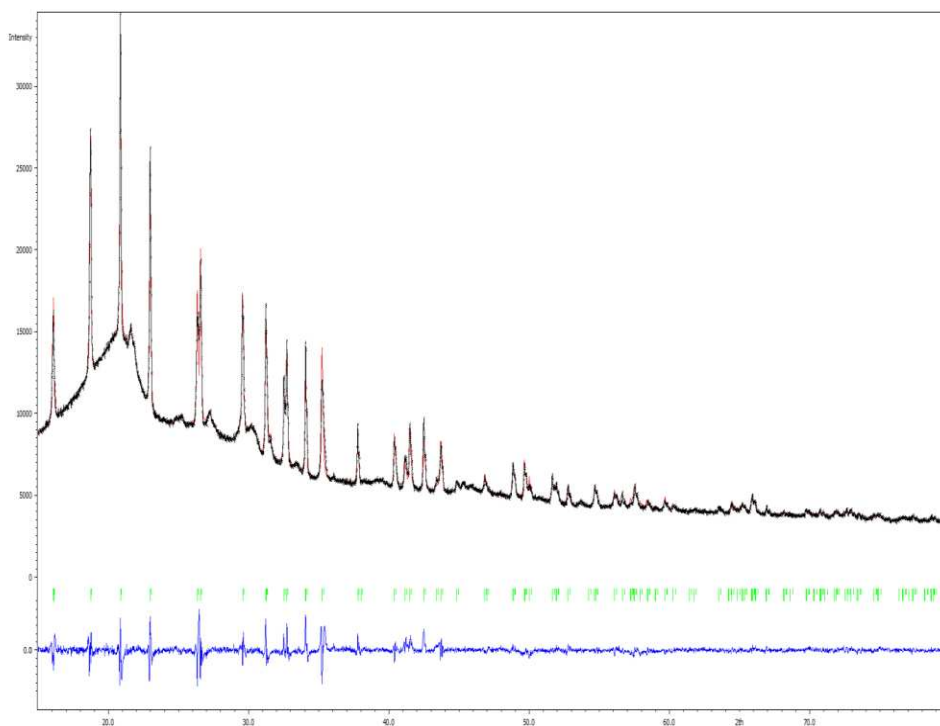


**Figure 6.** Observed (black line) and calculated (red line) powder XRD profile for the Rietveld refinement of RbHB, differences of the plots (blue line), and calculated angles for Bragg peaks in  $2\theta$  (green lines).

**Table 3.** Experimental structural parameters of RbHB (S.G.  $P2_1$  No. 4) at room temperature

Atom	Site	Occupancy	x	y	z	$U_{\text{iso}}$ (Å)
Rb			0.2315(5)	0.0029(4)	0.1235(5)	0.0359(10)
B1			0.379(5)	0.48(2)	0.196(5)	0.0359(10)
N1			0.116(5)	0.635(4)	0.410(4)	0.0359(10)
N2			0.2044(3)	0.447(4)	0.359(5)	0.0359(10)
H1	2a	1	0.27776	0.60148	0.03141	1.2
H2			0.56132	0.56955	0.31909	1.2
H3			0.42699	0.34464	0.11324	1.2
H4			0.02349	0.60979	0.48099	1.2
H5			0.25411	0.70648	0.55068	1.2
H6			0.30867	0.38206	0.52378	1.2

Another collaboration with Mr. Guillaume Maurin (ICGM UMR5253 Montpellier) was done, where he calculated the position of the H atoms of the molecule. The locations of the H atoms linked to the N and B atoms were determined by performing a geometry constrained optimization of the structure (Rb, B and N atoms fixed in their initial positions) at the force-field level. All atoms of the system were represented as Lennard-Jones charged sites with LJ parameters taken from the UFF force field while the charges were calculated using the QeQ method.<sup>61,62</sup>

RbHB was indexed as a single phase in a monoclinic  $P2_1$  (No. 4) unit cell (Figure 7);  $Z=2$ ;  $a=5.8128(2)$  Å,  $b=6.7010(2)$  Å,  $c=5.8143(2)$  Å and  $\beta=108.915(2)^\circ$ . RbHB is isostructural with KHB<sup>42</sup>, whereas  $\alpha$ -LiHB and NaHB crystallize in different monoclinic cells ( $P2_1/c$  and  $P2_1/n$  respectively).<sup>25,28</sup>

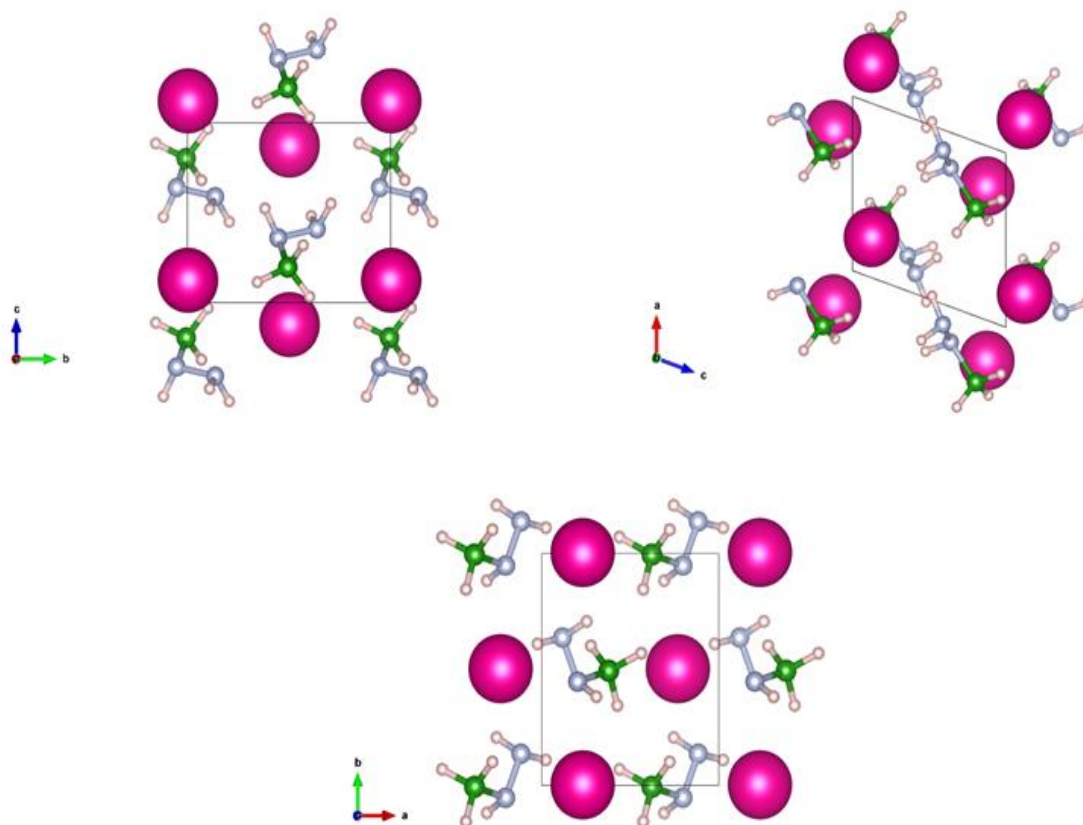


**Figure 7.** Crystal structure of  $\text{RbN}_2\text{H}_3\text{BH}_3$  along the [100], [010], and [001] directions. H, B, and N atoms are represented by pink, green, and blue spheres. Rb atoms are represented by fuchsia spheres.

As a derivative of AB,  $\text{RbNH}_2\text{BH}_3$  shows a different monoclinic cell ( $P2_1/c$ ) and a volume per formula unit of  $94.24 \text{ \AA}^3$ ,<sup>37,38</sup> which is slightly smaller than the volume per formula unit of  $107.22 \text{ \AA}^3$  of  $\text{RbHB}$ ; this is consistent with the bigger size of the anion  $[\text{N}_2\text{H}_3\text{BH}_3]^-$ . The volume per formula unit of  $\text{HB}$  is also smaller with  $80.154 \text{ \AA}^3$ ,<sup>25</sup> which is consistent with the presence of the bulkier cation  $\text{Rb}^+$ . In  $\text{RbHB}$ , the cation  $\text{Rb}^+$  is octahedrally coordinated with 6  $[\text{N}_2\text{H}_3\text{BH}_3]^-$  anions (Figure 8). This is consistent also with the bigger size of  $\text{Rb}^+$ . The coordination number for  $\text{Li}^+$ ,  $\text{Na}^+$  and  $\text{K}^+$  in the corresponding hydrazinidoboranes were lower, being 4, 5 and 4, respectively.<sup>26,28,42</sup> In  $\text{RbNH}_2\text{BH}_3$  also, it was found a pseudo-octahedron around each  $\text{Rb}^+$  cation.<sup>37,38</sup>

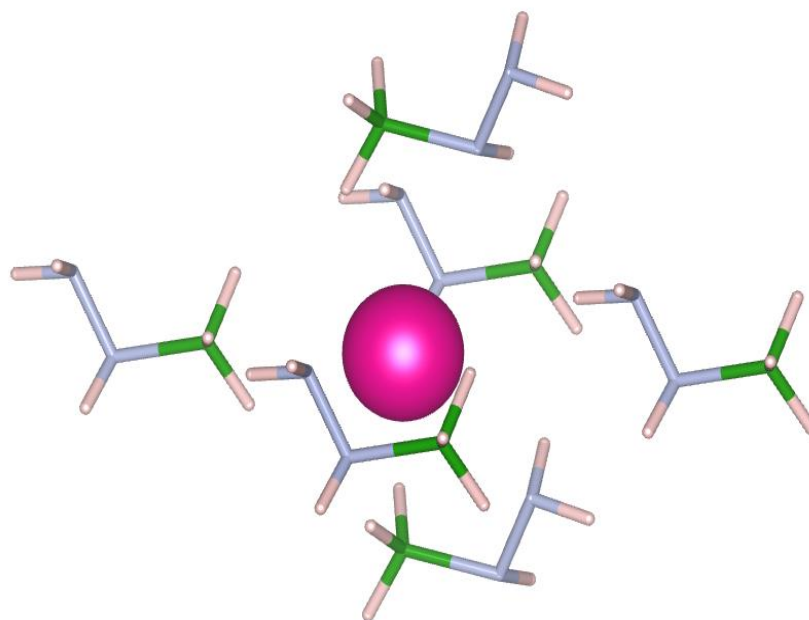


**Figure 8.** Coordination sphere of the cation  $\text{Rb}^+$  surrounded by 6  $[\text{N}_2\text{H}_3\text{BH}_3]^-$  anions.

The locations of the H atoms linked to the N and B atoms were computationally determined, bringing out the interatomic distances (**Figure 9**). The shortest  $\text{Rb}\cdots\text{Rb}$  distance is  $4.246(2) \text{ \AA}$ . This is slightly higher than the distance  $4.025 \text{ \AA}$  calculated for  $\text{RbNH}_2\text{BH}_3$ , due to the bigger size of the anion  $[\text{N}_2\text{H}_3\text{BH}_3]^-$ . The shortest  $\text{Rb}-\text{N}$  distance was determined as  $3.132(3) \text{ \AA}$  (vs  $3.06 \text{ \AA}$  for  $\text{RbNH}_2\text{BH}_3$ ). This is a longer distance than the shortest one in  $\text{KHB}$  ( $2.959 \text{ \AA}$ ) because of the bigger size of  $\text{Rb}^+$  compared to  $\text{K}^+$ .<sup>42</sup> The B-N bond was determined as being of  $1.55 \text{ \AA}$ , which is

consistent with the values 1.54-1.55 Å found for LiHB, NaHB and KHB.<sup>26,28,42</sup> This bond is besides shorter than the B-N bond of HB (1.59 Å).<sup>24,25</sup> This is in good agreement with the aforementioned shortening of the B-N bond by Rb<sup>+</sup> insertion as suggested by <sup>11</sup>B MAS NMR and FTIR spectroscopy. All of this is in favor of the formation of an ionic salt where the anion [N<sub>2</sub>H<sub>3</sub>BH<sub>3</sub>]<sup>-</sup> underwent strong electronic rearrangement due to the presence of Rb<sup>+</sup>.

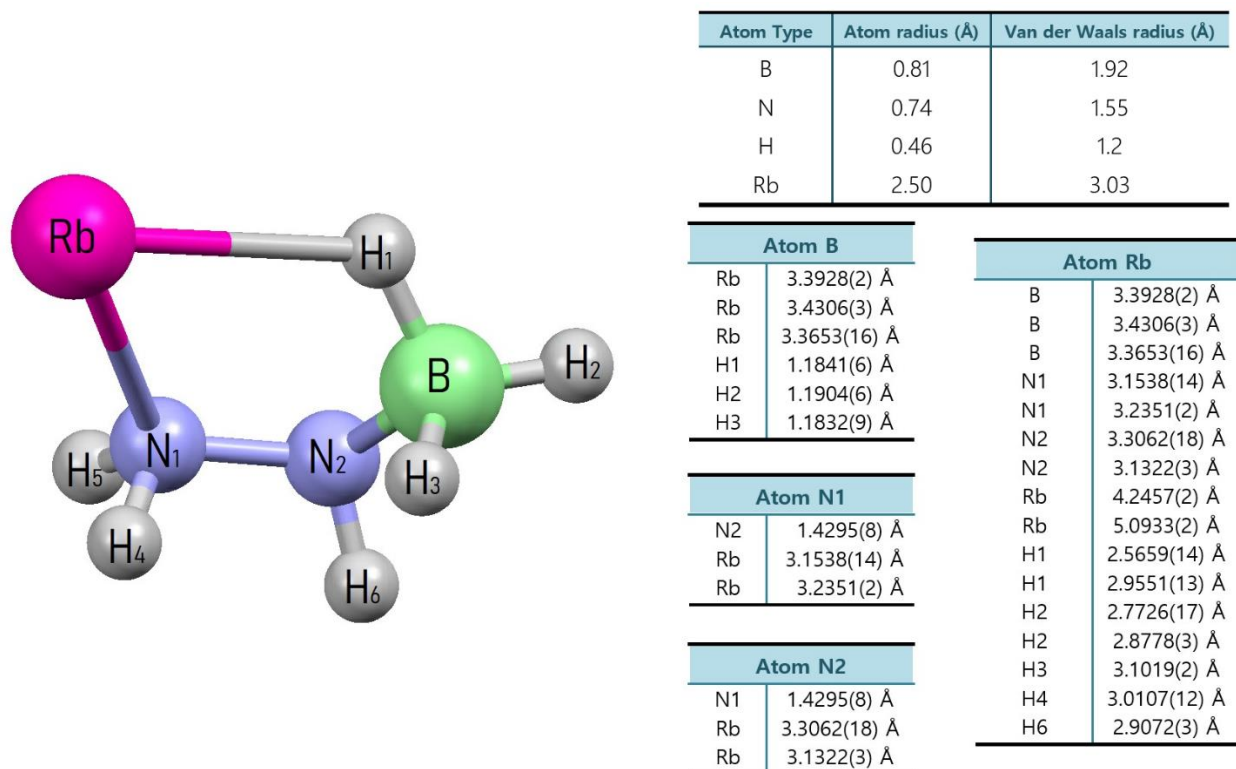


Figure 9. Calculated interatomic distances for rubidium hydrazinidoborane.

### 3.3 Thermal characterization

#### 3.3.1 TG-MS and DSC analyses

Thermal decomposition of RbHB was studied by TG analysis (heating rate of 5°C min<sup>-1</sup>) and the gases released were analyzed by MS. The material is stable up to ca. 60°C and then it starts to decompose (Figure 10). Over the range 60-100°C, RbHB loses ca. 5 wt. % of its initial weight, due

to the release of  $\text{H}_2$  and  $\text{NH}_3$ . The second decomposition step takes place in the range 115-145°C where the mass loss is 0.5 wt. %.

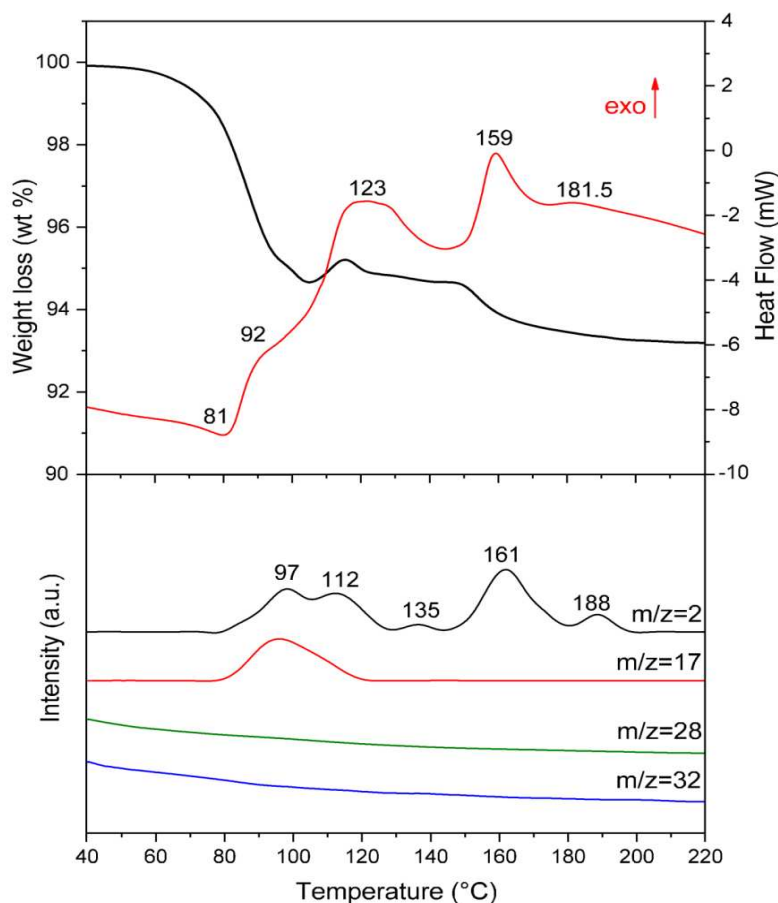


**Figure 10.** TGA-DSC ( $5^\circ\text{C min}^{-1}$ ) and MS results ( $m/z = 2, 17, 28, 32$  for  $\text{H}_2$ ,  $\text{NH}_3$ ,  $\text{B}_2\text{H}_6$  or  $\text{N}_2$ ,  $\text{N}_2\text{H}_4$  respectively) of RbHB. The peak temperatures ( $^\circ\text{C}$ ) observed by DSC and MS are given.

A third decomposition step occurs between 150-200°C, with a mass loss of 1.3 wt. %. For both of the last two steps, only  $\text{H}_2$  was detected by MS. The overall weight loss in the range 60-200°C is 6.8 wt. %. This is higher than the 4.65 wt. % H carried by RbHB and such a difference may be explained by the loss of a significant amount of  $\text{NH}_3$ . In our conditions, there was no detection of any other volatile by-products (like  $\text{B}_2\text{H}_6$ ,  $\text{N}_2\text{H}_4$  or  $\text{B}_3\text{N}_3\text{H}_6$ ). There is one slight gain of mass (hump) at around 110°C present in the TG analysis. A similar feature was reported for HB, NaHB and KHB. This is explained by a “buoyancy effect” that takes place when the melted borane solidifies while

releasing  $H_2$  and it displaces the heavier argon gas inside the semi-closed crucible. The foaming of the sample generally intensifies the aforementioned hump (Figure 11). In terms of the onset temperature of dehydrogenation, RbHB shows better properties in comparison to HB, and is comparable to LiHB. In contrast, NaHB and KHB have better features. In terms of purity of the released  $H_2$ , LiHB, NaHB and KHB are more attractive.<sup>26,28,42</sup> It is noticeable that the amount of the unwanted volatile product  $NH_3$  seems to increase with the size of the alkali cation  $M^+$  down in the group.

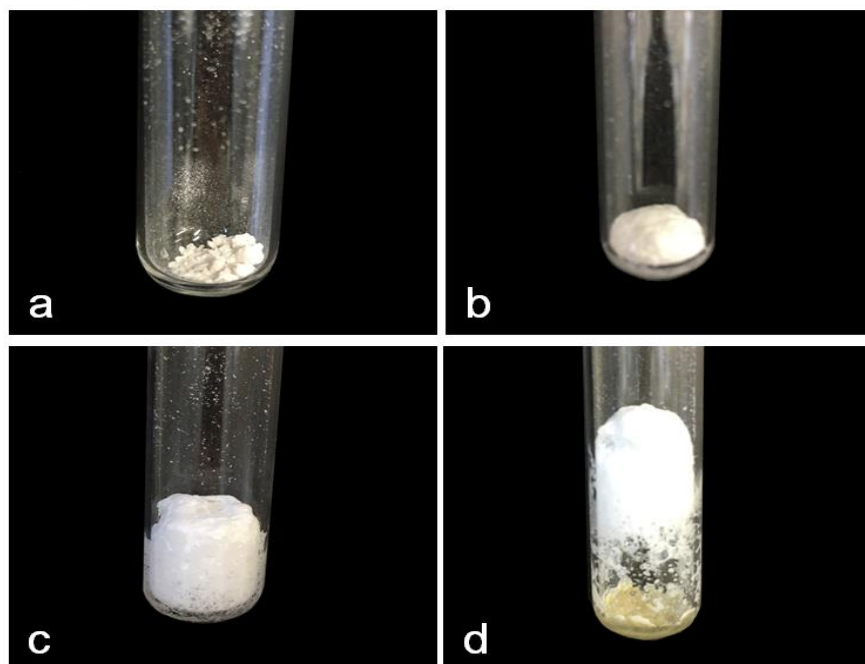


**Figure 11.** Pictures of the evolution of RbHB under heating: a) RbHB at room temperature; b) Foaming starting to occur at ca. 60 °C; c) Expansion of the foam due to the evolution of volatile products; d) Solidification of the foam resulting in a polymeric residue at ca. 100°C

RbHB was also analyzed by DSC (Figure 10). The DSC profile clearly suggests a complex decomposition path. A first endothermic event peaks at 80°C. As for HB, NaHB and KHB melting takes place and precedes the dehydrogenation of RbHB.<sup>24,28,42</sup> Following, there are several exothermic events. The DSC and MS analyses suggest five successive steps. According to MS, these dehydrogenation steps peak at 97, 112, 135, 161 and 188°C. The first dehydrogenation step is concomitant with a deamination step peaking at 95°C. These results again confirm the

complicated dehydrogenation mechanism of RbHB. Due to the exothermicity of the dehydrogenation process, re-hydrogenation of the dehydrogenated samples is considered not possible under normal conditions.<sup>14–17</sup> If the regeneration is considered, it should be done by other means, like the reduction of the spent fuel using hydrazine in  $\text{NH}_3$  medium, or the digestion and ammoniation of the solid residue.<sup>63,64</sup>

### 3.3.2 Calculation of the apparent activation energy by the Kissinger method

The activation energy and kinetics parameters of the thermolysis of RbHB were calculated using the Kissinger method (For more details, see Annex I).<sup>65</sup> Figure 12 presents the superposition of the DSC analyses at different heating rates: 1, 3, 5, 7 and 10  $^\circ\text{C min}^{-1}$ , and also the values obtained by the linear regression. We analyzed the two main exothermic signals indicated by the dashed lines.

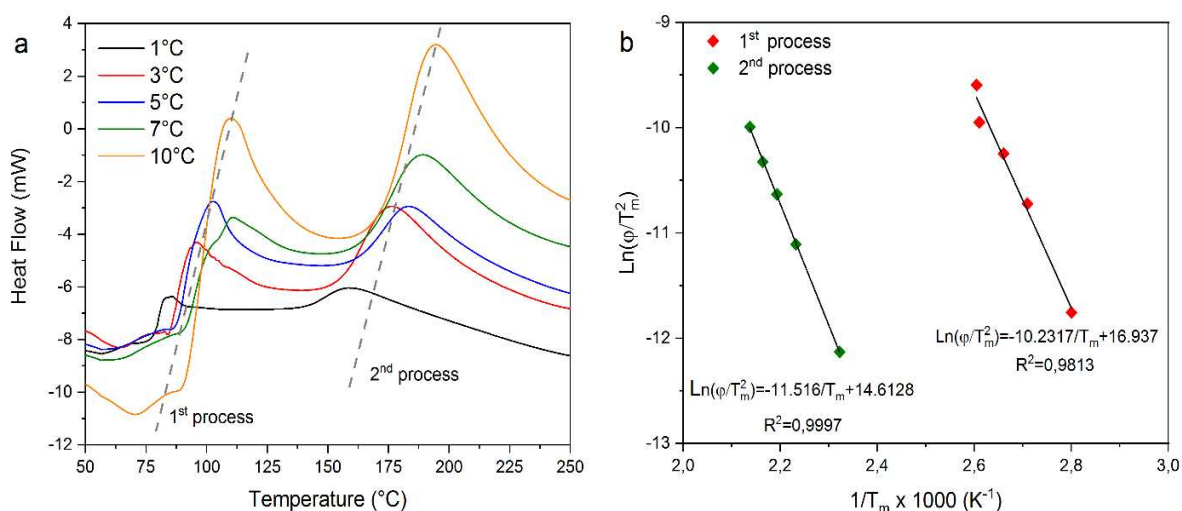


**Figure 12.** a) DSC curves for RbHB at different heating rates (1, 3, 5, 7, 10  $^\circ\text{C min}^{-1}$ ); b) Linear regression for the Kissinger method of the two exothermic events.

The first process corresponds to the dehydrogenation and deammoniation of the sample while the second corresponds only for dehydrogenation. The calculated activation energies of the first and second processes are  $E_{a1} = 85 \text{ kJ mol}^{-1}$  and  $E_{a2} = 94 \text{ kJ mol}^{-1}$  respectively. These values are close and indicate a similar energetic barrier for both processes. In comparison with another BNH materials considered for hydrogen storage, these values are lower. For example, hydrazine

bisborane HBB has a activation energy of  $106.4 \text{ kJ mol}^{-1}$  for its first process of dehydrogenation and AB one activation energy of  $160 \text{ kJ mol}^{-1}$ .<sup>66,67</sup>

Table 4 shows the kinetic parameters calculated with Kissinger method. From the activation energies, it is observed that the decomposition of RbHB is thermodynamically favorable due to the exothermicity of the processes. This means that we need to supply less energy to start the thermal decomposition of RbHB than for other BNH compounds. With these results, we confirm that the  $\text{Rb}^+$  has a destabilization effect on the molecule. As it is evidenced by the TGA, RbHB starts its dehydrogenation at a lower temperature than HB but it releases a huge amount of ammonia that was detected by MS. RbHB presents a lower activation energy for the decomposition process in comparison with other BNH compounds that are used as potential hydrogen storage materials.<sup>66,67</sup>

**Table 4.** Kinetics parameters of RbHB dehydrogenation process calculated by Kissinger method and Arrhenius equation.

Process	$E_a$ ( $\text{kJ mol}^{-1}$ )	A ( $\text{min}^{-1}$ )	k ( $\text{min}^{-1}$ )			
			80°C	100°C	120°C	140°C
1	84.91	$2.3163 \times 10^{11}$	$6.31 \times 10^{-2}$	$2.98 \times 10^{-1}$	1.20	4.22
2	94.07	$2.5118 \times 10^{10}$	$3.02 \times 10^{-4}$	$1.68 \times 10^{-3}$	$7.88 \times 10^{-3}$	$3.18 \times 10^{-2}$

### 3.3.3 Dehydrogenation experiments on RbHB

Experiments under isothermal conditions were carried out in a stainless reactor at 80, 100, 120 and 140°C to evaluate the dehydrogenation properties of RbHB. The dehydrogenation of RbHB is a two-step process (**Figure 13**). Similar profiles were reported for LiHB and NaHB, though for RbHB the break in the slope is more prominent.<sup>26,28</sup> The first step takes place in the first 23, 20, 17 and 13 minutes for the sample heated at 80, 100, 120 and 140°C respectively. After a slow release of hydrogen, the second step takes place.

The H<sub>2</sub> evolution curves were exploited to determine the apparent activation energy E<sub>a</sub> of the first step. The slope of the curves, denoted as a<sub>0</sub>, within the first minutes of the reaction was used as the hydrogen generation rate (equiv H<sub>2</sub> min<sup>-1</sup>). The rate was plotted as a function of the inverse of the temperature (T in K<sup>-1</sup>) using the “linearized” Arrhenius equation (**Figure 13**):

$$\ln a_0 = -\frac{E_a}{RT} + \ln A \quad (3)$$

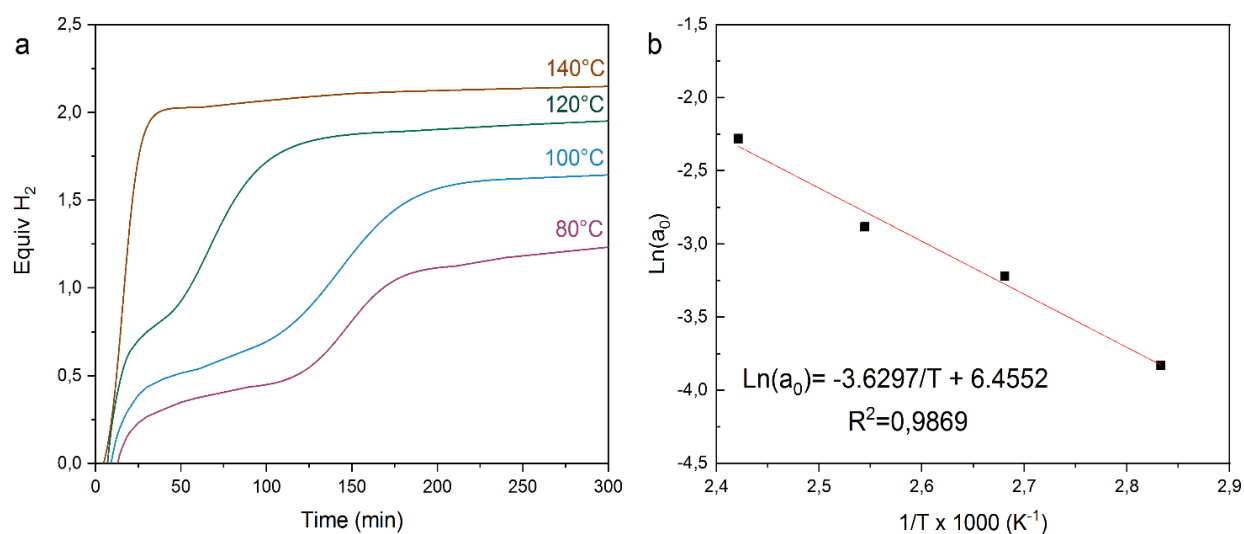


**Figure 13.** a) Time evolution of H<sub>2</sub> release from RbHB under heating at constant temperature (80, 100, 120 and 140°C); b) Arrhenius plot for the determination of the apparent activation energy.

An apparent activation energy of 30.1 kJ mol<sup>-1</sup> was calculated with the Arrhenius equation. This value is lower compared to other boron and nitrogen-based materials. Pure ammonia borane and LiH-doped ammonia borane have respective apparent activation energies of 183 and 75 kJ mol<sup>-1</sup>, calculated by the same method.<sup>68</sup> Another example is lithium amidoborane LiNH<sub>2</sub>BH<sub>3</sub> and the mixture LiBH<sub>4</sub>/LiNH<sub>2</sub>BH<sub>3</sub>, with apparent activation energies of 71 and 61 kJ mol<sup>-1</sup>, respectively.<sup>69</sup> In the case of the hydrazinidoboranes, the calculated apparent activation energy for LiHB is 58 kJ mol<sup>-1</sup>, while NaH-doped NaHB possesses a lower activation energy of 14.4 kJ mol<sup>-1</sup>.<sup>26,70</sup>

The gases released by the sample in the isothermal experiments were analyzed by gas chromatography (Figure 14). There is only one signal that appeared after 0.46 min that corresponds to the retention time of hydrogen for our GC column. It can be observed also that

the higher the temperature, the more the amount of H<sub>2</sub>. This is in good agreement with the aforementioned discussion.

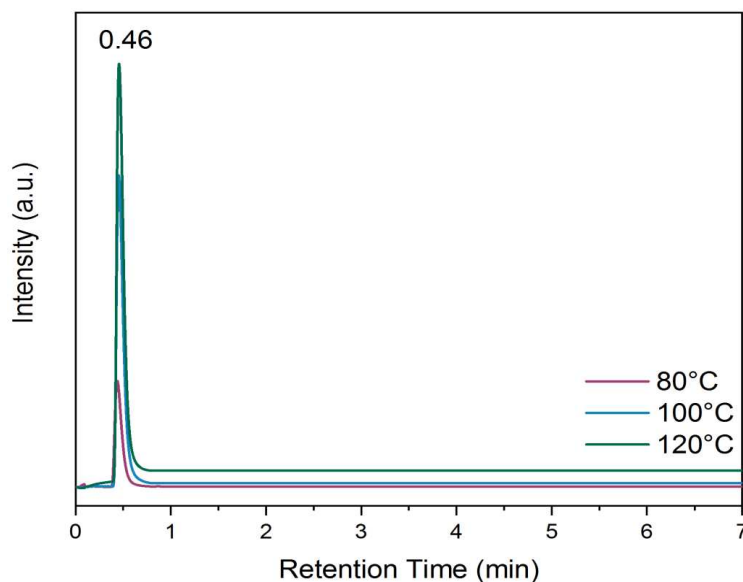


**Figure 14.** GC analyses of the gases liberated by RbHB in isothermal conditions (under heating at the constant temperature of 80, 100 and 120°C). The retention time for H<sub>2</sub> in min is indicated.

The equiv H<sub>2</sub> released by RbHB were compared to the available data reported for HB, LiHB and NaHB after 1 h of heat treatment at constant temperature.<sup>24,26,28</sup> The data are shown in Table 5.

**Table 5.** Equivalents of H<sub>2</sub> liberated by different alkali hydrazinidoboranes after 1 h of heat treatment at constant temperature

Temperature	Compound			
	HB <sup>24</sup>	LiHB <sup>26</sup>	NaHB <sup>28</sup>	RbHB
80°C	0.4	-	0.62	0.38
100°C	0.65	0.6	2.6	0.55
120°C	-	-	-	1.1
140°C	1.1	2.2	-	2

Heated at 100°C, RbHB, HB and LiHB release a similar amount of H<sub>2</sub> in one hour (ca. 0.6 equiv H<sub>2</sub>). This is less than the 2.6 equiv H<sub>2</sub> liberated by NaHB. Heated at 140°C for 1 h, RbHB releases 2 equiv H<sub>2</sub> vs 1.1 for HB. Slightly better performance was reported for LiHB with 2.2 equiv H<sub>2</sub>. In resume, RbHB has improved dehydrogenation properties in comparison to those of pristine hydrazine borane, is comparable to LiHB, but is less attractive than NaHB. The destabilization effect of Rb<sup>+</sup> is thus confirmed.

### 3.4 Analysis of the solid residues

The solid residues recovered upon the completion of the isothermal experiments were analyzed by FTIR (Figure 15). The intensity of the N–H and B–H stretching bands decays as the heating temperature increases. A similar behavior can be observed for the signal assigned to the N–H asymmetric bending. All of these bands almost disappeared for the solid heated at 140°C. This is consistent with the formation and release of H<sub>2</sub> from RbHB.

The solid residues were also analyzed by PXRD (Figure 16). No peaks can be founded in any of the patterns, which suggest a total composition of amorphous polymeric compounds.

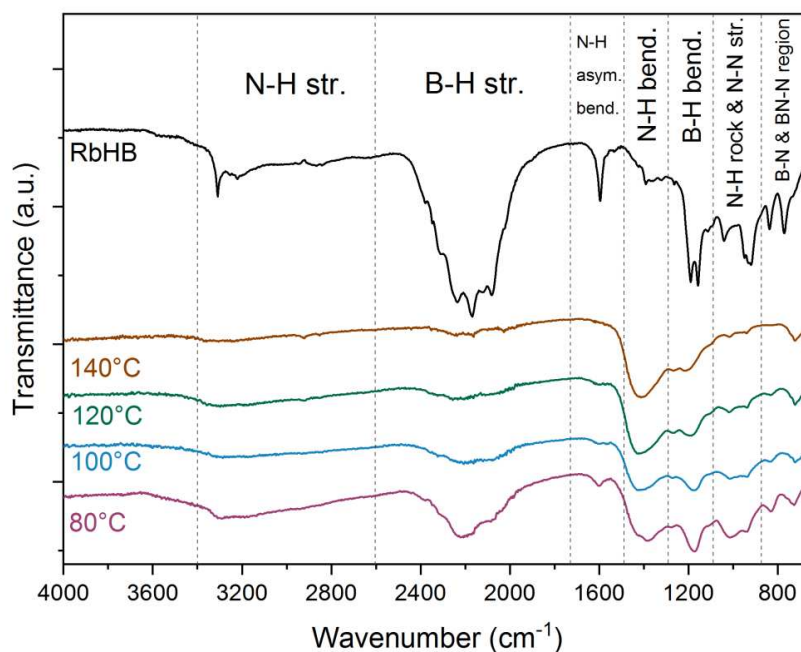


**Figure 15.** FTIR spectra of RbHB and of the solid residues recovered upon heating a sample of RbHB at 80, 100, 120 and 140°C. The bands have been assigned.

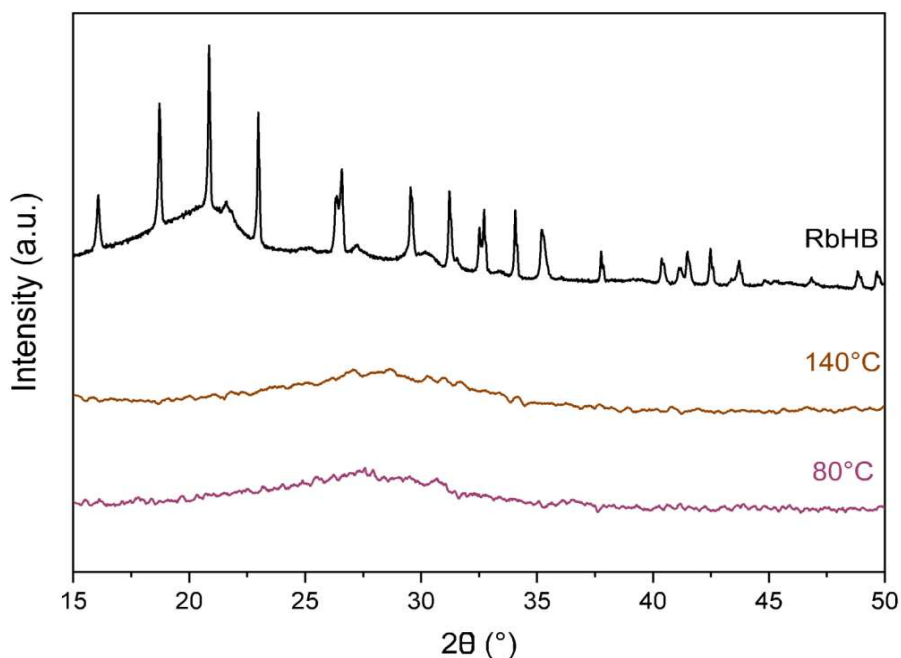


**Figure 16.** XRD patterns of RbHB and of the solid residues recovered upon heating a sample of RbHB at 80 and 140°C.

A better characterization was achieved by analyzing the solid residues by  $^{11}\text{B}$  MAS NMR (Figure 17). A resonance centered at -34.4 ppm appeared in all heated samples. This signal is characteristic of a  $\text{BH}_4$  environment. As discussed in section 3.2.2 for fresh RbHB, this boron environment may be explained by the formation of an ionic dimer like  $[(\text{RbN}_2\text{H}_3)_2\text{BH}_2]^+ [\text{BH}_4]^-$ .<sup>26,28</sup> The existence of such dimer implies an additional resonance due to a  $\text{N}_2\text{BH}_2$  environment that can be seen at -16 ppm. The intensity of this signal decreases as the temperature of the isothermal experiment increases.

For the sample heated at 80°C the asymmetric signal can be deconvoluted into two Gaussian signals centered at -14 and -17 ppm. The former is due the  $\text{N}_2\text{BH}_2$  environment. The latter can be attributed to the  $\text{NBH}_3$  environment, suggesting remaining RbHB and/or unreacted  $\text{NH}_3$  groups. Referring to the literature dedicated to alkali derivatives of ammonia borane, several possible complex intermediates were tentatively identified via experimental analyses and theoretical calculations, and such intermediates (that are adapted to  $\text{N}_2\text{H}_3\text{BH}_3^-$ ) might help in the association

of the aforementioned signals: for instance,  $[\text{N}_2\text{H}_4\text{Rb}]^+ [\text{BH}_3(\text{N}_2\text{H}_2\text{Rb})\text{BH}_3]^-$ ,  $\text{Rb}\cdot\text{H}\cdots\text{H}_3\text{N}_2\text{BH}_2$ ,  $\text{Rb}\cdot\text{H}\cdots\text{RbN}_2\text{H}_3\text{BH}_2\text{N}_2\text{H}_3\text{BH}_3$ ,  $[\text{RbN}_2\text{H}_3\text{BH}_2\text{RbN}_2\text{H}_3]^+ [\text{BH}_4]^-$ .<sup>32,33,40,55,71,72</sup>

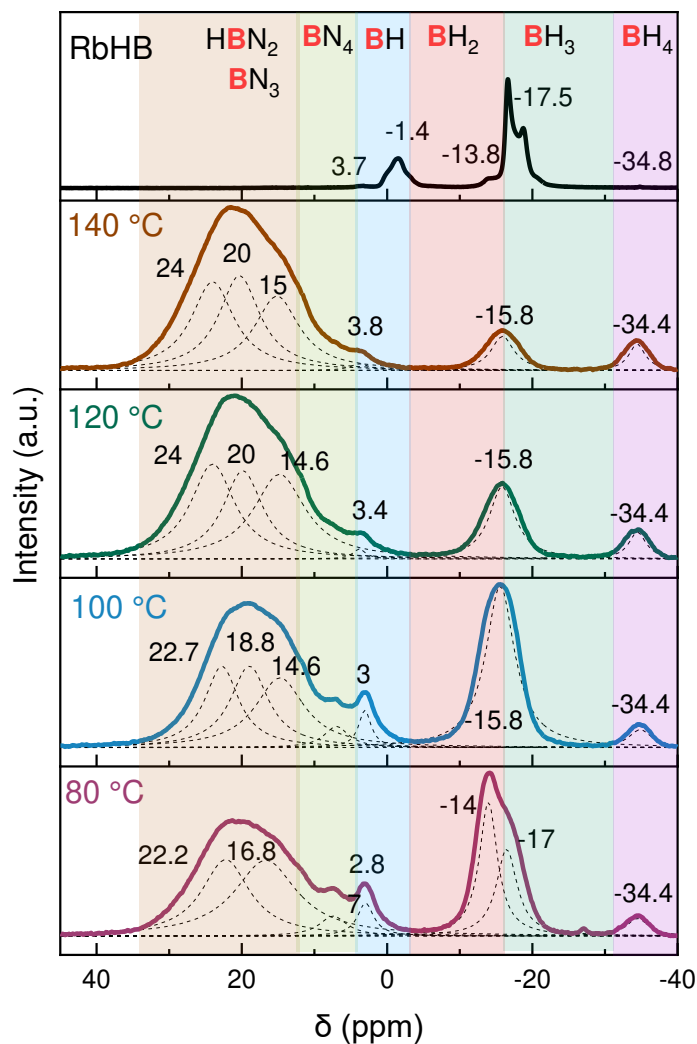


**Figure 17.**  $^{11}\text{B}$  MAS NMR spectra of RbHB and of the solid residues recovered upon heating the sample at 80, 100, 120 and 140°C. The signals for the residues were deconvoluted. The chemical shifts in ppm are indicated.

The  $^{11}\text{B}$  MAS NMR spectra also show a broad signal at positive chemical shifts and which contribution is larger as the temperature of the isothermal experiment increases. They are typical of trivalent boron environments.<sup>50–54</sup> At lower temperatures (80 and 100°C), there are two signals centered around 3.8 and 7 ppm that could indicate the presence of a tetravalent  $\text{BN}_4$ .<sup>49</sup> The broad

signal between 10 and 40 ppm is composed of mainly three signals centered on 14, 20 and 24 ppm. They are present due to the formation of borazine-linked polymeric species. The broadening of the signals is due to the quadrupolar effect of the trivalent boron, usually assigned to  $\text{BN}_2\text{H}$  and  $\text{BN}_3$ . It seems that like in the case of AB, dehydrocoupling of RbHB results in the formation of polyborazylene-like compounds.

### 3.5 Decomposition mechanism of rubidium hydrazinidoborane

The analyses of thermal decomposition and the samples after isothermal experiments showed that the decomposition of RbHB follows a complex path. The TGA-MS analysis allowed us to identify  $\text{NH}_3$  and  $\text{H}_2$ . The  $^{11}\text{B}$  MAS NMR and the XRD showed that after the isothermal experiments, the sample evolved to form a mixture of amorphous compounds, i.e. boron and nitrogen-based polymers with boron atoms with  $\text{sp}^2$  and  $\text{sp}^3$  hybridization. Based on the species identified by the MAS NMR analyses and previous computational works on LiHB,<sup>30</sup> we propose a tentative decomposition mechanism of RbHB. We should remind that the mechanism is speculative due to the difficulty to identify the intermediates that are formed in the decomposition path of BNH materials in the solid state. The proposed mechanism is presented in Figure 18.

We start from the molecules of RbHB in step ①. After the isothermal experiments we can observe two chemical shifts around -34 and -14 ppm. As discussed before, this was identified as an analogous compound to diammoniate of diborane DADB. Applied to our case,  $[(\text{RbN}_2\text{H}_3)_2\text{BH}_2]^+[\text{BH}_4]^-$  (dirubidium dihydrazine of diborane) is formed in step ②. As proposed for LiHB,<sup>30</sup> the formation of  $\text{NH}_3$  is explained by the migration of one atom of H across the N–N bond to break this bond after the process (step ③ and ④). Besides, it has been reported that the anion  $[\text{BH}_4]^-$  participate in the dehydrogenation of ammonia borane,<sup>73</sup> resulting in the concomitant release of  $\text{NH}_3$  and  $\text{H}_2$ . Such a path is likely in our conditions. After this process, the species could lose more dihydrogen, or react with another molecule of RbHB followed by dehydrocoupling of the formed species (step ⑤). Either path leads to the formation of the polymeric species identified in the positive chemical shifts of the  $^{11}\text{B}$  MAS NMR (step ⑥).

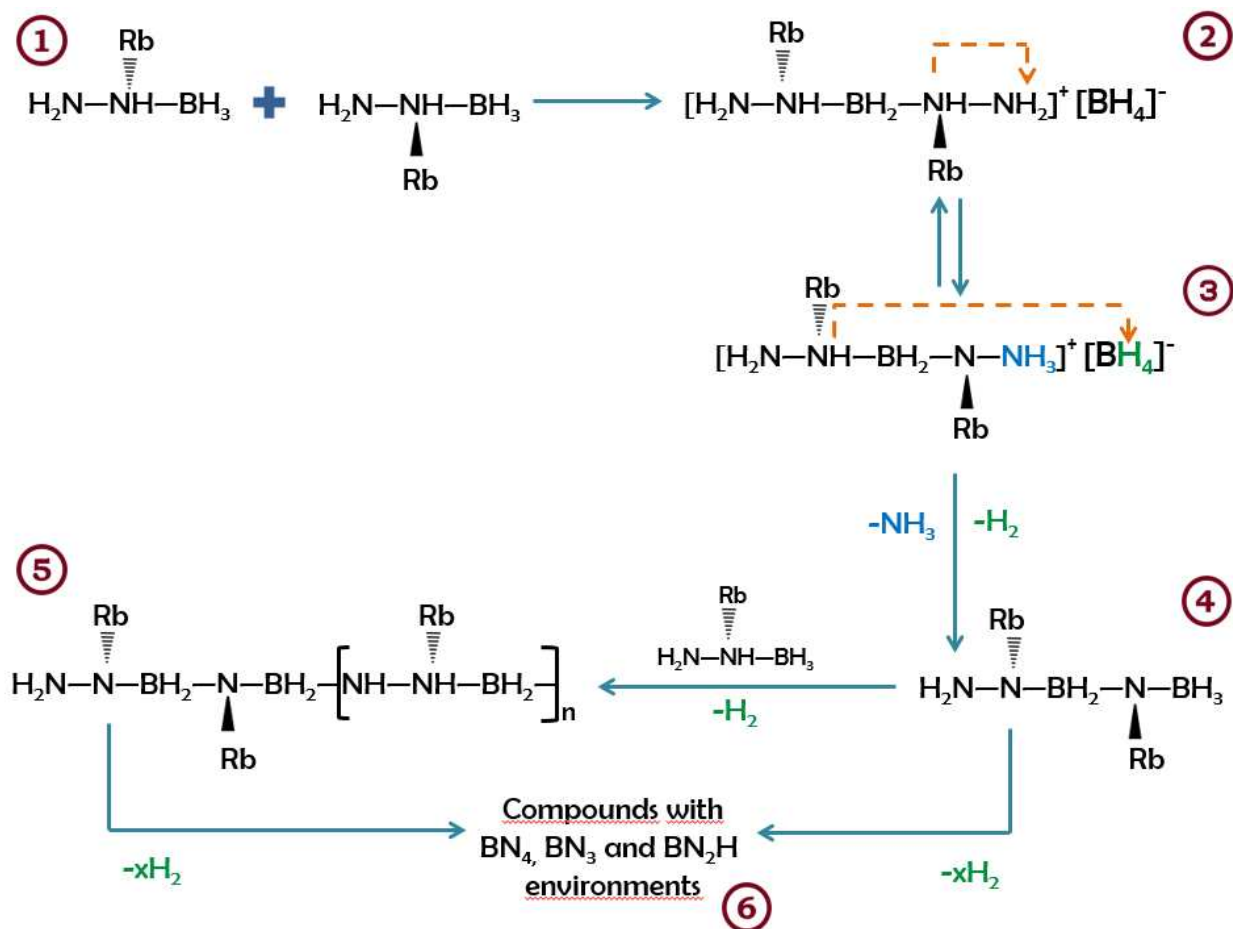


Figure 18. Proposed mechanism for the decomposition of RbHB. The proposed steps are indicated in circled numbers.

## 4. Conclusions

Rubidium hydrazinidoborane  $RbN_2H_3BH_3$  (RbHB; 4.65 wt. % H) was synthesized and characterized for the first time. The substitution of one of the  $H^{\delta+}$  of the hydrazine moiety of  $N_2H_4BH_3$  by  $Rb^+$  was successful evidenced by  $^{11}B$  MAS NMR and FTIR spectroscopy. RbHB is a crystalline material with a monoclinic unit cell, with a space group  $P2_1$  (No.4) with cell parameters of  $a = 5.8128(2) \text{ \AA}$ ,  $b = 6.7010(2) \text{ \AA}$ ,  $c = 5.8143(2) \text{ \AA}$ , and  $\beta = 108.915^\circ$ , and it is isostructural with  $KN_2H_3BH_3$ .

The thermal characterization of RbHB was also carried out, under heating at a constant rate ( $5^\circ C \text{ min}^{-1}$ ) and in isothermal conditions. RbHB shows improved dehydrogenation properties in

comparison to the parent HB. The presence of the  $\text{Rb}^+$  has a destabilization effect on the molecule. The performance of RbHB is comparable to  $\text{LiN}_2\text{H}_3\text{BH}_3$ , but is less attractive than  $\text{NaN}_2\text{H}_3\text{BH}_3$  in terms of onset temperature of dehydrogenation and  $\text{H}_2$  release kinetics. RbHB releases  $\text{H}_2$  and an important amount of  $\text{NH}_3$  during the dehydrogenation. Upon the evolution of  $\text{H}_2$ , an amorphous polymeric solid, mainly polyborazylene-like compound forms. A deeper investigation would be helpful in going further in the identification of this dehydrogenated solid, the reaction mechanisms, and the exact role that  $\text{Rb}^+$  plays on it.

The synthesis and characterization of RbHB have provided results that first add knowledge about boron and nitrogen-based materials. Second, the results presented on this chapter have shown that the dehydrogenation properties of RbHB are interesting and better than those of HB, but for an application in the field of chemical hydrogen storage, rubidium hydrazinidoborane is not the best candidate. The behavior of RbHB is comparable to LiHB in terms of dehydrogenation properties whereas it carries less hydrogen (a theoretical amount of 4.65 wt. % H vs 11.7 wt. % H). Third, we now have one more HB derivative and future works could open new perspectives, such as exploring its potential as a precursor of boron nitride-based ceramics. The presence of the alkali cation might act as a possible crystallization promoter for the formation of hexagonal boron nitride at low temperature, or to obtain it with a crystalline structure different from the hexagonal one.<sup>74</sup> However, to start these investigations, it would be better to start with the more-known amidoboranes of Na and Li.

## 5. References

1. International Energy Agency. *World Energy Outlook 2016*. International Energy Agency [http://www.iea.org/publications/freepublications/publication/WEB\\_WorldEnergyOutlook2015ExecutiveSummaryEnglishFinal.pdf](http://www.iea.org/publications/freepublications/publication/WEB_WorldEnergyOutlook2015ExecutiveSummaryEnglishFinal.pdf) (2016).
2. Parry, I. Fossil-fuel subsidies assessed predators hunt prey. *Nature* **554**, 175–176 (2018).
3. Wigley, T. M. L. The Paris warming targets: emissions requirements and sea level consequences. *Clim. Change* **147**, 31–45 (2018).
4. Mazloomi, K. and Gomes, C. Hydrogen as an energy carrier: Prospects and challenges. *Renew. Sustain. Energy Rev.* **16**, 3024–3033 (2012).
5. Zhang, F. *et al.* The survey of key technologies in hydrogen energy storage. *Int. J. Hydrogen Energy* **41**, 14535–14552 (2016).
6. Møller, K. T. *et al.* Hydrogen - A sustainable energy carrier. *Prog. Nat. Sci. Mater. Int.* **27**, 34–40 (2017).
7. Abdalla, A. M. *et al.* Hydrogen production, storage, transportation and key challenges with applications: A review. *Energy Convers. Manag.* **165**, 602–627 (2018).
8. Sinigaglia, T. *et al.* Production, storage, fuel stations of hydrogen and its utilization in automotive applications-a review. *Int. J. Hydrogen Energy* **42**, 24597–24611 (2017).
9. Durbin, D. J. and Malardier-Jugroot, C. Review of hydrogen storage techniques for on board vehicle applications. *Int. J. Hydrogen Energy* **38**, 14595–14617 (2013).
10. Lai, Q. *et al.* Hydrogen storage materials for mobile and stationary applications: current state of the art. *ChemSusChem* **8**, 2789–2825 (2015).
11. He, T. *et al.* Hydrogen carriers. *Nat. Rev. Mater.* **1**, 1–17 (2016).
12. Ren, J. *et al.* Current research trends and perspectives on materials-based hydrogen storage solutions: A critical review. *Int. J. Hydrogen Energy* **42**, 289–311 (2017).
13. Berenguer-Murcia, Á. *et al.* Hydrogen storage in porous materials: status, milestones, and challenges. *Chem. Rec.* **18**, 900–912 (2018).

14. Hamilton, C. W. *et al.* B-N compounds for chemical hydrogen storage. *Chem. Soc. Rev.* **38**, 279–293 (2009).
15. Staubitz, A. *et al.* Ammonia-borane and related compounds as dihydrogen sources. *Chem. Rev.* **110**, 4079–4124 (2010).
16. Chua, Y. S. *et al.* Development of amidoboranes for hydrogen storage. *Chem. Commun.* **47**, 5116–5129 (2011).
17. Moussa, G. *et al.* Boron-based hydrides for chemical hydrogen storage. *Int. J. Energy Res.* **37**, 825–842 (2013).
18. Shore, S. G. and Parry, R. W. The crystalline compound ammonia-borane,  $\text{H}_3\text{NBH}_3$ . *J. Am. Chem. Soc.* **77**, 6084–6085 (1955).
19. Li, H. *et al.* Ammonia borane, past as prolog. *J. Organomet. Chem.* **751**, 60–66 (2014).
20. Akbayrak, S. and Özkar, S. Ammonia borane as hydrogen storage materials. *Int. J. Hydrogen Energy* **43**, 18592–18606 (2018).
21. Demirci, U. B. Ammonia borane, a material with exceptional properties for chemical hydrogen storage. *Int. J. Hydrogen Energy* **42**, 9978–10013 (2017).
22. Hügler, T. *et al.* Hydrazine borane: A promising hydrogen storage material. *J. Am. Chem. Soc.* **131**, 7444–7446 (2009).
23. Yot, P. G. *et al.* Unraveling the mechanical behaviour of hydrazine borane ( $\text{NH}_2\text{-NH}_2\text{-BH}_3$ ). *Phys. Chem. Chem. Phys.* **20**, 2845–2850 (2018).
24. Moury, R. *et al.* Hydrazine borane: Synthesis, characterization, and application prospects in chemical hydrogen storage. *Phys. Chem. Chem. Phys.* **14**, 1768–1777 (2012).
25. Wu, H. *et al.* Metal hydrazinoborane  $\text{LiN}_2\text{H}_3\text{BH}_3$  and  $\text{LiN}_2\text{H}_3\text{BH}_3 \cdot 2\text{N}_2\text{H}_4\text{BH}_3$ : crystal structures and high-extent dehydrogenation. *Energy Environ. Sci.* **5**, 7531 (2012).
26. Moury, R. *et al.* Lithium hydrazinidoborane: A polymorphic material with potential for chemical hydrogen storage. *Chem. Mater.* **26**, 3249–3255 (2014).
27. Pylypko, S. *et al.* Metal hydride-hydrazine borane: Towards hydrazinidoboranes or

- composites as hydrogen carriers. *Int. J. Hydrogen Energy* **40**, 14875–14884 (2015).
28. Moury, R. *et al.* Sodium hydrazinidoborane: A chemical hydrogen-storage material. *ChemSusChem* **6**, 667–673 (2013).
  29. Chua, Y. S. *et al.* Alkali metal hydride modification on hydrazine borane for improved dehydrogenation. *J. Phys. Chem. C* **118**, 11244–11251 (2014).
  30. Banu, T. *et al.* Dehydrogenation of lithium hydrazinidoborane: Insight from computational analysis. *Int. J. Hydrogen Energy* **41**, 18953–18962 (2016).
  31. Li, T. and Zhang, J.-G. Theoretical study of the metal-controlled dehydrogenation mechanism of  $MN_2H_3BH_3$  ( $M = Li, Na, K$ ): A new family of hydrogen storage material. *J. Phys. Chem. A* **122**, 1344–1349 (2018).
  32. Kim, D. Y. *et al.* Hydrogen-release mechanisms in lithium amidoboranes. *Chem. Eur. J.* **15**, 5598–5604 (2009).
  33. Shevlin, S. A. *et al.* Dehydrogenation mechanisms and thermodynamics of  $MNH_2BH_3$  ( $M = Li, Na$ ) metal amidoboranes as predicted from first principles. *Phys. Chem. Chem. Phys.* **13**, 7649–7659 (2011).
  34. Wolstenholme, D. J. *et al.* Homopolar dihydrogen bonding in alkali metal amidoboranes: Crystal engineering of low-dimensional molecular materials. *J. Am. Chem. Soc.* **135**, 2439–2442 (2013).
  35. Wolstenholme, D. J. *et al.* Homopolar dihydrogen bonding in alkali-metal amidoboranes and its implications for hydrogen storage. *J. Am. Chem. Soc.* **133**, 16598–16604 (2011).
  36. Tan, Y. *et al.* The decomposition of  $\alpha$ - $LiN_2H_3BH_3$ : An unexpected hydrogen release from a homopolar proton-proton pathway. *J. Mater. Chem. A* **2**, 15627–15632 (2014).
  37. Kazakov, I. V. *et al.* Reversible structural transformations of rubidium and cesium amidoboranes. *Polyhedron* **127**, 186–190 (2017).
  38. Owarzany, R. *et al.* Amidoboranes of rubidium and caesium: The last missing members of the alkali metal amidoborane family. *Dalton Trans.* **46**, 16315–16320 (2017).
  39. Weng, B. *et al.* Hydrogen generation from hydrolysis of  $MNH_2BH_3$  and  $NH_3BH_3/MH$  ( $M=Li,$

- Na) for fuel cells based unmanned submarine vehicles application. *Energy* **38**, 205–211 (2012).
40. Kim, D. Y. *et al.* Rules and trends of metal cation driven hydride-transfer mechanisms in metal amidoboranes. *Phys. Chem. Chem. Phys.* **12**, 5446–5453 (2010).
  41. Zhang, Y. *et al.* First-principles prediction of intermediate products in the decomposition of metal amidoboranes. *J. Phys. Chem. C* **116**, 26728–26734 (2012).
  42. Chua, Y. S. *et al.* Alkali metal hydride modification on hydrazine borane for improved dehydrogenation. *J. Phys. Chem. C* **118**, 11244–11251 (2014).
  43. Xiong, Z. *et al.* High-capacity hydrogen storage in lithium and sodium amidoboranes. *Nat. Mater.* **7**, 138–141 (2008).
  44. Eaton, G. R. NMR of boron compounds. *J. Chem. Educ.* **46**, 547–556 (1969).
  45. Smith, W. L. Boron-11 NMR. *J. Chem. Educ.* **54**, 469–473 (1977).
  46. Hansen, M. R. *et al.*  $^{11}\text{B}$  chemical shift anisotropies in borates from  $^{11}\text{B}$  MAS, MQMAS, and single-crystal NMR spectroscopy. *J. Phys. Chem. A* **108**, 586–594 (2004).
  47. Weiss, J. W. E. and Bryce, D. L. A solid-state  $^{11}\text{B}$  NMR and computational study of boron electric field gradient and chemical shift tensors in boronic acids and boronic esters. *J. Phys. Chem. A* **114**, 5119–5131 (2010).
  48. Stowe, A. C. *et al.* In situ solid state  $^{11}\text{B}$  MAS-NMR studies of the thermal decomposition of ammonia borane: Mechanistic studies of the hydrogen release pathways from a solid state hydrogen storage material. *Phys. Chem. Chem. Phys.* **9**, 1831–1836 (2007).
  49. Kobayashi, T. *et al.* Mechanism of solid-state thermolysis of ammonia borane: A  $^{15}\text{N}$  NMR study using fast magic-angle spinning and dynamic nuclear polarization. *J. Phys. Chem. C* **118**, 19548–19555 (2014).
  50. Kim, D. P. *et al.* Synthesis and characterization of poly-(aminoborane) as a new boron nitride precursor. *Polym. Adv. Technol.* **10**, 702–712 (1999).
  51. Gervais, C. *et al.* Chemically derived BN ceramics: Extensive  $^{11}\text{B}$  and  $^{15}\text{N}$  solid-state NMR study of a preceramic polyborazilene. *Chem. Mater.* **13**, 1700–1707 (2001).

52. Gervais, C. *et al.*  $^{11}\text{B}$  and  $^{15}\text{N}$  solid state NMR investigation of a boron nitride preceramic polymer prepared by ammonolysis of borazine. *J. Eur. Ceram. Soc.* **25**, 129–135 (2005).
53. Li, L. *et al.* Two novel derivatives of ammonia borane for hydrogen storage: Synthesis, structure, and hydrogen desorption investigation. *J. Mater. Chem. A* **1**, 12263–12269 (2013).
54. Roy, B. *et al.* Supported ammonia borane decomposition through enhanced homopolar B-B coupling. *Dalton Trans.* **47**, 6570–6579 (2018).
55. Luedtke, A. T. and Autrey, T. Hydrogen release studies of alkali metal amidoboranes. *Inorg. Chem.* **49**, 3905–3910 (2010).
56. Kim, D.-P. *et al.* Synthesis and characterization of poly(aminoborane) as a new boron nitride precursor. *Polym. Adv. Technol.* **10**, 702–712 (1999).
57. Bernard, S. *et al.* Preparation of polyborazylene-derived bulk boron nitride with tunable properties by warm-pressing and pressureless pyrolysis. *Chem. Mater.* **22**, 2010–2019 (2010).
58. Favre-Nicolin, V. and Černý, R. FOX, 'free objects for crystallography': A modular approach to ab initio structure determination from powder diffraction. *J. Appl. Crystallogr.* **35**, 734–743 (2002).
59. Petráček, V. *et al.* Crystallographic computing system JANA2006: General features. *Z. Kristallogr. Cryst. Mater.* **229**, 345–352 (2014).
60. Baerlocher, C. *et al.* Charge flipping combined with histogram matching to solve complex crystal structures from powder diffraction data. *Z. Kristallogr. Cryst. Mater.* **222**, 47–53 (2007).
61. Colwell, K. S. *et al.* UFF, a full periodic table force field for molecular mechanics and molecular dynamics simulations. *J. Am. Chem. Soc.* **114**, 10024–10035 (2005).
62. Rappé, A. K. and Goddard, W. A. Charge equilibration for molecular dynamics simulations. *J. Phys. Chem.* **95**, 3358–3363 (1991).
63. Summerscales, O. T. and Gordon, J. C. Regeneration of ammonia borane from spent fuel materials. *Dalton Trans.* **42**, 10075–10084 (2013).

64. Sutton, A. D. *et al.* Regeneration of ammonia borane spent fuel by direct reaction with hydrazine and liquid ammonia. *Science*. **331**, 1426–1429 (2011).
65. Kissinger, H. E. Reaction kinetics in differential thermal analysis. *Anal. Chem.* **29**, 1702–1706 (1957).
66. Sepehri, S. *et al.* Tuning dehydrogenation temperature of carbon-ammonia borane nanocomposites. *J. Mater. Chem.* **18**, 4034–4037 (2008).
67. Sun, W. *et al.* Hydrazine bisborane as a promising material for chemical hydrogen storage. *Int. J. Hydrogen Energy* **36**, 13640–13644 (2011).
68. Kang, X. *et al.* Ammonia borane destabilized by lithium hydride: An advanced on-board hydrogen storage material. *Adv. Mater.* **20**, 2756–2759 (2008).
69. Chen, J. *et al.* Synthesis and hydrogen storage properties of lithium borohydride amidoborane complex. *Int. J. Hydrogen Energy* **38**, 10944–10949 (2013).
70. Moury, R. *et al.* Pure hydrogen-generating 'doped' sodium hydrazinidoborane. *Int. J. Hydrogen Energy* **40**, 7475–7482 (2015).
71. Fijałkowski, K. J. and Grochala, W. Substantial emission of  $\text{NH}_3$  during thermal decomposition of sodium amidoborane,  $\text{NaNH}_2\text{BH}_3$ . *J. Mater. Chem.* **19**, 2043–2050 (2009).
72. Shimoda, K. *et al.* Solid state NMR study on the thermal decomposition pathway of sodium amidoborane  $\text{NaNH}_2\text{BH}_3$ . *J. Mater. Chem.* **21**, 2609–2615 (2011).
73. Shaw, W. J. *et al.* In situ multinuclear NMR spectroscopic studies of the thermal decomposition of ammonia borane in solution. *Angew. Chem. Int. Ed.* **47**, 7493–7496 (2008).
74. Yuan, S. *et al.* How to increase the h-BN crystallinity of microfilms and self-standing nanosheets: A review of the different strategies using the PDCs route. *Crystals* **6**, (2016).

# Chapter 4

CESIUM

HYDRAZINIDOBORANE

---



# 4 Cesium Hydrazinidoborane

---

## 1. Introduction

Fossil fuels allowed the development of our society and technology. However, they are limited resources and their extraction is becoming more and more difficult. Besides, the burning of fossil fuels releases gases (mainly CO<sub>2</sub>, but also CH<sub>4</sub>, NO<sub>x</sub> and fluorinated gases) to the atmosphere that have a negative impact on the society and the environment.<sup>1,2</sup> Therefore, the transition to other sources of energy is necessary. One of the best options to obtain clean energy is hydrogen.

Molecular hydrogen (H<sub>2</sub>) is a clean, non-toxic and renewable fuel that only releases water when it is burned.<sup>3,4</sup> Hydrogen as an element is the most abundant in the universe. As molecular hydrogen, it possesses a high energy density (between 120 and 142 MJ kg<sup>-1</sup>) that represents more than three times the energy density of gasoline or diesel. Nevertheless, one of the most challenging issues about hydrogen is its storage.<sup>4</sup> To find a cost-effective and safe method to store hydrogen is still a major task. Currently, hydrogen can be stored in three ways: i) at high pressure, whose major drawbacks are the inefficiency in volumetric and gravimetric terms, the compatibility of the tank's material with the gas and the conditions of operation; ii) in cryogenic tanks at subzero temperatures, that is also not so efficient due to the cost of the tanks and the hydrogen losses; and iii) stored in a material.<sup>5,6</sup> The most attractive method is the last one. Hydrogen can be stored reversibly in solid materials at different pressures and temperatures, and it can be liberated irreversibly by hydrolysis or thermolysis of different compounds. There are different materials capable to store hydrogen: carbon nanotubes, metal organic frameworks, covalent organic frameworks, metal hydrides, polymers, thin films, zeolites and other inorganic materials.<sup>7-14</sup> In recent years, boron and nitrogen –based compounds have received attention because they are good candidates to store atomic hydrogen through B–H and N–H bonds.<sup>15-18</sup>

They possess some advantages over other materials: i) they have a high hydrogen content due to the lightness of the B and N atoms and their capacity of multiple bonding; ii) they present interactions between protic  $H^{\delta+}$  and hydridic  $H^{\delta-}$  hydrogens, which allow the destabilization of the molecule in solid state at lower temperatures in comparison with other materials; iii) many of these compounds are quite safe to handle.<sup>19</sup> Examples of these materials are metal borohydrides, metal-N-H systems, ammonia and amine-/hydrazine-boranes.<sup>20</sup>

For example, ammonia borane  $NH_3BH_3$  (AB) is a widely investigated BNH material for hydrogen storage. Reported for the first time in 1955,<sup>21</sup> it is a solid crystalline with high gravimetric hydrogen content (19.6 wt. % H). One of the most critical issues for a chemical storage material is the easiness and purity of the releasing  $H_2$ . Despite its high hydrogen content, AB presents a high dehydrogenation temperature (it releases up to 2 equivalents  $H_2$  at ca. 200°C) and it produces undesired and toxic by-products like ammonia  $NH_3$  and borazine  $B_3N_3H_6$ .<sup>22,23</sup> Different approaches have been investigated in order to overcome these drawbacks. The use of catalysts for the hydrolysis in protic and non protic solvents, and for the thermolysis of AB has been investigated.<sup>24-26</sup> There has been a progress in this area, but there are some challenges to afford, like reducing the amount of  $NH_3$  produced and the issues regarding the recyclability of the products of the reactions. Another approach is the infiltration of AB in a porous host material. Different works have been published in the recent years, showing faster kinetics and a cleaner hydrogen when AB is confined, for example, into a MOF.<sup>27-31</sup> A last approach is the chemical modification of ammonia borane. Amidoboranes (MAB) are compounds where one of the  $H^{\delta+}$  of the molecule has been substituted by a metal cation, usually by the reaction of ammonia borane and a metal hydride. These compounds show improved dehydrogenation properties in comparison with AB. Different compounds have been synthesized during the last decade, including alkali, alkaline earth and mixed cation amidoboranes.<sup>32-40</sup> Despite the efforts, the development of new materials is necessary to evaluate them and obtain suitable candidates for large-scale applications.

Hydrazine borane  $N_2H_4BH_3$  (HB) is another material that has been investigated as a chemical hydrogen storage material.<sup>41,42</sup> As well as AB, HB possesses high gravimetric hydrogen content

(15.4 wt. % H) and it is stable at room temperature under an inert atmosphere. But unlike AB, it has four  $H^{\delta+}$  and three  $H^{\delta-}$  hydrogens, which gives different properties to the molecule: for example, hydrazine borane can be dehydrogenated at a lower temperature than AB. However, HB also presents drawbacks: the dehydrogenation temperature is still considered high, it produces undesired by-products ( $NH_3$ ,  $B_2H_6$ ,  $N_2H_4$  and  $B_3N_3H_6$ ) and if the material is heated above  $300^\circ C$ , the formation of a shock-sensitive product is obtained.<sup>42</sup> Due to this safety issue, it is difficult to think in a viable technology that could use pristine HB in the solid state. As in the case of AB, there are different approaches envisaged to improve the dehydrogenation properties of HB. Analogous to amidoboranes, hydrazinidoboranes (MHB) are obtained through the chemical modification of hydrazine borane. Hydrazinidoboranes are compounds where one of the  $H^{\delta+}$  of the middle N atom of the molecule has been substituted by a metal cation. The first alkali hydrazinidoborane that was reported is lithium hydrazinidoborane  $LiN_2H_3BH_3$  (LiHB, 11.7 wt. % H). This compound presents two crystalline phases: Wu *et al.*<sup>43</sup> obtained the high temperature phase  $\alpha$ -LiHB (monoclinic, s.g.  $P2_1/c$ ) and Moury *et al.*<sup>44</sup> the low temperature phase  $\beta$ -LiHB (orthorhombic, s.g.  $Pbca$ ). This compound can release 2.6 equivalents of  $H_2$  below  $150^\circ C$ . The gas liberated is free of  $B_2H_6$  and  $B_3N_3H_6$  but the presence of  $NH_3$  was detected. Sodium hydrazinidoborane  $NaN_2H_3BH_3$  (NaHB, 8.9 wt. % H) was synthesized by Moury *et al.* by mechanochemical synthesis.<sup>45</sup> As NaH is highly reactive towards HB ( $-27.7 \text{ kJ mol}^{-1}$ ),<sup>46</sup> the synthesis has to be carried out in cold conditions (ca.  $-30^\circ C$ ). The product obtained is a crystalline solid (monoclinic, s.g.  $P2_1/n$ ) that starts the dehydrogenation process at ca.  $60^\circ C$ , releasing  $H_2$  with traces of  $NH_3$  and  $N_2$ . Potassium hydrazinidoborane  $KN_2H_3BH_3$  (KHB, 7.2 wt. % H; monoclinic, s.g.  $P2_1$ ) was synthesized by Chua *et al.*<sup>47</sup> by wet synthesis in a stainless steel reactor because the reactivity of KH towards HB is even higher than for NaH ( $70.3 \text{ kJ mol}^{-1}$ ).<sup>46</sup> It shows better dehydrogenation properties than the previous alkali hydrazinidoboranes, as it starts to decompose at ca.  $50^\circ C$ . Rubidium hydrazinidoborane  $RbN_2H_3BH_3$  (RbHB, 4.6 wt. % H; monoclinic, s.g.  $P2_1$ ) was also synthesized by wet method by the reaction between metallic rubidium and hydrazine borane.<sup>48</sup> RbHB shows better dehydrogenation properties than HB and comparable to the ones of LiHB. Nevertheless, RbHB is not a stable compound: it evolves with time when stored under argon atmosphere, decomposing and favoring the formation of B- and N-based polymers,

and during its dehydrogenation, it releases a considerable amount of  $\text{NH}_3$ . At present, those are all the alkali hydrazinidoboranes reported.

Cesium hydrazinidoborane  $\text{CsN}_2\text{H}_3\text{BH}_3$  (CsHB, 3.4 wt. % H) is presented in this work. The synthesis and characterization of CsHB have provided of a better understanding on the chemistry and behavior of this kind of B- and N-based compounds. It also allowed completing the family of alkali derivatives of HB, providing us a more complete landscape on the knowledge of hydrazinidoboranes.

## 2. Experimental section

### 2.1 Reagents

Hydrazine borane was synthesized from commercial hydrazine hemisulphate  $\text{N}_2\text{H}_4 \cdot \frac{1}{2}\text{H}_2\text{SO}_4$  ( $\geq 98\%$ , Sigma-Aldrich), sodium borohydride  $\text{NaBH}_4$  ( $\geq 98\%$ , Sigma-Aldrich) and 1,4-dioxane (anhydrous,  $\geq 99.8\%$ , Sigma-Aldrich). In order to obtain cesium hydrazinidoborane, cesium (ingot,  $\geq 99.95\%$ , Sigma-Aldrich) and THF (99.5%, extra dry, Acros Organics) were used. Metallic cesium was used due to the commercial unavailability of CsH.

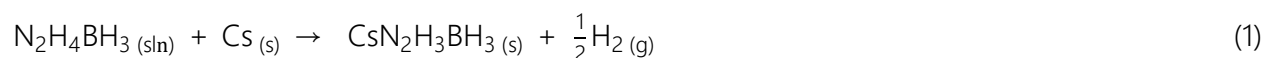
### 2.2 Synthesis

#### 2.2.1 Synthesis of hydrazine borane

All the experiments were carried out under an inert atmosphere of argon, either in a glove box (MBraun M200B;  $\text{O}_2 < 0.1$  ppm and  $\text{H}_2\text{O} < 0.1$  ppm) or a Schlenk line. Hydrazine borane was synthesized at the laboratory with a route that was developed by our team before.<sup>42</sup> Typically, 21.59 g of  $\text{N}_2\text{H}_4 \cdot \frac{1}{2}\text{H}_2\text{SO}_4$  and 10.12 g of  $\text{NaBH}_4$  are weighted in the glove box and then suspended under stirring in 150 mL of 1,4-dioxane in a round-bottom Schlenk at  $30^\circ\text{C}$  for 48 h. After this time, the suspension is filtered and a solution is obtained. The solvent is removed under vacuum and HB is obtained (A purity of 99.6% and a yield around 80% is achieved with this method).<sup>42</sup>

## 2.2.2 Synthesis of cesium hydrazinidoborane

As ammonia borane, hydrazine borane also readily reacts with metallic cesium when they are put into contact.<sup>35,49</sup> Under inert atmosphere, HB (120 mg, 2.59 mmol) was solved in 20 mL of THF; metallic cesium (300 mg, 2.25 mmol) was weighted and put into a round bottom flask. The HB solution was then poured into the flask that contained the Cs. The reaction was left under stirring for 6 h. After this time, the solid precipitate was washed two times with THF. The product was dried for 24 h under vacuum, the remaining cesium was removed and the solid product was recovered. The synthesis was carried out at -20°C and at room temperature in order to compare the effect of the temperature on the synthesis of the compound. The reaction can be written as follows:



At best, we recovered 340 mg of CsHB, which represents a yield of 85% with respect to Cs.

## 2.3 Characterization

### 2.3.1 Structural characterization

CsHB and the solid residues after decomposition experiments were analyzed by solid-state <sup>11</sup>B magic angle spinning nuclear magnetic resonance (MAS NMR; Varian VNMR4000, 128.31 MHz). Due to safety reasons, the dehydrogenated samples of CsHB were analyzed only by <sup>11</sup>B MAS NMR (Section 3.1). All the samples were prepared in the glovebox, in the corresponding rotors. The preparation of the samples and analyses were done by Mr. Emmanuel Fernandez and Mr. Philippe Gaveau, both from the Platform Balard from the University of Montpellier. CsHB was also analyzed by Fourier Transformed Infrared (FTIR) spectroscopy (NEXUS instrument, ThermoFisher Scientific, equipped with an attenuated total reflection accessory from 600 to 4000 cm<sup>-1</sup> wavelength). The samples were prepared in closed vials inside the glovebox, and were analyzed under an air atmosphere. The samples were maintained in the vial just before the analysis, and avoiding exposing the samples to the air for a long time.

Powder X-ray diffraction (PXRD) analysis was done in a PANalytical X'Pert Pro Multipurpose diffractometer equipped with an X'Celerator detector (Cu-K $_{\alpha 1/\alpha 2}$  radiation  $\lambda=1.5418$  Å, 45 kV, 30 mA) equipped with fixed divergence slits. The pattern was collected using Bragg-Brentano geometry on a spinning glass sample holder loaded into the glovebox. The diffraction pattern was recorded in the 10-80° angle range in  $2\theta$  using a step size of 0.017, with a scan step time of ~450 seconds. The powder was protected using Parafilm® "M" to prevent any contact with O<sub>2</sub> and H<sub>2</sub>O. It is important to remark that a Kapton foil was used in the first measurements, but we realized that CsHB reacted with the Kapton film during the analyses forming an orange powder, which made difficult the interpretation of the diffraction pattern. This phenomenon could not be deeply investigated due to a lack of time. The managing of the XRD equipment was done by Ms. Dominique Granier from the Platform Balard from the University of Montpellier.

### 2.3.2 Thermal characterization

For preliminary tests, CsHB was analyzed by simultaneous thermogravimetric (TG) and differential scanning calorimetry (DSC) analyses (SDT Q600, TA Instruments, N<sub>2</sub> atmosphere). Besides this, a TG analysis (Netzsch STA 449 F1 Jupiter, Ar atmosphere) coupled to a mass spectrometer (MS; Netzsch QMS 403 D Aëolos Quadro) was done to characterize the thermal behavior of the sample. Differential scanning calorimetry (DSC) was carried out at different heating rates to analyze the apparent activation energy of the decomposition of CsHB. The TG-MS analysis was carried out by Mr. Amine Geneste from the Platform Balard from the University of Montpellier. The preparation of the samples for thermal analyses was done inside the glovebox, where the powder was enclosed in a Tzero hermetic pan to protect it from air. This pan was pierced with a needle right before the analysis to allow the gases to escape.

The gases released by the decomposition reaction at isothermal conditions were analyzed by a gas chromatograph (GC; PerkinElmer Clarus 400 equipped with a ShinCarbon ST column) coupled to a mass spectrometer (MS; PerkinElmer Clarus 600 T). Typically, after the reaction had finished and the reactor was cooled down at room temperature, a sample of the gas was taken and injected into the GC with a glass syringe.

## 2.4 Decomposition experiments at isothermal conditions

The thermal behavior of CsHB was analyzed at isothermal conditions (90, 100, 110 and 120°C) in a stainless steel reactor. 100 mg of the sample was weighted and placed in a vial inside the reactor in the glovebox. Once outside, the reactor was connected to a pressure controller and immersed in an oil bath at the required temperature. The reaction of decomposition was monitored by the change of pressure inside the reactor. The equivalents of hydrogen liberated (i.e. equiv H<sub>2</sub>) were calculated and plotted as a function of time, considering H<sub>2</sub> as an ideal gas.

## 3. Results and discussion

### 3.1 Synthesis conditions and security issues regarding CsHB

CsHB is a white fine powder. It is insoluble in anhydrous organic solvents like 1,4-dioxane, toluene, THF or dimethyl carbonate. CsHB reacts when it is solved in protic solvents like water, ethanol and methanol, releasing hydrogen. This is the same behavior reported for amidoboranes and the other hydrazinidoboranes.<sup>44,45,48,50</sup>

It is important to highlight some security observations about the materials and synthesis used in this work:

- Cesium is highly reactive and presents a violent reaction in contact with water. Thus, all the works were carefully done in an inert atmosphere (glove box or Schlenk line). HB must be solved in THF before putting into contact with the metallic cesium.
- We also remark some issues about the handling of CsHB: at first, the compound was stored in a freezer in a closed vial under argon atmosphere and covered with Parafilm<sup>®</sup>. However, when the vial was recovered and the Parafilm<sup>®</sup> was removed, some of the powder inside exploded. We decided then to store the CsHB directly into the glovebox. The diffusion of some humidity inside the vial is much likely the reason of the explosive reaction.

- Some of the solid products obtained after the decomposition experiments at isothermal conditions showed spontaneous reactivity: when the sample heated at 100°C was being recovered, it suddenly exploded. Later, the same samples recovered after isothermal experiments were tried to be analyzed by FTIR but all of them ignited when they were put into contact with air. That is the reason why the solid residues were analyzed only by  $^{11}\text{B}$  MAS NMR (at low temperature).

We emphasize that this compound should be treated with caution, due to its high reactivity and the probable formation of shock sensitive compounds after heating.

## 3.2 Molecular structure of CsHB

### 3.2.1 Fourier Transformed Infrared Spectroscopy (FTIR)

Cesium hydrazinidoborane was analyzed by FTIR and the resulting spectrum was compared to the one of hydrazine borane (Figure 1). CsHB presents a similar pattern as other hydrazinidoboranes. Particularly, it is close to the spectral fingerprint of RbHB.<sup>48</sup> The N–H stretching bands ( $3500\text{--}2600\text{ cm}^{-1}$ ) are less complex in comparison to those for HB. This indicates a weaker interaction between the  $\text{H}^{\delta+}$  of the  $\text{CsN}_2\text{H}_3$  and the  $\text{H}^{\delta-}$  of the  $\text{BH}_3$  moiety and thus, a lesser stability in comparison to HB. As suggested for amidoborane and hydrazinidoborane compounds, this is the result of the insertion of the alkali cation in the molecule (in this case the  $\text{Cs}^+$ ).<sup>44,45,51</sup> The BN–N bond is also different for CsHB, being more intense in comparison to HB.

In the case of the B–H region, the hydrazinidoborane shows the bands at a lower wavelength than HB does. These observations are all due to the presence of the  $\text{Cs}^+$ , which modifies the chemical environment and the electronic properties of the molecule. The B–N and BN–N bands are stronger for CsHB, which indicates a shorter bond between the boron and nitrogen atoms due to the size of the alkali cation. This is a well-known fact in several amidoboranes and hydrazinidoboranes and in all cases is due to the substitution of the metal cation for one of the  $\text{H}^{\delta+}$  of the molecule.<sup>33–35,44,45,47,52</sup>

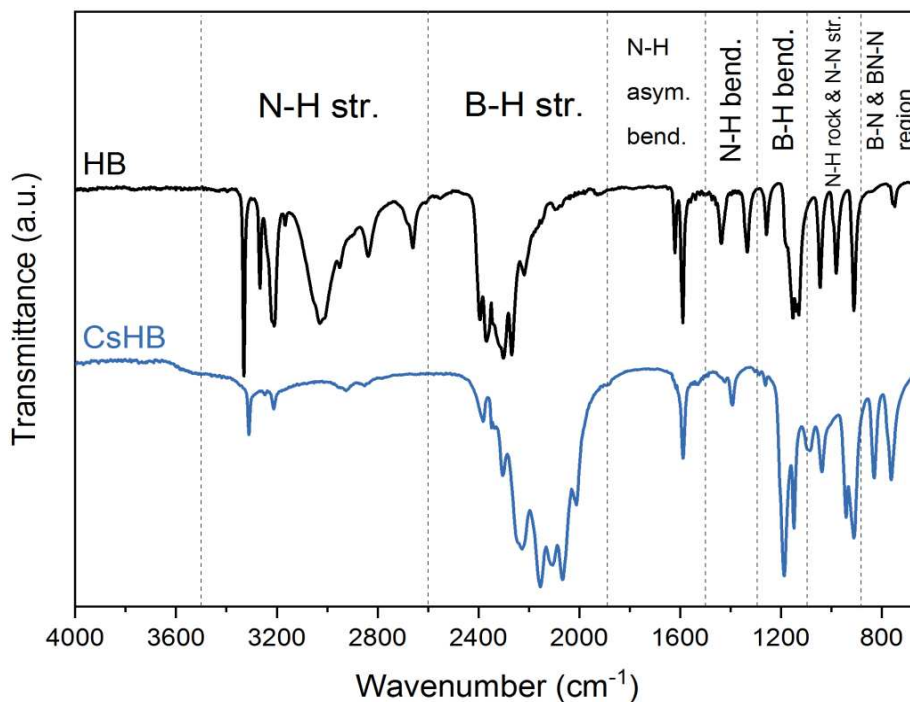


**Figure 1.** FTIR spectra of HB and CsHB with their respective bands.

### 3.2.2 <sup>11</sup>B Magic Angle Spinning Nuclear Magnetic Resonance (MAS NMR)

Figure 2 presents the comparison between the <sup>11</sup>B MAS NMR spectra of CsHB and HB. Hydrazine borane presents a single split shape at -24 ppm, due to the quadrupolar effect of the boron atom.<sup>53-55</sup> On the other hand, CsHB presents the main signal at -16.3 ppm (for a NBH<sub>3</sub> environment). The displacement on the chemical shift indicates the presence of the Cs<sup>+</sup> in the molecule. It is a symmetric signal that it has been observed in others alkali derivatives of AB and HB.<sup>44,45,49</sup> The change from one split signal to a single signal indicates the disappearance of the quadrupolar effect of HB before mentioned, and shows that the Cs<sup>+</sup> has a strong effect over the electronic array around the boron atom, presenting an isotropic environment.

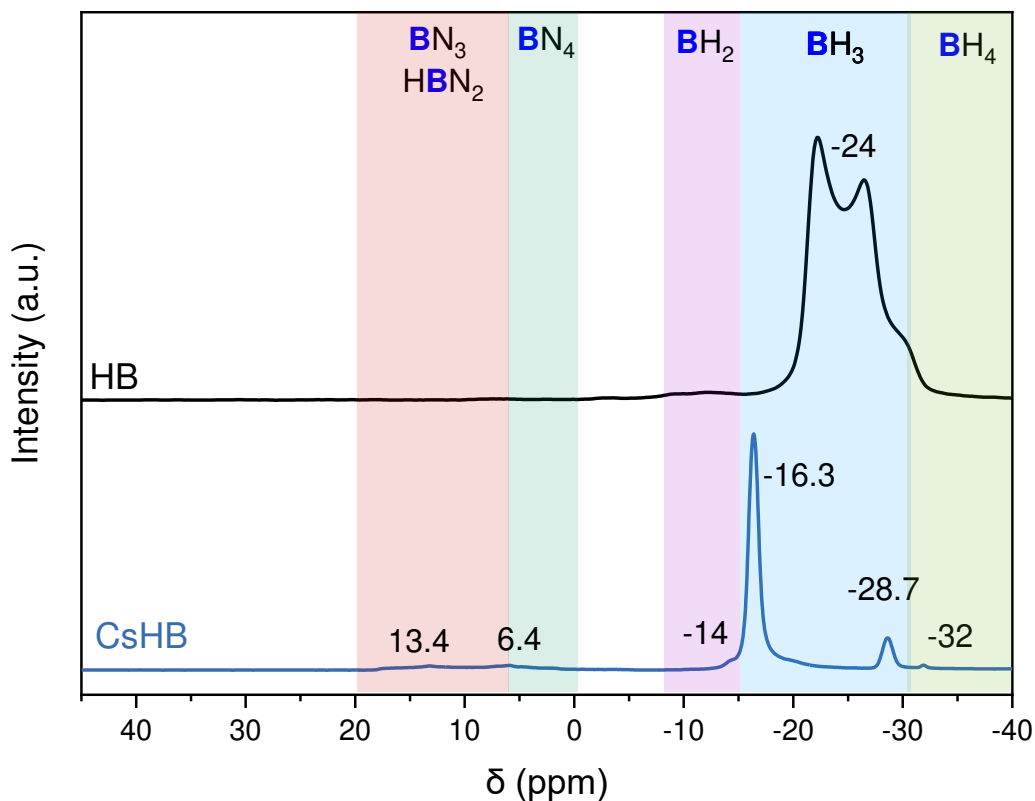


**Figure 2.**  $^{11}\text{B}$  MAS NMR spectra of HB and CsHB. The chemical shifts in ppm and the assigned boron environments are indicated in the figure.

Other signals on the CsHB spectrum can be observed at -32, -28.7, -14, 6.4 and 13.4 ppm. The signals presented at -32 and -14 ppm can be assigned to an intermediate analogous to diammoniate diborane (DADB)<sup>56</sup> formed during the decomposition of AB, but in this case applied to CsHB that could have the formulae  $[\text{CsN}_2\text{H}_3\text{BH}_2\text{CsN}_2\text{H}_3]^+[\text{BH}_4]^-$ . The signal at -32 ppm would correspond to the  $\text{BH}_4$  environment and the peak at -14 ppm to the  $\text{BH}_2$  environment. The less intense signals at 6.4 and 13.4 ppm are attributed to the formation of  $\text{BN}_4$ ,  $\text{BN}_3$  and  $\text{BN}_2\text{H}$  species, indicating the formation of amorphous boron and nitrogen-based polymeric species, typical in the decomposition of BNH compounds.<sup>57-62</sup> The signal at -28.7 ppm suggests a  $\text{BH}_3$  environment of an undesired by-product during the reaction. This signal could not be assigned to a known compound.

### 3.2.3 Stability of cesium hydrazinidoborane under inert atmosphere

CsHB was stored for two months inside the glovebox after its synthesis to be further analyzed by FTIR and  $^{11}\text{B}$  MAS NMR. As it is observed in **Figure 3**, the FTIR analysis shows that the two compounds present almost identical bands. There is a slight broadening of the N–H stretching and bending region of the spectrum for the sample stored for 2 months. This could be explained due to the formation of the before mentioned polymeric species.

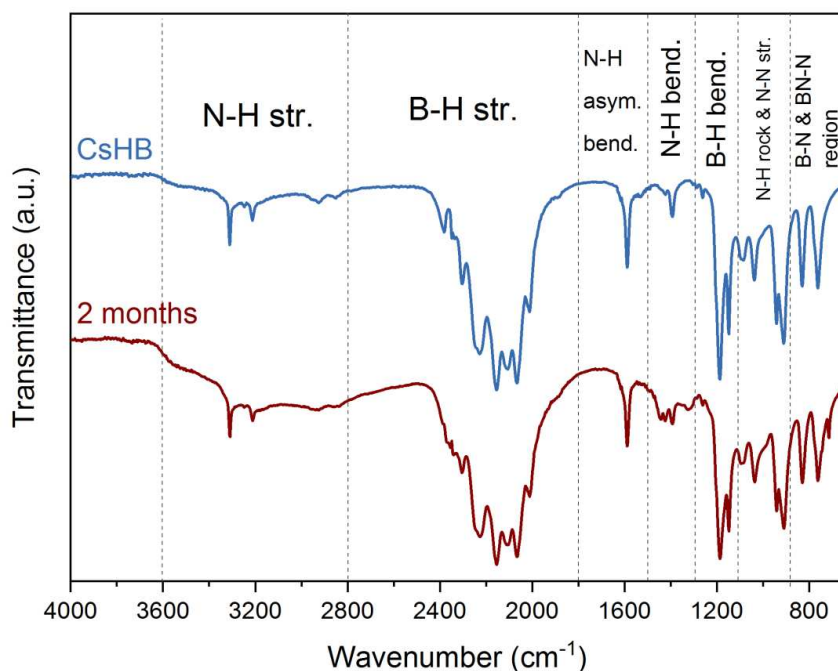


**Figure 3.** FTIR spectra of CsHB and CsHB after 2 months of its synthesis (stored at room temperature and under argon atmosphere). The bands have been assigned.

Regarding the  $^{11}\text{B}$  MAS NMR spectra (**Figure 4**), the spectra do not present big changes between the two samples. The  $\text{BH}_3$  environment at  $-16.3$  ppm is the main peak in both spectra, showing the stability of the compound. The single peak neglects any changes on the isotropy of the molecule around the boron atom, contrary to the behavior of  $\text{RbHB}$ .<sup>48</sup>

There are slight changes that are observed in the sample after two months: the signals at  $-32$  and  $-14$  ppm have disappeared. This indicates the evolution of the aforementioned intermediate

$[\text{CsN}_2\text{H}_3\text{BH}_2\text{CsN}_2\text{H}_3]^+[\text{BH}_4]^-$ . In the positive chemical shifts, a peak appeared at 1.7 ppm. This implies the slow evolution of CsHB into boron and nitrogen-based polymers. Both  $^{11}\text{B}$  MAS NMR and FTIR analyses confirm the formation of some polymeric species (e.g. polyaminoborane), but both spectra show that this decomposition is very slow and after two months, both samples present similar spectra. This is a different behavior than the one presented by rubidium hydrazinidoborane, where the decomposition of the compound is more pronounced after one month of its synthesis.<sup>48</sup> In other words, when stored under argon at room temperature, CsHB is more stable than RbHB.

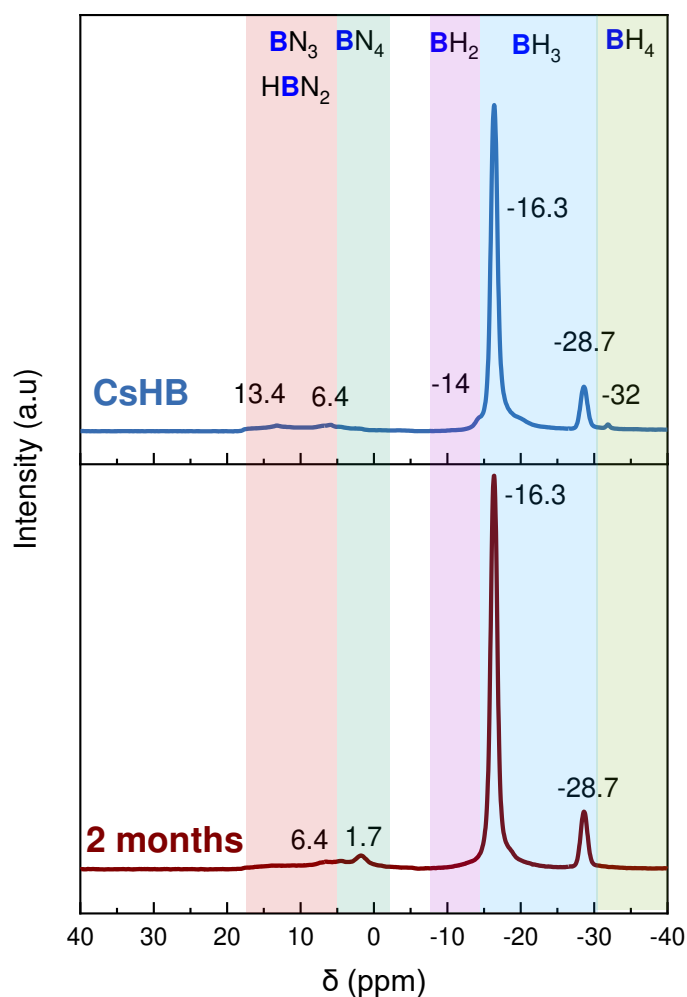


**Figure 4.**  $^{11}\text{B}$  MAS NMR spectra of a fresh sample of CsHB and one stored for 2 months at room temperature and under argon atmosphere. The chemical shifts in ppm and the assigned boron environments are indicated.

### 3.2.4 Effect of the temperature on the synthesis of CsHB

Rubidium and cesium amidoboranes have been synthesized at 0°C to avoid the decomposition of these compounds and the side reactions due to the high reactivity of metal Rb and Cs towards AB.<sup>49</sup> The synthesis of CsHB was carried out at room temperature and at low temperature (-20°C), in order to evaluate the effect of the temperature on the synthesis of the compound. The products of both syntheses were characterized by FTIR, <sup>11</sup>B MAS NMR and PXRD. **Figure 5** shows the FTIR spectra of CsHB synthesized at -20°C and room temperature (R.T.). There are small changes between the two samples. In the sample synthesized at room temperature, the N-H stretching region presents a slight broadening of the signal, similar to the CsHB aged for two months in the glove box. The B-H stretching region has more defined bands in the case of the synthesis at -20°C.

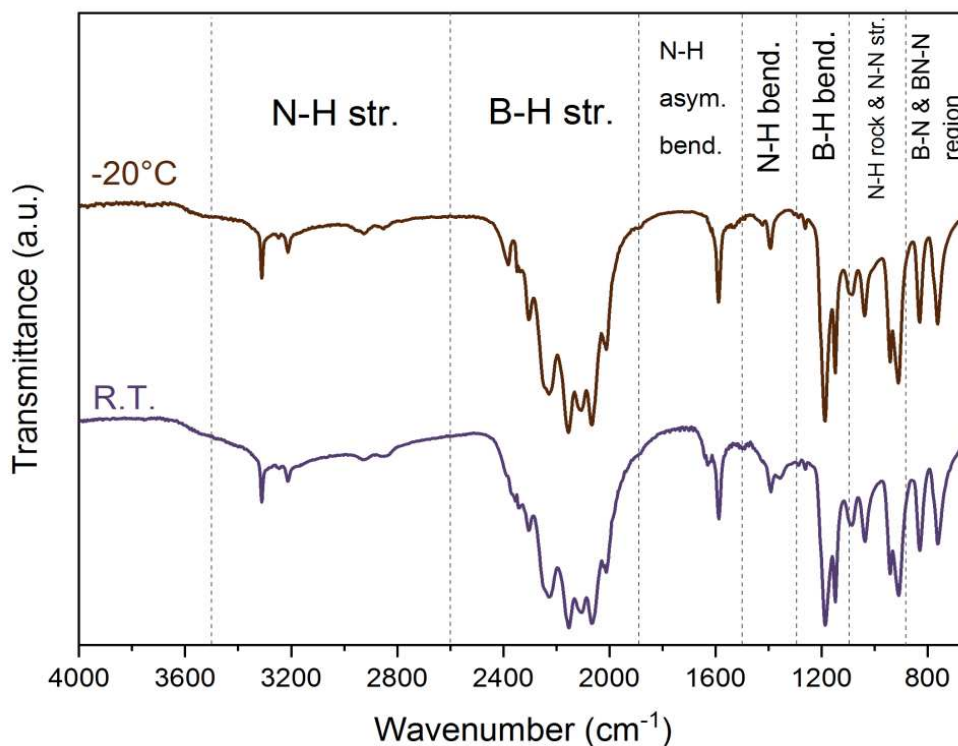


**Figure 5.** FTIR spectra of CsHB synthesized at -20°C and at room temperature.

**Figure 6** shows the analysis performed by  $^{11}\text{B}$  MAS NMR for CsHB at the two temperatures of synthesis. As observed, there is a noticeable difference: when the synthesis was carried out at  $-20^\circ\text{C}$ , the signal at  $-28$  ppm is more intense and the signals at positive chemical shifts are smaller. The opposite occurs when the compound was synthesized at room temperature: the before mentioned signals related to polymeric species due to the decomposition of CsHB increase, and the signal at  $-28$  ppm decreases. The main signal at  $-16.3$  ppm remains.

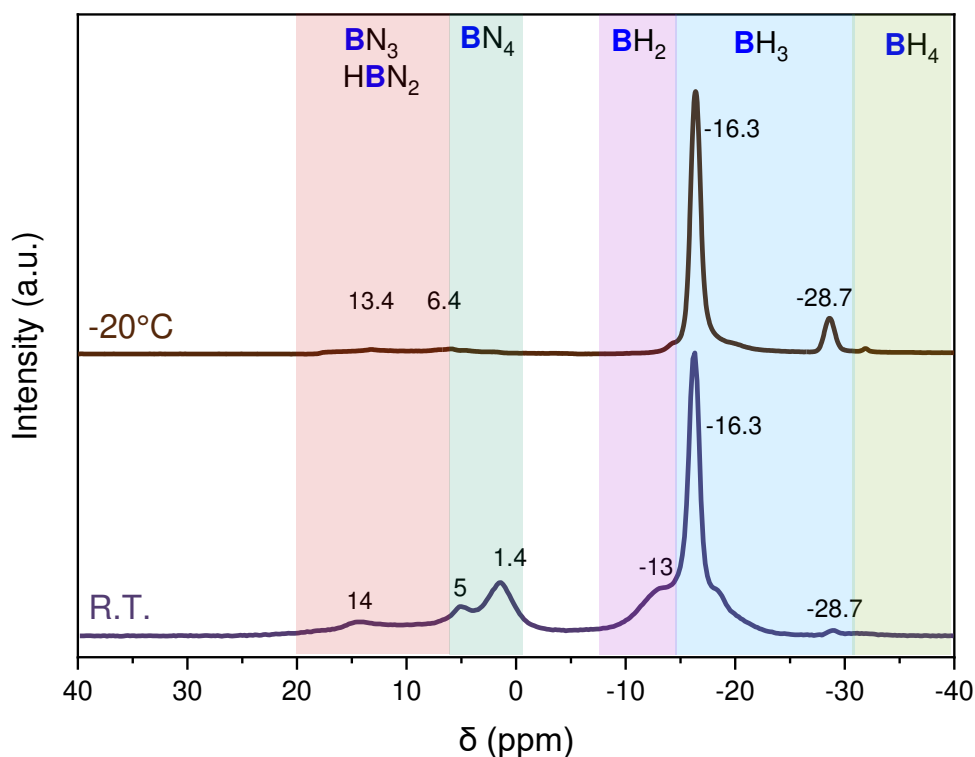


**Figure 6.**  $^{11}\text{B}$  MAS NMR spectra of CsHB synthesized at  $-20^\circ\text{C}$  and at room temperature. The chemical shifts in ppm and the assigned boron environments are indicated.

The analysis done by PXRD confirms the previous results. **Figure 7** shows that the pattern of the compound synthesized at  $-20^\circ\text{C}$  has additional diffractions peaks of an unidentified phase that do not belong to CsHB. In contrast, the pattern of the synthesis at room temperature does not show these unassigned peaks. Unfortunately, it is evident that it is not possible to obtain a pure compound, nor at room temperature nor at subzero conditions. This highlights again the high

reactivity between metallic cesium and HB. It is likely that the undesired solid byproducts are formed during the synthesis reactions. In any case, the experiments were useful to obtain the crystal structure of CsHB.

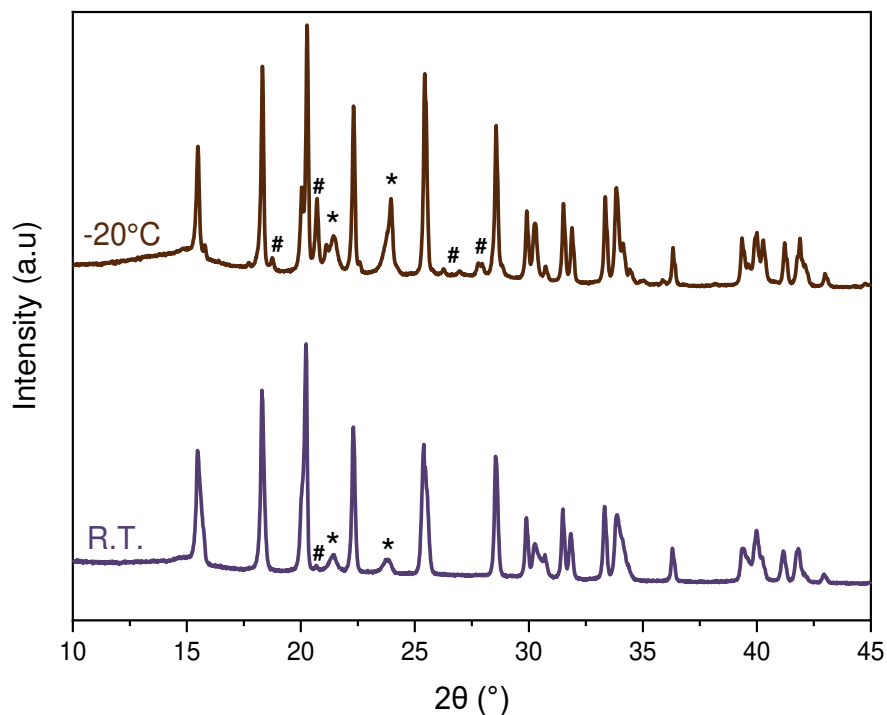


**Figure 7.** Comparison of PXRD patterns of CsHB synthesized at  $-20^{\circ}\text{C}$  and at room temperature. The # indicate the diffraction peaks of an unidentified phase formed during the synthesis and the \* symbol indicates the peaks belonging to the Parafilm<sup>®</sup> used to protect the sample from air.

### 3.2.5 Powder X-ray Diffraction (PXRD)

The patterns of HB and CsHB were compared (**Figure 8**). The peaks of the CsHB pattern are not comparable to those of HB, indicating a new phase. The three extra peaks (at  $20.6$ ,  $21.6$  and  $23^{\circ}$ ) correspond to the unidentified phase and the Parafilm<sup>®</sup> were excluded from the analysis to obtain the correct crystallographic parameters. To index the pattern of CsHB, the FoX software was used.<sup>63</sup> The Rietveld refinement was carried out in the JANA2006 package by Mr. Pascal Yot (ICGM UMR5253 Montpellier) and the determination of the position of the Cs atoms was done

with the 'SuperFlip' algorithm included in the software.<sup>64</sup> After this, FOX was used to reach the position of the  $\text{N}_2\text{H}_3\text{BH}_3^-$  anions. The crystallographic parameters obtained are shown in Table 1.

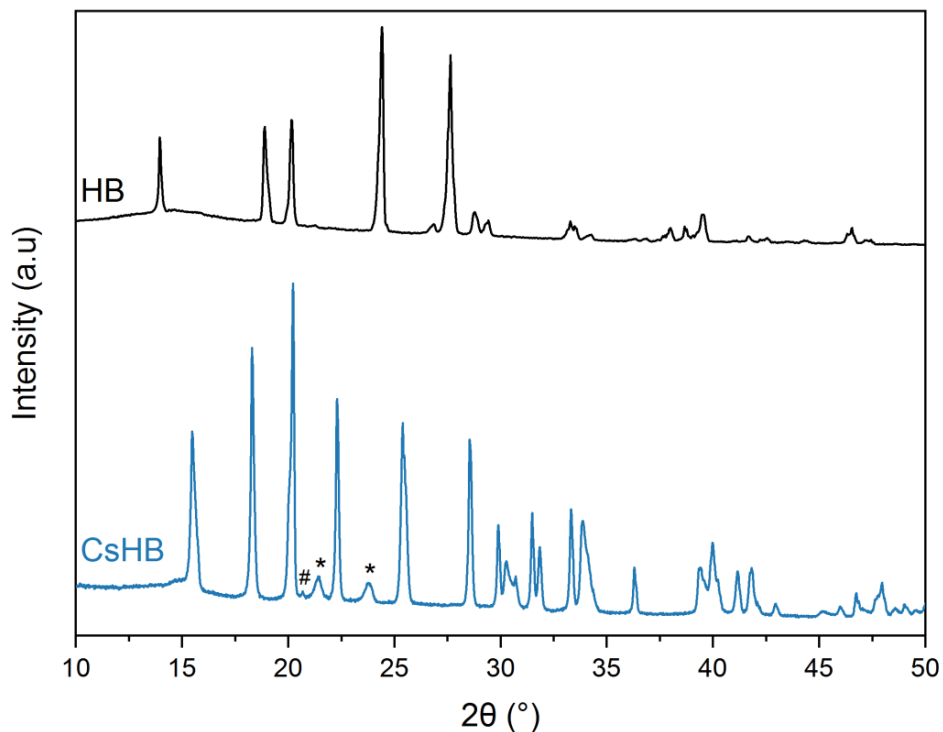


**Figure 8.** PXRD patterns of HB and CsHB. The # symbol indicates the diffraction peaks of an unidentified phase formed during the synthesis; the \* indicates the diffraction peaks of Parafilm<sup>®</sup>.

**Table 1.** Crystallographic parameters of CsHB

CsHB							
Unit cell	S.G.	a (Å)	b (Å)	c (Å)	$\beta$ (°)	Z	V (Å <sup>3</sup> )
Monoclinic	$P2_1$	5.9156(5)	7.0091(5)	6.0023(5)	108.389(4)	2	236.16(3)
Crystallographic density		2.5	Rp	6.66	$R_{(all)}/WR_{(all)}$	7.32/9.03	
Temperature (K)		293	wRp	10.17			
GoF		5.08	$R_{(obs)}/WR_{(obs)}$	7.32/9.03			

The Rietveld refinement of the pattern was carried out using a Pseudo-Voight peak shape. The peaks asymmetry was corrected using Howard model (Boole's rule) and preferred orientation using March-Dollase model following the (010) direction. As it is shown in Figure 9, the calculated pattern (red line) is in good fit with the experimental one (black line). As discussed before, the peaks highlighted in gray were omitted in the analysis. The B–H and N–H distances were constrained to 1.20 Å and 1.04 Å respectively in accordance with the optimization realized by the FoX software. The uncertainties of the atomic coordinates for hydrogen atoms are not reported here because they were not freely refined. The isotropic thermal parameters ( $U_{iso}$ ) were constrained to be identical for all atom types (Table 2).

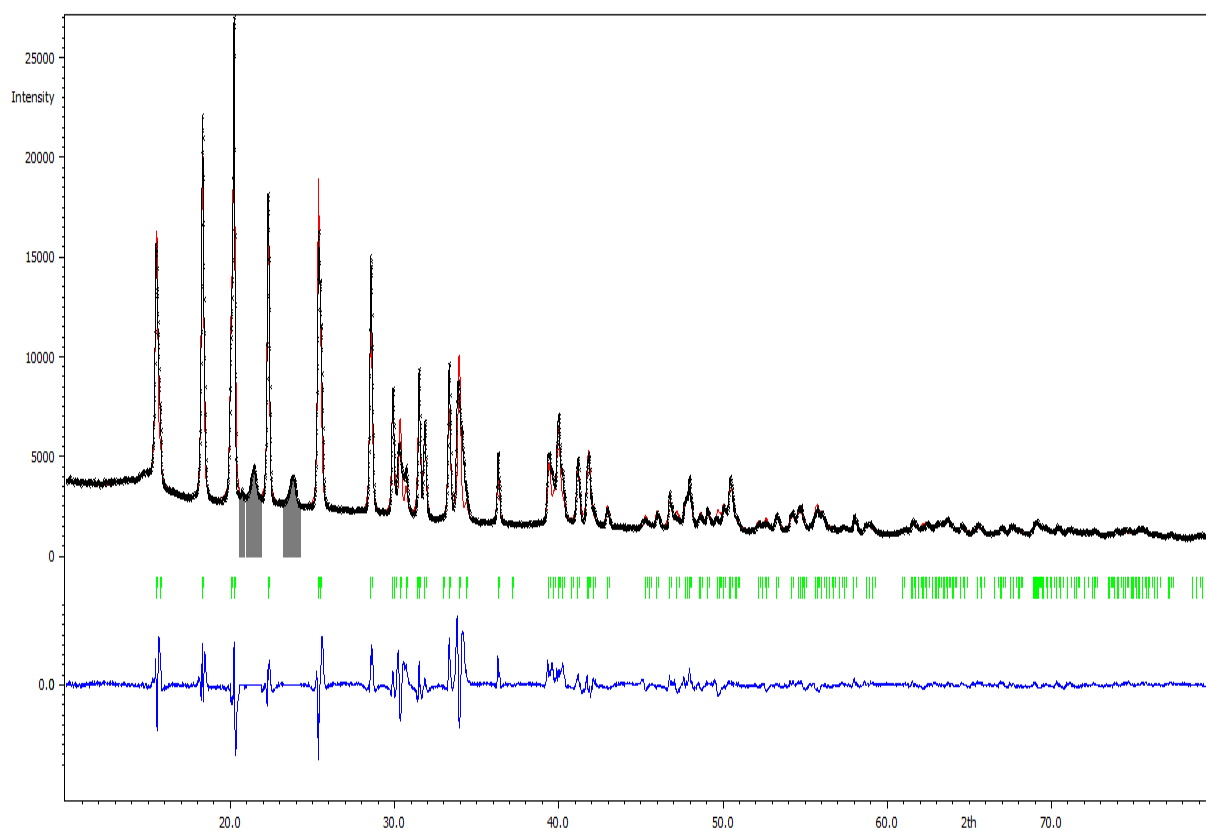


**Figure 9.** Observed (black line) and calculated (red line) PXRD profile for the Rietveld refinement of CsHB, differences of the plots (blue line), calculated angles for Bragg peaks in  $2\theta$  (green lines) and omitted peaks (gray peaks).

**Table 2.** Experimental structural parameters of CsHb (S.G.  $P2_1$ No.4) at room temperature.

Atom	Site	Occupancy	x	y	z	$U_{iso}$ (Å)
Cs			0.2208(5)	0.00019(12)	0.1133(5)	0.0477(9)
B1			0.658(6)	0.51(7)	0.805(6)	0.0477 (9)
N1			0.917(9)	0.067(11)	0.604(10)	0.0477 (9)
N2			0.723(9)	0.079(10)	0.660(10)	0.0477 (9)
H1	2a	1	0.03790	0.66835	0.29572	1.2
H2			0.00563	0.43052	0.35935	1.2
H3			0.41855	0.58430	0.49358	1.2
H4			0.17829	0.34395	0.11181	1.2
H5			0.52963	0.37079	0.28512	1.2
H6			0.33969	0.52748	0.02213	1.2

The locations of the hydrogen atoms linked to N and B atoms were determined by performing a constrained geometry optimization of the structure (Cs, B and N atoms fixed in their initial positions) at the force-field level. This work was done by Mr. Guillaume Maurin (ICGM UMR5253 Montpellier). The atoms of the system were represented as Lennard-Jones charged sites with LJ parameters taken from the UFF force field while the charges were calculated using the QeQ method.

Cesium hydrazinidoborane was successfully indexed as a single phase in a monoclinic  $P2_1$ (No. 4) unit cell (Figure 10) with  $Z=2$ ,  $a=5.9156(5)$ ,  $b=7.0091(5)$ ,  $c=6.0023(5)$  and  $\beta=108.389(4)^\circ$ . Except for  $\beta$ -LiHB (orthorhombic, s.g.  $Pbca$ )<sup>44</sup>, all the other hydrazinidoboranes crystallize in a monoclinic unit cell, though with different space groups (Table 3):  $\alpha$ -LiHB does in a  $P2_1/c$  group while NaHB does in a  $P2_1/n$  group.<sup>43,45</sup> CsHB is isostructural with KHB and with RbHB.<sup>47,48</sup> In comparison with HB,<sup>42</sup> CsHB has a bigger unit cell volume per formula  $V/Z$  (80.153 vs. 118.083 Å<sup>3</sup>). This is due to the effect of the big size of the Cs<sup>+</sup> in the molecule. If we compare CsHB with the low temperature phase of its analogous amidoborane CsAB (orthorhombic, s.g.  $Pnam$ ),<sup>35,49</sup> we find

that CsHB has also a bigger unit cell volume per formula (99.42 vs 118.083 Å<sup>3</sup>). This is in good agreement with the smaller size of the [NH<sub>2</sub>BH<sub>3</sub>]<sup>-</sup> anion of the amidoborane.

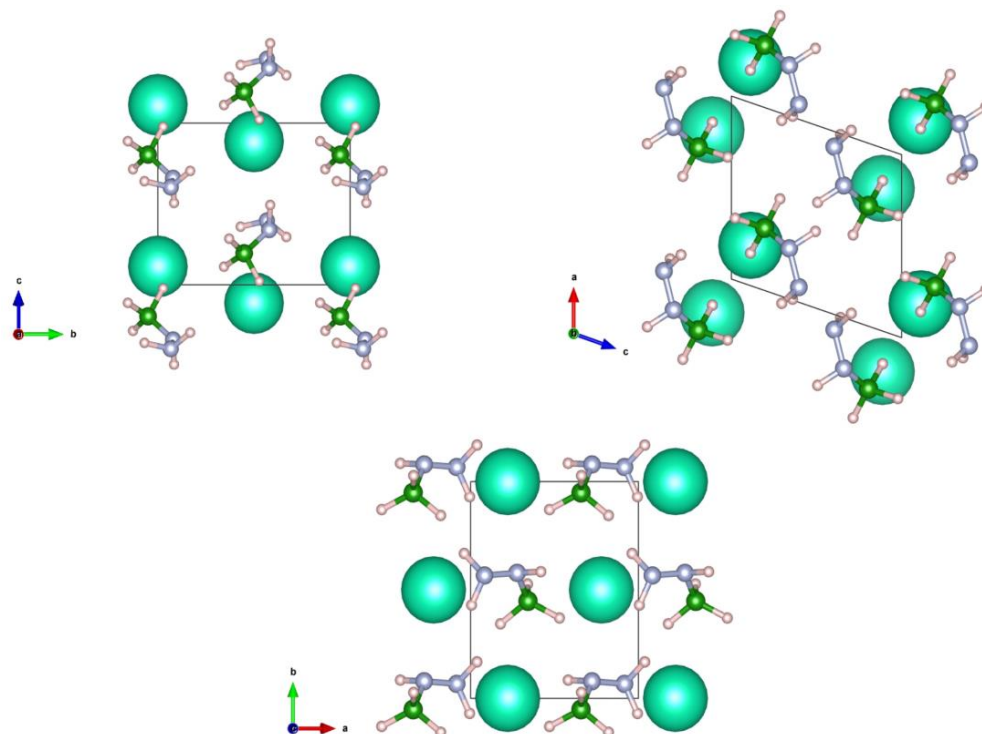


**Figure 10.** Crystal structure of CsHB along the [100], [010] and [001] directions. H, B and N atoms are represented by pink, green and blue spheres. Cs atoms are represented by turquoise spheres.

**Table 3.** Cell parameters of hydrazine borane and alkali hydrazinidoboranes.

MHB	Unit cell	S.G.	a (Å)	b (Å)	c (Å)	$\beta$ (°)	Z	V/Z (Å <sup>3</sup> )
HB	Orthorhombic	<i>Pbcn</i>	12.979(5)	5.062(2)	9.509(4)	90	8	78.081
$\alpha$ -LiHB <sup>43</sup>	Monoclinic	<i>P2<sub>1</sub>/c</i>	5.850(11)	7.467(11)	8.893(15)	122.329(6)	4	82.068
$\beta$ -LiHB <sup>44</sup>	Orthorhombic	<i>Pbca</i>	10.252(11)	8.479(10)	7.469(8)	90	4	162.313
NaHB <sup>45</sup>	Monoclinic	<i>P2<sub>1</sub>/n</i>	4.974(11)	7.958(15)	9.292(19)	93.814(11)	4	91.747
KHB <sup>47</sup>	Monoclinic	<i>P2<sub>1</sub></i>	6.721(23)	5.892(20)	5.778(17)	108.279(13)	2	108.054
RbHB <sup>48</sup>	Monoclinic	<i>P2<sub>1</sub></i>	5.813(2)	6.701(2)	5.814(2)	108.915(2)	2	107.121
CsHB	Monoclinic	<i>P2<sub>1</sub></i>	5.916(5)	7.009(5)	6.002(5)	108.389(4)	2	118.083

Figure 11 shows the coordination sphere of the  $\text{Cs}^+$  where the cation is surrounded by 6  $[\text{N}_2\text{H}_3\text{BH}_3]^-$  anions. The other hydrazinidoborane have coordination numbers of 4 (LiHB),<sup>44</sup> 5 (NaHB),<sup>45</sup> 4 (KHB)<sup>47</sup> and 6 (RbHB).<sup>48</sup> RbHB and CsHB can coordinate more anions due to the size of the cation. In comparison with the amidoboranes, CsAB is surrounded by 7  $[\text{NH}_2\text{BH}_3]^-$  anions.<sup>35</sup>

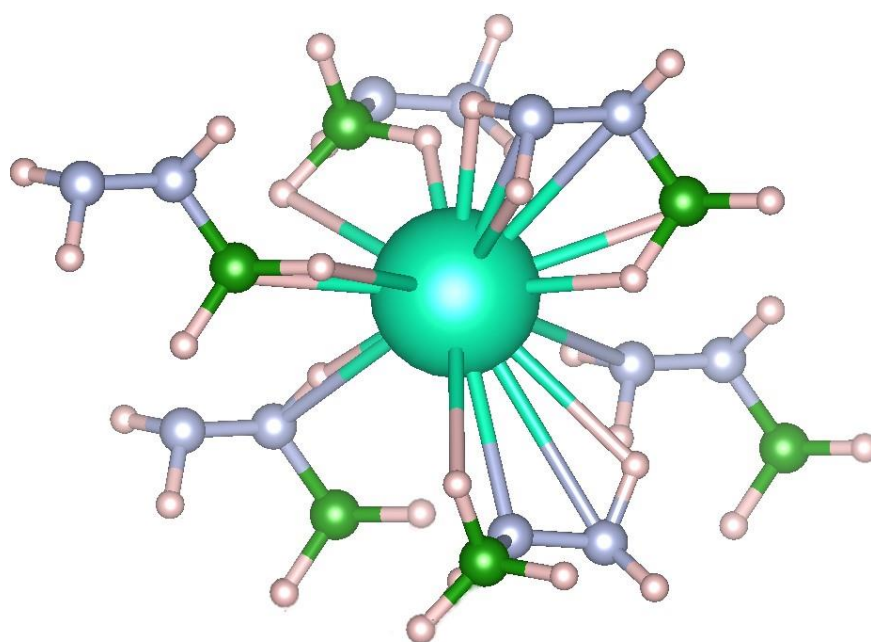


**Figure 11.** Coordination sphere of the Cs cation, surrounded by six  $[\text{N}_2\text{H}_3\text{BH}_3]^-$  anions.

The positions of the hydrogen atoms of the molecule were obtained by computational methods, allowing us to determine the interatomic distances (**Figure 12**). The shortest interatomic distance between the metal ( $\text{Cs}\cdots\text{Cs}$ ) is 4.32(4) Å and the shortest for the Cs–N bond of 3.22(7) Å. In comparison with the analogous amidoborane  $\text{CsNH}_2\text{BH}_3$ , these values are shorter (4.60(6) and 3.28(13) Å respectively).<sup>35</sup> This can be explained because unlike CsHB, the  $\text{Cs}^+$  in CsAB is surrounded by 7  $[\text{NH}_2\text{BH}_3]^-$  anions, which allows more interactions between the atoms and increasing the interatomic distances between them. In comparison with other alkali hydrazinidoboranes, the Cs–N distance decreases as the size of the alkali cation reduces: a value of 3.13 Å was found for RbHB,<sup>48</sup> 2.96 Å for KHB,<sup>47</sup> 2.41 Å for NaHB<sup>45</sup> and 2.11 Å for LiHB.<sup>44</sup> This may indicate that the bond M–N has a higher ionicity for CsHB. The B–N bond is shorter for CsHB

(1.40(8) Å) in comparison with HB (1.59 Å),<sup>42,43</sup> that is in good agreement with the changes observed in the <sup>11</sup>B MAS NMR and FTIR analyses.

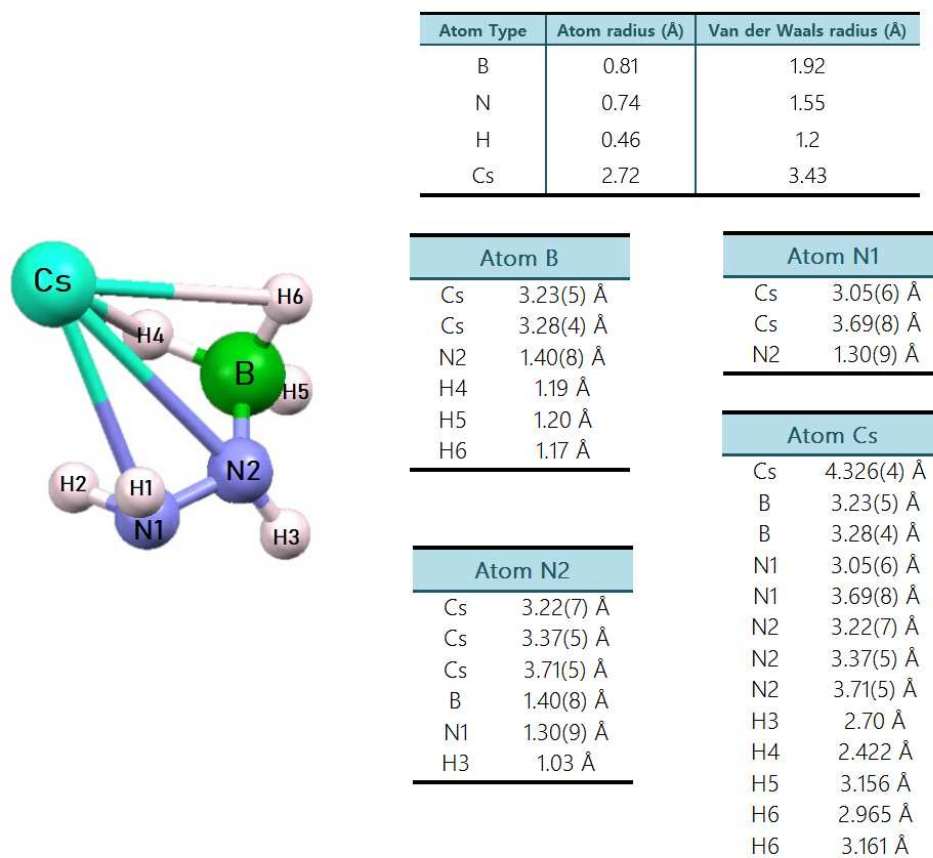


Figure 12. Calculated interatomic distances for cesium hydrazinidoborane.

### 3.3 Thermal characterization

#### 3.3.1 TGA-MS and DSC measurements

The thermal characterization of CsHB was done by TGA (heating rate of 5°C min<sup>-1</sup>) coupled to a MS to analyze the produced gases (Figure 13). CsHB starts to decompose at ca. 75°C and in the range 75-160°C, it loses 3.5 wt % of the original weight releasing mainly hydrogen, but ammonia and diborane too. There is a second mass loss in the range of 160-190°C of ca. 1.4 wt % and a last loss after 190°C of ca. 2 wt %. The total weight loss between 75 and 250°C is of 6.9%. This is twice

the 3.4 wt % H carried by cesium hydrazinidoborane. As seen in the MS analysis, this is due to the release of  $\text{NH}_3$  and the intermittent releasing of  $\text{B}_2\text{H}_6$ . The other hydrazinidoborane compounds (Li, Na, K) release purer hydrogen and we see that as bigger is the metal alkali cation, the compound tends to release more ammonia and unwanted byproducts like  $\text{B}_2\text{H}_6$ .<sup>44,45,47</sup>

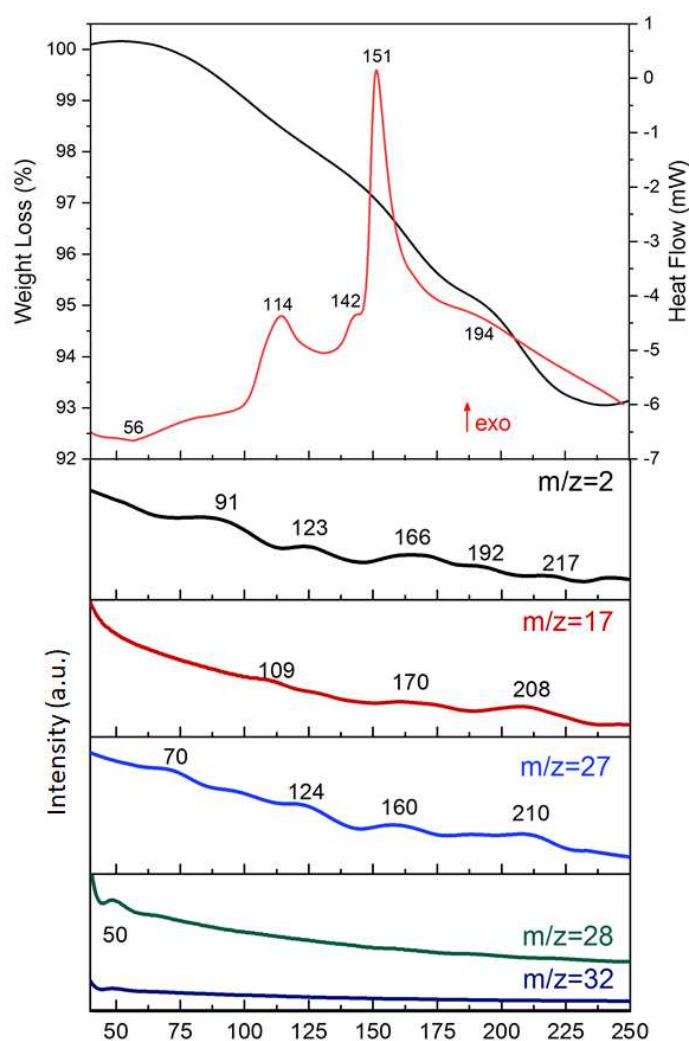


**Figure 13.** TGA-DSC ( $5^\circ\text{C min}^{-1}$ ) and MS results ( $m/z=2, 17, 27, 28, 32$  for  $\text{H}_2, \text{NH}_3, \text{B}_2\text{H}_6, \text{N}_2, \text{N}_2\text{H}_4$  or  $\text{O}_2$  respectively) of CsHB. The peak temperatures ( $^\circ\text{C}$ ) observed by DSC and MS are given.

The MS shows peaks for  $\text{H}_2$ ,  $\text{NH}_3$  and  $\text{B}_2\text{H}_6$ . There are two signals presented for  $m/z=28$  and  $m/z=32$  at  $50^\circ\text{C}$ . As at this temperature there is none important weight loss, and as both signals

appear at the same temperature, we assume that small quantities of air entered into the apparatus and the analysis indicate the presence of  $N_2$  ( $m/z=28$ ) and  $O_2$  ( $m/z=32$ ). In these conditions, the MS could not detect other possible volatile by-products of the decomposition of CsHB, such as hydrazine ( $N_2H_4$ ) or borazine ( $B_3N_3H_6$ ). It is also observed that the release of  $H_2$ ,  $NH_3$  and  $B_2H_6$  it is concomitant during all the heat treatment, suggesting a complicated path of decomposition.

**Figure 13** also shows the results of the DSC analysis. The curve confirms the complex decomposition path. There is a first endothermic event at  $56^\circ C$  related to the melting of the compound ( $CsHB_{(s)} \rightarrow CsHB_{(l)}$ ), a behavior also presented by HB, NaHB, KHB and RbHB.<sup>42,45,47,48</sup> After, there are four exothermic events that take place at 114, 142, 151 and  $194^\circ C$  and some of them can be related to the emission of the byproducts identified by MS. For example, the exothermic peak at  $114^\circ C$  is preceded by the release of some  $NH_3$  and followed by the liberation of  $H_2$ . The strongest signal presented at  $151^\circ C$  is followed by the liberation of hydrogen. The last exothermic peak at  $194^\circ C$  is preceded by the release of hydrogen. Because of the exothermicity of this process, the possibility of reusing or recycling the materials becomes difficult.

### 3.3.2 Calculation of apparent activation energy by the Kissinger method

The activation energy and kinetics parameters of the decomposition of a solid can be calculated using the Kissinger method, assuming a first order reaction (for further description of the method, see Annex I).<sup>65</sup> CsHB was analyzed by DSC at different heating rates of 1, 3, 5 and  $7^\circ C \text{ min}^{-1}$ . Figure 14 presents the superposition of the DSC curves and the linear regression analysis. We analyzed the three most important exothermic peaks of the process. These processes are related to the decomposition of CsHB. We decided to discard the first experimental point of the 3<sup>rd</sup> process, as the error was high. The apparent energies of activation of the processes 1, 2 and 3 are:  $E_{a1}=226 \text{ kJ mol}^{-1}$ ,  $E_{a2}=157 \text{ kJ mol}^{-1}$  and  $E_{a3}=202.8 \text{ kJ mol}^{-1}$ . These values are comparable with the values of others BNH materials used for hydrogen storage using the same method. For example, hydrazine bisborane possesses an  $E_a=106.4 \text{ kJ mol}^{-1}$  and LiHB  $E_a=156$  for the first decomposition step.<sup>44,66</sup> Table 4 presents the kinetic data calculated for the selected exothermic events during the decomposition of CsHB. As expected, the value of k increases with the temperature.

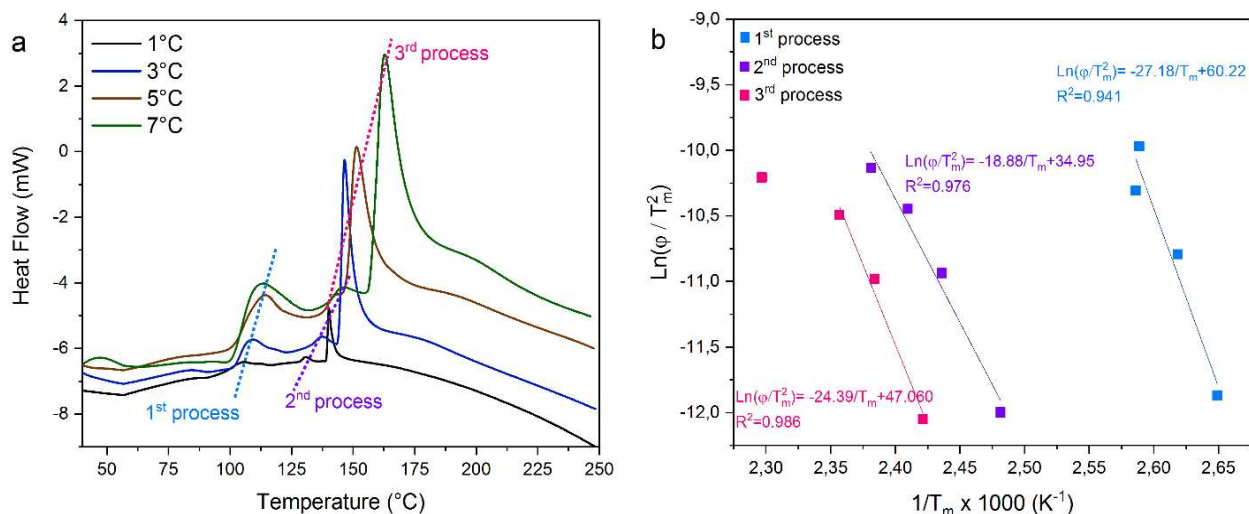


**Figure 14.** DSC curves for CsHB at different heating rates (1, 3, 5 and 7 °C min<sup>-1</sup>); and linear regression for the Kissinger method of the three exothermic events.

**Table 4.** Kinetic parameters of the thermal decomposition of CsHB obtained by the Kissinger method and Arrhenius equation.

Process	$E_a$ (kJ mol <sup>-1</sup> )	A (min <sup>-1</sup> )	k (min <sup>-1</sup> )			
			90°C	100°C	110°C	120°C
1	226	$3.8682 \times 10^{30}$	$1.163 \times 10^{-2}$	$8.659 \times 10^{-2}$	$5.805 \times 10^{-1}$	3.533
2	157	$2.8489 \times 10^{19}$	$7.278 \times 10^{-4}$	$2.935 \times 10^{-3}$	$1.101 \times 10^{-2}$	$3.86 \times 10^{-2}$
3	202.8	$6.6858 \times 10^{24}$	$4.383 \times 10^{-5}$	$2.655 \times 10^{-4}$	$1.464 \times 10^{-3}$	$7.405 \times 10^{-3}$

### 3.3.3 Decomposition experiments of CsHB

The evaluation of the decomposition behavior of CsHB was done by a heat treatment under isothermal conditions at 90, 100, 110 and 120°C. The decomposition of CsHB presents curves with a first short step where the hydrogen is slowly released and a second fast step (**Figure 15**). This same behavior is presented by the other alkali hydrazinidoboranes.<sup>44,45,48</sup> Below 100°C, the slope of the second step of the decomposition of CsHB is the most pronounced in comparison with the

other hydrazinidoboranes. It is interesting how a smaller cation like  $\text{Na}^+$  can destabilize the material in a better way than  $\text{Cs}^+$ , as  $\text{NaHB}$  releases a higher amount of hydrogen at lower temperature and in a shorter time.<sup>45</sup> This phenomenon can be due to the formation of more stable by-products during the decomposition process, making more difficult the release of hydrogen.  $\text{CsHB}$  releases almost 2 equiv  $\text{H}_2$  at  $110^\circ\text{C}$  and 2.5 equiv  $\text{H}_2$  at  $120^\circ\text{C}$  in less than 20 min of treatment. This second fast step requires more time to occur at lower temperatures.

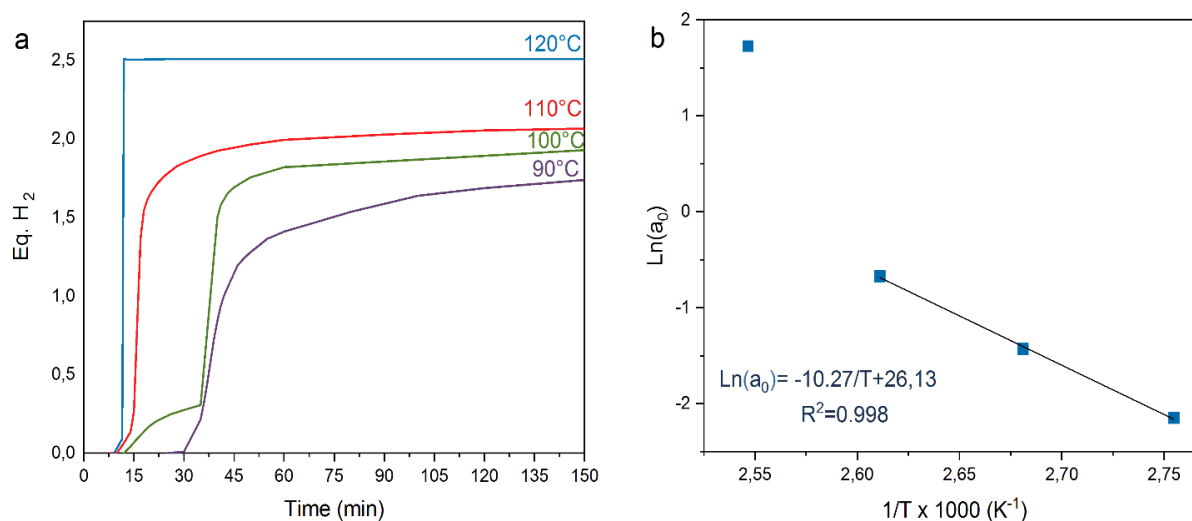


**Figure 15.** a) Time evolution of  $\text{H}_2$  release from  $\text{CsHB}$  under heating at isothermal conditions (90, 100, 110 and  $120^\circ\text{C}$ ); b) Arrhenius plot for the determination of the apparent activation energy.

The curves of **Figure 15** were used to determine the apparent activation energy of the decomposition process. As observed in **Figure 15b**, the first point was not taken into account for the calculations, due to a high error in the linear regression model. This point corresponds to  $T=120^\circ\text{C}$ , in which the decomposition is highly fast. This might occur due to the formation of shock sensitive products and because of the rapid decomposition of the sample at this temperature. The linear form of the Arrhenius equation was used with this purpose:

$$\ln a_0 = -\frac{E_a}{RT} + \ln A \quad (2)$$

Where  $a_0$  is the hydrogen generation rate,  $E_a$  the apparent energy activation,  $T$  the temperature,  $R$  the universal gas constant and  $A$  the pre-exponential factor. The generation rate (the slope of the

curves in mol H<sub>2</sub> min<sup>-1</sup>) is plotted as function of the inverse of the temperature (in K) and E<sub>a</sub> can be obtained. An apparent energy activation of 85.37 kJ mol<sup>-1</sup> was obtained. Table 5 presents the value of the apparent energy activation for different BNH compounds. The value for CsHB is higher than the values presented for other compounds such as LiH and LiBH<sub>4</sub> doped AB, LiAB and the other hydrazinidoboranes, but not as high as pure AB<sup>44,48,67–69</sup>

**Table 5.** Apparent activation energy for different BNH compounds.

Compound	E <sub>a</sub> (kJ mol <sup>-1</sup> )	Reference
Ammonia borane	183	67
LiH-doped ammonia borane	75	67
Lithium amidoborane	71	68
LiBH <sub>4</sub> -doped lithium amidoborane	61	68
α-Lithium amidoborane	157	70
β-Lithium amidoborane	272	70
Lithium hydrazinidoborane	58	44
NaH-doped sodium hydrazinidoborane	14.4	69
Rubidium hydrazinidoborane	30.1	48
Cesium hydrazinidoborane	85.37	-

The decomposition properties of CsHB were compared with those of hydrazine borane and the alkali derivatives (even if the experimental procedures are not the same for the case of HB, LiHB and NaHB). Table 6 presents the equivalents of H<sub>2</sub> released by these compounds after 1 h of isothermal treatment at different temperatures. At 100°C HB, LiHB and RbHB release a similar amount of hydrogen. CsHB releases a higher quantity of hydrogen (1.8 equivalents). However, we can observe that KHB releases a similar amount at just 88°C. The cesium cation has improved the dehydrogenation properties over HB and even from LiHB and RbHB. However, NaHB still has the best performance with 2.6 equivalents of hydrogen after 1 h of heat treatment at 100°C.

**Table 6.** Equivalents of H<sub>2</sub> liberated by the alkali hydrazinidoboranes and hydrazine borane after 1 h of heat treatment at isothermal conditions.

Temperature	Compound					
	HB <sup>45</sup>	LiHB <sup>44</sup>	NaHB <sup>45</sup>	KHB <sup>47</sup>	RbHB <sup>48</sup>	CsHB
80°C	0.4	-	0.62	-	0.38	-
88°C	0.46	-	-	1.75	-	-
90°C	0.63	-	1.15	-	-	1.4
100°C	0.65	0.6	2.6	-	0.55	1.8
110°C	-	0.9	2.7	-	-	1.9
120°C	-	-	-	-	1.1	2.5
140°C	1.1	2.2	-	-	2	-

The gases produced during the dehydrogenation experiments at isothermal conditions were analyzed by gas chromatography (GC). In the GC, the presence of hydrogen is confirmed by the single peak that appears at around 0.6 min for all temperatures, which represents the retention time for H<sub>2</sub> in the column used on the chromatograph (Figure 16).

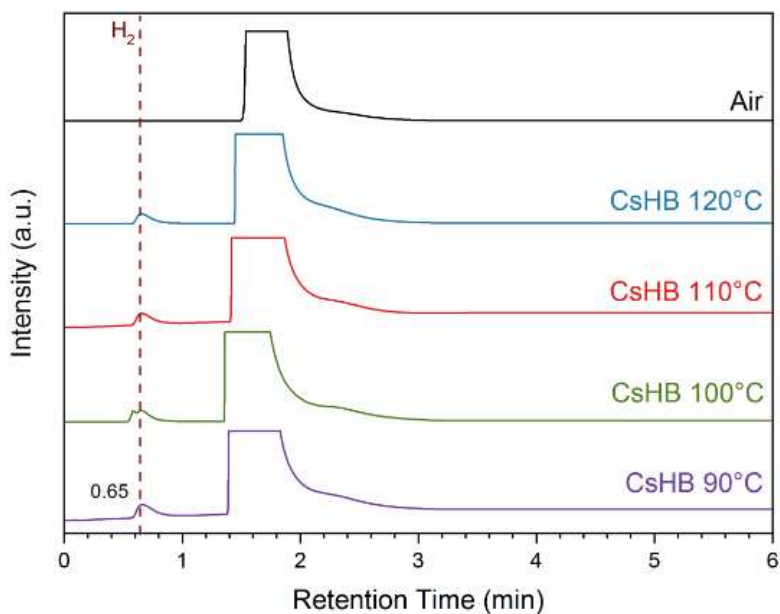


**Figure 16.** GC analyses of the gases liberated by CsHB at isothermal conditions (under heating at constant temperature of 90, 100, 110 and 120°C). The retention time in min is indicated.

A second signal can be observed after 1.3 min, corresponding to the retention time of air (introduced while injecting the sample). As a reference, air was injected in the GC and shown in the chromatogram.

The gases released by the samples treated at 100 and 120°C were analyzed by MS. The analysis showed that the gas produced is a mixture of different compounds. Besides  $H_2$  we detected the presence of ammonia  $NH_3$ , hydrazine  $N_2H_4$ , diborane  $B_2H_6$  and nitrogen  $N_2$  at 120°C. In the case of the sample heated at 100°C, no hydrazine or diborane were found (Figure 17 and Figure 18).

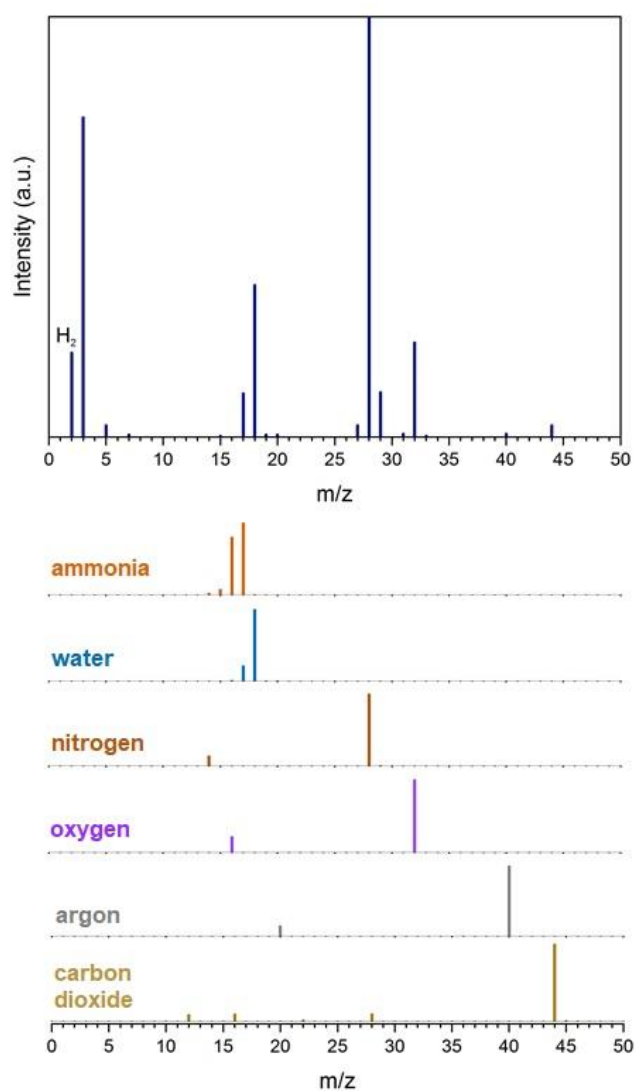


**Figure 17.** MS spectra of the gases released by the sample heated isothermally at 100°C. The m/z signals of the identified species are shown below.

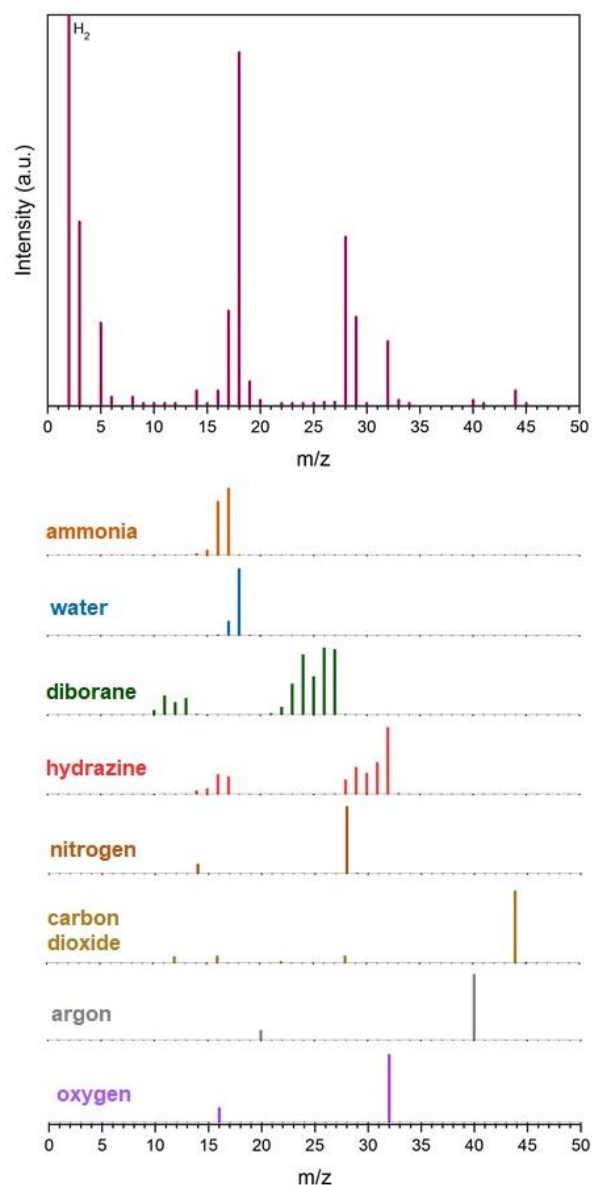


**Figure 18.** MS spectra of the gases released by the sample heated isothermally at 120°C. The  $m/z$  signals of the identified species are shown below.

The decomposition behavior presented by CsHB is different from other alkali hydrazinidoboranes.<sup>69</sup> This could be explained by any of the two following reasons (or both): (i) the by-products detected in the synthesis of CsHB by  $^{11}\text{B}$  MAS NMR and PXRD are the responsible of the emission of these compounds or (ii) the big size of the  $\text{Cs}^+$  and the longer Cs–N bond distance means a higher degree of freedom on the molecule, which could result in the formation

of such compounds. As there is a lack of computational calculations to affirm exactly which compounds are formed, we propose possible mechanisms that are probably to take place during the thermolysis of CsHB, as shown in Figure 19 to Figure 21. We may recall that the presence of  $N_2$  can be due to small quantities of air that enter when injecting the sample, because signals belonging to  $O_2$ ,  $H_2O$  and  $CO_2$  were identified too. Other signals assigned as impurities from the carrier gas were also identified at  $m/z=3$ , 5 and 6.

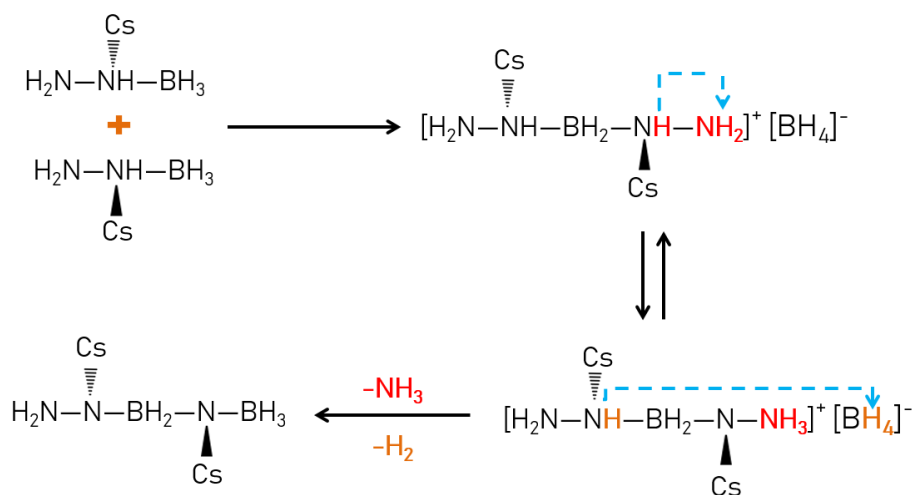


**Figure 19.** Formation of the dimer  $[(CsN_2H_3)_2BH_2]^+[BH_4]^-$ , which will release  $H_2$  and  $NH_3$ .

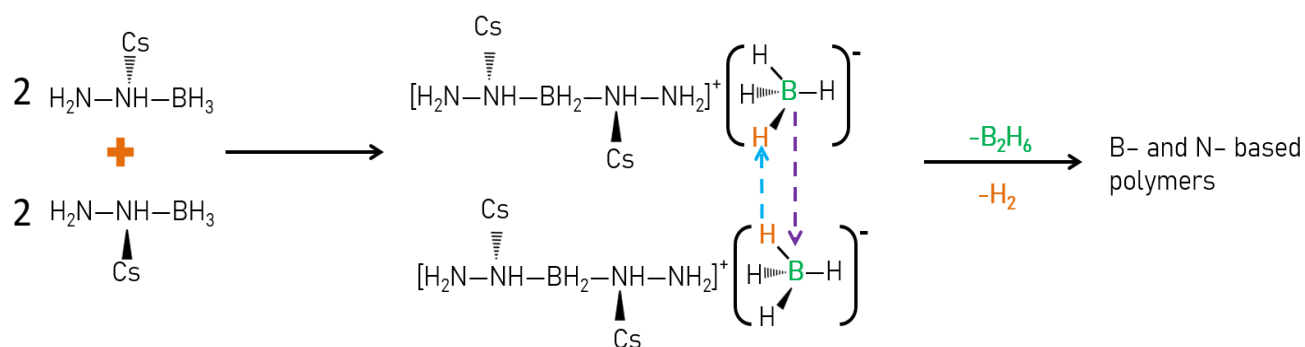


**Figure 20.** Formation of the dimer  $[(CsN_2H_3)_2BH_2]^+[BH_4]^-$ , which continues reacting to form B- and N-based polymers with the release of  $H_2$  and  $B_2H_6$ .

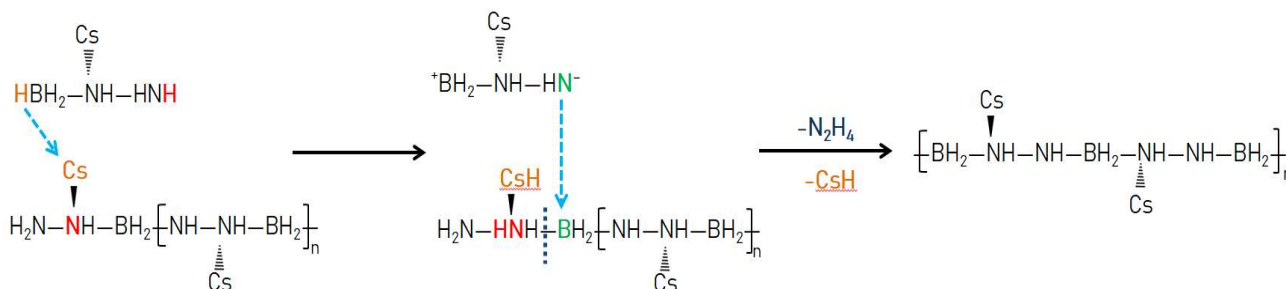


**Figure 21.** Reaction of a polymer chain product of the thermolysis of CsHB and a molecule of CsHB. This leads to a continued growth of the chain, forming CsH and releasing  $\text{N}_2\text{H}_4$ .

In any case, the release of these gaseous by-products is in good agreement with the TGA analysis, due to the high mass loss of CsHB during the decomposition (6.9 wt. % of mass loss, when the content of hydrogen is 3.4 wt. % H). A phenomenon present in the decomposition experiments of hydrazinidoboranes is the difference between the detected gases at different experimental conditions. This is explained because for example, in the TG-MS analysis the gases released by the sample are being carried away by the carrier gas of the apparatus. The isothermal experiments are carried out in a closed system, so the possible intermediates have the time to react and form these compounds, instead of being carried away.

### 3.4 Analyses of solid residues

As previously mentioned in section 3.1, the solid residues after isothermal experiments could only be analyzed by  $^{11}\text{B}$  MAS NMR due to security issues. It is important to remind that the preparation of the rotors was carried out in a glove box and the analysis was performed at a low temperature to avoid any risk of explosion of the sample. Figure 22 shows the comparison of the spectra of the samples obtained after the heat treatment at isothermal conditions (90, 100, 110 and  $120^\circ\text{C}$ ) and CsHB by  $^{11}\text{B}$  MAS NMR.

As mentioned in section 3.2.2, the  $\text{BH}_4$  environment is assigned to the presence of a ionic dimer  $[(\text{CsN}_2\text{H}_3)_2\text{BH}_2]^+[\text{BH}_4]^-$ . The signal centered at -13 ppm was deconvoluted in two signals. The one at -14.7 ppm suggests a  $\text{NBH}_3$  group, which indicates some unreacted  $\text{BH}_3$  groups; the one at

-12.7 ppm indicates a  $\text{N}_2\text{BH}_2$  environment, suggesting the presence of the dimer  $[\text{CsN}_2\text{H}_3\text{BH}_2\text{CsN}_2\text{H}_3]^+[\text{BH}_4]^-$ , or the formation of some other compounds like  $\text{Cs-H}\cdots\text{CsN}_2\text{H}_3\text{BH}_2\text{N}_2\text{H}_3\text{BH}_3$ .<sup>57,58,61,62,71</sup> At 120°C, these signals have disappeared, indicating an evolution of these compounds, and a new peak has appeared at -1.1 ppm suggesting the formation of  $\text{N}_3\text{BH}$  species.

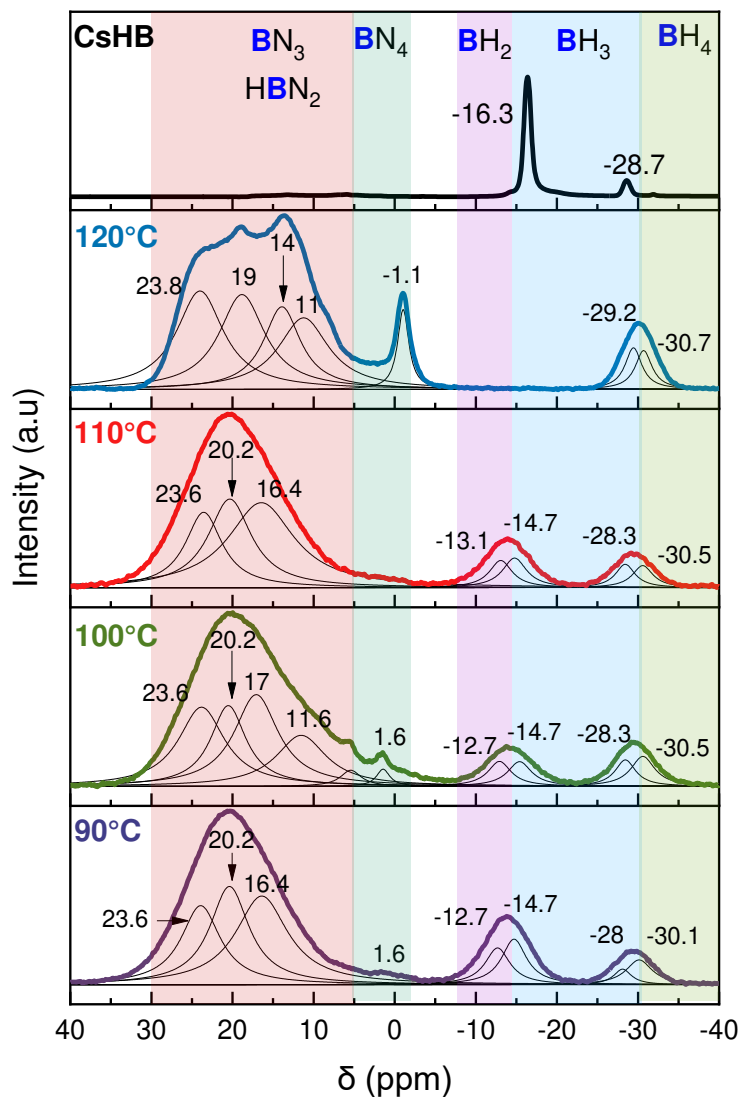


**Figure 22.**  $^{11}\text{B}$  MAS NMR spectra of CsHB and the solid residues recovered after the isothermal treatment at 90, 100, 110 and 120°C. The signals for the residues were deconvoluted. The chemical shifts in ppm and the assigned boron environments are indicated.

The signal centered at -28.7 ppm broadens for all samples, and the intensity of this signal increases the temperature rises. At 120°C the  $\text{BH}_2$  and  $\text{BH}_3$  environments have disappeared, but the signal at -28.7 ppm is still present. This suggests a compound with a different **B** environment. One possibility is the presence of a cesium salt of  $\text{B}_3\text{H}_8^-$ . It has been reported that in the presence of a  $\text{BH}_3$  environment, a pure alkali metal can react to form such salts:<sup>72,73</sup>



Other work reported that environment for the B atom in  $\text{CsB}_3\text{H}_8$  corresponds to a chemical shift of -29.8 ppm when analyzed in  $\text{THF-d}_8$ .<sup>74</sup> The formation of this salt is likely due to the high reactivity of Cs, but is still speculative and it requires of a deeper investigation to confirm or discard such hypothesis. However, without computational analyses the identification of this compound is challenging by other characterization techniques due to safety reasons, as the heated samples ignite when they are put in contact with air.

For all the studied temperatures, a broad and intense signal appears at positive chemical shifts, typical from a  $\text{sp}^2$  hybridized boron atom.<sup>58,59,61</sup> At 90 and 100°C there is one signal that appears at lower positive chemical shifts (1.6 ppm), which can indicate the formation of a  $\text{BN}_4$  environment.<sup>57</sup> The broad signal presented by all samples after 10 ppm was deconvoluted in mainly 3 signals centered around 16, 20 and 23 ppm. The environments are assigned to  $\text{BN}_3$  and  $\text{BN}_2\text{H}$ . Typical compounds that can form in the decomposition of ammonia borane include polymeric species like polyborazilene and polyiminoborane.<sup>75</sup> Analogous species might form during the decomposition of  $\text{CsHB}$ .

## 4. Conclusions

The last of the alkali derivatives of hydrazine borane, cesium hydrazinidoborane  $\text{CsN}_2\text{H}_3\text{BH}_3$  ( $\text{CsHB}$ ; 3.3 wt. % H) was synthesized and characterized in this work. The displacement of the  $\text{H}^{\delta+}$  of the hydrazine moiety by  $\text{Cs}^+$  was demonstrated by FTIR and  $^{11}\text{B}$  MAS NMR techniques. The synthesis of a completely pure compound could not be obtained (neither at room or subzero temperature), but the experiments carried out allowed us to obtain the crystal structure of

CsN<sub>2</sub>H<sub>3</sub>BH<sub>3</sub>. CsHB is a crystalline material isostructural to KN<sub>2</sub>H<sub>3</sub>BH<sub>3</sub> and RbN<sub>2</sub>H<sub>3</sub>BH<sub>3</sub>, with a monoclinic unit cell and a *P*2<sub>1</sub> space group (No. 4) with cell parameters of *a*=5.916 Å, *b*=7.009 Å, *c*=6.002 Å and  $\beta$ =108.389°.

The behavior of CsHB under heating at constant rate (5°C min<sup>-1</sup>) and at isothermal conditions was analyzed. The effect of the Cs<sup>+</sup> on the molecule was confirmed: CsHB starts to decompose at a lower temperature than HB does, confirming the destabilization that the cation has on the molecule. CsHB can release more equivalents of gas in 1 hour of heat treatment than LiHB and RbHB; however, the MS analyses showed that the composition of this gas is hydrogen accompanied by ammonia, hydrazine and diborane. This also explains the mass loss of CsHB during the TG analysis: while CsHB possesses 3.3 wt. % H, it loses more than 6 wt. % during its decomposition. However, it is not still clear if such gaseous by-products are emitted only by CsHB or if the other unidentified compounds formed in the synthesis reaction also have a contribution. The compounds obtained after the decomposition of CsHB presents a similar composition to dehydrogenated hydrazinidoboranes, which is a mixture of solid polymers composed mainly of polyborazylene-like compounds. The identification of such compounds still represents a challenge in the field, so deeper works should be performed in order to elucidate the intermediates and species that participate in the reaction and the exact products obtained.

Cesium hydrazinidoborane was obtained and its characteristics were evaluated in this work. This allowed us to complete the alkali family of hydrazine borane derivatives and let us to have a better landscape of these borane compounds. Although the thermal behavior of CsHB is improved in comparison to HB, the presence of undesired by-products in the released gas shows that it is not the best option as a chemical hydrogen storage material. Besides, the management of the thermolytic residues of CsHB represent a risk. Otherwise, this compound might be considered as an energetic material.

## 5. References

1. Li, H. *et al.* An analysis of research hotspots and modeling techniques on carbon capture and storage. *Sci. Total Environ.* **687**, 687–701 (2019).
2. Dong, K. *et al.* CO<sub>2</sub> emissions, natural gas and renewables, economic growth: Assessing the evidence from China. *Sci. Total Environ.* **640–641**, 293–302 (2018).
3. Dunn, S. Hydrogen futures: Toward a sustainable energy system. *Int. J. Hydrogen Energy* **27**, 235–264 (2002).
4. Züttel, A. *et al.* Hydrogen: The future energy carrier. *Philos. Trans. R. Soc. A Math. Phys. Eng. Sci.* **368**, 3329–3342 (2010).
5. Niaz, S. *et al.* Hydrogen storage: Materials, methods and perspectives. *Renew. Sustain. Energy Rev.* **50**, 457–469 (2015).
6. Barthélémy, H. *et al.* Hydrogen storage: Recent improvements and industrial perspectives. *Int. J. Hydrogen Energy* **42**, 7254–7262 (2017).
7. Yu, X. *et al.* Recent advances and remaining challenges of nanostructured materials for hydrogen storage applications. *Prog. Mater. Sci.* **88**, 1–48 (2017).
8. Rusman, N. A. A. and Dahari, M. A review on the current progress of metal hydrides material for solid-state hydrogen storage applications. *Int. J. Hydrogen Energy* **41**, 12108–12126 (2016).
9. Eftekhari, A. and Fang, B. Electrochemical hydrogen storage: Opportunities for fuel storage, batteries, fuel cells, and supercapacitors. *Int. J. Hydrogen Energy* **42**, 25143–25165 (2017).
10. Ren, J. *et al.* Current research trends and perspectives on materials-based hydrogen storage solutions: A critical review. *Int. J. Hydrogen Energy* **42**, 289–311 (2017).
11. Dündar-Tekkaya, E. and Yürüm, Y. Mesoporous MCM-41 material for hydrogen storage: A short review. *Int. J. Hydrogen Energy* **41**, 9789–9795 (2016).
12. Jin, J. *et al.* Carbon hybridized halloysite nanotubes for high-performance hydrogen storage capacities. *Sci. Rep.* **5**, 1–10 (2015).

13. Ke, Z. *et al.* Modification of COF-108 via impregnation/functionalization and Li-doping for hydrogen storage at ambient temperature. *Int. J. Hydrogen Energy* **42**, 11461–11468 (2017).
14. Adeniran, B. and Mokaya, R. Low temperature synthesized carbon nanotube superstructures with superior CO<sub>2</sub> and hydrogen storage capacity. *J. Mater. Chem. A* **3**, 5148–5161 (2015).
15. Huang, Z. and Autrey, T. Boron-nitrogen-hydrogen (BNH) compounds: Recent developments in hydrogen storage, applications in hydrogenation and catalysis, and new syntheses. *Energy Environ. Sci.* **5**, 9257–9268 (2012).
16. Jepsen, L. H. *et al.* Boron-nitrogen based hydrides and reactive composites for hydrogen storage. *Mater. Today* **17**, 129–135 (2014).
17. Moussa, G. *et al.* Boron-based hydrides for chemical hydrogen storage. *Int. J. Energy Res.* **37**, 825–842 (2013).
18. Wang, K. *et al.* Metal B-N-H hydrogen-storage compound: Development and perspectives. *J. Alloys Compd.* **794**, 303–324 (2019).
19. Hamilton, C. W. *et al.* B-N compounds for chemical hydrogen storage. *Chem. Soc. Rev.* **38**, 279–293 (2009).
20. Lu, Z. H. and Xu, Q. Recent progress in boron- and nitrogen-based chemical hydrogen storage. *Funct. Mater. Lett.* **5**, 1–9 (2012).
21. Shore, S. G. and Parry, R. W. The crystalline compound ammonia-borane, H<sub>3</sub>NBH<sub>3</sub>. *J. Am. Chem. Soc.* **77**, 6084–6085 (1955).
22. Akbayrak, S. and Özkar, S. Ammonia borane as hydrogen storage materials. *Int. J. Hydrogen Energy* **43**, 18592–18606 (2018).
23. Demirci, U. B. Ammonia borane, a material with exceptional properties for chemical hydrogen storage. *Int. J. Hydrogen Energy* **42**, 9978–10013 (2017).
24. Zhan, W. W. *et al.* Dehydrogenation of ammonia borane by metal nanoparticle catalysts. *ACS Catal.* **6**, 6892–6905 (2016).
25. Jiang, H. L. and Xu, Q. Catalytic hydrolysis of ammonia borane for chemical hydrogen

- storage. *Catal. Today* **170**, 56–63 (2011).
26. Patel, N. *et al.* Improved dehydrogenation of ammonia borane over Co-P-B coating on Ni: A single catalyst for both hydrolysis and thermolysis. *Appl. Catal. B Environ.* **111–112**, 178–184 (2012).
  27. Li, Z. *et al.* Ammonia borane confined by a metal-organic framework for chemical hydrogen storage: Enhancing kinetics and eliminating ammonia. *J. Am. Chem. Soc.* **132**, 1490–1491 (2010).
  28. Li, Z. *et al.* Improved thermal dehydrogenation of ammonia borane by MOF-5. *RSC Adv.* **5**, 10746–10750 (2015).
  29. Chung, J. Y. *et al.* Influence of metal-organic framework porosity on hydrogen generation from nanoconfined ammonia borane. *J. Phys. Chem. C* **121**, 27369–27378 (2017).
  30. Zhong, R. Q. *et al.* Improved hydrogen release from ammonia-borane with ZIF-8. *Inorg. Chem.* **51**, 2728–2730 (2012).
  31. Srinivas, G. *et al.* Nanoconfined ammonia borane in a flexible metal-organic framework Fe-MIL-53: Clean hydrogen release with fast kinetics. *J. Mater. Chem. A* **1**, 4167–4172 (2013).
  32. Xiong, Z. *et al.* High-capacity hydrogen storage in lithium and sodium amidoboranes. *Nat. Mater.* **7**, 138–141 (2008).
  33. Wu, H. *et al.* Alkali and alkaline-earth metal amidoboranes: Structure, crystal chemistry, and hydrogen storage properties. *J. Am. Chem. Soc.* **130**, 14834–14839 (2008).
  34. David, W. I. F. *et al.* Potassium(I) amidotrihydroborate: Structure and hydrogen release. *J. Am. Chem. Soc.* **132**, 11836–11837 (2010).
  35. Owarzany, R. *et al.* Amidoboranes of rubidium and caesium: The last missing members of the alkali metal amidoborane family. *Dalton Trans.* **46**, 16315–16320 (2017).
  36. Zhang, Q. *et al.* Synthesis, crystal structure, and thermal decomposition of strontium amidoborane. *J. Phys. Chem. C* **114**, 1709–1714 (2010).
  37. Genova, R. V. *et al.* Towards  $\text{Y}(\text{NH}_2\text{BH}_3)_3$ : Probing hydrogen storage properties of  $\text{YX}_3/\text{MNH}_2\text{BH}_3$  ( $\text{X}=\text{F}, \text{Cl}$ ;  $\text{M}=\text{Li}, \text{Na}$ ) and  $\text{YH}_{x-3}/\text{NH}_3\text{BH}_3$  composites. *J. Alloys Compd.* **499**,

- 144–148 (2010).
38. Fijalkowski, K. J. *et al.* Na[Li(NH<sub>2</sub>BH<sub>3</sub>)<sub>2</sub>] - The first mixed-cation amidoborane with unusual crystal structure. *Dalton Trans.* **40**, 4407–4413 (2011).
  39. Kang, X. *et al.* Combined formation and decomposition of dual-metal amidoborane NaMg(NH<sub>2</sub>BH<sub>3</sub>)<sub>3</sub> for high-performance hydrogen storage. *Dalton Trans.* **40**, 3799–3801 (2011).
  40. Luo, J. *et al.* Synthesis, formation mechanism, and dehydrogenation properties of the long-sought Mg(NH<sub>2</sub>BH<sub>3</sub>)<sub>2</sub> compound. *Energy Environ. Sci.* **6**, 1018–1025 (2013).
  41. Hügler, T. *et al.* Hydrazine borane: A promising hydrogen storage material. *J. Am. Chem. Soc.* **131**, 7444–7446 (2009).
  42. Moury, R. *et al.* Hydrazine borane: Synthesis, characterization, and application prospects in chemical hydrogen storage. *Phys. Chem. Chem. Phys.* **14**, 1768–1777 (2012).
  43. Wu, H. *et al.* Metal hydrazinoborane LiN<sub>2</sub>H<sub>3</sub>BH<sub>3</sub> and LiN<sub>2</sub>H<sub>3</sub>BH<sub>3</sub>·2N<sub>2</sub>H<sub>4</sub>BH<sub>3</sub>: crystal structures and high-extent dehydrogenation. *Energy Environ. Sci.* **5**, 7531 (2012).
  44. Moury, R. *et al.* Lithium hydrazinidoborane: A polymorphic material with potential for chemical hydrogen storage. *Chem. Mater.* **26**, 3249–3255 (2014).
  45. Moury, R. *et al.* Sodium hydrazinidoborane: A chemical hydrogen-storage material. *ChemSusChem* **6**, 667–673 (2013).
  46. Pylypko, S. *et al.* Metal hydride-hydrazine borane: Towards hydrazinidoboranes or composites as hydrogen carriers. *Int. J. Hydrogen Energy* **40**, 14875–14884 (2015).
  47. Chua, Y. S. *et al.* Alkali metal hydride modification on hydrazine borane for improved dehydrogenation. *J. Phys. Chem. C* **118**, 11244–11251 (2014).
  48. Castilla-Martinez, C. A. *et al.* Rubidium hydrazinidoborane: Synthesis, characterization and hydrogen release properties. *Int. J. Hydrogen Energy* **44**, 28252–28261 (2019).
  49. Kazakov, I. V. *et al.* Reversible structural transformations of rubidium and cesium amidoboranes. *Polyhedron* **127**, 186–190 (2017).
  50. Weng, B. *et al.* Hydrogen generation from hydrolysis of MNH<sub>2</sub>BH<sub>3</sub> and NH<sub>3</sub>BH<sub>3</sub>/MH (M=Li,

- Na) for fuel cells based unmanned submarine vehicles application. *Energy* **38**, 205–211 (2012).
51. Kim, D. Y. *et al.* Rules and trends of metal cation driven hydride-transfer mechanisms in metal amidoboranes. *Phys. Chem. Chem. Phys.* **12**, 5446–5453 (2010).
  52. Kang, X. D. *et al.* Efficient and highly rapid hydrogen release from ball-milled  $3\text{NH}_3\text{BH}_3/\text{MMgH}_3$  (M = Na, K, Rb) mixtures at low temperatures. *Int. J. Hydrogen Energy* **37**, 4259–4266 (2012).
  53. Hermanek, S.  $^{11}\text{B}$  NMR spectra of boranes, main-group heteroboranes, and substituted derivatives. Factors influencing chemical shifts of skeletal atoms. *Chem. Rev.* **92**, 325–362 (1992).
  54. Hansen, M. R. *et al.*  $^{11}\text{B}$  chemical shift anisotropies in borates from  $^{11}\text{B}$  MAS, MQMAS, and single-crystal NMR spectroscopy. *J. Phys. Chem. A* **108**, 586–594 (2004).
  55. Weiss, J. W. E. and Bryce, D. L. A solid-state  $^{11}\text{B}$  NMR and computational study of boron electric field gradient and chemical shift tensors in boronic acids and boronic esters. *J. Phys. Chem. A* **114**, 5119–5131 (2010).
  56. Shevlin, S. A. *et al.* Dehydrogenation mechanisms and thermodynamics of  $\text{MNH}_2\text{BH}_3$  (M = Li, Na) metal amidoboranes as predicted from first principles. *Phys. Chem. Chem. Phys.* **13**, 7649–7659 (2011).
  57. Kobayashi, T. *et al.* Mechanism of solid-state thermolysis of ammonia borane: A  $^{15}\text{N}$  NMR study using fast magic-angle spinning and dynamic nuclear polarization. *J. Phys. Chem. C* **118**, 19548–19555 (2014).
  58. Kim, D.-P. *et al.* Synthesis and characterization of poly(aminoborane) as a new boron nitride precursor. *Polym. Adv. Technol.* **10**, 702–712 (1999).
  59. Gervais, C. *et al.* Chemically derived BN ceramics: Extensive  $^{11}\text{B}$  and  $^{15}\text{N}$  solid-state NMR study of a preceramic polyborazilene. *Chem. Mater.* **13**, 1700–1707 (2001).
  60. Bernard, S. *et al.* Preparation of polyborazylene-derived bulk boron nitride with tunable properties by warm-pressing and pressureless pyrolysis. *Chem. Mater.* **22**, 2010–2019 (2010).

61. Gervais, C. *et al.*  $^{11}\text{B}$  and  $^{15}\text{N}$  solid state NMR investigation of a boron nitride preceramic polymer prepared by ammonolysis of borazine. *J. Eur. Ceram. Soc.* **25**, 129–135 (2005).
62. Stowe, A. C. *et al.* In situ solid state  $^{11}\text{B}$  MAS-NMR studies of the thermal decomposition of ammonia borane: Mechanistic studies of the hydrogen release pathways from a solid state hydrogen storage material. *Phys. Chem. Chem. Phys.* **9**, 1831–1836 (2007).
63. Favre-Nicolin, V. and Černý, R. FOX, 'free objects for crystallography': A modular approach to ab initio structure determination from powder diffraction. *J. Appl. Crystallogr.* **35**, 734–743 (2002).
64. Petříček, V. *et al.* Crystallographic computing system JANA2006: General features. *Z. Kristallogr. Cryst. Mater.* **229**, 345–352 (2014).
65. Kissinger, H. E. Reaction kinetics in differential thermal analysis. *Anal. Chem.* **29**, 1702–1706 (1957).
66. Sun, W. *et al.* Hydrazine bisborane as a promising material for chemical hydrogen storage. *Int. J. Hydrogen Energy* **36**, 13640–13644 (2011).
67. Kang, X. *et al.* Ammonia borane destabilized by lithium hydride: An advanced on-board hydrogen storage material. *Adv. Mater.* **20**, 2756–2759 (2008).
68. Chen, J. *et al.* Synthesis and hydrogen storage properties of lithium borohydride amidoborane complex. *Int. J. Hydrogen Energy* **38**, 10944–10949 (2013).
69. Moury, R. *et al.* Pure hydrogen-generating 'doped' sodium hydrazinidoborane. *Int. J. Hydrogen Energy* **40**, 7475–7482 (2015).
70. Liu, X., Wang, S., Wu, Y., Li, Z., Jiang, L., Guo, X., Ye, J. Dehydrogenation properties of two phases of  $\text{LiNH}_2\text{BH}_3$ . *Int. J. Hydrogen Energy* **45**, 2127–2134 (2020).
71. Li, L. *et al.* Two novel derivatives of ammonia borane for hydrogen storage: Synthesis, structure, and hydrogen desorption investigation. *J. Mater. Chem. A* **1**, 12263–12269 (2013).
72. Grinderslev, J. B. *et al.* Potassium octahydridotriborate: Diverse polymorphism in a potential hydrogen storage material and potassium ion conductor. *Dalton Trans.* **48**, 8872–8881 (2019).

73. Chen, X. *et al.* Facile synthesis of unsolvated alkali metal octahydrotriborate salts  $MB_3H_8$  (M=K, Rb, and Cs), mechanisms of formation, and the crystal structure of  $KB_3H_8$ . *Angew. Chem.* **131**, 2746–2750 (2019).
74. Hill, T. G. *et al.* Reduction of  $BH_3 \cdot THF$  by alkali metal (K, Rb, Cs) and ytterbium mercury amalgams to form salts of a simple procedure for the synthesis of tetraborane(10). *Inorg. Chem.* **30**, 2952–2954 (1991).
75. Frueh, S. *et al.* Pyrolytic decomposition of ammonia borane to boron nitride. *Inorg. Chem.* **50**, 783–792 (2011).



# Chapter 5

AMIDOBORANES-DERIVED BORON NITRIDE

---



# 5 Amidoborane-derived boron nitride

---

## 1. Introduction

At present, the primary source of energy is fossil fuels, but they are limited resources and the burning of such fuels releases pollutant emissions to the atmosphere, especially carbon dioxide (CO<sub>2</sub>). Different sectors (transport, industrial, domestic) contribute to the enormous quantities of CO<sub>2</sub> released, which have a direct impact on global warming. Around 99 % of the CO<sub>2</sub> emissions are produced by the combustion of fossil fuels.<sup>1</sup> One approach to decrease these emissions, are the CO<sub>2</sub> capture and storage (CCS) technologies.<sup>2,3</sup> For example, the physical and chemical sorption of CO<sub>2</sub> by materials; however, most of these technologies are not mature enough to be implemented in all kind of industrial processes.<sup>4</sup>

Different materials have been proposed to capture CO<sub>2</sub>: zeolites, ionic liquids, metal organic frameworks, porous carbons, amines, boron nitride, silica, among others.<sup>4-6</sup> In the last years, boron nitride (BN) has received attention due to its unique properties and potential application in different fields, such as water treatment, photonics or coatings.<sup>7-12</sup> BN has also been considered for CO<sub>2</sub> capture. According to different studies, nitrogen atoms with a partial negative charge act as potential active sites for carbon dioxide chemisorption.<sup>13,14</sup> Back in 1994, porous BN was already studied as a selective gas adsorbent for a mixture of CH<sub>4</sub>/CO<sub>2</sub>.<sup>15</sup> More recently, in 2010, a theoretical study predicted the strong CO<sub>2</sub> adsorption in boron-rich boron nitride nanotubes (BNNT).<sup>16</sup> The work suggested that the BNNT could capture CO<sub>2</sub> at ambient conditions. Another work calculated the capture of CO<sub>2</sub> by different kind of structures. For example, CO<sub>2</sub> was weakly adsorbed by uncharged BN nanosheets and nanotubes; however, when extra electrons are introduced to the materials (negatively charged), CO<sub>2</sub> molecules are strongly adsorbed and the BN presents a selectivity for this gas.<sup>17</sup> Other studies point to the possible ways to enhance the CO<sub>2</sub> capture by BN, like vacancies of

boron atoms or the doping of the BN structures.<sup>13,18</sup> A few experimental works have reported the CO<sub>2</sub> capture by BN structures like porous nanofibers, nanosheets, foam or 3D structures.<sup>19–25</sup> All of these studies have evidenced the uptake of CO<sub>2</sub> at near ambient conditions. For example, porous BN modified with P123 surfactant can capture 60.2 cm<sup>3</sup> g<sup>-1</sup> (25°C, 1 bar), while BN nanosheets functionalized with polyethylenimine (PEI) can capture 69.9 cm<sup>3</sup> g<sup>-1</sup> (120°C, 1 bar).<sup>20,21</sup> In comparison, a CO<sub>2</sub> uptake of 10 cm<sup>3</sup> g<sup>-1</sup> was reported for a mesostructured silica (SBA-15).<sup>26</sup>

Beyond of being a potential material for CO<sub>2</sub> sorption applications, BN can be also considered for H<sub>2</sub> storage. Through ab-initio simulations, it has been estimated that BN could uptake 8.6 % wt. H<sub>2</sub> at room temperature.<sup>27</sup> Other computational studies have determined different approaches to improve the sorption properties of BN, like the surface functionalization with alkali atoms, the increase of the specific surface area, and/or the substitution of B atoms in the structure by C and/or O atoms.<sup>28–31</sup>

Different boron- and nitrogen-containing precursors can be used to obtain BN. Ammonia borane (AB) is one of them.<sup>32,33</sup> AB is a stable, crystalline solid at room temperature with a high hydrogen content (19.6 % wt.). During its thermolysis, AB undergoes a three step decomposition,<sup>34</sup> releasing one equivalent of H<sub>2</sub> in each stage. These steps take place at ca. 100, 150 and >400°C respectively. In this sense, metal amidoboranes (MAB) might also be precursors of boron nitride. MAB are derivatives of AB, formed when one of the protic hydrogens of the NH<sub>3</sub> moiety of AB is substituted by a metal cation. These derivatives have proved to improve the dehydrogenation properties of the former AB: they start to dehydrogenate at lower temperatures and they suppress some unwanted byproducts, releasing purer hydrogen.<sup>35</sup> Different amidoboranes have been synthesized up to now, starting with the alkali derivatives (Li, Na, K, Rb, Cs) followed by the alkaline-earth amidoboranes (Be, Mg, Ca, Sr, Ba), covering other metals such as yttrium, and the mixed cation amidoboranes.<sup>36–48</sup>

Up to our knowledge, no work has reported the synthesis of BN using amidoboranes as precursors. MAB may offer some advantages over AB as precursors of BN:<sup>49</sup> i) a lower temperature to achieve the conversion due to the lower dehydrogenation temperature; ii) a higher ceramic yield due to lower emission of volatile byproducts; and iii) the role of the metal cation could favor a higher degree of crystallization of BN.<sup>50</sup> Accordingly, the present work selected the lithium (LiAB) and sodium (NaAB)

amidoboranes as a starting point to study them as precursors of BN. These materials were pyrolyzed at different temperatures and they were characterized.

Originally, the intention was to study these materials for both H<sub>2</sub> storage and CO<sub>2</sub> capture. However, due to the sanitary crisis of covid-19, this could not be done. A few preliminary tests for some of the samples showed that they were not able to uptake hydrogen at room temperature (1-100 bar, 25°C). The CO<sub>2</sub> capture was also intended to be analyzed more in depth, however due to technical delays related to the same crisis, we could only perform one set of measurements at 30°C and 1.5 bar. For this reason, this chapter is mostly focused on the characterization of the materials. The results are presented in the following sections.

## 2. Experimental section

### 2.1 Reagents

Commercial AB (NH<sub>3</sub>BH<sub>3</sub>) (Sigma Aldrich, 97%), lithium hydride (LiH) (Sigma Aldrich, 95%) and sodium hydride (NaH) (Sigma Aldrich, dry, 90%) were used as received. AB and the metal hydrides were used to obtain the respective alkali amidoboranes.

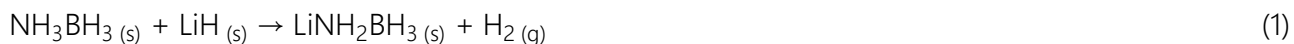
### 2.2 Synthesis

The reagents before synthesis were prepared in an argon-filled glovebox (MBraun M200B, H<sub>2</sub>O ≤ 0.1 ppm; O<sub>2</sub> ≤ 0.1 ppm). A RETSCH PM100 planetary ball mill was used for the mechanochemical syntheses to obtain the alkali amidoboranes.

#### 2.2.1 Synthesis of lithium amidoborane (LiAB)

LiAB was prepared by ball milling under an argon atmosphere. An equimolar mixture of AB (0.168 g) and LiH (0.043 g) was prepared in a stainless-steel reactor, containing 5 stainless-steel balls. The weight ratio of balls ( $R_{ball}$ ) over reactants was set as 100. The reactor was taken outside the glovebox and the mixture was ball milled during 4 cycles consisting of 1 h of milling at 400 rpm and 15 min of

break. After the milling, the reactor was transferred into the glovebox and the sample was recovered. LiAB was then handled and stored into the glovebox. The overall reaction can be written as:



### 2.2.2 Synthesis of sodium amidoborane (NaAB)

NaAB was prepared in a similar way. An equimolar mixture of AB (0.117 g) and NaH (0.091 g) was prepared inside the stainless-steel reactor containing 5 stainless steel balls ( $R_{\text{ball}}=100$ ), in the glovebox. The reactor was closed and transferred to the planetary ball mill, where the mixture was milled for 10 min at 250 rpm. The synthesis of NaAB is faster because NaH presents a higher reactivity towards AB than LiH does. Once the process was finished, the reactor was taken to the glovebox and the product was recovered. NaAB was handled and stored inside the glovebox. The reaction can be written as follows:



## 2.3 Heat treatment

AB, LiAB and NaAB were pyrolyzed at 200, 600, 800 and 1000°C. For the heat treatment at 200°C, the sample was put into a stainless-steel reactor, and transferred to the furnace. The temperature was increased in 20°C every 30 min. Once at 200°C, the temperature was kept for 20 h and then cooled down to room temperature. After, the solid products were recovered and stored in the glovebox

For AB and NaAB, the solid treated at 200°C was used to do the pyrolysis at 600, 800 and 1000°C. LiAB was directly pyrolyzed without a pre-treatment. To perform the pyrolysis, the sample was weighted and put into a ceramic crucible boat inside the glovebox, and then transferred into a closed glass cylinder. The sample was introduced into a tubular furnace and heated under  $\text{N}_2$  atmosphere. The heating ramp was  $1^\circ\text{C min}^{-1}$  starting from room temperature up to the desired temperature. When the required temperature was reached, it was kept for 90 min, and then decreased to room temperature. The sample was recovered and stored in the glovebox for further analyses. Most of the heat treatment at high temperature (600, 800 and 1000°C) were performed by Ms. Rimeh Mighri, PhD

student at the University of Montpellier. It is important to recall that the samples could have entered in contact with air during the process, but efforts were done to avoid this at much as possible. The yield of the samples after heat treatment was calculated by a simple rule of three and is presented in Table 1. The resume of the heat treatment and the reference of each sample is presented in Table 2.

**Table 1.** Yield (wt. %) of the recovered samples after heat treatment.

Sample ↓	Yield			
	200°C	600°C	800°C	1000°C
AB	55 %	51 %	49 %	49 %
LiAB	96 %	83 %	82 %	76 %
NaAB	94 %	56 %	54 %	53 %

**Table 2.** Reference of the samples in function of the heat treatment.

Temperature ↓	Sample name		
	AB	LiAB	NaAB
Pristine	AB	LiAB	NaAB
200°C	AB200	LiAB200	NaAB200
600°C	AB600	LiAB600	NaAB600
800°C	AB800	LiAB800	NaAB800
1000°C	AB1000	LiAB1000	NaAB1000

## 2.4 Characterization

### 2.4.1 Structural characterization

All samples were analyzed by solid-state  $^{11}\text{B}$  Magic Angle Spinning Nuclear Magnetic resonance (MAS NMR). LiAB, NaAB and the pyrolyzed samples were analyzed by  $^7\text{Li}$  and  $^{23}\text{Na}$  MAS NMR, respectively. The NMR spectra were obtained by a spectrometer Varian (VNMRS400, 400 MHz) at 0°C. The

references for boron, lithium and sodium were  $\text{NaBH}_4$  (at -42.1 ppm),  $\text{LiCl}$  (at 0 ppm) and  $\text{NaCl}$  (at 0 ppm) respectively.  $\text{ZrO}_2$  rotors of 3.2 mm of diameter were used. Mr. Emmanuel Fernandez and Mr. Philippe Gaveau from the Platform Balard from the University of Montpellier prepared the samples and performed the NMR analyses.

All the samples were analyzed by Fourier Transformed Infrared (FTIR) spectroscopy by a NEXUS instrument (ThermoFisher) equipped with an attenuated total reflection accessory from 600 to 4000  $\text{cm}^{-1}$  wavelength. To perform the analysis, the samples were put into a closed vial inside the glovebox, transferred to the equipment and then taken out of the vial right before the analysis. The exposure of the samples to air is kept at minimum as possible. The samples were analyzed by Raman Spectroscopy by a Horiba Yvon LabRAM apparatus, equipped with a laser quantum gem 660 nm of 100 mW and an Olympus BX40 microscope. Mr. Eddy Petit performed the analyses of Raman spectroscopy. Powder X-ray diffraction (PXRD) was used to characterize all the samples. A PANalytical X'pert Pro diffractometer in Bragg-Brentano geometry was used. The samples were analyzed over the  $2\theta$  range 20-60°. All the samples were prepared inside the glovebox and they were protected from air by a Kapton film. X-ray photoelectron spectroscopy (XPS) was performed using an ESCALAB 250 (ThermoElectron) equipped with an  $\text{Al-K}_\alpha$  monochromatized source (1486.6 eV), and analyzing an area of 500  $\mu\text{m}$  of diameter. Ms. Valérie Flaud from the Platform Balard from the University of Montpellier did the XPS analyses.

Some of the amidoboranes samples were analyzed by Scanning Electron Microscopy and Energy Dispersive X-ray analysis (SEM and EDX). The SEM analysis was done in a Hitachi S4800 microscope equipped with a secondary and backscattered electron detector. The samples were coated with platinum using an ion sputter coater. A Zeiss EVO HD15 equipped with an Oxford Instrument X-Max<sup>N</sup> SDD detector was used for the EDX analysis. Mr. Didier Cot and Mr. Bertrand Rebiere did the SEM and EDX analyses respectively. Some of the pyrolyzed samples were analyzed by the Brunauer-Emmet-Teller (BET) method to analyze the possible porosity of the samples. A Micromeritics TriFlex equipment was used. The samples were degassed for 15 h at 200°C before the measurements. These analyses were done by Ms. Rimeh Mighri, PhD student at the University of Montpellier. The amidoborane-derived samples treated at 1000°C were analyzed by High Resolution Transmission

Electron Microscopy (HRTEM) using a JEOL 2200 FS microscope (200 kV). This analysis was performed by Mr. Erwan Oliviero from the Platform Balard from the University of Montpellier.

## 2.5 Sorption of CO<sub>2</sub>

The CO<sub>2</sub> sorption measurements were performed in a Sieverts system made in our laboratory. The Sieverts method is useful to determine the uptake of a determined gas by a material. In a typical experiment, a calibrated reference volume is filled with the gas at a known pressure and then it is injected to the chamber where the sample is. The change of pressure in the chamber is measured as a function of time. The equilibrium is reached when the maximum quantity of gas is sorbed, and the quantity of gas taken by the material can be calculated through an equation of state.

The diagram of the system is shown in Figure 1. It is equipped with three pressure controllers (Keller PA-33X, range 0-3 bar, precision of  $\pm 1.5$  mbar) and a temperature sensor (PT100 with a precision of  $\pm 0.15^\circ\text{C}$  at  $30^\circ\text{C}$ ). All the valves and connections are from Swagelok. The system is contained in an incubation hood (Sartorius Certomat HK) which keeps a constant temperature during the measurements. Previous all experiments, the volumes of each part of the apparatus were carefully determined with He gas. For more accuracy during the measurements, the temperature and the pressure are followed at the sample chamber.

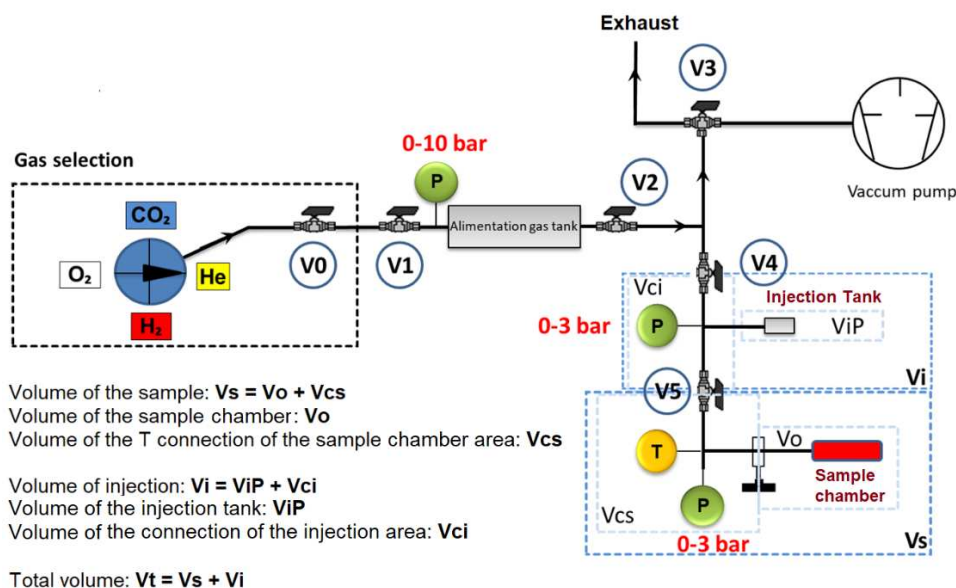


Figure 1. Diagram of the Sieverts system used for the CO<sub>2</sub> sorption experiments.

### 2.5.1 Sorption experiments

Before the first CO<sub>2</sub> sorption measurement, each material was outgassed overnight at 150°C at the Schlenk line. After this, the sample was put into the sample chamber inside the glovebox, and then the chamber was transferred and connected to the Sieverts apparatus. Once in the system, the samples were degassed under vacuum for 5 h at 50°C before each analysis. After this time, the system was cooled down to 30°C and the CO<sub>2</sub> was charged into the injection tank while the sample was kept under vacuum. Once all variables stabilized, the gas was allowed to enter the sample chamber. A software registered the change on the temperature and pressure. All measurements were performed at 30°C and at an initial CO<sub>2</sub> pressure of 1.5 bar. The samples were left under CO<sub>2</sub> atmosphere for a maximum equilibration time of 180 min. The experiments were repeated twice. CO<sub>2</sub> was considered as an ideal gas.

## 3. Results

### 3.1 Preliminary commentaries

As shown in Table 1, the yield obtained from AB at 200°C is 55 wt. %. This is explained by the loss of 2 equivalents of H<sub>2</sub> and the evolution of other gaseous species such as NH<sub>3</sub>, B<sub>3</sub>N<sub>3</sub>H<sub>6</sub> and B<sub>2</sub>H<sub>6</sub>. At higher temperatures, we obtained a yield between 89-93 wt. % with respect to the sample heated at 200°C. This is in good agreement with the expected yield of boron nitride obtained from polyborazylene PB (93-84 wt. %).<sup>51</sup> These yields are expected for PB with a high molecular weight ( $M_w=3000-8000 \text{ g mol}^{-1}$ ). In the case of the LiAB-derived samples, the yield is higher in comparison with AB. This is explained by the suppression of byproducts through the thermolysis and the release of purer H<sub>2</sub>.<sup>52</sup> However, the losses greater than the H<sub>2</sub> content (10.9 wt. %) of LiAB indicate the formation of some of the before mentioned gaseous byproducts, or by the decomposition products formed by parallel reactions. Regarding NaAB, the yields are lower than the ones of LiAB but higher than those of AB. This could be due to a considerable emission of NH<sub>3</sub> along with H<sub>2</sub>.<sup>53</sup> In addition, the boiling point of Na is ~880°C, which can lead to a lower yield at high temperatures. As in the case of LiAB, additional products might form during pyrolysis, causing losses in the yield of this compound.

The density of all pyrolyzed samples were measured by a pycnometer (Micromeritics AccuPyc II 1340). The calibration was done with two metal balls of known volume. All the samples were degassed at 200°C overnight before the analysis.

As we wanted to test our samples for CO<sub>2</sub> sorption, we wanted to confirm the bulk state of the obtained materials. We performed BET analysis for the samples. For some of the samples treated between 200 and 600°C, the equipment could not measure the porosity (due to the lack of pores). For the materials obtained at 800°C, a low value was registered. We stopped the experiments after this pyrolysis temperature. The results of both density and BET measurements are shown in Table 3.

**Table 3.** Density and specific surface area of the pyrolyzed samples derived from AB, LiAB and NaAB.

Sample	$\rho$ (g cm <sup>-3</sup> )	S (m <sup>2</sup> g <sup>-1</sup> )
AB200	1.3	- <sup>a</sup>
AB600	1.6	- <sup>a</sup>
AB800	1.8	- <sup>b</sup>
AB1000	1.4	- <sup>b</sup>
LiAB200	1.00	1
LiAB600	1.4	- <sup>a</sup>
LiAB800	1.6	4
LiAB1000	2.0	- <sup>b</sup>
NaAB200	1.5	2
NaAB600	1.8	- <sup>a</sup>
NaAB800	1.4	10
NaAB1000	1.7	- <sup>b</sup>

<sup>a</sup> Not registered by the device. <sup>b</sup> Experiment not performed.

The LiAB- and NaAB-derived materials treated at 600, 800 and 1000°C were also analyzed by SEM analysis (**Figure 2**). The form of the materials in the bulk state was confirmed. As it shown, only

agglomeration of the materials is observed, and no signs of pores were detected. By the EDX analysis, we found a B/N atomic ratio around 1 on the surface of the materials (Annex I, Figures A1 to A8).

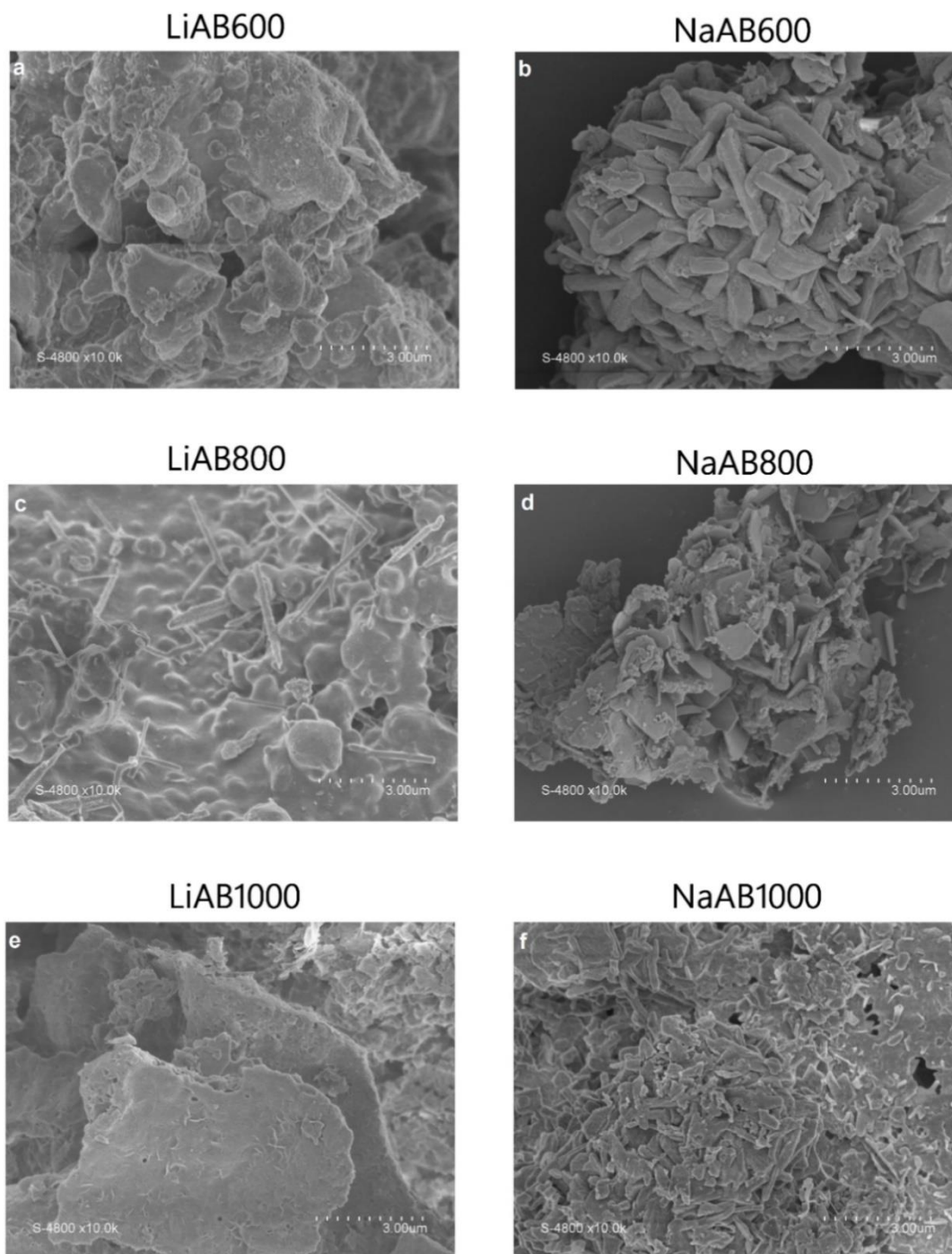


**Figure 2.** SEM images of pyrolyzed samples of LiAB and NaAB at 600, 800 and 1000°C at 10.0k.

## 3.2 Molecular characterization

### 3.2.1 Fourier Transformed Infrared Spectroscopy (FTIR)

Figure 3 presents the FTIR spectra of AB and the pyrolyzed solid products. The spectrum of our commercial AB matches well with the ones reported in the literature.<sup>54</sup>

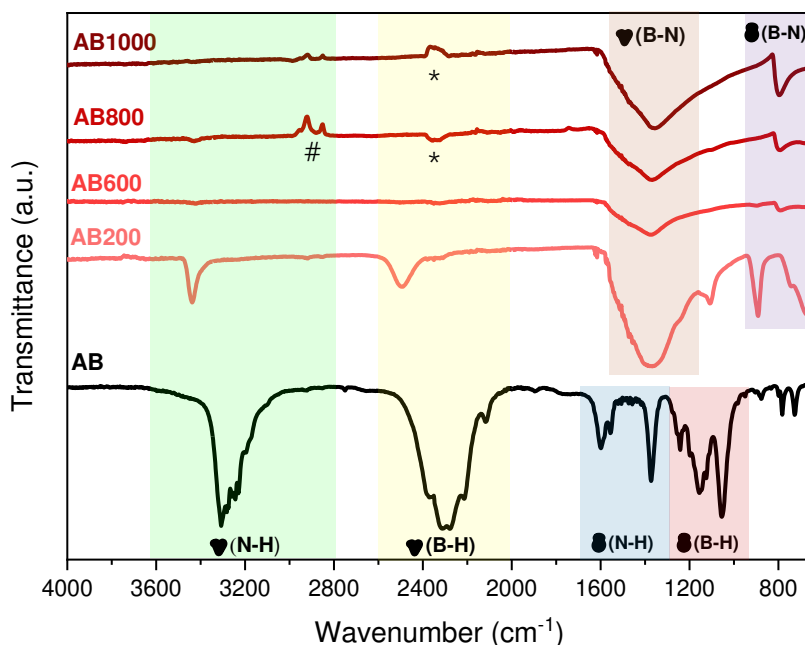


**Figure 3.** FTIR spectra of AB and the products after pyrolysis at 200, 600, 800 and 1000°C. The vibrational bands of interest have been assigned. The signals indicated by \* point the presence of atmospheric CO<sub>2</sub> and by # the KBr film that protects the diamond of the apparatus.

The bands in the range 3100-3500 cm<sup>-1</sup> belong to the N-H stretching modes and the ones centered at 2000-2500 cm<sup>-1</sup> belong to the B-H stretching mode. Deformations of the NH<sub>3</sub> and BH<sub>3</sub> moieties can be seen at 1400-1600 and 1000-1300 cm<sup>-1</sup> respectively. The bands below 800 cm<sup>-1</sup> correspond to the B-N stretching modes. In the case of AB200, the main bands observed at 3500, 2400 and 1500 cm<sup>-1</sup> can be assigned to N-H, B-H and B-N stretching modes respectively, involving  $\pi$  bonded nitrogen and boron atoms.<sup>55</sup> The lower intensity in the N-H and B-H stretching regions, and the

strong band in the B–N region indicate the formation of N- and B-based polymers with formula  $\text{BNH}_x$  ( $x \leq 2$ ).<sup>56</sup> The spectrum is also comparable to the one of polyaminoborane (PAB), polyborazylene (PB) or polyiminoborane (PIB).<sup>51,57,58</sup> All of these products have been found in the thermolytic decomposition of AB (Figure 4).<sup>59–61</sup> At 200°C, the product is likely to be PB and PIB.

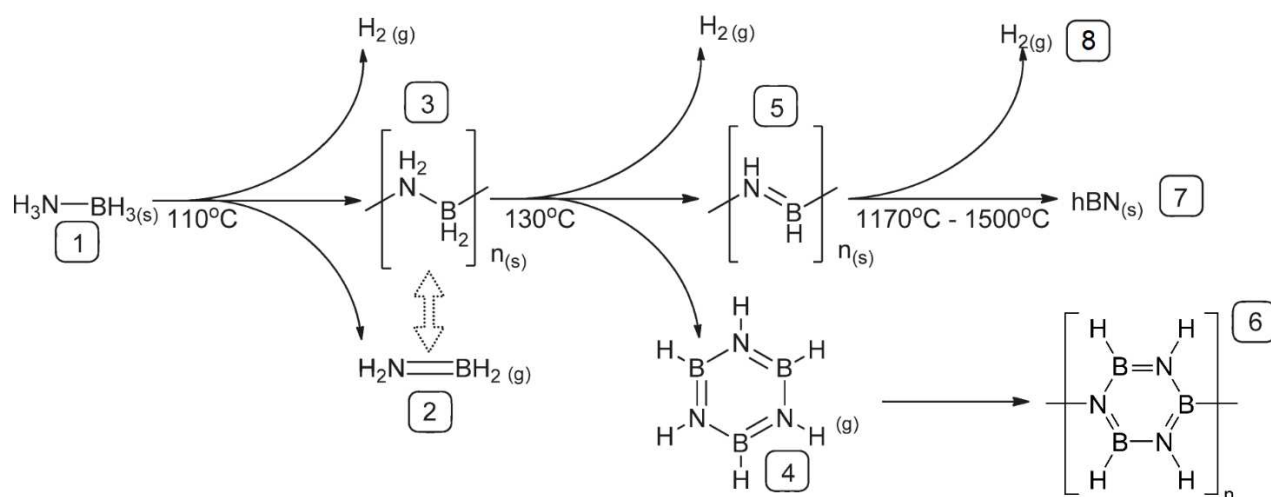


**Figure 4.** Species involved in AB thermal decomposition, adapted from reference <sup>55</sup>. (1) AB (2) molecular aminoborane; (3) Polyaminoborane (PAB); (4) Borazine; (5) Polyiminoborane (PIB); (6) Polyborazylene (PB); (7) semi-crystalline hexagonal boron nitride; (8) hydrogen evolution of molecular hydrogen at high temperature. The reversibility between (2) and (3) is inferred and likely to depend on temperature and chain length of PAB.

The spectra of AB600, AB800 and AB1000 are similar. The stretching bands of N–H and B–H have disappeared, indicating the almost-complete dehydrogenation of the sample. The intensity of the bands at  $\sim 1360$  and  $\sim 790$   $\text{cm}^{-1}$  increases with the increase on the temperature. The spectrum of AB1000 resembles to the one reported for hexagonal boron nitride (h-BN).<sup>62–64</sup> Pure BN presents two characteristics bands: one strong broad band at  $1373$   $\text{cm}^{-1}$  assigned to the B–N stretching vibrations and a second less intense band at  $815$   $\text{cm}^{-1}$  attributed to B–N–B bending vibrations. The differences in the wavenumbers between the spectra of AB1000 and h-BN is associated to differences in the

crystallinity and anisotropy of pure h-BN, as lattice vibrations are expected to be more pronounced in a material with high crystallinity.<sup>55</sup>

The spectra of LiAB and the pyrolyzed samples are shown in **Figure 5a**. LiAB presents a spectrum similar to those reported in the literature.<sup>46,65,66</sup> LiAB shows two main bands assigned to N–H (3000–3500  $\text{cm}^{-1}$ ) and B–H (1800–2500  $\text{cm}^{-1}$ ) stretching vibrations. In comparison with AB, the N–H stretching region is different: the bands are less intense due to the different chemical environment caused by the substitution of one of the protic hydrogens ( $\text{H}^{\delta+}$ ) of the  $\text{NH}_3$  moiety by the  $\text{Li}^+$  cation. The vibrational bending modes of N–H and B–H appear in the ranges 1400–1700 and 1000–1300  $\text{cm}^{-1}$  respectively. The bands observed at  $\sim 800 \text{ cm}^{-1}$  belong to BN–B vibration modes. For LiAB200, the stretching band of the N–H vibration has disappeared. The B–H stretching bands are present, but with a low intensity. The vibration related to B–N stretching starts to appear at  $\sim 1300 \text{ cm}^{-1}$ . This spectrum is comparable to a dehydrogenated LiAB under similar conditions.<sup>52</sup> LiAB600, LiAB800 and LiAB1000 present mainly 2 signals at  $\sim 1350$  and  $780 \text{ cm}^{-1}$  similar to the spectrum of h-BN.

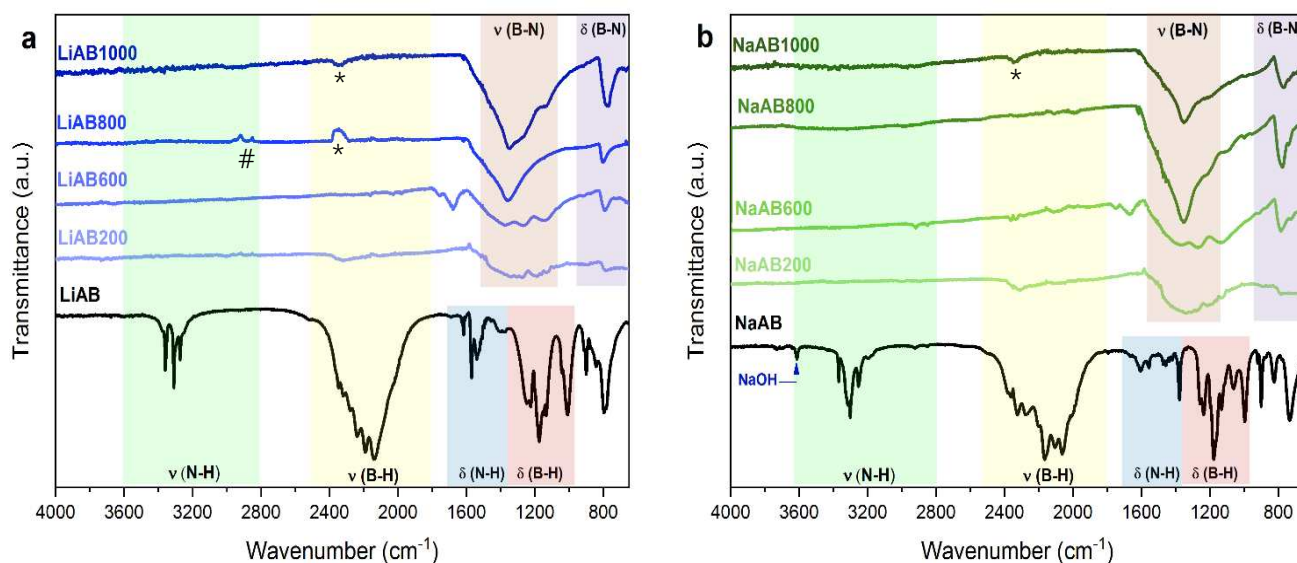


**Figure 5.** FTIR spectra of the alkali amidoboranes and the products after pyrolysis at 200, 600, 800 and 1000°C for a) LiAB and b) NaAB. The vibrational bands of interest have been assigned. The signals indicated by \* point the presence of atmospheric  $\text{CO}_2$  and by # the KBr film that protects the diamond of the apparatus.

Figure 5b presents the spectra of NaAB and the products after pyrolysis. The spectrum of NaAB matches with the ones reported in the literature.<sup>46,65,67</sup> As AB and LiAB, NaAB presents strong bands for the N–H and B–H stretching vibrations in the range of 3100–3500 and 1900–2500  $\text{cm}^{-1}$ . The small signal presented at 3600  $\text{cm}^{-1}$  belongs to impurities of NaOH, formed when the sample is exposed to air during the FTIR measurements. The characteristic bending bands of the N–H and B–H bonds are also present. After the treatment at 200°C, the N–H bands have disappeared. However, the sample presents bands in both B–H stretching and bending regions. This is consistent with other works, where it has been reported the emission of  $\text{H}_2$  and the evolution of  $\text{NH}_3$  during the decomposition of NaAB, indicating an incomplete dehydrogenation of the  $\text{BH}_3$  moiety.<sup>53</sup> As observed for LiAB, the samples treated above 600°C presents two main signals at  $\sim 1350$  and 780  $\text{cm}^{-1}$ , similar to h-BN spectrum.

A comparison between the spectra of the samples treated at the highest temperature and h-BN was made (Figure 6).<sup>68</sup> The samples treated at 1000°C show broader bands in both B–N stretching and bending regions, suggesting the presence of both crystalline and amorphous materials.

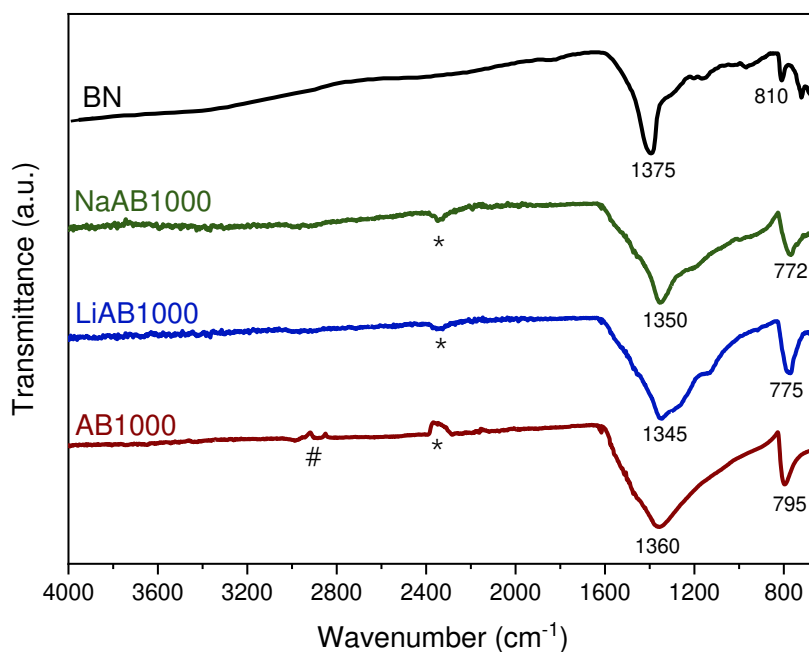


**Figure 6.** Comparison between the spectra of pure boron nitride and the samples pyrolyzed at 1000°C. The signals indicated by \* point the presence of atmospheric  $\text{CO}_2$  and by # the KBr film that protects the diamond of the apparatus.

### 3.2.2 Raman Spectroscopy

AB, LiAB, NaAB and their respective pyrolyzed samples were analyzed by Raman spectroscopy. The spectra of AB and the solid products obtained at different temperatures are shown in Figure 7. The characteristic vibrational modes of AB are indicated in Figure 7a. The spectrum matches well with the ones reported in the literature.<sup>69–71</sup> The N–H stretches are located at high frequencies located at 3254 and 3316  $\text{cm}^{-1}$ , corresponding to the symmetric and asymmetric modes. In the B–H stretching region, two peaks can be located at 2280 and 2381  $\text{cm}^{-1}$ . The bending modes of the N–H bonds are located in 1376 (symmetric) and 1605  $\text{cm}^{-1}$  (asymmetric). The bending vibrational modes of B–H can be seen at 1160 and 1190  $\text{cm}^{-1}$ . Finally, the B–N stretching mode is observed at 780 (asymmetric bending) and 795  $\text{cm}^{-1}$  (stretching).

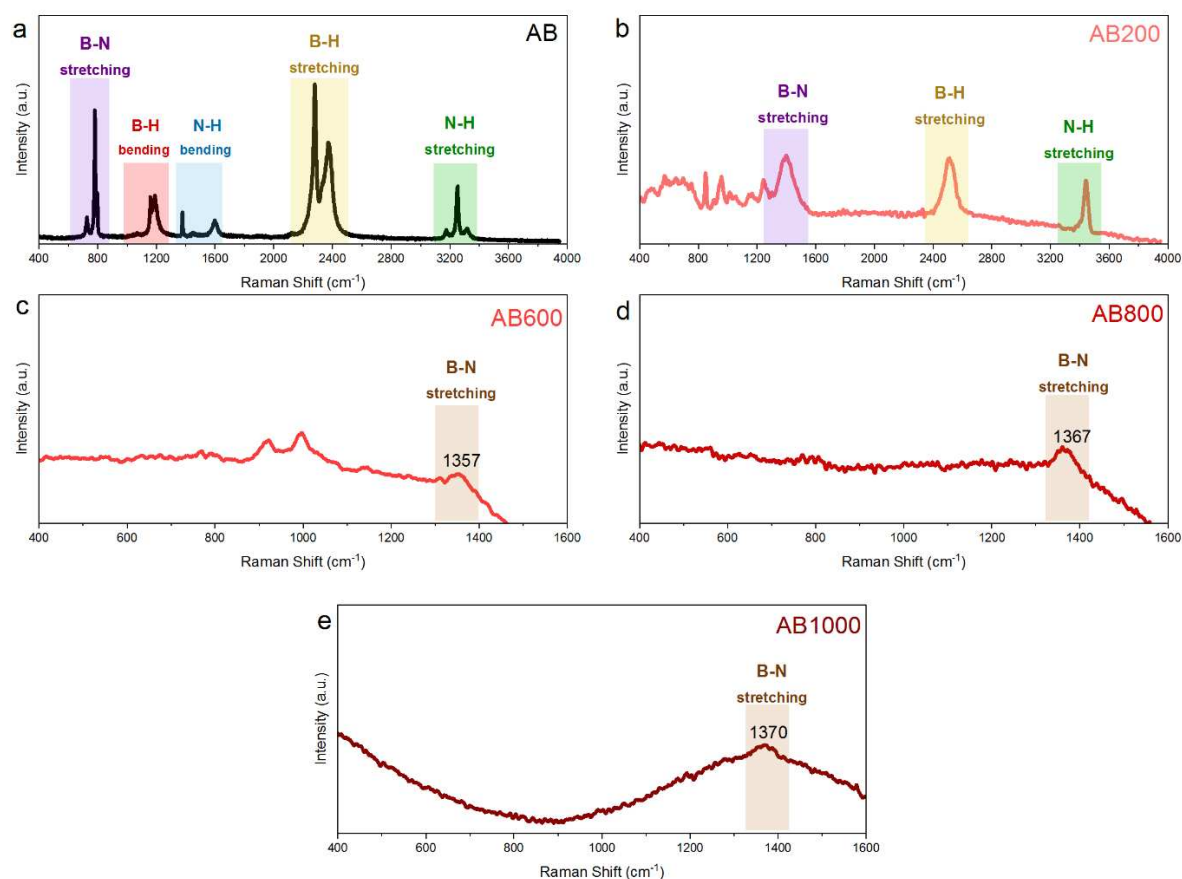


**Figure 7.** Raman spectra of AB at a) room temperature and pyrolyzed at b) 200°C; c) 600°C; 800°C and 1000°C.

Figure 7b shows the Raman spectrum of AB200. The sharp signal of the B–N bond below  $800\text{ cm}^{-1}$  has disappeared. Other signals have appeared below  $1000\text{ cm}^{-1}$ , but they do not belong to this vibrational mode. However, a new broad signal appeared at  $1390\text{ cm}^{-1}$ , that coincides with the stretch of the B–N graphitic-layered in h-BN.<sup>72</sup> Each B–H and N–H stretching bands have merged in a single broad signal, and they have shifted to higher frequencies. These bands are characteristic of NH and BH groups (bonded to a single H atom),<sup>73</sup> indicating the formation of mostly PB. Figure 7c shows two signals at below  $1000\text{ cm}^{-1}$  that belong to B–H, due to an incomplete dehydrogenation. The B–H and N–H bands disappear in Figure 7d and Figure 7e and only a broad signal can be observed at  $\sim 1360\text{ cm}^{-1}$ , belonging to the stretching B–N bond in boron nitride.

The Raman spectra of LiAB, NaAB and their respective products pyrolysis are presented in Figure 8.

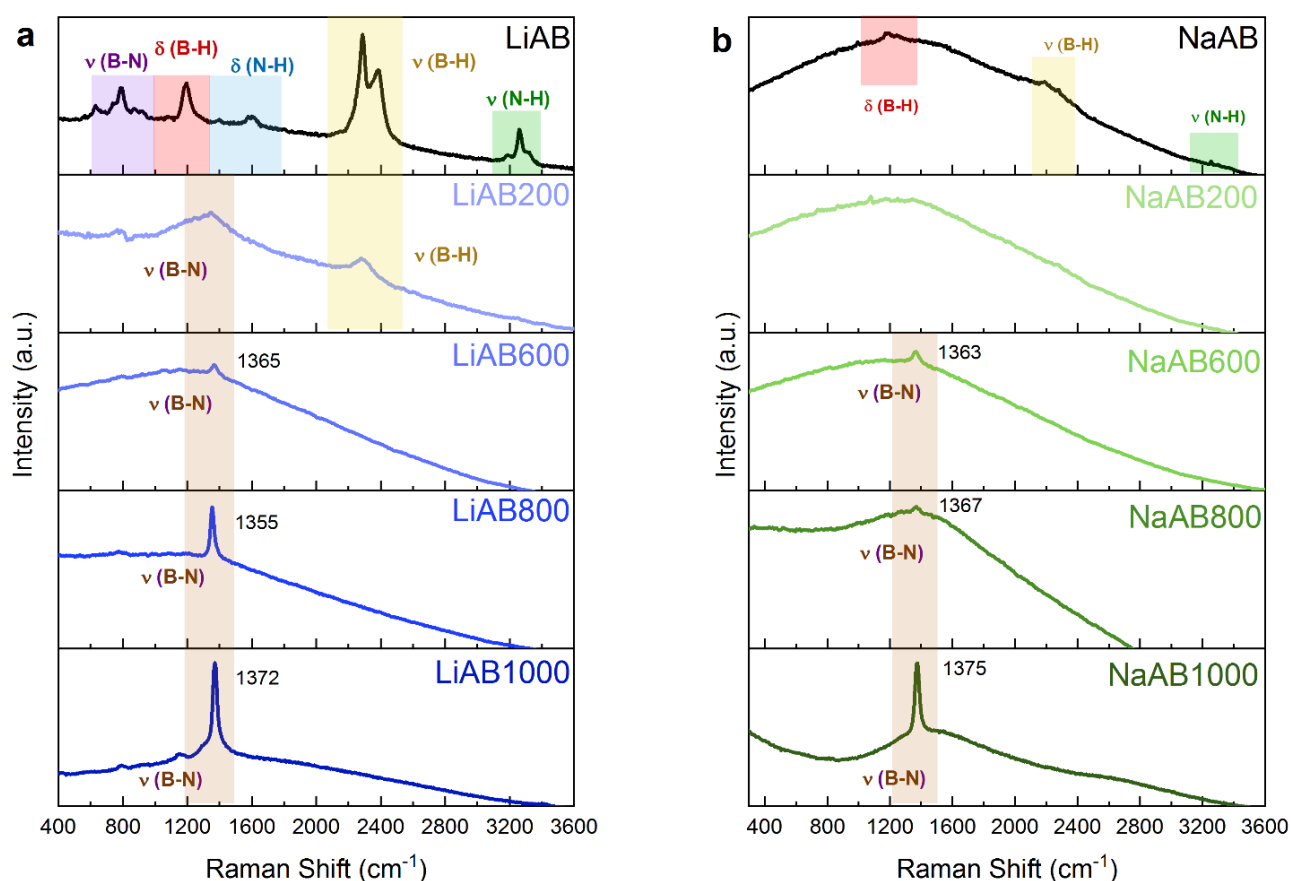


**Figure 8.** Raman spectra of the alkali amidoboranes and the products after pyrolysis at 200, 600, 800 and 1000°C for a) LiAB and b) NaAB. The vibrational bands of interest have been assigned.

The spectrum of LiAB at room temperature resembles the spectra that have been previously reported.<sup>65</sup> The spectrum of NaAB is not clearly seen, though poor intense bands can be observed. This phenomenon happens because the fluorescence of the synthesized NaAB could overlap the measured spectrum.

Regarding LiAB200, the B–H stretching band has merged and appears as one single band that has blueshifted (from 2270 to 2290  $\text{cm}^{-1}$ ). This indicates the evolution from  $\text{BH}_3$  species to BH species. The N–H band has disappeared and a broad signal centered at 1300  $\text{cm}^{-1}$  appeared, like the stretching B–N vibrational mode in boron nitride. On the other hand, the poor intense signals have disappeared for NaAB200. It is likely that species such as  $(\text{LiNBH})_n$  and  $(\text{NaNBH})_n$  have formed, in agreement with the proposed mechanisms for the decomposition of both amidoboranes:<sup>48</sup>



Like AB, the samples of amidoboranes treated at 600, 800 and 1000°C show a single peak in the B–N stretching region associated to h-BN. The peak becomes sharper as the temperature is increased. This characteristic signal (B–N) has been assigned to the  $E_{2g}$  vibrational mode within sheets of hexagonal boron nitride. Back in 1981, Nemanich reported that changes in the Raman spectra of BN is related to the crystals grain size of the sample.<sup>74</sup> There is a correlation between the width broadening (full width at half maximum FWHM) of the peak and the energy of this  $E_{2g}$  mode with the average crystal grain size of h-BN. In other words, when the  $E_{2g}$  mode shifts to higher frequency and the peak broadens, the average crystal grain size of BN nanoparticles decreases. This relationship has been observed in different BN nanostructures.<sup>63,75,76</sup> For example, it has been reported that h-BN microcrystals present a signal at 1367  $\text{cm}^{-1}$  with a FWHM of 13  $\text{cm}^{-1}$  (estimated grain size of 33 nm by Equation 4).<sup>77</sup> In comparison, BN nanothorns and BN nanotubes present a shift to 1370  $\text{cm}^{-1}$  and a FWHM of 28 and 38  $\text{cm}^{-1}$ , with a calculated grain size of 27 and 14 nm respectively.

In the case of AB, the  $E_{2g}$  vibrational mode is seen as a broad signal, probably because of the formation of amorphous BN. For AB600, this signal is centered at 1357  $\text{cm}^{-1}$  and then it shifts to 1367  $\text{cm}^{-1}$  for AB800 and 1370  $\text{cm}^{-1}$  for AB1000. However, in the case of the amidoboranes the  $E_{2g}$  mode starts to appear from 600°C as a sharp peak. In the case of LiAB, there is no clear trend (**Table 4**). The peak is

centered at  $1365\text{ cm}^{-1}$  for LiAB600, it shifts to  $1355\text{ cm}^{-1}$  for LiAB800 and finally it appears at  $1372\text{ cm}^{-1}$  for LiAB1000. However, the FWHM decreases as the temperature increases. Concerning to NaAB, the trend is clear. As the temperature increases, the peak of the  $E_{2g}$  mode shifts towards higher frequencies and the FWHM decreases. The trend seen in the FWHM indicates that for both amidoboranes, when the temperature is increased, the crystallite size does too. The Raman analyses shows that a higher degree of crystallization is achieved at lower temperatures in comparison with AB, and that the alkali cation in the amidoborane plays a role in the crystallization of h-BN, as suggested elsewhere.<sup>76,78</sup> To obtain the average crystallite size, the FWHM was obtained by fitting the  $E_{2g}$  peak with a Lorentzian function and using the relation given by Nemanich:<sup>74</sup>

$$\Gamma_{1/2} = \frac{1417}{L_a} + 8.70 \quad (4)$$

Where  $\Gamma_{1/2}$  is the full width at half maximum of the Lorentzian curve fitting the band and  $L_a$  is the equivalent grain size of the crystal in angstroms.

**Table 4.** Position of the  $E_{2g}$  vibrational mode in the materials, the calculated FWHM and average grain size.

Compound	Raman shift ( $\text{cm}^{-1}$ )	FWHM ( $\text{cm}^{-1}$ )	$L_a$ (nm)
LiAB600	1365	26.9	7.7
LiAB800	1355	24.3	9.1
LiAB1000	1372	23.6	9.5
NaAB600	1363	34.9	5.4
NaAB800	1367	33.6	5.7
NaAB1000	1375	28.3	7.2

### 3.2.3 Powder X-Ray Diffraction (PXRD)

All samples were analyzed by PXRD. The PXRD patterns of AB and the solid products after heat treatment are presented in Figure 9a. The diffraction pattern of commercial AB matches with the one

reported in literature at ambient temperature.<sup>79</sup> The crystal structure of AB has been widely investigated,<sup>54</sup> and at room temperature it has a body-centered tetragonal structure, with a space group  $I4mm$ . AB200 does not present the peaks of neat AB and the formed species are amorphous, confirming the presence of polymeric compounds such as PB. Two broad signals start to appear at  $\sim 26$  and  $\sim 42^\circ$ , with a low intensity. As it is observed from AB600 to AB1000, the intensity of these two broad bands starts to increase. h-BN presents diffraction peaks at  $26.6^\circ$  (002 peak),  $41.5^\circ$ ,  $43.8^\circ$ ,  $50.1^\circ$ ,  $54.9^\circ$  and  $59.3^\circ$ . The sample AB1000 presents broad peaks centered at  $26^\circ$  and  $42^\circ$ , corresponding to the signals of h-BN (Figure 9b). This will be discussed later.

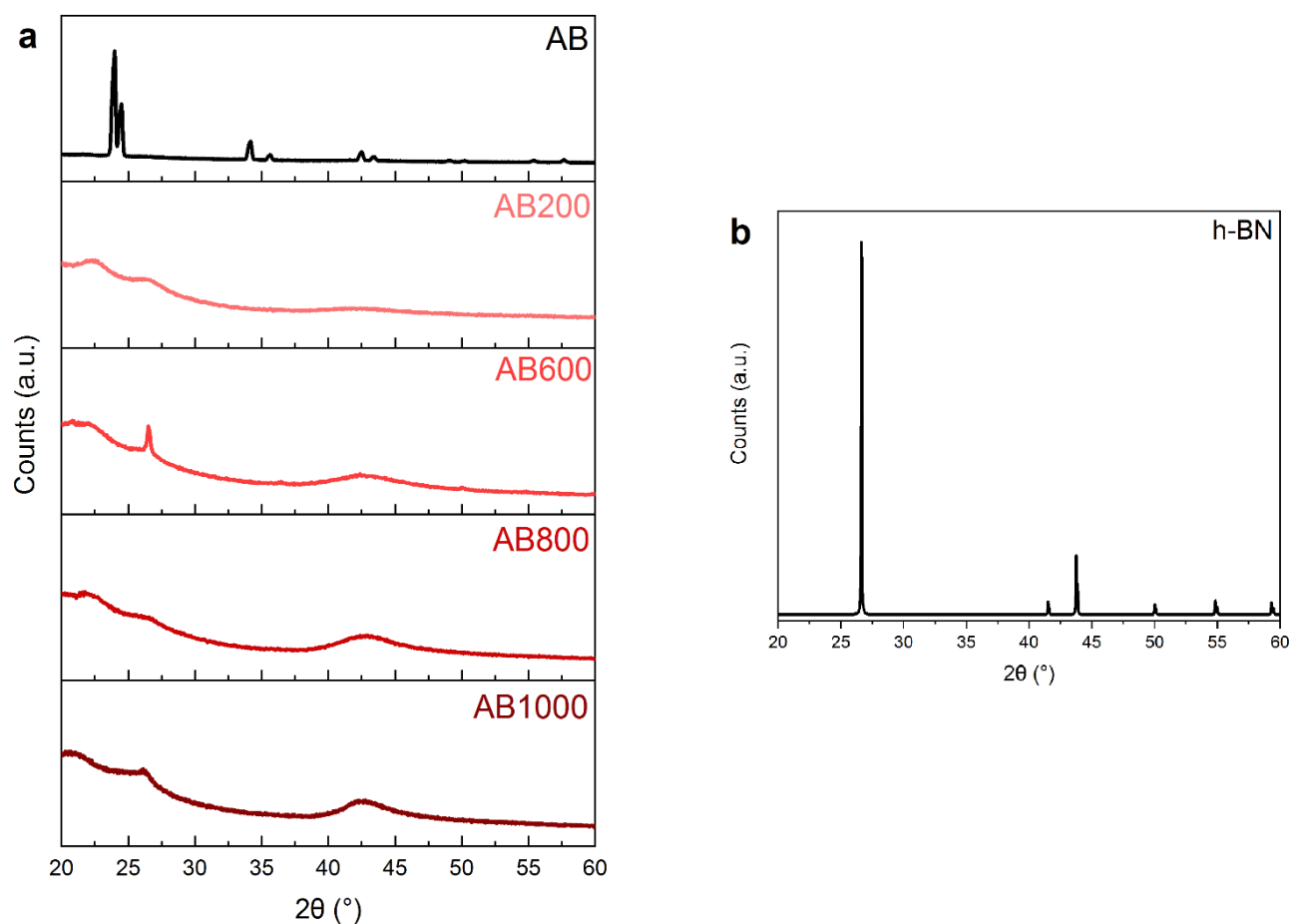


**Figure 9.** PXRD patterns of a) AB and the solid products after pyrolysis at 200, 600, 800 and 1000°C and b) hexagonal boron nitride.

The PXRD patterns of LiAB and the pyrolyzed samples are presented in Figure 10a. LiAB presents two allotropes:  $\alpha$ -LiAB and  $\beta$ -LiAB.<sup>80-82</sup> They present an orthorhombic unit cell with a *Pbca* space group, but the lattice parameters of  $\beta$ -LiAB are almost twice of  $\alpha$ -LiAB. It was reported that the  $\beta$  phase is formed under energetic ball milling and can revert to the  $\alpha$  phase after prolonged milling or by recrystallization.<sup>81</sup> The pattern presented in Figure 10a corresponds to  $\beta$ -LiAB.

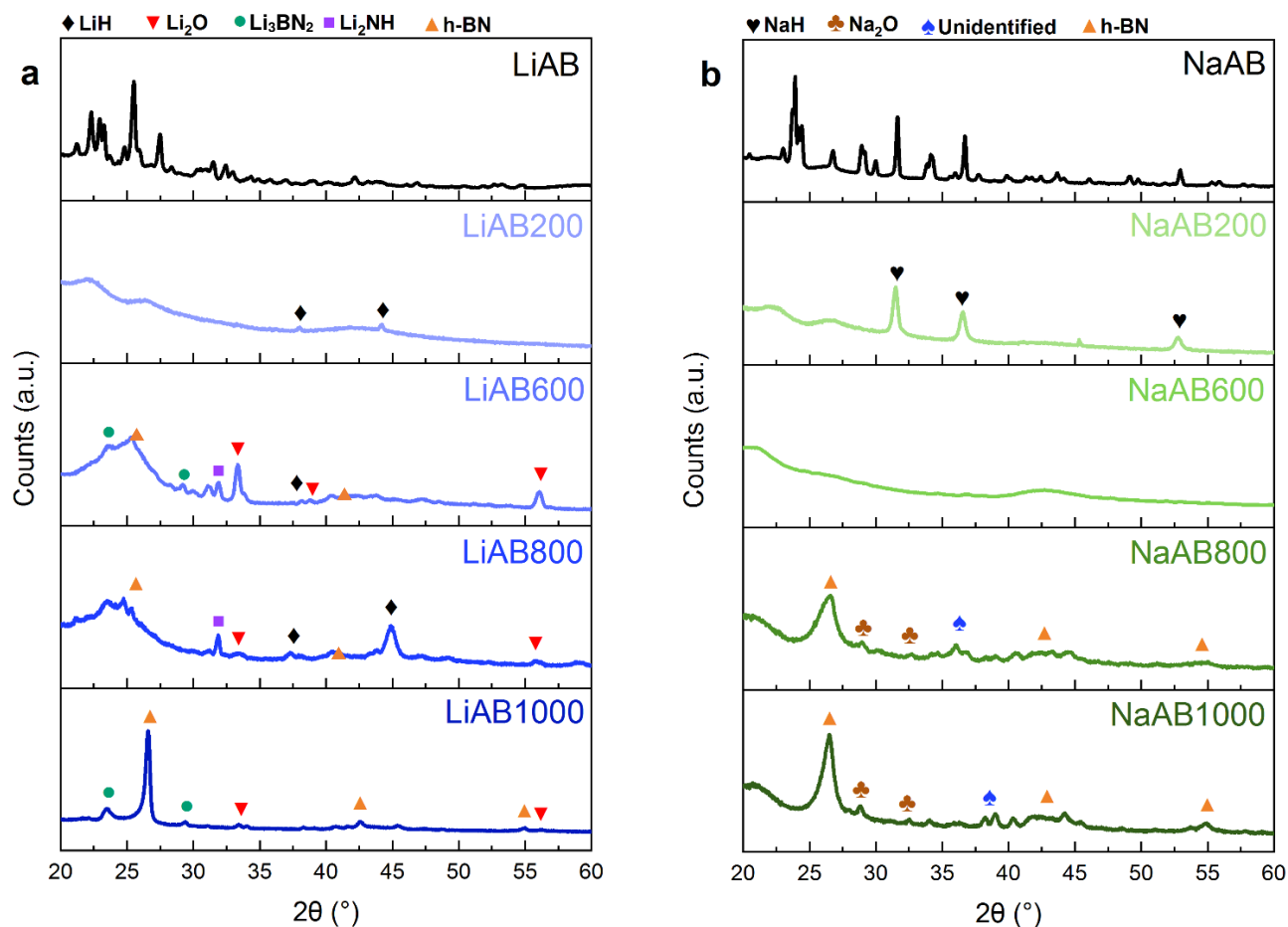


**Figure 10.** PXRD patterns of the alkali amidoboranes and the solids products treated at 200, 600, 800 and 1000°C for a) LiAB and b) NaAB. The possible byproducts are indicated by the colored figures.

LiAB200 does not present any peaks related to the former LiAB. There are two peaks at 38° and 44°, identified as diffraction peaks of LiH (stable up to ca. 720°C).<sup>83</sup> These two small signals can be still

detected for the samples LiAB600 and LiAB800, but they disappear as the other signals become stronger. For LiAB600, LiAB800 and in a minor extent for LiAB1000, other peaks are observed. They have been assigned to possible species that have formed during the pyrolysis of the samples.  $\text{Li}_2\text{O}$  is likely to form if some oxygen entered to the furnace when the sample was introduced, or by impurities in the gas stream.  $\text{Li}_2\text{NH}$  is likely to form between 300 and 450°C, and it is stable up to 750°C, when it can decompose following Equation 5.<sup>84</sup> Some of the metallic lithium could react to form  $\text{Li}_3\text{N}$  (Equation 6), and further interact with the BN-like structures to form  $\text{Li}_3\text{BN}_2$ ,<sup>78</sup> identified by the peaks centered at  $\sim 25^\circ$  and  $\sim 28^\circ$ .



The diffraction pattern of NaAB and the treated samples at different temperatures are shown in Figure 10b. The NaAB patterns matches well with the ones reported in the literature.<sup>67,85</sup> The presence of unreacted NaH is a recurrent problem in the synthesis of NaAB.<sup>67,85</sup> NaAB200 is clearly amorphous, with the exception of the peaks of NaH that are clearly seen. Unlike LiAB600, NaAB600 does not show diffraction peaks. In fact, the pattern is more similar to the one of AB600. However, at 800°C, the sample starts to show some diffraction peaks. Finally, at 1000°C the characteristic diffraction peaks of h-BN at 26, 42 and 55° can be observed. The other peaks present in the pattern were assigned to  $\text{Na}_2\text{O}$  and to an unidentified phase. For the latter, it is possible that some intermediates can form before the complete evolution of the sample to BN. For example, when a mixture of  $\text{NaNH}_2$  and  $\text{NaBH}_4$  is heated at 220°C,  $\text{Na}_2\text{BNH}_6$  is formed, which would dehydrogenate to form  $\text{Na}_3\text{BN}_2$  at 600°C. Between 680 and 1100°C,  $\text{Na}_3\text{BN}_2$  decomposes following the next reaction:<sup>86</sup>



For a better comparison, the respective diffraction patterns of the samples treated at the highest temperature were analyzed (Annex I, Figure A 9). In the case of AB, the relatively low intensity and the broadening of the peaks centered at 26° and 42° implies the formation of thin BN layers and weaker stacking.<sup>87</sup> Besides, the shift of the 26° peak to lower angles, and the merge of the peaks centered at 42° indicate that the BN phase is poorly crystallized and might present a turbostratic phase,

characterized by graphitic layers stacked nearly parallel with a random orientation.<sup>44,88–90</sup> Turbostratic boron nitride (t-BN) can be seen as an intermediate between h-BN and amorphous BN; in the past years has received attention due to its properties, such as polymer-like time-dependent deformation characteristics, a wide band gap of 6.0 eV and the incomplete crystallinity.<sup>91–93</sup>

LiAB1000 and NaAB1000 present the peaks associated to h-BN at 26°, 42°, 55° and 75°.

Table 5 shows the interlayer lattice  $d$ , the FWHM and the crystallite size  $D$  calculated for the peak centered at 26° for LiAB1000 and NaAB1000, calculated by Equation 8 and by Equation 9 (Scherrer equation).

$$d = \frac{\lambda}{2\sin\theta} \quad (8)$$

$$D = \frac{0.9\lambda}{\beta\cos\theta} \quad (9)$$

Where  $d$  is the distance between adjacent layers (in nm),  $\lambda$  is the X-ray wavelength (0.154 nm),  $\theta$  is the diffraction angle (radians),  $D$  is the crystallite size (nm) and  $\beta$  is the FWHM (radians).

**Table 5.** Diffractogram data for the (002) peak in LiAB1000 and NaAB1000.

Sample	Reflection	2 $\theta$ (°)	$d$ (Å)	FWHM (°)	$D$ (nm)
LiAB1000	(002)	26.54	0.335	0.3609	21.1
NaAB1000	(002)	26.48	0.336	0.8470	9.6

The interlayer layer distance for both samples has a close value to the theoretical one calculated for a well crystallized boron nitride (0.333 nm).<sup>78,94</sup> LiAB1000 and NaAB1000 were also analyzed by HRTEM (**Figure 11** and **Figure 12**). The results obtained are in good agreement with the PXRD results. The interlayer lattice ( $d$ ) for LiAB1000 was estimated as an average value of 0.344 nm, while the average value for NaAB1000 is 0.343 nm. According to the Selected Area Electron Diffraction pattern, both samples are polycrystalline. NaAB1000 showed different size of crystals, ranging from small crystals of

~17 nm up to larger crystals of more of 30 nm. In concordance with the Raman spectroscopy analyses, this confirms that the alkali cations ( $\text{Li}^+$  and  $\text{Na}^+$ ) play a role in the crystallization of h-BN during the pyrolysis of the amidoboranes at lower temperatures than neat AB or PB.

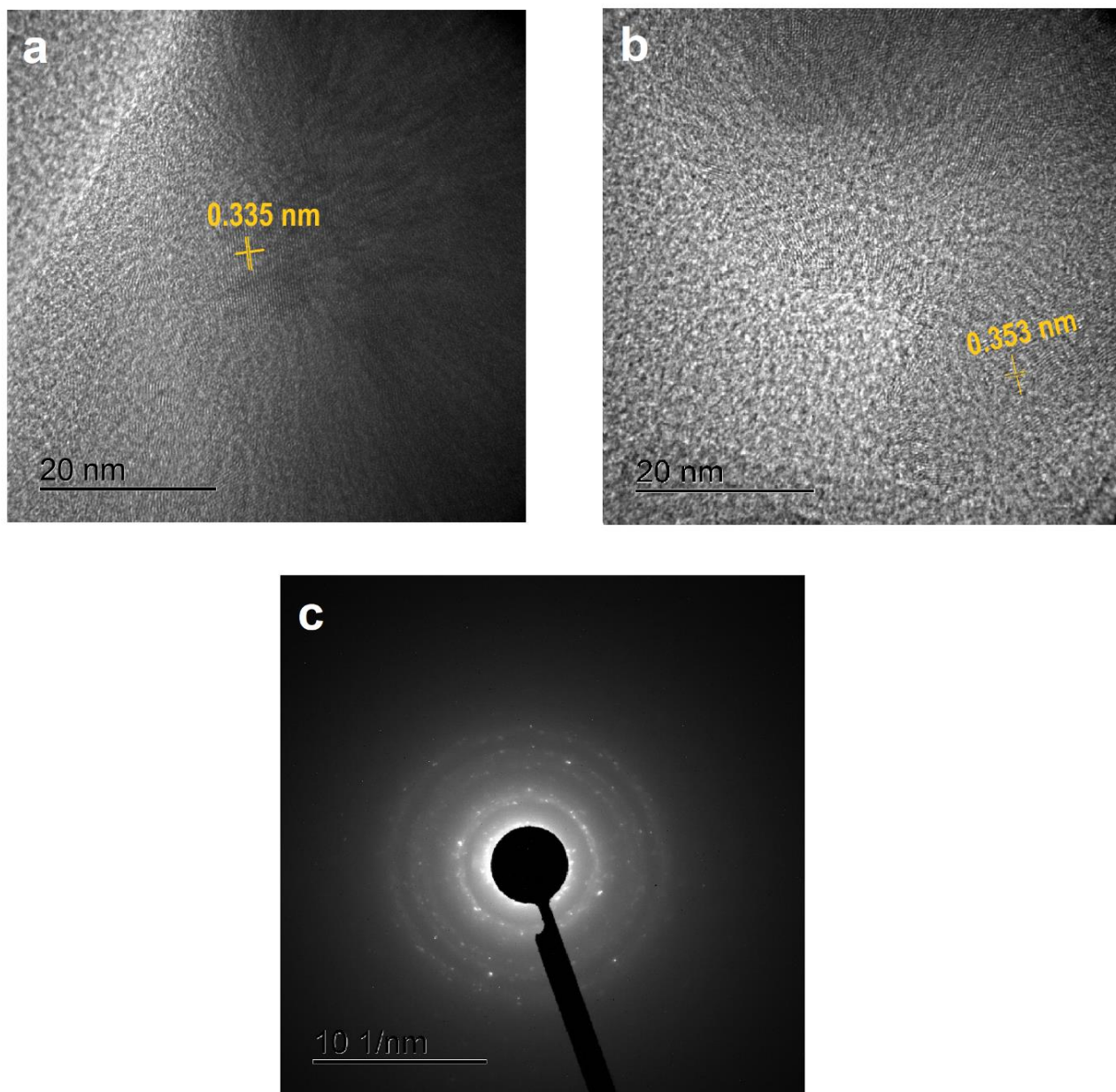


**Figure 11.** a,b) HRTEM images of LiAB1000 showing the interlayer distance and c) selected area electron diffraction showing a polycrystalline solid.

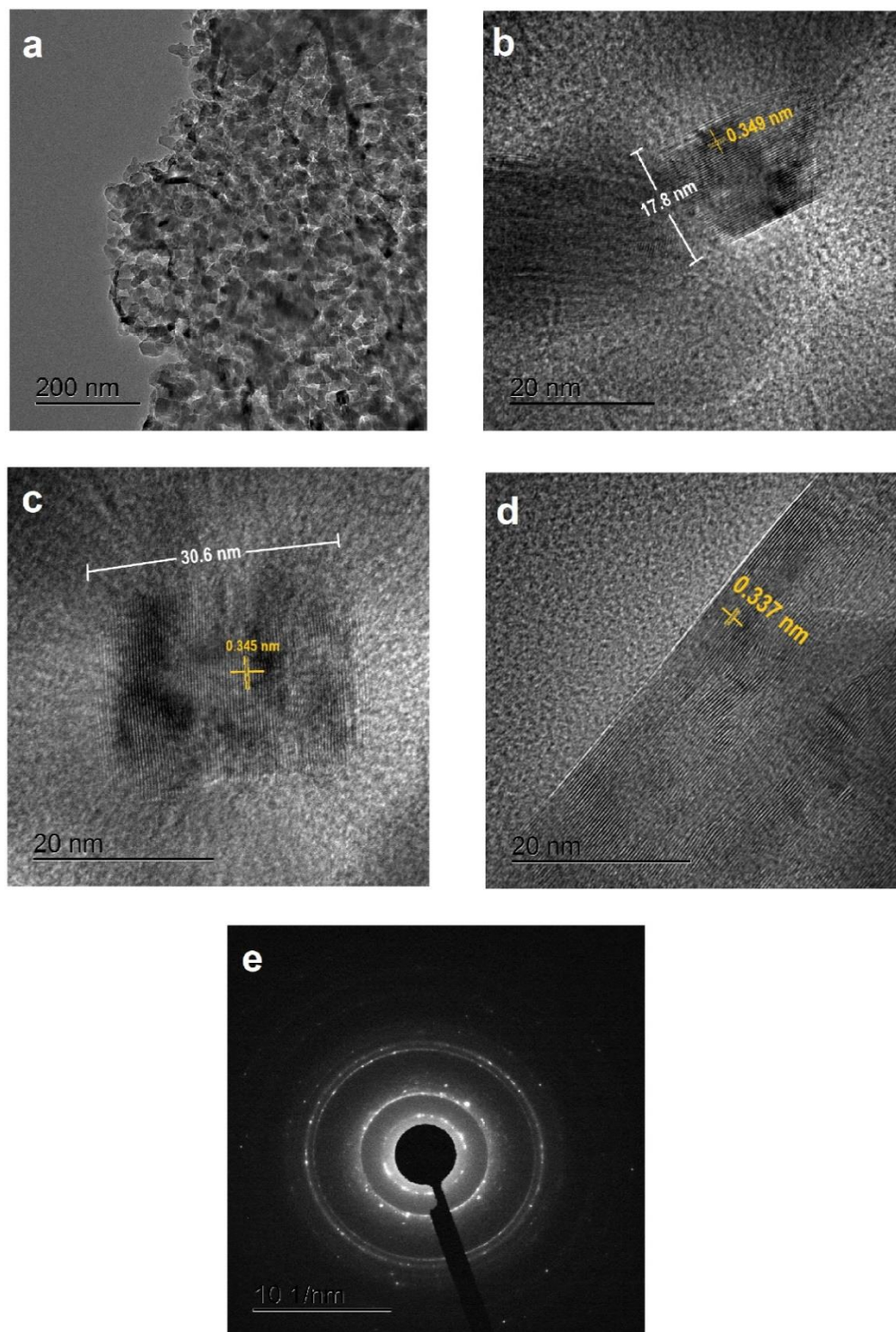


**Figure 12.** a) Multiple crystals in a particle of NaAB1000; b), c), d) crystals of different size and interlayer distances and e) selected area electron diffraction of NaAB1000 showing a polycrystalline composition.

### 3.2.4 Magic Angle Spinning Nuclear Magnetic Resonance (MAS NMR)

$^{11}\text{B}$  MAS NMR analyses were performed on all samples. **Figure 13** presents the  $^{11}\text{B}$  MAS NMR spectra of AB and the solid products after pyrolysis. AB shows a single split-shaped signal at -26 ppm due to the quadrupolar effect of the boron atom.<sup>95,96</sup> The peak corresponds to a chemical environment  $\text{NBH}_3$ .

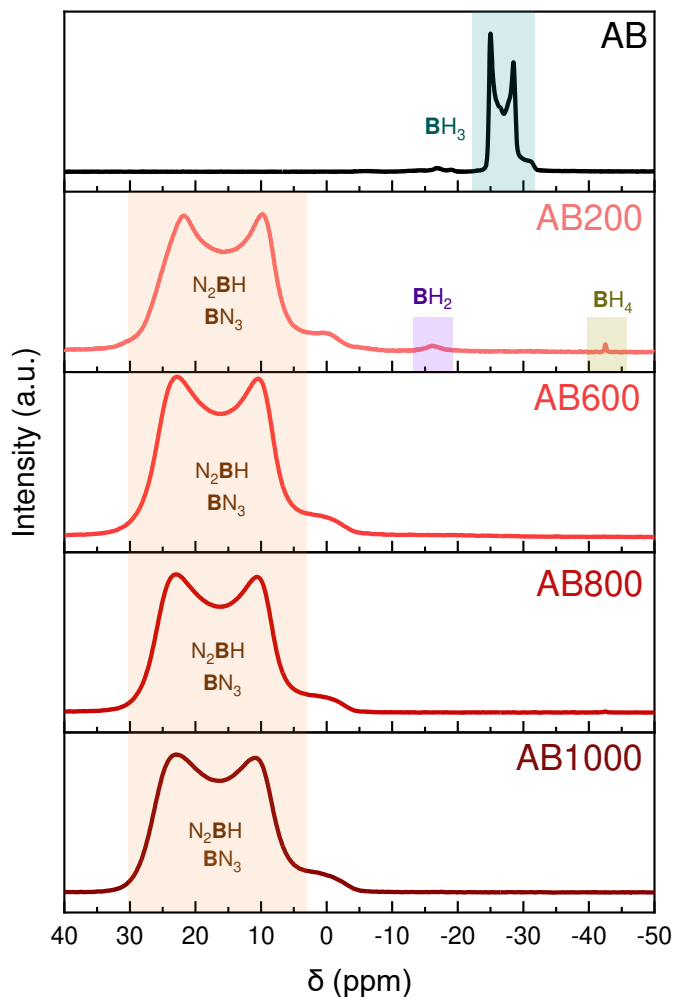


**Figure 13.**  $^{11}\text{B}$  MAS NMR spectra of AB and the solid products heated at 200, 600, 800 and 1000°C.

The chemical environments have been assigned in the colored squares.

In the case of AB200, the environment belonging to  $\text{NBH}_3$  has completely disappeared. Three new signals arise. In the negative chemical shifts (tetra-coordinated boron  $\text{B}^{\text{IV}}$ ), two signals are present at

-42 and -16 ppm. These peaks are assigned to  $\text{BH}_4$  and  $\text{N}_2\text{BH}_2$  environments. The broad peak of the  $\text{N}_2\text{BH}_2$  environment indicates that polymerization reactions took place at this temperature and suggests the presence of the ion pair diammoniate of diborane DADB ( $[\text{H}_3\text{NBH}_2\text{NH}_3]^+[\text{BH}_4]^-$ ), DADB-ionic like species (i.e.  $[\text{NH}_3\text{BH}_2\text{NH}_2\text{BH}_2\text{NH}_3]^+[\text{BH}_4]^-$ ) or PAB.<sup>97-101</sup> In the positive chemical shifts (tri-coordinated boron  $\text{B}^{\text{III}}$ ), a broad double shaped signal is observed. Several studies have reported the presence of such signal at above 200°C in the decomposition of AB of B- and N-based polymers,<sup>102-106</sup> and it indicates  $\text{BN}_3$  and  $\text{N}_2\text{BH}$  environments, such as PB. From AB600, all the  $\text{B}^{\text{IV}}$  environments have disappeared, and the signal at positive chemical shifts broadens, and it resembles to the pyrolyzed spectra of PB and boron nitride.<sup>106</sup> The chemical environments assigned for this signal are  $\text{BN}_3$  and  $\text{N}_2\text{BH}$ . As the temperature of pyrolysis is high (>600°C), the major part of the hydrogen should have been released and we should expect a major presence of the  $\text{BN}_3$  species.

The  $^{11}\text{B}$  MAS NMR spectra of LiAB and the solid products at the different temperatures are presented in **Figure 14a**. The synthesized LiAB shows a single peak at -21 ppm, corresponding to a  $\text{NBH}_3$  environment.<sup>48,107</sup> A small signal at -9 ppm indicates the probable evolution of the sample during the MAS NMR analysis that we have observed systematically in our works. In the case of LiAB200, there are four main signals in the spectrum. The two signals at  $\text{B}^{\text{IV}}$  chemical shifts centered at -9 and -42 ppm belong to  $\text{N}_2\text{BH}_2/\text{N}_3\text{BH}$  and  $\text{BH}_4$  environments, respectively. The  $\text{N}_3\text{BH}$  environment might indicate the formation of a compound close to the formula  $\text{LiNBH}_{1.4}$ , reported elsewhere.<sup>108</sup> Regarding the  $\text{N}_2\text{BH}_2$  and  $\text{BH}_4$  species, structures analogues to DADB have been reported by computational studies in the case of amidoboranes.<sup>109</sup>  $\text{LiDADB}$  ( $[\text{LiNH}_2\text{BH}_2\text{LiNH}_2]^+[\text{BH}_4]^-$ ) might explain the appearance of both signals. However, we do not discard the formation of  $\text{LiBH}_4$  that can have a contribution for the peak centered at -42 ppm. On the other hand, the broadening of the  $\text{NBH}_3$  peak (-22 ppm) indicates an amorphization of the species,<sup>110</sup> in concordance with the PXRD pattern of LiAB200. Coiled polymers such as  $\text{LiNH}_2\text{BH}_2\text{LiNHBH}_3$  may be the source of the signal.<sup>109</sup> In the  $\text{B}^{\text{III}}$  area, a characteristic quadrupolar line shape is seen and can be assigned to  $\text{N}_2\text{BH}$  and/or  $\text{N}_3\text{B}$  species.<sup>102,103</sup> This peak is the only signal present in the spectra of LiAB600, LiAB800 and LiAB1000. However, one might notice that the shape of the signal evolves when the temperature is increased (is more symmetric at higher temperatures). In concordance with the previous analyses, this signal indicates the presence of BN.

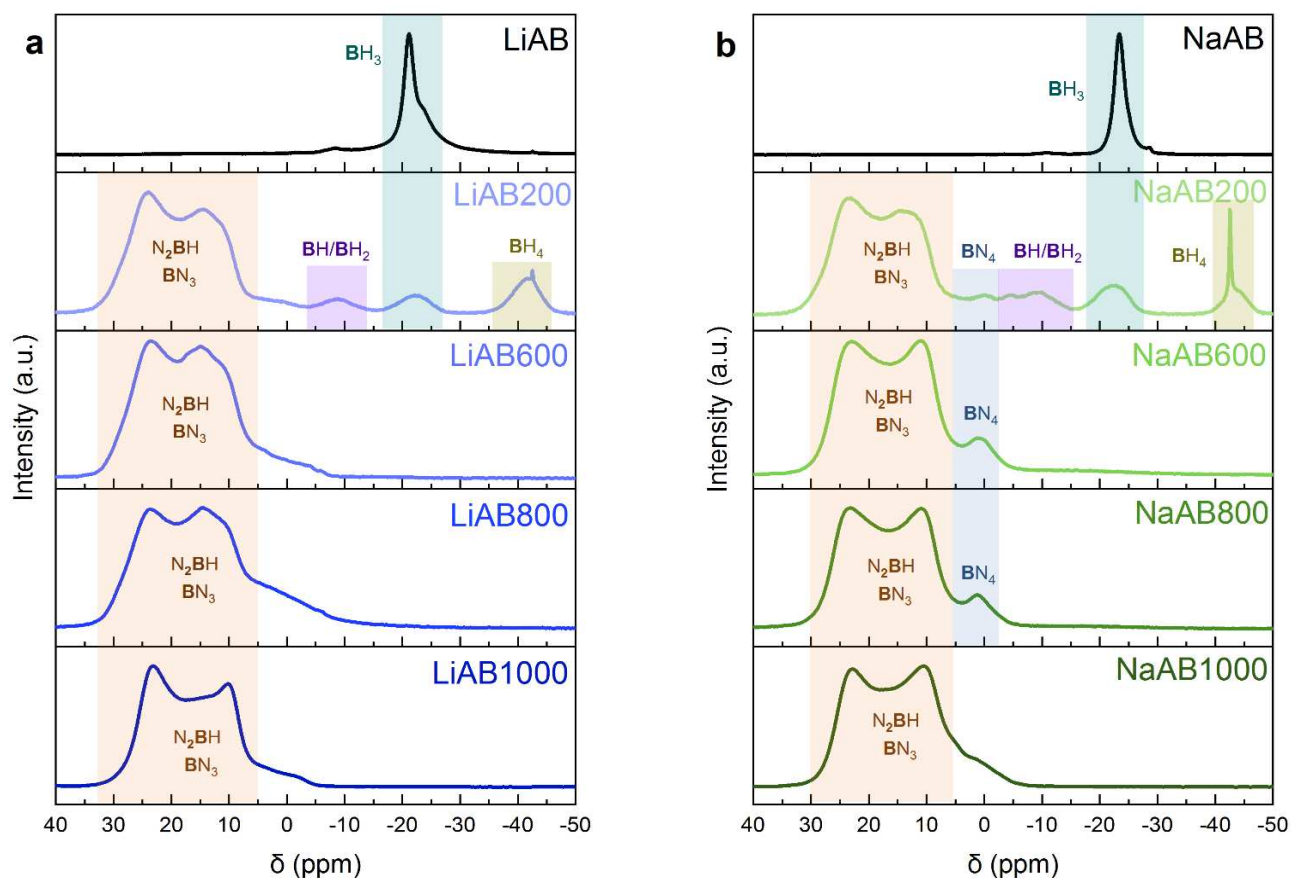
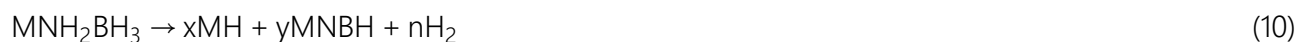


**Figure 14.**  $^{11}\text{B}$  MAS NMR spectra of the alkali amidoboranes and the solid products pyrolyzed at 200, 600, 800 and 1000°C for a) LiAB and b) NaAB. The chemical environments have been assigned in the colored squares.

The spectra of NaAB and the solid products after pyrolysis is shown in **Figure 14b**. NaAB has a single peak centered at -23 ppm indicating the boron site  $\text{NBH}_3$  of the amidoborane.<sup>46,48</sup> The pyrolyzed samples of NaAB present a similar behavior than the ones of LiAB. The  $\text{NBH}_3$  peak has broadened for NaAB200, indicating an amorphization of the compound.<sup>111</sup> Two new signals in the  $\text{B}^{\text{III}}$  area of the spectrum appears (from 0 to -12 ppm) and they belong to  $\text{N}_2\text{BH}/\text{NBH}_2$ . A  $\text{BH}_4$  environment is also present with a peak at -43 ppm indicating the formation of a Na-containing DADB-like species, such as  $[\text{NaNH}_2\text{BH}_2\text{NaNH}_2]^+[\text{BH}_4]^-$ .<sup>109</sup> The signal at  $\text{B}^{\text{III}}$  sites belongs to  $\text{BN}_3/\text{N}_2\text{BH}$  species. This signal is the principal at higher temperatures and the double shape characteristic of the quadrupolar effect in the boron atom is more defined from 600°C. For NaAB600 and NaAB800, the signal at 1 ppm indicates

the presence of a  $\text{BN}_4$  or  $\text{BN}_x\text{O}_y$  environment. It has been observed that the decomposition of alkali amidoboranes follows a similar path and a general formula was proposed:<sup>110</sup>



Where the amorphous MNBH phase is formed by the polymerization of  $\text{M}^+[\text{NH}_2\text{BH}_3]^-$  molecules, that will finally form a composite of  $\text{MH}+\text{BN}$  if the amidoborane is completely dehydrogenated.<sup>35,110–112</sup>

A quantitative analysis of the  $^{11}\text{B}$  MAS NMR was carried out, in order to observe the evolution of boron environments (Annex I, Figure A 10). For AB, almost all the  $\text{NBH}_3$  environment (99 %) has been transformed into tri-coordinated boron at 200°C. Only a small fraction of  $\text{BH}_4$  and  $\text{N}_2\text{BH}_2$  is present (0.7 and 0.3 % respectively). This points again that the resulting compound is mostly PIB or PB. The  $\text{B}^{\text{III}}$  signal remains up to 1000°C, in agreement with the two-step dehydrogenation of AB.<sup>55,113</sup>

Regarding LiAB, 86 % of the sample have transformed to  $\text{B}^{\text{III}}$  species at 200°C. The  $\text{BH}_4$  species are present in an 8 %. As the  $\text{N}_2\text{BH}_2$  is present in 2.1 %, the formation of a DADB-analogue species is confirmed. The higher proportion of  $\text{BH}_4$  suggests the presence of amorphous  $\text{LiBH}_4$  (as the PXRD pattern of LiAB200 did not show any peaks belonging to the borohydride). From 600°C, the only environment present is the  $\text{B}^{\text{III}}$  species. A tentative reaction is proposed and it can occur at high temperature (Equation 11).<sup>110</sup> This would also explain the  $\text{Li}_2\text{NH}$  peaks identified in the PXRD analyses.



For NaAB200, 76 % of the species have converted to  $\text{B}^{\text{III}}$  species. The percentage of  $\text{BH}_4$  species in NaAB (5.7 %) is lower in comparison with LiAB. However, the quantities of  $\text{NBH}_3$  and  $\text{N}_2\text{BH}_2/\text{N}_3\text{BH}$  are higher than for LiAB (7 and 11.3 % vs. 3.8 and 2.1 %). This might indicate the presence of more branched structures to compensate the  $\text{NBH}_3$  species.<sup>110</sup> There are some differences in the percentages obtained in this work and the ones reported in the literature.<sup>110,111</sup> This suggests that the conditions of heat treatment have an impact in the final composition of the pyrolyzed products. In order to have a better overview in the possible formed species during the pyrolysis of AB, LiAB and NaAB, a recapitulative of proven and suggested compounds found in the literature is presented in **Figure 15**, according to the different chemical environments detected in the  $^{11}\text{B}$  MAS NMR analyses.

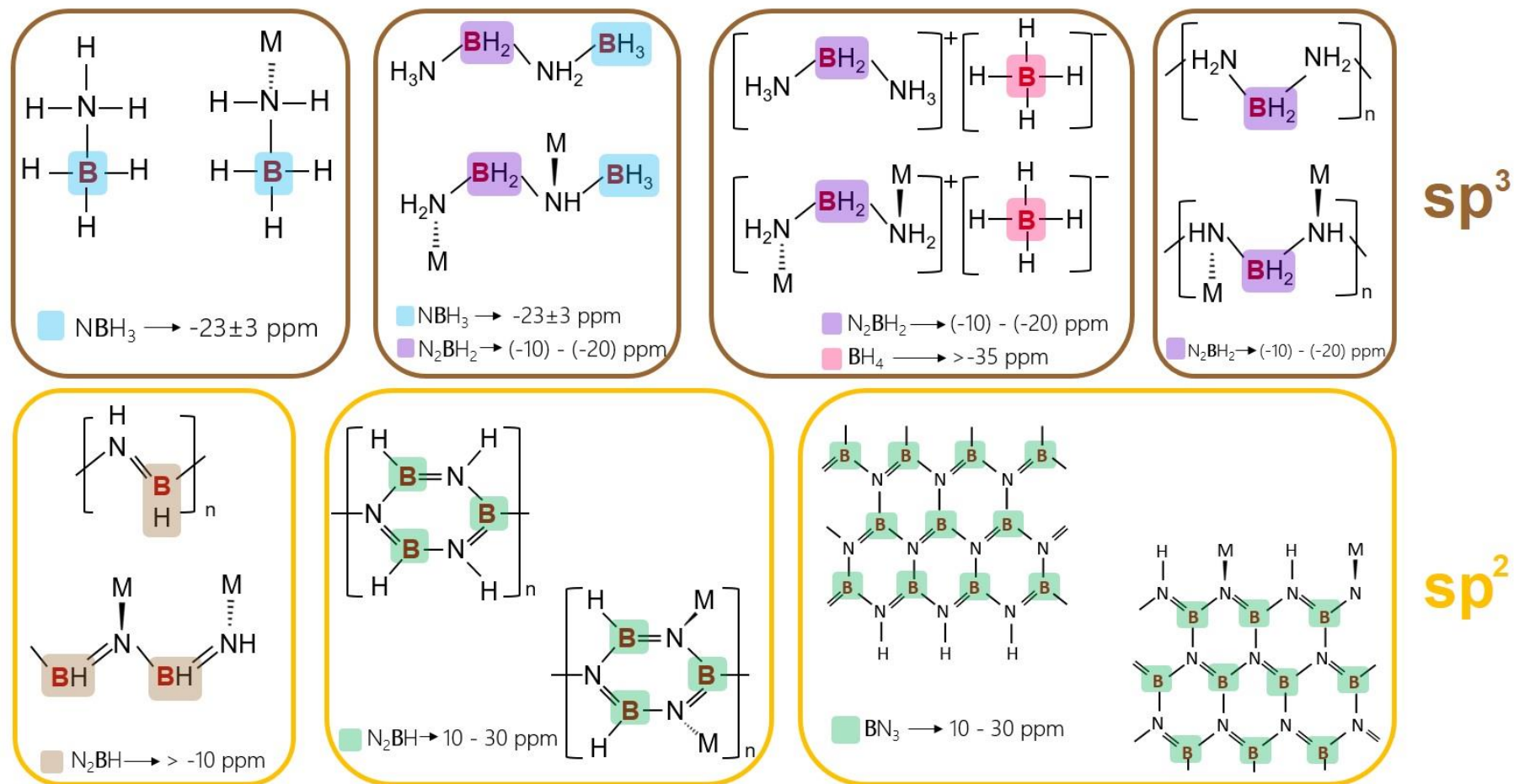


**Figure 15.** Possible compounds formed during the decomposition of AB, LiAB and NaAB ( $M = \text{Li}, \text{Na}$ ) according to the  $^{11}\text{B}$  MAS NMR spectra and reported in the literature.<sup>35,55,103,104,109,114–118</sup> The brown squares indicate a  $sp^3$  hybridization of the B atom ( $\text{B}^{\text{IV}}$ ) and the yellow ones, a  $sp^2$  hybridization ( $\text{B}^{\text{III}}$ ). The boron environments are indicated in colored squares: blue for  $\text{NBH}_3$ , purple for  $\text{N}_2\text{BH}_2$ , red for  $\text{BH}_4$ , brown for linear  $\text{N}_2\text{BH}$  and green for cyclic  $\text{N}_2\text{BH}$  or  $\text{BN}_3$ .

### 3.2.5 X-Ray Photoelectron Spectroscopy (XPS)

The pyrolyzed samples of AB were analyzed by XPS and the spectra for B 1s and N 1s are shown in Figure 16. The B 1s spectra for every compound was deconvoluted in two signals (Figure 16a). The peak at 190.2 eV in AB200 is assigned to a B–N bonding in disordered BN,<sup>119</sup> and the shift of this peak to higher energies is an evidence of the formation of h-BN,<sup>120</sup> in agreement with the PXRD analyses. The second peak is assigned to  $B_xN_yO_z$  species.<sup>121–124</sup> The peak related to  $B_xN_yO_z$  has been reported before and is attributed to an substitutional oxygen in the place of a nitrogen atom. The shift of the binding energy might depend on the atoms bonded to boron (i.e.  $BNO_2$  or  $BN_2O$ ).<sup>124,125</sup> However, we do not know if the oxygen comes from impurities during the pyrolysis or while performing the XPS analyses. The latter can happen because the samples are handed over 3 days before the analysis; besides, we are not aware if the samples were strictly handled under inert atmosphere all the time.

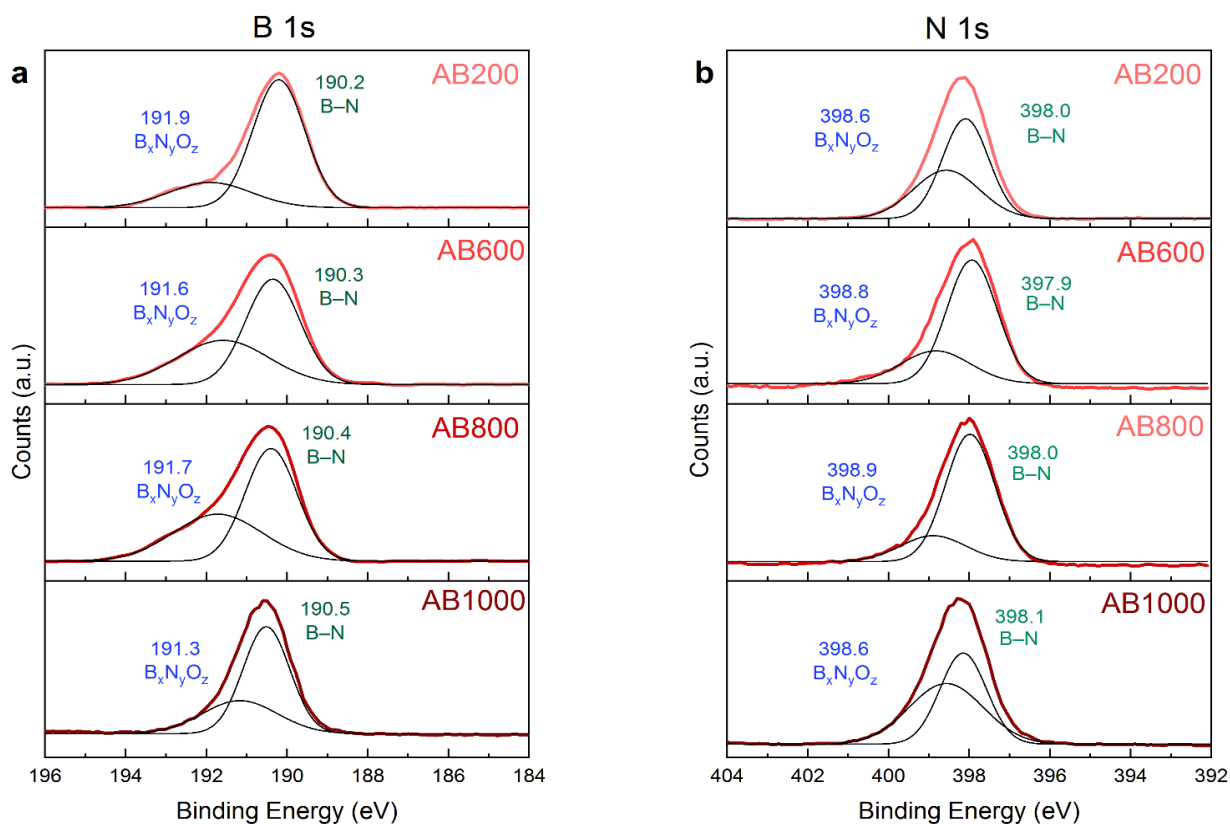


**Figure 16.** XPS spectra of AB and the solid products after pyrolysis at 200, 600, 800 and 1000°C for a) B 1s and b) N 1s. Component peaks were deconvoluted using a Gaussian fit.

Figure 16b shows the N 1s spectra of the pyrolyzed samples for AB. All curves were deconvoluted in two signals. The peak centered at 398.0 eV ( $\pm 0.1$  eV) is assigned to the N–B bond that correspond for borazine-like species at 200°C, and for boron nitride at higher temperatures.<sup>119,126</sup> The second deconvoluted signal, centered at 398.8 eV ( $\pm 0.3$  eV) is assigned to the  $B_xN_yO_z$  species.<sup>122</sup>

The B 1s XPS spectra of LiAB, NaAB and the respective pyrolyzed samples are shown in Figure 17. Pristine LiAB and NaAB spectra show two deconvoluted signals. The peak at  $\sim 188.3$  eV is assigned to B–H bonds.<sup>127</sup> The presence of the signal at  $\sim 191.4$  eV assigned to  $B_xN_yO_z$  might suggest the partial hydrolysis of the  $BH_3$  moiety when the samples are exposed to air during the XPS analysis. Amidoborane salts are highly sensitive to moisture and humidity.<sup>65</sup>

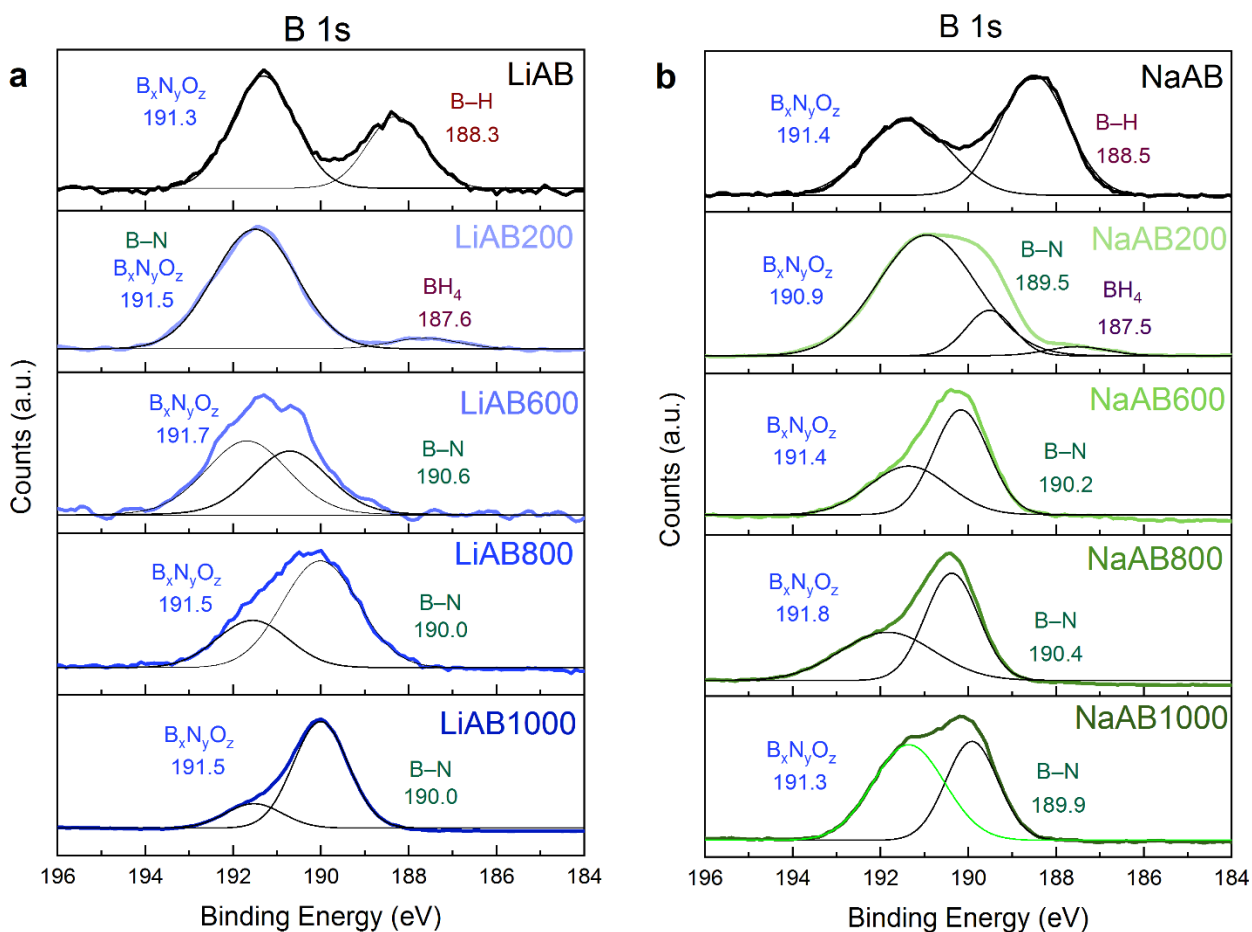


**Figure 17.** B 1s XPS spectra of the amidoboranes and the solid products after pyrolysis at 200, 600, 800 and 1000°C for a) LiAB and b) NaAB. Component peaks were deconvoluted using a Gaussian fit.

LiAB200 and NaAB200 show a small signal that appeared at  $\sim 187.5$  eV that might indicate the formation of  $\text{BH}_4$ -containing species, such as  $\text{NaBH}_4$ ,  $\text{LiBH}_4$  or the DADB-like structures.<sup>128</sup> This result is in good agreement with the  $\text{BH}_4$  environment identified by  $^{11}\text{B}$  MAS NMR for the same samples. In the case of LiAB200, a broad band centered at 191.5 eV is observed. It is possible that LiAB200 oxidizes rapidly in contact with air, and this big signal (related to  $\text{B}_x\text{N}_y\text{O}_z$  species) overlaps the expected B–N peak at  $\sim 190$  eV. For NaAB200, the two signals are visible: one at 189.5 eV assigned to the B–N species and other at 190.9 eV, which belongs to the  $\text{B}_x\text{N}_y\text{O}_z$ . Both LiAB and NaAB treated at 600, 800 and 1000°C present two signals. The one at  $\sim 190$  eV is characteristic of the B–N bond in boron nitride-like structures.<sup>129,130</sup> Also, for all the samples the  $\text{B}_x\text{N}_y\text{O}_z$  signal is present at  $\sim 191.5$  eV. However, for NaAB1000, this signal is as intense as the B–N one. This is probably due to  $\text{O}_2$  contamination during the pyrolysis process at 1000°C, and the higher sensitivity of NaAB towards water, as observed in the FTIR spectra through the formation of NaOH during the analysis.

Regarding the N 1s, the spectra of the compounds are shown in Figure 18. Both LiAB and NaAB show a peak centered at  $\sim 399.5$  eV, that is assigned to the N–H bond. When the materials are pyrolyzed at 200°C, the spectra was deconvoluted in two signals: one centered at  $\sim 397.4$  eV that is assigned to the N–B bond, and the one at  $\sim 398.8$  eV that is assigned to  $\text{B}_x\text{N}_y\text{O}_z$ .<sup>124</sup> However, we do not discard that the bonds N–Li or N–Na can have a contribution to the signal for each one of the amidoboranes.<sup>129</sup> In the case of LiAB, the sample treated at 600°C starts to show one peak centered at  $\sim 398$  eV, that is assigned to the N–B bond. As the temperature is increased to 1000°C, this signal can be better appreciated. The other signal assigned to the  $\text{B}_x\text{N}_y\text{O}_z$  species is still present. The same happens with the NaAB-derived samples. In both cases, it is noticeable that from 200 to 600°C, the binding energy of the N–B bond shifts from  $\sim 397.3$  to  $\sim 397.8$  eV.

The XPS analyses demonstrate that BN is formed through the thermolysis of AB, LiAB and NaAB. However, the identification of  $\text{B}_x\text{N}_y\text{O}$  indicates that oxygen is systematically introduced in the BN matrix, either for contamination while the pyrolysis takes place, and/or during the XPS analyses. However, as XPS analyzes only the surface material, it is difficult to determine the exact reason. The doping of BN structures with oxygen has been suggested as a way to improve the sorption capacities of boron nitride.<sup>131</sup> Nevertheless, there is a lack of information in order to do a proper comparison of

free-oxygen BN and O-doped BN. The XPS survey of all the samples can be found in the Annex I, Figures A11 to A13.

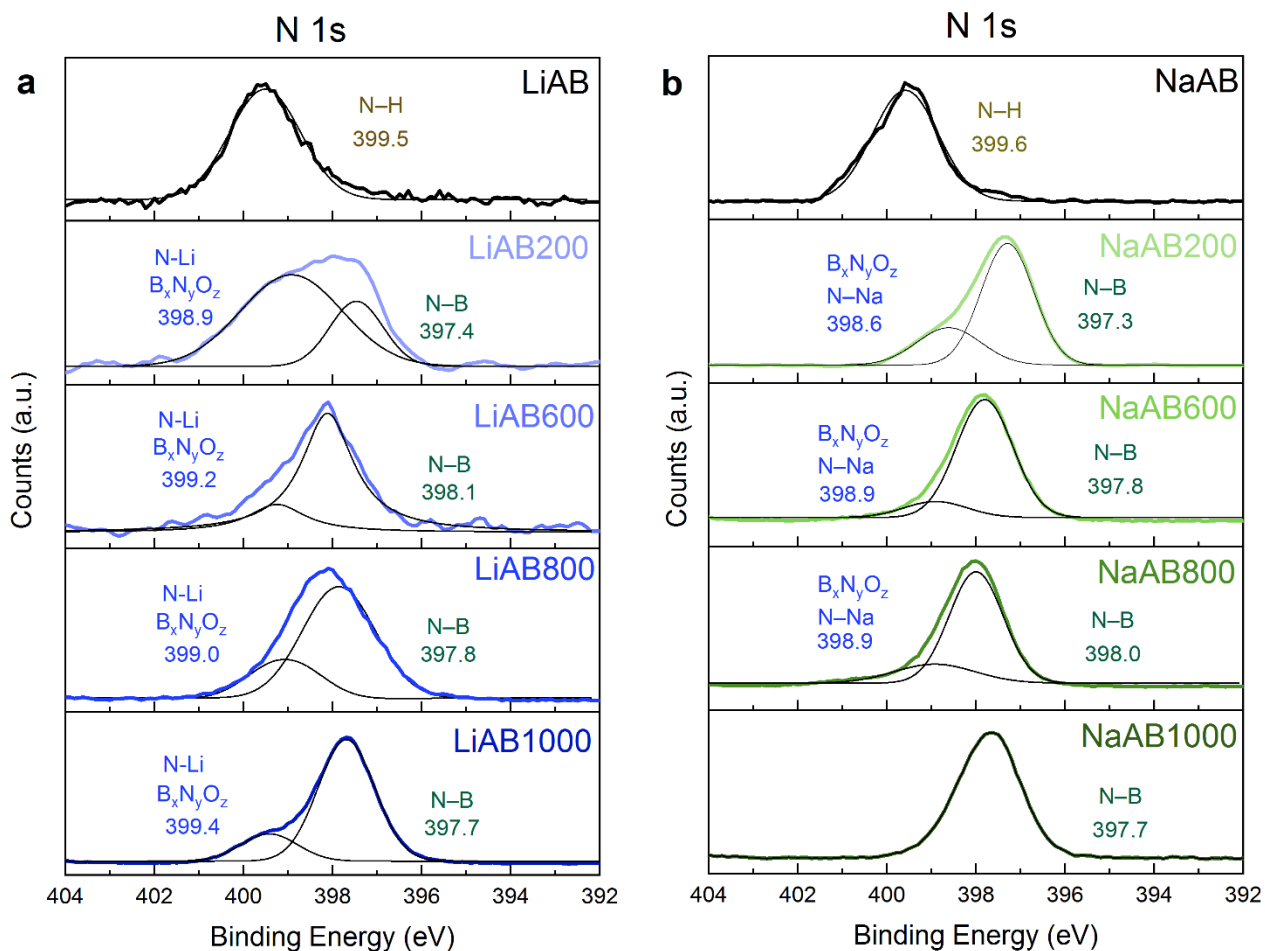


**Figure 18.** N 1s XPS spectra of the amidoboranes and the solid products after pyrolysis at 200, 600, 800 and 1000°C for a) LiAB and b) NaAB. Component peaks were deconvoluted using a Gaussian fit.

### 3.3 Information about the Li and Na elements

#### 3.3.1 $^7\text{Li}$ MAS NMR

The pyrolyzed samples derived from LiAB were analyzed by  $^7\text{Li}$  MAS NMR, and the spectra is shown in Figure 19. LiAB shows a broad signal centered at 2.36 ppm that can be assigned to the  $\text{LiNH}_2\text{BH}_3$

environment. LiAB200 shows a peak centered at 0.1 ppm. In another work, a mixture of AB and LiH was analyzed by  $^7\text{Li}$  MAS NMR and a single broad peak appeared at 1.5 ppm.<sup>114</sup> After dehydrogenation at 95°C of the AB/LiH mixture, this peak shifted to 1 ppm. The shift was related to the removal of hydrogen from  $\text{LiNH}_2\text{BH}_3$ , due to the reduction of the electronegativity of the N atom and the increase of the electron density on the Li atom. In agreement, in our case the original peak at 2.4 ppm of LiAB shifted to 0.1 ppm. In the case of LiAB600, LiAB800 and LiAB1000, a broad signal appears centered at 2.2 ppm. This might indicate a compound with a tentative formula  $(\text{LiNBH}_x)_n$  ( $x \leq 2$ ). For comparison,  $\text{LiNH}_2$  presents a signal at  $\sim 2.4$  ppm in  $^7\text{Li}$  MAS NMR.<sup>132-134</sup> LiAB800 presents also two other peaks in the spectrum: one at -0.3 ppm and another at -5.5 ppm. LiH presents a peak at 0.5 ppm,<sup>132</sup> so the first signal might belong to a dehydrogenated species of LiH. The peak at -5.5 ppm could not be assigned. Due to the lack of a database for these compounds, especially for  $^7\text{Li}$  MAS NMR, no conclusive identification of these bands can be done at this point.

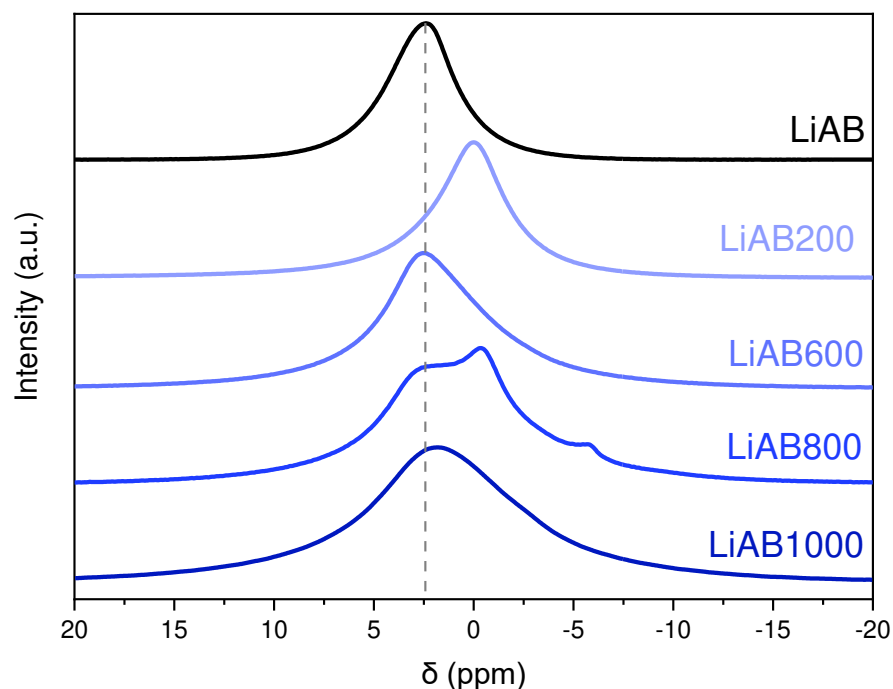


**Figure 19.**  $^7\text{Li}$  MAS NMR spectra for LiAB and the solid products recovered after pyrolysis at 200, 600, 800 and 1000°C.

### 3.3.2 $^{23}\text{Na}$ MAS NMR

NaAB and the pyrolyzed products were investigated by  $^{23}\text{Na}$  MAS NMR (Figure 20). For all samples there is one sharp signal at  $\sim 18$  ppm, corresponding to NaH.<sup>111,134,135</sup> The broad signal seen at negative chemical shifts belongs to the Na site in  $\text{NaNH}_2\text{BH}_3$ ; broadened because of the amorphization of NaAB due to the effect of the temperature. In the case of NaAB800 a new peak was observed at  $\sim 1130$  ppm (insert on Figure 20) that is attributed to the formation of metallic Na due to the decomposition of NaH,<sup>111</sup> or by the reaction proposed in Equation 7 in section 3.2.3. In the case of NaAB1000, a new signal appeared at  $-1.5$  ppm and it might indicate a Na site in a boron nitride-like structure. The formation of NaH during the decomposition of NaAB is explained by the formation of an unstable intermediate following the next mechanism:<sup>117</sup>

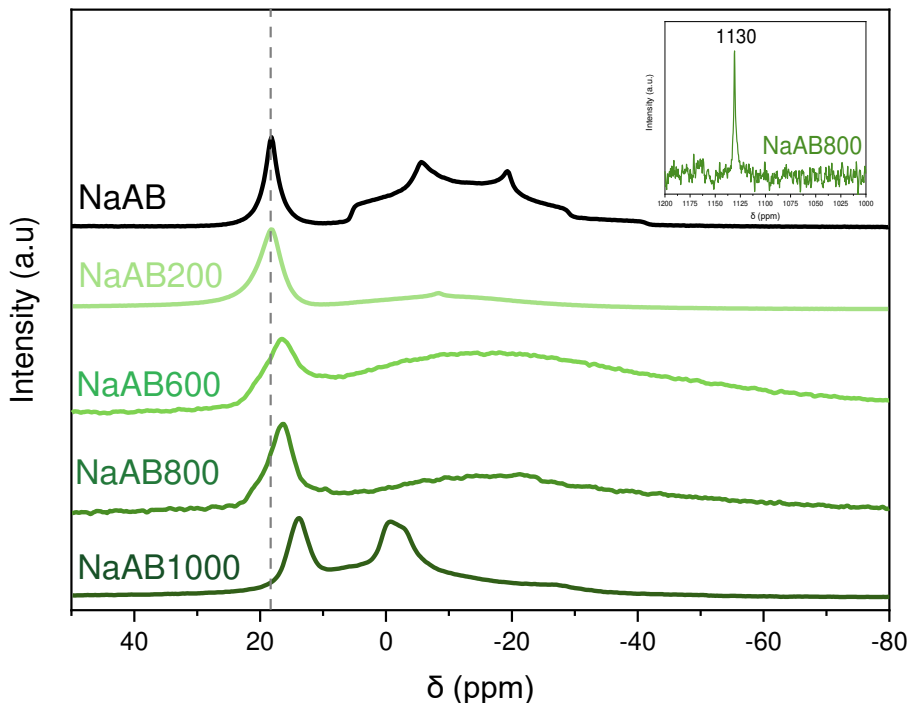
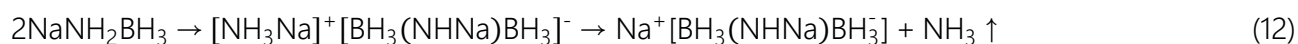


**Figure 20.**  $^{23}\text{Na}$  MAS NMR spectra for NaAB and the solid products recovered after pyrolysis at 200, 600, 800 and 1000°C.

## 3.3.3 XPS

LiAB, NaAB and the pyrolyzed samples were analyzed by XPS for the Li 1s and Na 1s atoms. The spectra are presented in Figure 21.

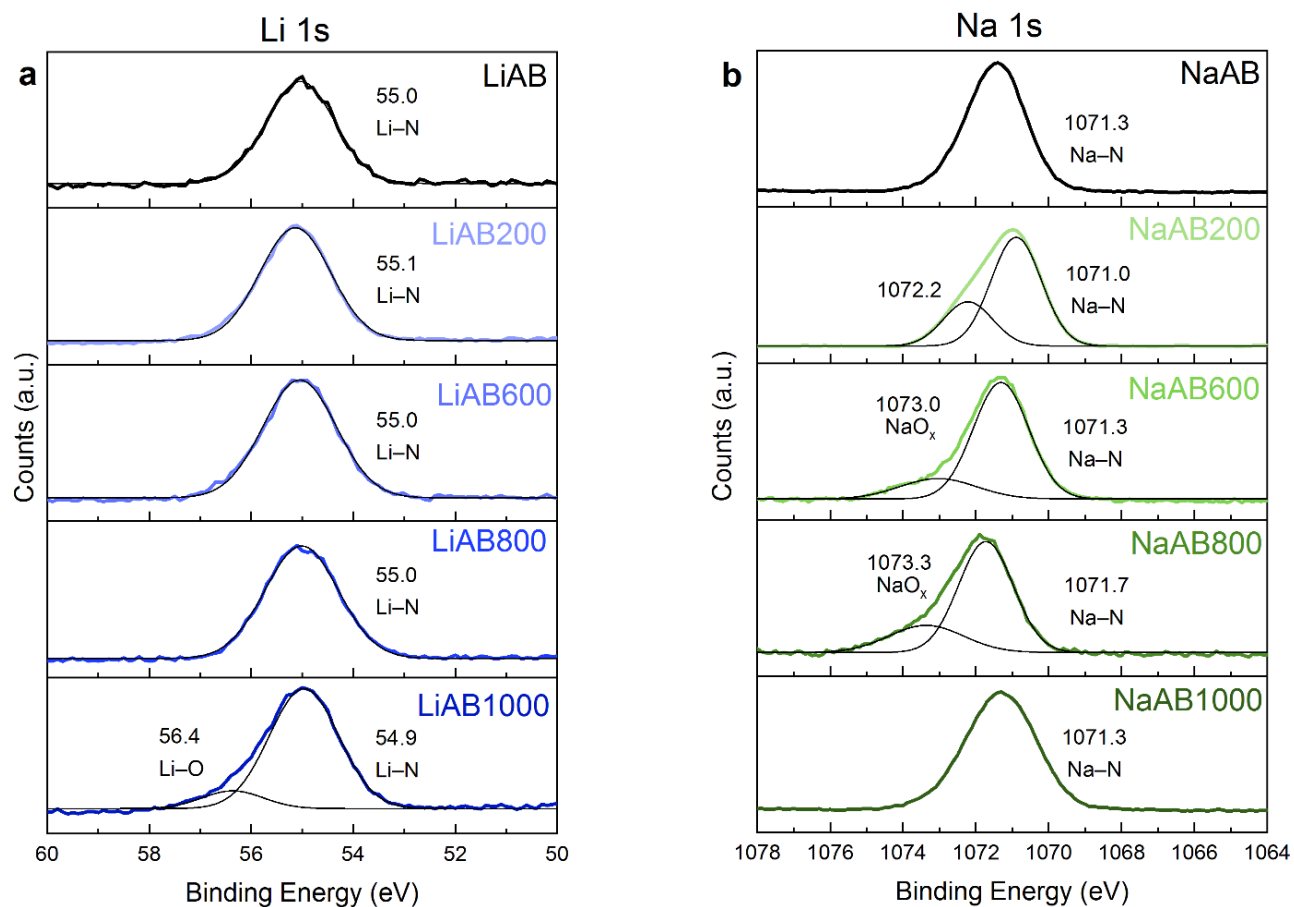


**Figure 21.** XPS spectra of the amidoboranes and the solid products after pyrolysis at 200, 600, 800 and 1000°C of a) Li 1s for LiAB and b) Na 1s for NaAB.

The spectrum of LiAB shows a broad symmetric signal at 55.0 eV that is assigned to the Li-N bond. As the temperature increases, this peak does not change. LiAB1000 shows a small shoulder at 56.4 eV that is assigned to a Li-O bond,<sup>129</sup> which can be present due to a partial oxidation of metallic Li.

The spectrum of NaAB presents a broad symmetric signal centered at 1071.3 eV that is assigned to the Na–N bond. As LiAB, this peak lasts for all samples up to the heat treatment of 1000°C. NaAB200 present an unidentified peak at 1072.2 eV. NaAB600 and NaAB800 present another signal at 1073.0 eV ( $\pm 0.3$ eV) that might indicate the oxidation of some metallic sodium formed during the heat treatment (as evidenced by the MAS NMR analysis). We do not discard the presence of some metallic sodium in NaAB800 (detected by  $^{23}\text{Na}$  MAS NMR), but this signal (expected at  $\sim 1071.8$  eV)<sup>68</sup> can be overlapping with the **Na–N** broad peak.

In any case, the MAS NMR and XPS analyses confirm the previous results about the formation of different species during the thermolysis of the alkali amidoboranes, like oxides due to the presence of air, or even the formation of pure elements, like Na.

### 3.4 Carbon dioxide sorption properties

The CO<sub>2</sub> sorption capacity of the samples was investigated for all the pyrolyzed samples. All of them were exposed for 3 h to CO<sub>2</sub> at 1.5 bar. As reference, we measured the CO<sub>2</sub> capture capacity of commercial silica (Silica SBA-15, mesostructured, 99 % trace metal basis, Sigma-Aldrich) in our system. A value of 5.7 cm<sup>3</sup> g<sup>-1</sup> was obtained. We found a reported value of 6.1 cm<sup>3</sup> g<sup>-1</sup> at 30°C and ambient pressure in the literature.<sup>136</sup> The results of the pyrolyzed samples of AB, LiAB and NaAB are presented in Table 6 and Figure 22. As reference, the sorption properties of different materials are presented in Table 7. The CO<sub>2</sub> sorption capacities are also presented in different units in the Annex I, Table A 1.

**Table 6.** Estimated CO<sub>2</sub> sorption capacity (cm<sup>3</sup> g<sup>-1</sup>) by the materials studied in this work at 1.5 bar and 30°C.

	AB	LiAB	NaAB
200°C	8.0	4.4	3.8
600°C	23.6	3.1	16.7
800°C	15.2	4.5	8.0
1000°C	18.9	3.8	7.6

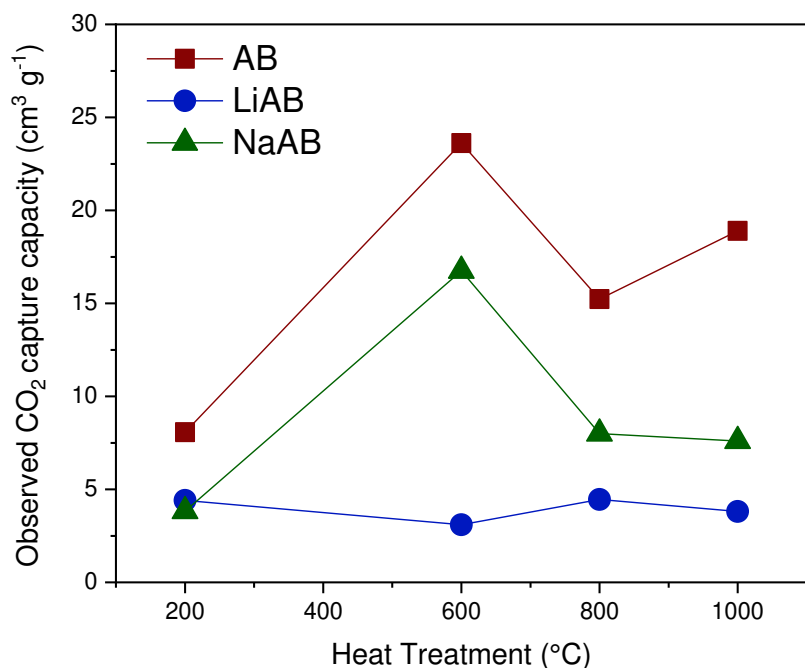


**Figure 22.** Estimated CO<sub>2</sub> sorption capacity (cm<sup>3</sup> g<sup>-1</sup>) of the pyrolyzed samples of AB, LiAB and NaAB, at 1.5 bar and 30°C.

As it can be observed, the samples treated at 200°C do not present a high uptake of CO<sub>2</sub>. As evidenced by the <sup>11</sup>B MAS NMR analysis, all samples present the **BN**<sub>3</sub> and **BN**<sub>2</sub>H environments. However, AB200 presents **BH**<sub>2</sub> and **BH**<sub>4</sub> environments, meanwhile LiAB200 and NaAB200 present **BH**<sub>4</sub>, **BH**<sub>3</sub>, **BH**<sub>2</sub> and **BH** environments. The presence of all the different intermediates that provoke these signals (i.e. DADB, PAB) might have an impact in the global uptake of CO<sub>2</sub>, inhibiting the sorption capacity of the materials at 200°C. It is likely that having a mixture of different boron- and nitrogen-based polymers does not favor the sorption of CO<sub>2</sub> by the samples. At this temperature, LiAB200 and NaAB200 present similar uptake values; however, AB200 presents the highest value.

With the heat treatment at 600°C, AB and NaAB present an increase on the capacity of CO<sub>2</sub> uptake. The increment of the uptake capacity of AB600 is almost 3 times the one of AB200. NaAB also increases the value in 4.4 times, passing from 3.8 to 16.7 cm<sup>3</sup> g<sup>-1</sup>. This could be related to the low degree of crystallinity showed by both samples in the PXRD analysis. On the other hand, LiAB600

shows poor results increasing the uptake in only 1.2 times in comparison with LiAB200. In fact, the CO<sub>2</sub> uptake capacity shown by the LiAB-derived samples is in general poor. In fact, the values found in this work for the LiAB-derived samples are close to the ones reported for h-BN.<sup>24</sup> The results of PXRD for the LiAB samples showed crystallinity from 600°C and this might be related with the sorption capacity of these samples. In any case, the values found in here are higher than the one of h-BN (1 bar, 25°C), suggesting that the Li atom might be enhancing the CO<sub>2</sub> capture properties of the material.

**Table 7.** CO<sub>2</sub> uptake by different materials. Adapted and completed from reference <sup>19</sup>.

Material	Temperature (°C)	Pressure (bar)	CO <sub>2</sub> uptake (cm <sup>3</sup> g <sup>-1</sup> )	Ref.
Sphere functionalized BN nanosheets/ZnO	0	1	63.4	19
Sphere functionalized BN nanosheets/ZnO	25	1	40	19
Cubic functionalized BN nanosheets/ZnO	0	1	27.8	19
Cubic functionalized BN nanosheets/ZnO	25	1	16.6	19
3D flower-like BN nanosheets	0	1	37.9	24
3D flower-like BN nanosheets	25	1	19.2	24
h-BN	0	1	3.3	24
h-BN	25	1	1.7	24
BN nanosheets	0	1	~16	25
BN nanosheets	25	1	~10	25
Cu-loaded BN nanofibers	0	1	62	22
Polyethyleneimine functionalized BN nanosheets	120	1	69.9	21
P123 <sup>a</sup> modified porous BN	25	1	60.2	20
Pristine porous BN	25	1	44.8	20
SBA-15 mesostructured silica	45	1	10	26
SBA-15 mesostructured silica (commercial)	30	1	5.7	136
SBA-15 functionalized with polyethyleneimine	40	1	31.3	137
Metal Organic Framework NJU-Bai20	25	1	68.0	138
Covalent Organic Framework FCTF-1	25	1	71.9	139

<sup>a</sup> Pluronic triblock copolymer surfactant

At 800°C the CO<sub>2</sub> capture capacity of the AB and NaAB pyrolyzed samples decreases. At 1000°C the uptake increases for AB and decreases for NaAB. It is clear that AB presented the highest CO<sub>2</sub> uptake values: AB600 presented the maximum uptake, and this might be related to its amorphous structure (Figure 9). The same is observed for NaAB600; however, the sorption capacity of NaAB800 and NaAB1000 decreased, which coincides with the apparition of the diffraction peaks of h-BN in the PXRD analysis, as observed on Figure 10b. In the case of the LiAB-derived samples, the diffraction peaks were observed from 600°C (Figure 10a), which might be related with the lower values of CO<sub>2</sub> uptake. Nevertheless, all the pyrolyzed samples of LiAB and NaAB show a higher CO<sub>2</sub> uptake than the one reported for bulk h-BN (1.7 cm<sup>3</sup> g<sup>-1</sup>), indicating that the incorporation of an alkali element in the material enhance the CO<sub>2</sub> uptake.

At this point, the results suggest a relation between the crystallinity and the CO<sub>2</sub> sorption capacity of the samples. This could be related to the crystalline conformation of the BN structures. For example, if the AB-derived samples pyrolyzed between 600 and 1000°C mainly have a turbostratic structure, the impurities, incomplete bonds and large surface area characteristics of t-BN might explain the high CO<sub>2</sub> uptake values.<sup>88</sup> The random orientation of the layers, the defects and the vacancies in t-BN may favor the sorption of CO<sub>2</sub>. In comparison, the pyrolysis of both amidoboranes led to a higher degree of crystallinity, and this is reflected in their lower CO<sub>2</sub> uptake. It is likely that a material with random layers conformation would present better sorption properties.

## 4. Conclusions

Two alkali derivatives of ammonia borane, lithium amidoborane LiNH<sub>2</sub>BH<sub>3</sub> (LiAB) and sodium amidoborane NaNH<sub>2</sub>BH<sub>3</sub> were studied as precursors of boron nitride for the first time. The synthesis, pyrolysis and characterization of these compounds were performed and compared with the former ammonia borane. All the characterization techniques used in this study confirmed the successful formation of crystalline hexagonal boron nitride from both amidoboranes. At low temperatures, AB, LiAB nor NaAB show any crystallinity, and their composition is mostly amorphous boron- and nitrogen-based polymers. However, at 600°C LiAB started to show the formation of crystalline BN evidenced by PXRD and Raman spectroscopy. The formation of crystalline BN was also detected in

the case of NaAB from 800°C. When the amidoboranes were treated at 1000°C, the presence of hexagonal boron nitride is more evident. In comparison, AB did not show any crystallinity up to 1000°C. This leads us to conclude that the amidoboranes can be used as precursors of crystalline BN. Also, that the alkali cation has an impact in the crystallization of BN. In our study, the LiAB-derived samples presented crystallinity at lower temperatures in comparison with NaAB. However, it is likely that the presence of the Li and Na atoms lead to side reactions and the consequent formation of other compounds during the pyrolysis, such as  $\text{Li}_2\text{NH}$  and metal oxides (if some oxygen is present during the heat treatment). However, the treatment at higher temperatures (1200-1400°C) might lead to a purer BN. In any case, alkali amidoboranes might be considered as viable sources to obtain crystalline BN at lower temperatures than the traditional synthesis.

In addition, the materials presented in this chapter were investigated as potential  $\text{CO}_2$  sorbents at nearly room conditions (1.5 bar and 30°C). The results of the sorption experiments showed that the materials were able to uptake  $\text{CO}_2$  at these conditions. The AB-derived samples had a better performance than the amidoborane-derived ones: the highest  $\text{CO}_2$  uptake was presented by AB pyrolyzed at 600°C. The lowest uptake was exhibited by the LiAB-derived samples. It is likely that the  $\text{CO}_2$  uptake capacity of the samples decreases as the crystallinity of the material increases. The AB-derived samples might present a turbostratic structure, so the random disposition of the BN layers and the presence of a higher number of defects may favor the uptake of  $\text{CO}_2$ . On the contrary, the Li and Na cations promoted the crystallinity of h-BN at lower temperatures so, in comparison, the uptake values are low. In any case, the LiAB- and NaAB-derived BN structures showed a higher  $\text{CO}_2$  uptake capacity in comparison with bulk h-BN,<sup>24</sup> possibly due to the incorporation of the Li and Na elements in the material. Besides, we highlight that the materials synthesized in this work are not porous. In this way, the synthesis of a porous structure based on these materials may enhance the  $\text{CO}_2$  sorption properties of the compounds.

## 5. References

1. Lee, S. Y. and Park, S. J. A review on solid adsorbents for carbon dioxide capture. *J. Ind. Eng. Chem.* **23**, 1–11 (2015).
2. Anwar, M. N. *et al.* CO<sub>2</sub> capture and storage: A way forward for sustainable environment. *J. Environ. Manage.* **226**, 131–144 (2018).
3. Middleton, R. S. and Eccles, J. K. The complex future of CO<sub>2</sub> capture and storage: Variable electricity generation and fossil fuel power. *Appl. Energy* **108**, 66–73 (2013).
4. Yu, C. H. *et al.* A review of CO<sub>2</sub> capture by absorption and adsorption. *Aerosol Air Qual. Res.* **12**, 745–769 (2012).
5. Nugent, P. *et al.* Porous materials with optimal adsorption thermodynamics and kinetics for CO<sub>2</sub> separation. *Nature* **495**, 80–84 (2013).
6. Ma, Y. *et al.* Review on porous nanomaterials for adsorption and photocatalytic conversion of CO<sub>2</sub>. *Chinese J. Catal.* **38**, 1956–1969 (2017).
7. Lei, W. *et al.* Porous boron nitride nanosheets for effective water cleaning. *Nat. Commun.* **4**, 1–7 (2013).
8. Zeng, H. *et al.* ‘White graphenes’: Boron nitride nanoribbons via boron nitride nanotube unwrapping. *Nano Lett.* **10**, 5049–5055 (2010).
9. Caldwell, J. D. *et al.* Photonics with hexagonal boron nitride. *Nat. Rev. Mater.* **4**, 552–567 (2019).
10. Zhou, C. *et al.* Semiconductor/boron nitride composites: Synthesis, properties, and photocatalysis applications. *Appl. Catal. B Environ.* **238**, 6–18 (2018).
11. Duan, L. *et al.* Efficient photocatalytic PFOA degradation over boron nitride. *Environ. Sci. Technol. Lett.* **7**, 613–619 (2020).
12. Wang, S. *et al.* Hierarchical porous boron nitride nanosheets with versatile adsorption for water treatment. *Colloids Surfaces A Physicochem. Eng. Asp.* **598**, 124865 (2020).
13. Jiao, Y. *et al.* A density functional theory study of CO<sub>2</sub> and N<sub>2</sub> adsorption on aluminium nitride

- single walled nanotubes. *J. Mater. Chem.* **20**, 10426–10430 (2010).
14. Sang, H. L. *et al.* 'Associative' electron attachment to azabenzene-(CO<sub>2</sub>)<sub>n</sub> van der Waals complexes: Stepwise formation of covalent bonds with additive electron affinities. *J. Am. Chem. Soc.* **130**, 16241–16244 (2008).
  15. Janik, J. F. *et al.* Boron nitride as a selective gas adsorbent. *Langmuir* **10**, 514–518 (1994).
  16. Choi, H. *et al.* Ambient carbon dioxide capture by boron-rich boron nitride nanotube. *J. Am. Chem. Soc.* **133**, 2084–2087 (2011).
  17. Sun, Q. *et al.* Charge-controlled switchable CO<sub>2</sub> capture on boron nitride nanomaterials. *J. Am. Chem. Soc.* **135**, 8246–8253 (2013).
  18. Paura, E. N. C. *et al.* Carbon dioxide adsorption on doped boron nitride nanotubes. *RSC Adv.* **4**, 28249–28258 (2014).
  19. Yang, C. *et al.* Three-dimensional functionalized boron nitride nanosheets/ZnO superstructures for CO<sub>2</sub> capture. *ACS Appl. Mater. Interfaces* **11**, 10276–10282 (2019).
  20. Hojatisaeidi, F. *et al.* Metal-free modified boron nitride for enhanced CO<sub>2</sub> capture. *Energies* **13**, 1–11 (2020).
  21. Huang, K. *et al.* Aminopolymer functionalization of boron nitride nanosheets for highly efficient capture of carbon dioxide. *J. Mater. Chem. A* **5**, 16241–16248 (2017).
  22. Liang, J. *et al.* In situ Cu-loaded porous boron nitride nanofiber as an efficient adsorbent for CO<sub>2</sub> capture. *ACS Sustain. Chem. Eng.* **8**, 7454–7462 (2020).
  23. Jiang, H. *et al.* Three-dimensional porous boron nitride foam for effective CO<sub>2</sub> adsorption. *Solid State Commun.* **294**, 1–5 (2019).
  24. Yang, C. *et al.* One-step template-free synthesis of 3D functionalized flower-like boron nitride nanosheets for NH<sub>3</sub> and CO<sub>2</sub> adsorption. *Nanoscale* **10**, 10979–10985 (2018).
  25. Xiao, F. *et al.* Controllable synthesis of few-layered and hierarchically porous boron nitride nanosheets. *Chem. Commun.* **52**, 3911–3914 (2016).

26. Sanz, R. *et al.* CO<sub>2</sub> adsorption on branched polyethyleneimine-impregnated mesoporous silica SBA-15. *Appl. Surf. Sci.* **256**, 5323–5328 (2010).
27. Shahsavari, R. and Zhao, S. Merger of energetic affinity and optimal geometry provides new class of boron nitride based sorbents. *Small* **14**, 1–10 (2018).
28. Kumar, E. M. *et al.* First principles guide to tune h-BN nanostructures as superior light-element-based hydrogen storage materials: Role of the bond exchange spillover mechanism. *J. Mater. Chem. A* **3**, 304–313 (2015).
29. Wang, Y. *et al.* Theoretical prediction of hydrogen storage on Li-decorated boron nitride atomic chains. *J. Appl. Phys.* **113**, 064309 (1–6) (2013).
30. Dai, J. *et al.* Porous boron nitride with tunable pore size. *J. Phys. Chem. Lett.* **5**, 393–398 (2014).
31. Liu, Y. *et al.* Hydrogen storage using Na-decorated graphyne and its boron nitride analog. *Int. J. Hydrogen Energy* **39**, 12757–12764 (2014).
32. Whittell, G. R. and Manners, I. Advances with ammonia-borane: Improved recycling and use as a precursor to atomically thin BN films. *Angew. Chem. Int. Ed.* **50**, 10288–10289 (2011).
33. Koepke, J. C. *et al.* Role of pressure in the growth of hexagonal boron nitride thin films from ammonia-borane. *Chem. Mater.* **28**, 4169–4179 (2016).
34. Bowden, M. *et al.* The thermal decomposition of ammonia borane: A potential hydrogen storage material. *Curr. Appl. Phys.* **8**, 498–500 (2008).
35. Chua, Y. S. *et al.* Development of amidoboranes for hydrogen storage. *Chem. Commun.* **47**, 5116–5129 (2011).
36. Diyabalanage, H. V. K. *et al.* Calcium amidotrihydroborate: A hydrogen storage material. *Angew. Chem. Int. Ed.* **46**, 8995–8997 (2007).
37. Luo, J. *et al.* Synthesis, formation mechanism, and dehydrogenation properties of the long-sought Mg(NH<sub>2</sub>BH<sub>3</sub>)<sub>2</sub> compound. *Energy Environ. Sci.* **6**, 1018–1025 (2013).
38. Diyabalanage, H. V. K. *et al.* Potassium(I) amidotrihydroborate: Structure and hydrogen release. *J. Am. Chem. Soc.* **132**, 11836–11837 (2010).

39. Owarzany, R. *et al.* Amidoboranes of rubidium and caesium: The last missing members of the alkali metal amidoborane family. *Dalton Trans.* **46**, 16315–16320 (2017).
40. Kazakov, I. V. *et al.* Reversible structural transformations of rubidium and cesium amidoboranes. *Polyhedron* **127**, 186–190 (2017).
41. Shcherbina, N. A. *et al.* Synthesis and characterization of barium amidoborane. *Russ. J. Gen. Chem.* **87**, 2875–2877 (2017).
42. Zhang, Q. *et al.* Synthesis, crystal structure, and thermal decomposition of strontium amidoborane. *J. Phys. Chem. C* **114**, 1709–1714 (2010).
43. Lisovenko, A. S. and Timoshkin, A. Y. Formation and unimolecular dehydrogenation of gaseous alkaline-earth metal amidoboranes  $M(\text{NH}_2\text{BH}_3)_2$  ( $M=\text{Be}-\text{Ba}$ ): Comparative computational study. *Z. Anorg. Allg. Chem.* **643**, 209–213 (2017).
44. Genova, R. V. *et al.* Towards  $\text{Y}(\text{NH}_2\text{BH}_3)_3$ : Probing hydrogen storage properties of  $\text{YX}_3/\text{MNH}_2\text{BH}_3$  ( $X=\text{F}, \text{Cl}$ ;  $M=\text{Li}, \text{Na}$ ) and  $\text{YH}_{x-3}/\text{NH}_3\text{BH}_3$  composites. *J. Alloys Compd.* **499**, 144–148 (2010).
45. Xia, G. *et al.* Mixed-metal (Li, Al) amidoborane: Synthesis and enhanced hydrogen storage properties. *J. Mater. Chem. A* **1**, 1810–1820 (2013).
46. Fijalkowski, K. J. *et al.*  $\text{Na}[\text{Li}(\text{NH}_2\text{BH}_3)_2]$  - The first mixed-cation amidoborane with unusual crystal structure. *Dalton Trans.* **40**, 4407–4413 (2011).
47. Wu, H. *et al.* Sodium magnesium amidoborane: The first mixed-metal amidoborane. *Chem. Commun.* **47**, 4102–4104 (2011).
48. Xiong, Z. *et al.* High-capacity hydrogen storage in lithium and sodium amidoboranes. *Nat. Mater.* **7**, 138–141 (2008).
49. Castilla-Martinez, C. A. *et al.* Amidoboranes and hydrazinidoboranes: State of the art, potential for hydrogen storage, and other prospects. *Int. J. Hydrogen Energy* **45**, 30731–30755 (2020).
50. Yuan, S. *et al.* Low-temperature synthesis of highly crystallized hexagonal boron nitride sheets with  $\text{Li}_3\text{N}$  as additive agent. *Eur. J. Inorg. Chem.* **2014**, 5507–5513 (2014).
51. Fazen, P. J. *et al.* Synthesis, properties, and ceramic conversion reactions of polyborazylene. A

- high-yield polymeric precursor to boron nitride. *Chem. Mater.* **7**, 1942–1956 (1995).
52. Tang, Z. *et al.* Regenerable hydrogen storage in lithium amidoborane. *Chem. Commun.* **48**, 9296–9298 (2012).
  53. Fijałkowski, K. J. and Grochala, W. Substantial emission of NH<sub>3</sub> during thermal decomposition of sodium amidoborane, NaNH<sub>2</sub>BH<sub>3</sub>. *J. Mater. Chem.* **19**, 2043–2050 (2009).
  54. Demirci, U. B. Ammonia borane, a material with exceptional properties for chemical hydrogen storage. *Int. J. Hydrogen Energy* **42**, 9978–10013 (2017).
  55. Frueh, S. *et al.* Pyrolytic decomposition of ammonia borane to boron nitride. *Inorg. Chem.* **50**, 783–792 (2011).
  56. Toche, F. *et al.* Ammonia borane thermolytic decomposition in the presence of metal (II) chlorides. *Int. J. Hydrogen Energy* **37**, 6749–6755 (2012).
  57. Baumann, J. *et al.* Thermal decomposition of polymeric aminoborane (H<sub>2</sub>BNH<sub>2</sub>)<sub>x</sub> under hydrogen release. *Thermochim. Acta* **430**, 9–14 (2005).
  58. Jepsen, L. H. *et al.* Investigations of the thermal decomposition of MBH<sub>4</sub>-2NH<sub>3</sub>BH<sub>3</sub>, M=Na, K. *J. Alloys Compd.* **580**, 287–291 (2013).
  59. Staubitz, A. *et al.* Ammonia-borane and related compounds as dihydrogen sources. *Chem. Rev.* **110**, 4079–4124 (2010).
  60. Sutton, A. D. *et al.* Regeneration of ammonia borane spent fuel by direct reaction with hydrazine and liquid ammonia. *Science*. **331**, 1426–1429 (2011).
  61. Davis, B. L. *et al.* Efficient regeneration of partially spent ammonia borane fuel. *Angew. Chem. Int. Ed.* **48**, 6812–6816 (2009).
  62. Sahu, S. *et al.* Formation of boron nitride thin films on β-Si<sub>3</sub>N<sub>4</sub> whiskers and α-SiC platelets by dip-coating. *J. Eur. Ceram. Soc.* **18**, 1037–1043 (1998).
  63. Termoss, H. *et al.* Preparation of boron nitride-based coatings on metallic substrates via infrared irradiation of dip-coated polyborazylene. *J. Mater. Chem.* **19**, 2671–2674 (2009).

64. Sudeep, P. M. *et al.* Functionalized boron nitride porous solids. *RSC Adv.* **5**, 93964–93968 (2015).
65. Owarzany, R. *et al.* Mono- and bimetallic amidoboranes. *Crystals* **6**, 1–32 (2016).
66. Yang, Z. *et al.* Hydrogen releasing of lithium amidoborane-LiNH<sub>2</sub>BH<sub>3</sub>. *Mater. Trans.* **52**, 651–653 (2011).
67. Sandra, F. P. R. *et al.* A simple preparation method of sodium amidoborane, highly efficient derivative of ammonia borane dehydrogenating at low temperature. *Int. J. Hydrogen Energy* **36**, 7423–7430 (2011).
68. NIST. National Institut of Standards and Technology, U.S. Department of Commerce. *Boron nitride* <https://webbook.nist.gov/cgi/cbook.cgi?ID=C10043115&Mask=80> (2020).
69. Hess, N. J. *et al.* Spectroscopic studies of the phase transition in ammonia borane: Raman spectroscopy of single crystal NH<sub>3</sub>BH<sub>3</sub> as a function of temperature from 88 to 330 K. *J. Chem. Phys.* **128**, (2008).
70. Trudel, S. and Gilson, D. F. R. High-pressure Raman spectroscopic study of the ammonia-borane complex. Evidence for the dihydrogen bond. *Inorg. Chem.* **42**, 2814–2816 (2003).
71. Xie, S. *et al.* In situ high-pressure study of ammonia borane by raman and IR spectroscopy. *Can. J. Chem.* **87**, 1235–1247 (2009).
72. Nyfín, J. *et al.* Thermal decomposition of ammonia borane at high pressures. *J. Chem. Phys.* **131**, (2009).
73. Chellappa, R. S. *et al.* High-pressure hydrogen interactions with polyaminoborane and polyiminoborane. *ChemPhysChem* **11**, 93–96 (2010).
74. Nemanich, R. J. *et al.* Light scattering study of boron nitride microcrystals. *Phys. Rev. B* **23**, 6348–6356 (1981).
75. Wu, J. *et al.* Raman spectroscopy and time-resolved photoluminescence of BN and B<sub>x</sub>C<sub>y</sub>N<sub>z</sub> nanotubes. *Nano Lett.* **4**, 647–650 (2004).
76. Yuan, S. *et al.* Synthesis of hexagonal boron nitride graphene-like few layers. *Nanoscale* **6**, 7838–7841 (2014).

77. Choi, H. C. *et al.* X-ray absorption near edge structure study of BN nanotubes and nanothorns. *J. Phys. Chem. B* **109**, 7007–7011 (2005).
78. 78, S. *et al.* How to increase the h-bn crystallinity of microfilms and self-standing nanosheets: A review of the different strategies using the PDCs route. *Crystals* **6**, (2016).
79. Yang, J. B. *et al.* Structural evolution of ammonia borane for hydrogen storage. *Appl. Phys. Lett.* **92**, 1–4 (2008).
80. Liu, X., Wang, S., Wu, Y., Li, Z., Jiang, L., Guo, X., Ye, J. Dehydrogenation properties of two phases of  $\text{LiNH}_2\text{BH}_3$ . *Int. J. Hydrogen Energy* **45**, 2127–2134 (2020).
81. Wu, C. *et al.* Stepwise phase transition in the formation of lithium amidoborane. *Inorg. Chem.* **49**, 4319–4323 (2010).
82. Liu, X. *et al.* Current progress and research trends on lithium amidoborane for hydrogen storage. *J. Mater. Sci.* **55**, 2645–2660 (2020).
83. Jepsen, L. H. *et al.* Nanostructured and complex hydrides for hydrogen storage. in *Nanotechnology for Energy Sustainability*. 415–432 (Wiley-VCH, 2017).
84. Zhang, J. and Hu, Y. H. Decomposition of lithium amide and lithium imide with and without anion promoter. *Ind. Eng. Chem. Res.* **50**, 8058–8064 (2011).
85. Milanović, I. and Biliškov, N. Mechanochemical pretreatment of ammonia borane: A new procedure for sodium amidoborane synthesis. *Int. J. Hydrogen Energy* **45**, 7938–7946 (2020).
86. Koz, C. *et al.*  $\text{Na}_3[\text{BN}_2]$  and  $\text{Na}_2\text{K}[\text{BN}_2]$ : A known and a novel alkali metal dinitridoborate obtained via mild thermal dehydrogenation. *Z. Anorg. Allg. Chem.* **640**, 279–285 (2014).
87. Lei, W. *et al.* Highly crumpled boron nitride nanosheets as adsorbents: scalable solvent-less production. *Adv. Mater. Interfaces* **2**, 2–7 (2015).
88. Alkoy, S. *et al.* Crystallization behavior and characterization of turbostratic boron nitride. *J. Eur. Ceram. Soc.* **17**, 1415–1422 (1997).
89. Salles, V. *et al.* Structural and thermal properties of boron nitride nanoparticles. *J. Eur. Ceram. Soc.* **32**, 1867–1871 (2012).

90. Zhong, W. *et al.* Fabrication of porous boron nitride by using polyborazylene as precursor, polymethylmeth-acrylate as reaction agent. *IOP Conf. Ser. Mater. Sci. Eng.* **612**, (2019).
91. Yang, H. *et al.* Peculiar deformation characteristics of turbostratic boron nitride thin film. *Thin Solid Films* **483**, 218–221 (2005).
92. Lian, J. *et al.* Ionothermal synthesis of turbostratic boron nitride nanoflakes at low temperature. *J. Phys. Chem. C* **113**, 9135–9140 (2009).
93. Zhong, B. *et al.* Large-scale fabrication and utilization of novel hexagonal/turbostratic composite boron nitride nanosheets. *Mater. Des.* **120**, 266–272 (2017).
94. Yuan, S. *et al.* New potential for preparation of performing h-BN coatings via polymer pyrolysis in RTA furnace. *J. Eur. Ceram. Soc.* **33**, 393–402 (2013).
95. Eaton, G. R. NMR of boron compounds. *J. Chem. Educ.* **46**, 547–556 (1969).
96. Smith, W. L. Boron-11 NMR. *J. Chem. Educ.* **54**, 469–473 (1977).
97. Stowe, A. C. *et al.* In situ solid state  $^{11}\text{B}$  MAS-NMR studies of the thermal decomposition of ammonia borane: Mechanistic studies of the hydrogen release pathways from a solid state hydrogen storage material. *Phys. Chem. Chem. Phys.* **9**, 1831–1836 (2007).
98. Kim, D.-P. *et al.* Synthesis and characterization of poly(aminoborane) as a new boron nitride precursor. *Polym. Adv. Technol.* **10**, 702–712 (1999).
99. Bluhm, M. E. *et al.* Amineborane-based chemical hydrogen storage: Enhanced ammonia borane dehydrogenation in ionic liquids. **3**, 7748–7749 (2006).
100. Jacquemin, D. First hyperpolarizability of polyaminoborane and polyiminoborane oligomers. 9260–9266 (2004).
101. Miranda, C. R. and Ceder, G. Ab initio investigation of ammonia-borane complexes for hydrogen storage. *J. Chem. Phys.* **184703**, 184703 (1–11) (2009).
102. Gervais, C. *et al.* Chemically derived BN ceramics: Extensive  $^{11}\text{B}$  and  $^{15}\text{N}$  solid-state NMR study of a preceramic polyborazylene. *Chem. Mater.* **13**, 1700–1707 (2001).

103. Gervais, C. *et al.*  $^{11}\text{B}$  and  $^{15}\text{N}$  solid state NMR investigation of a boron nitride preceramic polymer prepared by ammonolysis of borazine. *J. Eur. Ceram. Soc.* **25**, 129–135 (2005).
104. Kobayashi, T. *et al.* Mechanism of solid-state thermolysis of ammonia borane: A  $^{15}\text{N}$  NMR study using fast magic-angle spinning and dynamic nuclear polarization. *J. Phys. Chem. C* **118**, 19548–19555 (2014).
105. Roy, B. *et al.* Supported ammonia borane decomposition through enhanced homopolar B-B coupling. *Dalton Trans.* **47**, 6570–6579 (2018).
106. Li, J. *et al.* Preparation of polyborazylene-derived bulk boron nitride with tunable properties by warm-pressing and pressureless pyrolysis. *Chem. Mater.* **22**, 2010–2019 (2010).
107. Fijalkowski, K. J. *et al.* Insights from impedance spectroscopy into the mechanism of thermal decomposition of  $\text{M}(\text{NH}_2\text{BH}_3)$ ,  $\text{M} = \text{H}, \text{Li}, \text{Na}, \text{Li}_{0.5}, \text{Na}_{0.5}$ , hydrogen stores. *Phys. Chem. Chem. Phys.* **14**, 5778–5784 (2012).
108. Kang, X. *et al.* Ammonia borane destabilized by lithium hydride: An advanced on-board hydrogen storage material. *Adv. Mater.* **20**, 2756–2759 (2008).
109. Shevlin, S. A. *et al.* Dehydrogenation mechanisms and thermodynamics of  $\text{MNH}_2\text{BH}_3$  ( $\text{M} = \text{Li}, \text{Na}$ ) metal amidoboranes as predicted from first principles. *Phys. Chem. Chem. Phys.* **13**, 7649–7659 (2011).
110. Shimoda, K. *et al.* Comparative study of structural changes in  $\text{NH}_3\text{BH}_3$ ,  $\text{LiNH}_2\text{BH}_3$ , and  $\text{KNH}_2\text{BH}_3$  during dehydrogenation process. *J. Phys. Chem. C* **116**, 5957–5964 (2012).
111. Shimoda, K. *et al.* Solid state NMR study on the thermal decomposition pathway of sodium amidoborane  $\text{NaNH}_2\text{BH}_3$ . *J. Mater. Chem.* **21**, 2609–2615 (2011).
112. Luedtke, A. T. and Autrey, T. Hydrogen release studies of alkali metal amidoboranes. *Inorg. Chem.* **49**, 3905–3910 (2010).
113. Baitalow, F. *et al.* Thermal decomposition of B-N-H compounds investigated by using combined thermoanalytical methods. *Thermochim. Acta* **391**, 159–168 (2002).
114. Wang, Y. and Guo, Z. X. Enhanced hydrogen desorption of an ammonia borane and lithium

- hydride system through synthesised intermediate compounds. *J. Mater. Chem. A* **2**, 6801–6813 (2014).
115. Shimoda, K. *et al.* Solid state NMR study on the thermal decomposition pathway of sodium amidoborane  $\text{NaNH}_2\text{BH}_3$ . *J. Mater. Chem.* **21**, 2609–2615 (2011).
  116. Owarzany, R. *et al.* Mono- and bimetalic amidoboranes. *Crystals* **6**, (2016).
  117. Fijałkowski, K. J. and Grochala, W. Substantial emission of  $\text{NH}_3$  during thermal decomposition of sodium amidoborane,  $\text{NaNH}_2\text{BH}_3$ . *J. Mater. Chem.* **19**, 2043–2050 (2009).
  118. Stowe, A. C. *et al.* In situ solid state  $^{11}\text{B}$  MAS-NMR studies of the thermal decomposition of ammonia borane: Mechanistic studies of the hydrogen release pathways from a solid state hydrogen storage material. *Phys. Chem. Chem. Phys.* **9**, 1831–1836 (2007).
  119. Bachmann, P. *et al.* A HR-XPS study of the formation of h-BN on Ni(111) from the two precursors, ammonia borane and borazine. *J. Chem. Phys.* **149**, (2018).
  120. Yuan, S. *et al.* Pure & crystallized 2D Boron Nitride sheets synthesized via a novel process coupling both PDCs and SPS methods. *Sci. Rep.* **6**, 1–9 (2016).
  121. Schild, D. *et al.* XPS investigations of thick, oxygen-containing cubic boron nitride coatings. *Solid State Sci.* **12**, 1903–1906 (2010).
  122. Marincel, D. M. *et al.* Scalable purification of boron nitride nanotubes via wetthermal etching. *Chem. Mater.* **31**, 1520–1527 (2019).
  123. Badi, N. High temperature dielectric properties of  $(\text{B}_x\text{N}_y\text{O}_z)$  thin films deposited using ion source assisted physical vapor deposition. *J. Adv. Dielectr.* **5**, (2015).
  124. Bresnehan, M. S. *et al.* Prospects of direct growth boron nitride films as substrates for graphene electronics. *J. Mater. Res.* **29**, 459–471 (2014).
  125. Gouin, X. *et al.* Characterization of the nitridation process of boric acid. *J. Alloys Compd.* **224**, 22–28 (1995).
  126. Zou, C. *et al.* Fabrication and high-temperature mechanical properties of  $2.5\text{DSi}_3\text{N}_{4f}/\text{BN}$  fiber-reinforced ceramic matrix composite. *Mater. Des.* **92**, 335–344 (2016).

127. Oñate, J. I. *et al.* Deposition of hydrogenated B-C thin films and their mechanical and chemical characterization. *Surf. Coatings Technol.* **49**, 548–553 (1991).
128. Hendrickson, D. N. *et al.* Core-electron binding energies for compounds of boron, carbon and chromium. *Inorg. Chem.* **9**, 612–615 (1970).
129. Naumkin, A. V. *et al.* NIST XPS Database. <https://srdata.nist.gov/xps/Default.aspx> (2020).
130. CNRS. La surface XPS database. <http://www.lasurface.com/database/index.php#> (2020).
131. Lale, A. *et al.* Boron nitride for hydrogen storage. *ChemPlusChem* **83**, 893–903 (2018).
132. Xiong, Z. *et al.* Reversible hydrogen storage by a Li-Al-N-H complex. *Adv. Funct. Mater.* **17**, 1137–1142 (2007).
133. Lu, J. *et al.* Potential and reaction mechanism of Li-Mg-Al-N-H system for reversible hydrogen storage. *J. Phys. Chem. C* **111**, 16686–16692 (2007).
134. Dolotko, O. *et al.* Mechanochemical transformations in Li(Na)AlH<sub>4</sub>-Li(Na)NH<sub>2</sub> systems. *Acta Mater.* **55**, 3121–3130 (2007).
135. Singh, N. K. *et al.* Mechanochemical transformations in NaNH<sub>2</sub>-MgH<sub>2</sub> mixtures. *J. Alloys Compd.* **513**, 324–327 (2012).
136. Jing, Y. *et al.* Synthesis, characterization and CO<sub>2</sub> capture of mesoporous SBA-15 adsorbents functionalized with melamine-based and acrylate-based amine dendrimers. *Microporous Mesoporous Mater.* **183**, 124–133 (2014).
137. Henao, W. *et al.* Insights into the CO<sub>2</sub> capture over amine-functionalized mesoporous silica adsorbents derived from rice husk ash. *J. Environ. Chem. Eng.* **8**, 104362, (2020).
138. Lu, Z. *et al.* The utilization of amide groups to expand and functionalize metal-organic frameworks simultaneously. *Chem. Eur. J.* **22**, 6277–6285 (2016).
139. Zhao, Y. *et al.* A perfluorinated covalent triazine-based framework for highly selective and water-tolerant CO<sub>2</sub> capture. *Energy Environ. Sci.* **6**, 3684–3692 (2013).

# Chapter 6

## GENERAL CONCLUSION & PERSPECTIVES

---



# 6 General conclusion & perspectives

## 1. General conclusion

In this thesis, the last alkali members of the derivatives of hydrazine borane (HB,  $\text{N}_2\text{H}_4\text{BH}_3$ ), rubidium (RbHB,  $\text{RbN}_2\text{H}_3\text{BH}_3$ ) and cesium hydrazinidoborane (CsHB,  $\text{CsN}_2\text{H}_3\text{BH}_3$ ), were synthesized for the first time. Through the characterization of both materials, we showed the successful introduction of the alkali metal cation into the hydrazine borane molecule. RbHB is a crystalline solid (monoclinic, s.g.  $P2_1$ ) that carries 4.5 wt. % H; CsHB carries 3.4 wt. % H and is also crystalline (monoclinic, s.g.  $P2_1$ ). The destabilization effect of the metal cation was observed in both cases: the two compounds start to dehydrogenate at lower temperature in comparison to HB. Besides RbHB and CsHB release more equivalents of  $\text{H}_2$  at  $120^\circ\text{C}$  (1.1 and 2.5 equiv.  $\text{H}_2$  respectively) than HB at  $140^\circ\text{C}$  (1.1 equiv.  $\text{H}_2$ ) under isothermal conditions. Comparing the dehydrogenation of all the alkali hydrazinidoboranes, the rubidium and lithium ones have a similar behavior: LiHB and RbHB release 2 equiv.  $\text{H}_2$  after one hour of isothermal treatment at  $140^\circ\text{C}$ . The kinetics presented by CsHB are faster, as it releases nearly 2 equiv.  $\text{H}_2$  at only  $110^\circ\text{C}$ . However, none of the alkali hydrazinidoboranes overcome the performance of NaHB. In addition, the production of byproducts during the thermolysis was not avoided by RbHB and CsHB. While only ammonia was detected for RbHB, ammonia, hydrazine, and diborane were found in the decomposition of CsHB.

At this point, to have a realistic evaluation of the rubidium and cesium hydrazinidoboranes as hydrogen storage materials, different factors must be taken into account. First, the hydrogen storage capacity: RbHB (4.5 wt. % H) and CsHB (3.4 wt. % H) fall short in comparison with LiHB (11.6 wt. % H) or NaHB (8.8 wt. % H). The weight of the heavy elements like Rb and Cs outshine the gravimetric content of hydrogen the hydrazinidoboranes. Even in the case where the compounds were completely dehydrogenated, this would lead to another problem: the formation of boron

nitride complicates the regeneration of the materials because the hydrogenation of BN is thermodynamically unfavorable. Second, the management of alkali elements such as Rb and Cs is challenging due to their high reactivity, as well as the solid residues after dehydrogenation. Third, Rb and Cs are not abundant. Finally, the synthesis of these compounds did not lead to obtain a pure compound. Taking into account all of these factors, perhaps the Rb and Cs hydrazinidoboranes are not the best candidates for the chemical storage of hydrogen. Rather than hydrogen storage materials, RbHB and CsHB might be envisaged as energetic materials or as boron nitride precursors. However, the findings provided by the synthesis and characterization of RbHB and CsHB contribute to have a better knowledge of the chemistry of boron- and nitrogen-based materials. Some research still lies ahead for these compounds, especially regarding the complicated dehydrogenation mechanisms and the composition of the solid products after thermolysis.

The last part of this work studied the potential use of the alkali derivatives of ammonia borane as boron nitride precursors and their capacity to capture CO<sub>2</sub>. The starting point was lithium (LiAB, LiNH<sub>2</sub>BH<sub>3</sub>) and sodium (NaAB, NaNH<sub>2</sub>BH<sub>3</sub>) amidoboranes. It is clear that the alkali cation has an impact in the formation of crystalline hexagonal boron nitride (h-BN) when these compounds are pyrolyzed. Diffraction peaks belonging to h-BN appeared in the PXRD patterns of LiAB from 600°C and from 800°C for NaAB. At 1000°C, LiAB presented the highest degree of crystallization among the analyzed compounds, according to the Raman spectroscopy and PXRD analyses. In comparison, pure ammonia borane presented an amorphous structure even when it was pyrolyzed at 1000°C. The composition of the pyrolyzed amidoboranes contained impurities such as Li<sub>2</sub>O or Na<sub>2</sub>O, as shown by PXRD analysis. At 1000°C, the intensity of these impurities decreased. Further thermal treatment at higher temperatures might lead to obtain a purer h-BN phase.

The pyrolyzed materials from AB, LiAB and NaAB showed interesting results when they were exposed to CO<sub>2</sub>. The materials were able to uptake CO<sub>2</sub> at nearly ambient conditions (1.5 bar and 30°C). It is likely that there is a relation between the crystallinity and the sorption capacity of the BN structures. In the one hand, AB pyrolyzed at 600°C (23.6 cm<sup>3</sup> g<sup>-1</sup>) showed the highest CO<sub>2</sub> uptake, likely due to the poor crystallized BN structures and the higher number of defects and vacancies. On the other hand, the LiAB-derived samples presented the lowest CO<sub>2</sub> uptake values, likely due

to the higher degree of crystallization presented by these compounds. The amidoborane-derived materials with the highest degree of crystallization (pyrolyzed at 1000°C) exhibited a higher uptake capacity than bulk h-BN (3.8 cm<sup>3</sup> g<sup>-1</sup> for LiAB and 7.6 cm<sup>3</sup> g<sup>-1</sup> for NaAB vs. 1.7 cm<sup>3</sup> g<sup>-1</sup> of h-BN). This might confirm the positive effect of the incorporation of alkali elements in the BN structure for enhancing the CO<sub>2</sub> sorption properties. These results are promising, especially because the materials developed in this work are not porous. Thus, new perspectives have been opened.

## 2. Future perspectives

All of the alkali derivatives of HB have been synthesized and now we have a better overview of these materials. However, it would be interesting to explore new derivatives such as the alkaline-earth ones. Recently, the calcium derivative Ca(N<sub>2</sub>H<sub>3</sub>BH<sub>3</sub>)<sub>2</sub> was reported. In this sense, the magnesium derivative, namely magnesium hydrazinidoborane (Mg(HB)<sub>2</sub>, Mg(N<sub>2</sub>H<sub>3</sub>BH<sub>3</sub>)<sub>2</sub>), is attractive because it carries more hydrogen (10.5 wt. % H) than almost all of the alkali hydrazinidoboranes (with the exception of LiHB), and due to the earth abundance of magnesium. In the past, some unfruitful efforts have been done in order to obtain this compound. Recently, through a wet method and a different Mg precursor (di-n-butylmagnesium), magnesium hydrazinidoborane was successfully synthesized and identified by FTIR and <sup>11</sup>B MAS NMR (Figure 1). The fully characterization of this compound now should be carried out.

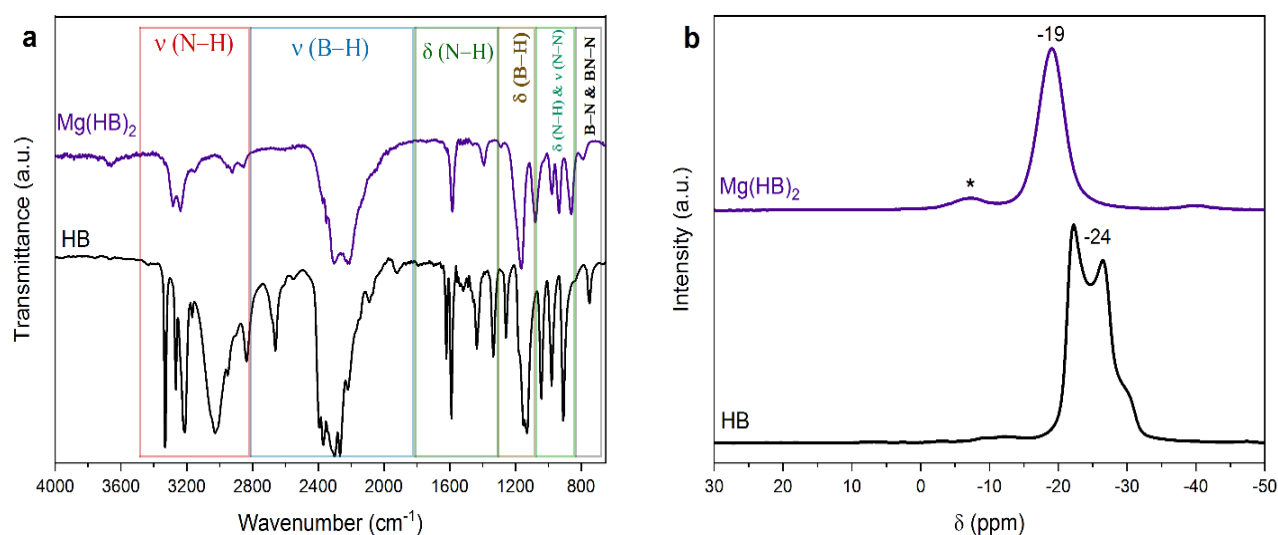
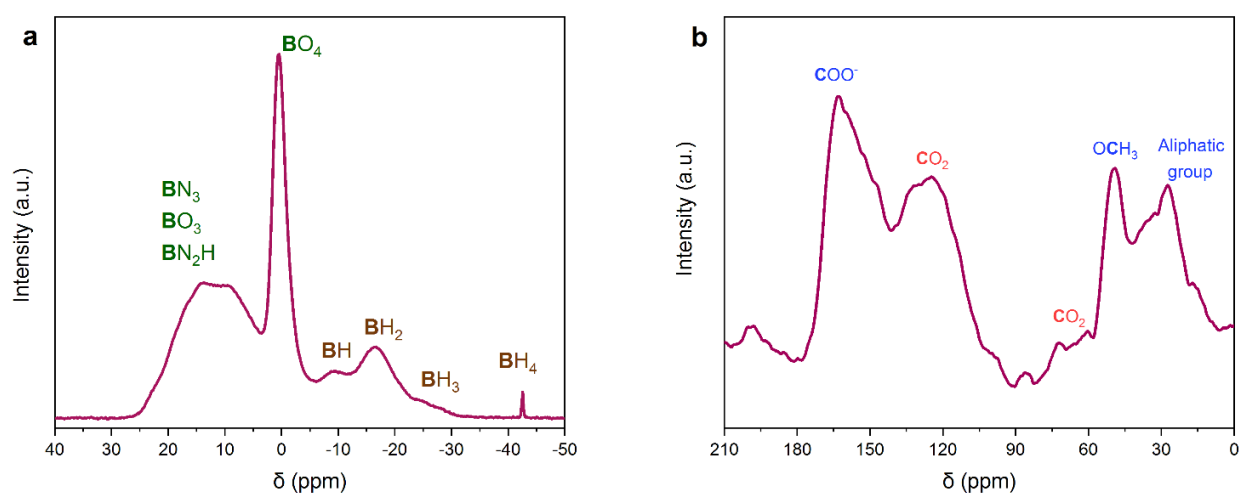


Figure 1. a) FTIR and b) <sup>11</sup>B MAS NMR spectra comparison of pristine HB and Mg(HB)<sub>2</sub>

Regarding the amidoboranes, the pyrolysis of LiAB and NaAB at higher temperatures ( $>1000^{\circ}\text{C}$ ) might lead to a higher degree of crystallization of boron nitride and this might help to reduce the compounds formed by side reactions detected in this work. The impact of other alkali elements (K, Rb, Cs) in the crystallization of amidoboranes to BN is worth to be analyzed too. The capture of  $\text{CO}_2$  by these materials should be evaluated at different conditions of temperature and pressure (for example, the temperature of outlet gas streams of combustion processes in thermal power station is  $45^{\circ}\text{C}$ ). Besides, as the materials obtained in this work are bulky, the development of nanostructures or porous structures based on these compounds might lead to improve their  $\text{CO}_2$  sorption properties. Finally, the investigation of amidoborane-derived compounds pyrolyzed at lower temperatures (i.e.  $300\text{-}500^{\circ}\text{C}$ ) might confirm the relation established between the crystallinity and the sorption capacity of the materials.

The capture of  $\text{CO}_2$  is not the only approach that can be considered for B- and N-based compounds related to  $\text{CO}_2$ . They might be also considered as reducing agents for the conversion of  $\text{CO}_2$ . For example,  $\text{PdCl}_2$  can dehydrogenate AB in a highly exothermic reaction. The energy and the  $\text{H}_2$  released by this reaction might help to reduce  $\text{CO}_2$ . Some experiments have been performed and evidence of the formation of B–O bonds and some  $\text{COO}^-$  has been found by  $^{11}\text{B}$  and  $^{13}\text{C}$  MAS NMR (Figure 2). The simultaneous capture of  $\text{CO}_2$  by the sample in these experiments was also observed.



**Figure 2.** MAS NMR spectra of the solid product after the dehydrogenation of AB catalyzed by  $\text{PdCl}_2$  in the presence of  $\text{CO}_2$  for a)  $^{11}\text{B}$  and b)  $^{13}\text{C}$ . The chemical environments are assigned.

Moreover, LiAB has been considered as a reductive agent for aldehydes and ketones. Accordingly, LiAB might be also considered for the reduction of  $\text{CO}_2$ . Preliminary experiments have shown that an exothermic reaction occurs during the thermolytic decomposition of LiAB under a  $\text{CO}_2$  atmosphere at ca.  $110^\circ\text{C}$ . The solid product obtained after the reaction shows different environments assigned to  $\text{BO}_x$ ,  $\text{BN}_3$  and  $\text{BN}_2\text{H}$  (Figure 3). These results allowed us to establish an international collaboration with the Yildiz Technical University in Istanbul, Turkey, in order to deepen in the research of these materials.

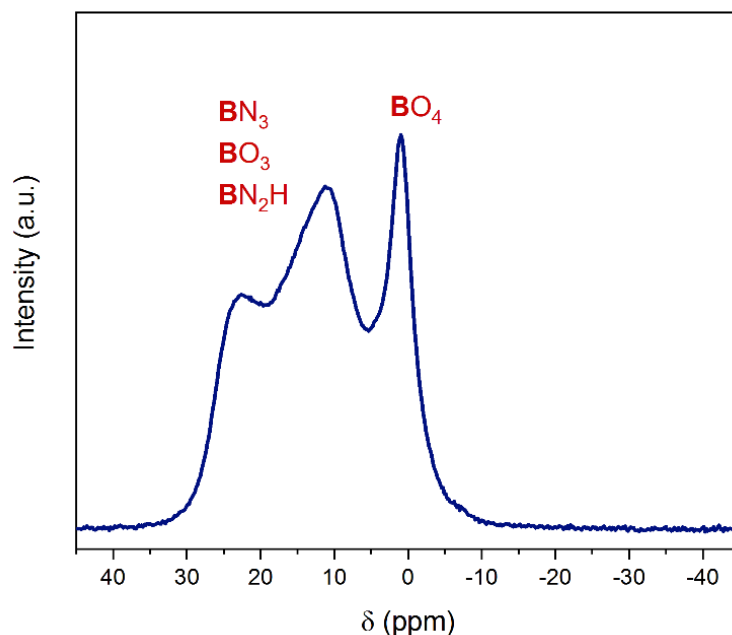


**Figure 3.**  $^{11}\text{B}$  MAS NMR spectrum of the solid product after the thermolysis of LiAB under a  $\text{CO}_2$  atmosphere.

In the two mentioned cases, the incorporation of oxygen into the compound evidences the reaction between  $\text{CO}_2$  and the borane. Further experiments might be performed to determine the reaction mechanisms and the products formed. A liquid-gas reaction approach between LiAB and  $\text{CO}_2$  can also be envisaged. We believe that the conversion/storage of  $\text{CO}_2$  by these compounds might open new research lines of the boron- and nitrogen-based compounds and might have an impact in the future. Further research in this field is now expected.



## Scientific contributions

---

### Publications

- Castilla-Martinez, C.A., Granier, D., Charmette, C., Maurin, G., Yot, P.G., Demirci, U.B. Rubidium hydrazinidoborane: Synthesis, characterization and hydrogen release properties. *Int. J. Hydrogen Energy* 44, 28252–28261 (2019).
- Castilla-Martinez, C.A., Granier, D., Charmette, C., Cartier, J., Yot, P.G., Demirci, U.B. Cesium hydrazinidoborane, the last of the alkali hydrazinidoboranes, studied as potential hydrogen storage material. *Int. J. Hydrogen Energy*. 45, 16634-16643 (2020).
- Castilla-Martinez, C.A., Moury, R. and Demirci, U.B. Amidoboranes and hydrazinidoboranes: state of the art, potential for hydrogen storage, and other prospects. *Int. J. Hydrogen Energy*. 45, 30731-30755 (2020).
- Turani-I-Belloto, K., Castilla-Martinez, C.A., Cot, D., Petit, E., Benarib, S., Demirci, U.B. Nanosized ammonia borane for solid-state hydrogen storage – Outcomes, limitations, challenges and opportunities. *Int. J. Hydrogen Energy*. 46, 7351-7370 (2021).

### Presentations

- New alkaline hydrazinidoborane compounds based on rubidium and cesium. EuroBoron8. June 24-27, 2019, Montpellier, France. Oral presentation.
- Rubidium and cesium hydrazinidoboranes: New derivatives of hydrazine borane as potential hydrogen storage materials. European Material Research Society, Symposium L. September 16-19, 2019, Warsaw, Poland. Oral presentation.



# Annex I

## SUPPLEMENTARY INFORMATION

---



# AI Supplementary information

---

## Description of Kissinger's method

The change of the heat content in a sample is observed as peaks in the DSC analysis. If all the conditions are constant, except the heating rate  $\phi$ , the position of the peaks will vary. Using the temperature at which the peaks appear, the apparent activation energy of the process can be calculated. Many reactions of the type solid  $\rightarrow$  solid + gas are described by the equation:

$$\frac{dx}{dt} = A(1-x)^n e^{-\frac{E_a}{RT}} \quad (1)$$

where A is the pre-exponential term, x the fraction reacted, n the order of the reaction,  $E_a$  the activation energy, R the universal gas constant and T the temperature in Kelvin. If the temperature rises due to the reaction, the rate  $\frac{dx}{dt}$  reaches a maximum, and when the reactant is consumed, it goes back to zero. The maximum temperature  $T_m$  occurs when  $\frac{d}{dt}\left(\frac{dx}{dt}\right)$  is zero:

$$\frac{dx}{dt} \left[ -\frac{E_a}{R T_m^2} \frac{dT}{dt} + A e^{-\frac{E_a}{RT_m}} n(1-x)^{n-1} \right] = 0 \quad (2)$$

Kissinger did some assumptions for the method: the heating rate ( $\phi = \frac{dT}{dt}$ ) is constant and the product  $n(1-x)^{n-1}$  is approximately 1. Substituting this in Equation 2, Kissinger equation is obtained:

$$\ln\left(\frac{\phi}{T_m^2}\right) = \alpha - \frac{E_a}{RT_m} \quad (3)$$

where  $\alpha = \ln\left(\frac{AR}{E_a}\right)$ . With this equation, the apparent activation energy is obtained from plotting  $\ln\left(\frac{\phi}{T_m^2}\right)$  against  $\frac{1}{T_m}$ .

## Energy Dispersive X-ray Analysis from pyrolyzed samples (LiAB, NaAB)

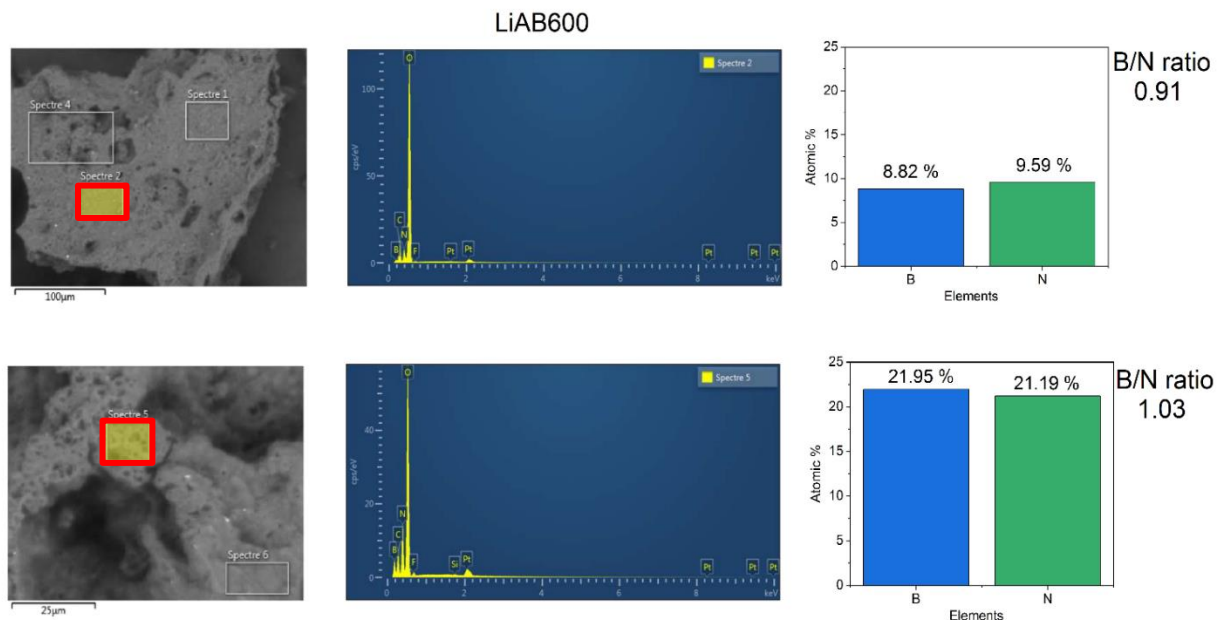


Figure A 1. SEM–EDX analysis of LiAB600 in different zones of the compound.

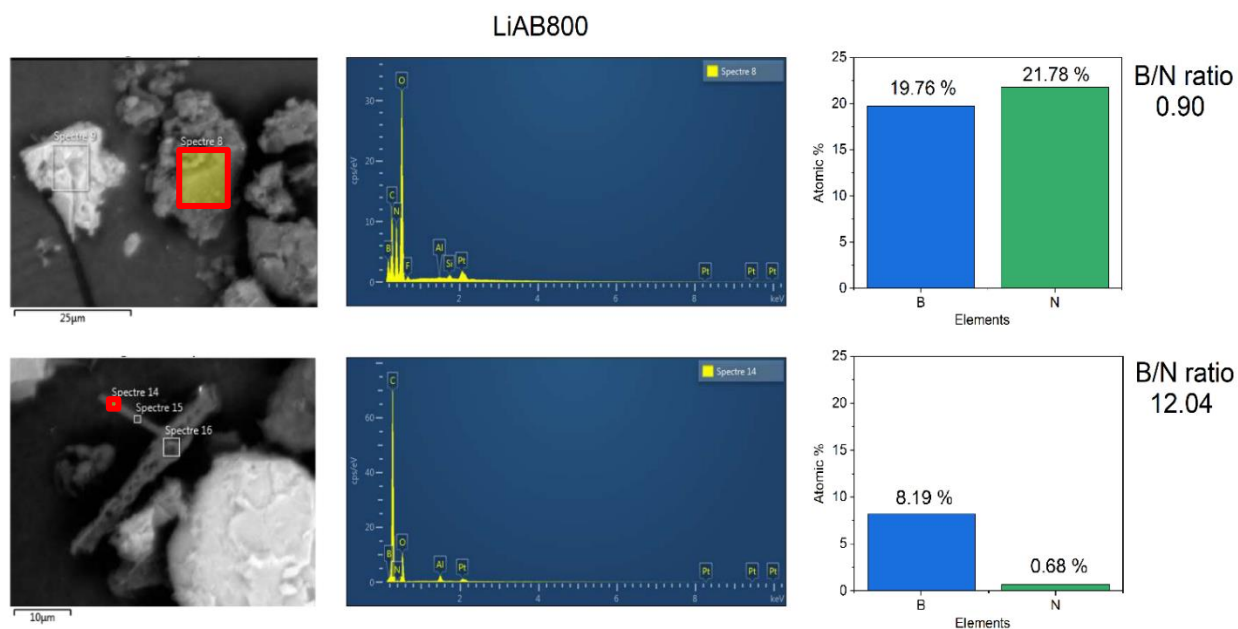


Figure A 2. SEM–EDX analysis of LiAB800 in different zones of the compound. The ratio of 12.04 might be due to some particles that are richer in B rather than N, as observed for BN obtained from polyborazylene.<sup>1</sup>

<sup>1</sup> Kho, J., Moon, K., Nouet, G., Ruterana, P., Kim, D. Boron-rich boron nitride (BN) films prepared by a single spin-coating process of a polymeric precursor. *Thin Solid Films*. **389**, 78-83 (2001).

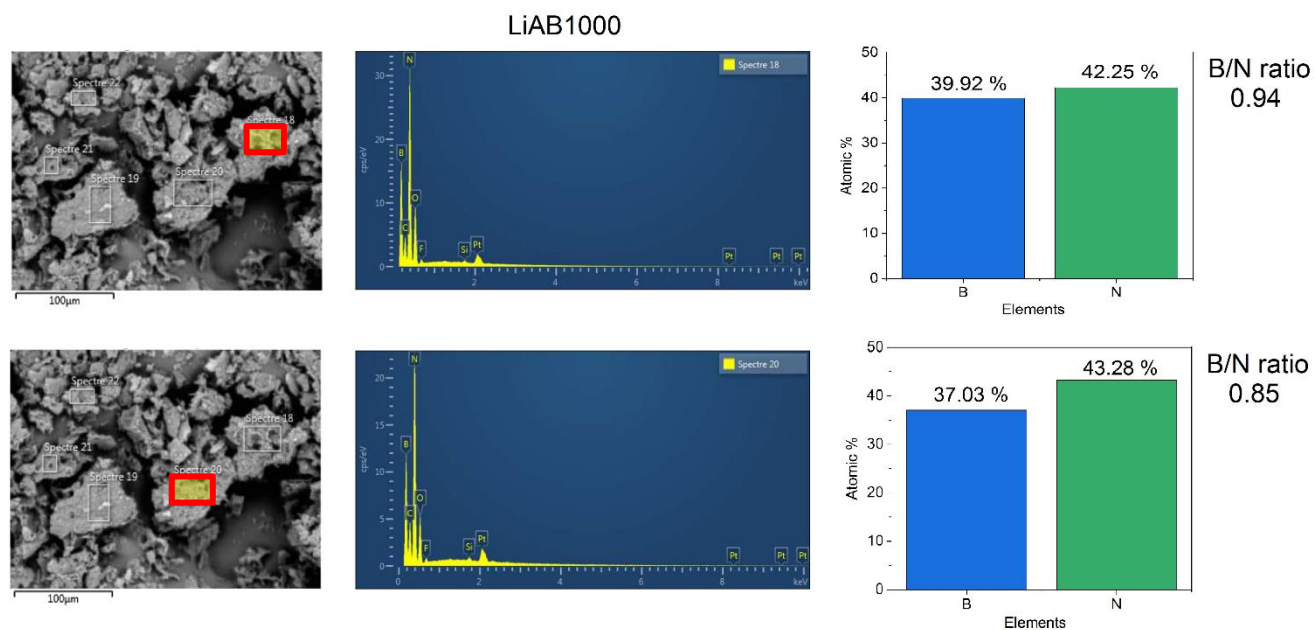


Figure A 3. SEM–EDX analysis of LiAB1000 in different zones of the compound.

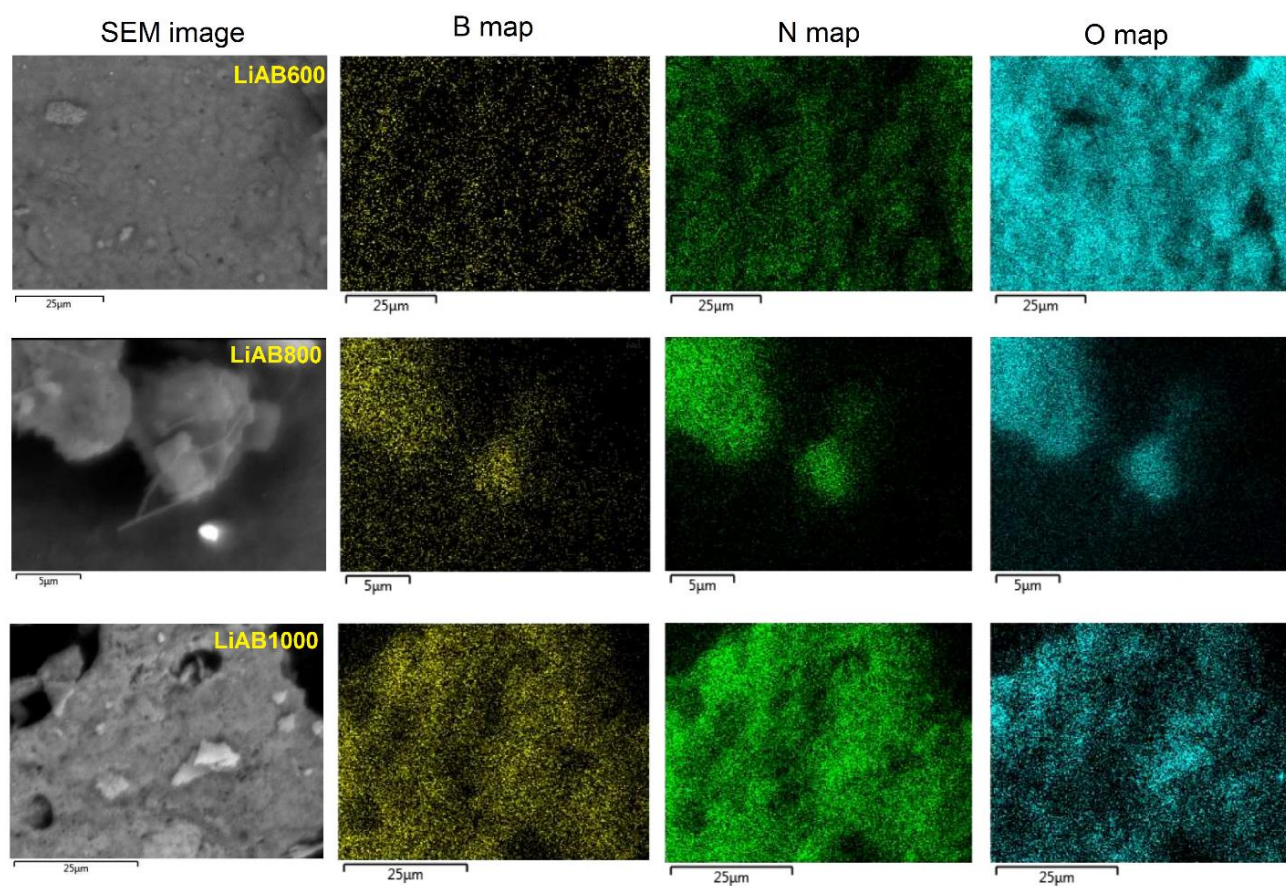


Figure A 4. SEM images and EDX elemental maps of LiAB600, LiAB800 and LiAB1000.

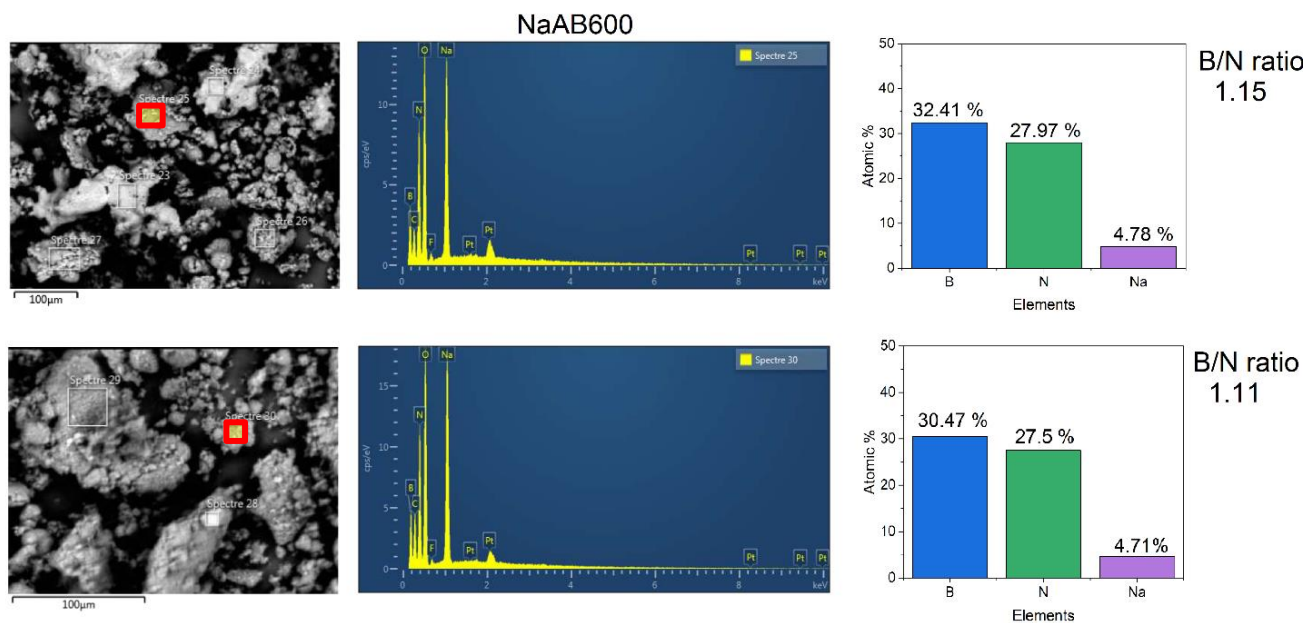


Figure A 5. SEM–EDX analysis of NaAB600 in different zones of the compound.

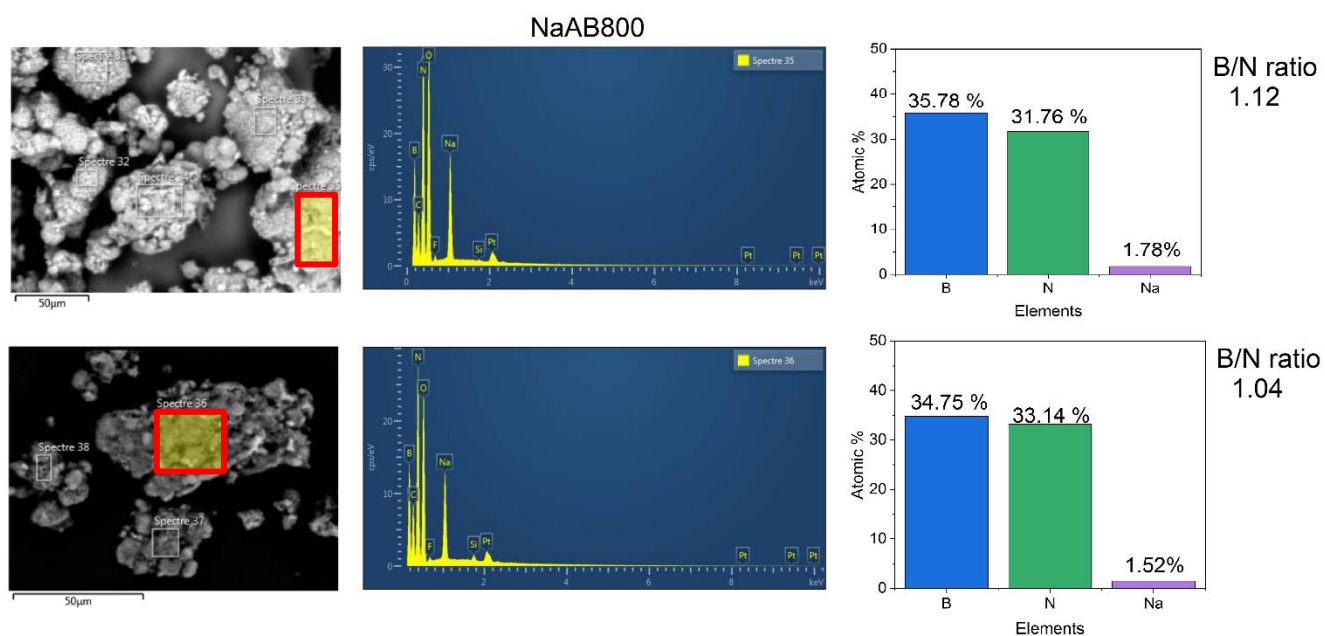


Figure A 6. SEM–EDX analysis of NaAB800 in different zones of the compound.

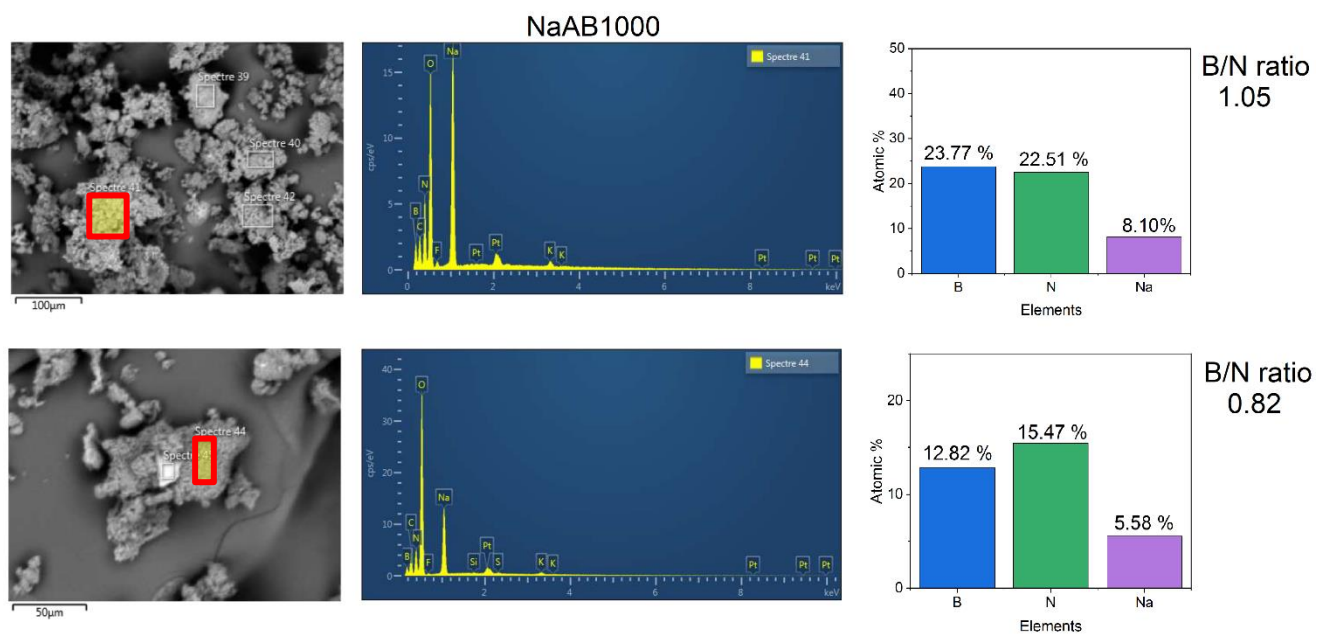


Figure A 7. SEM-EDX analysis of NaAB1000 in different zones of the compound.

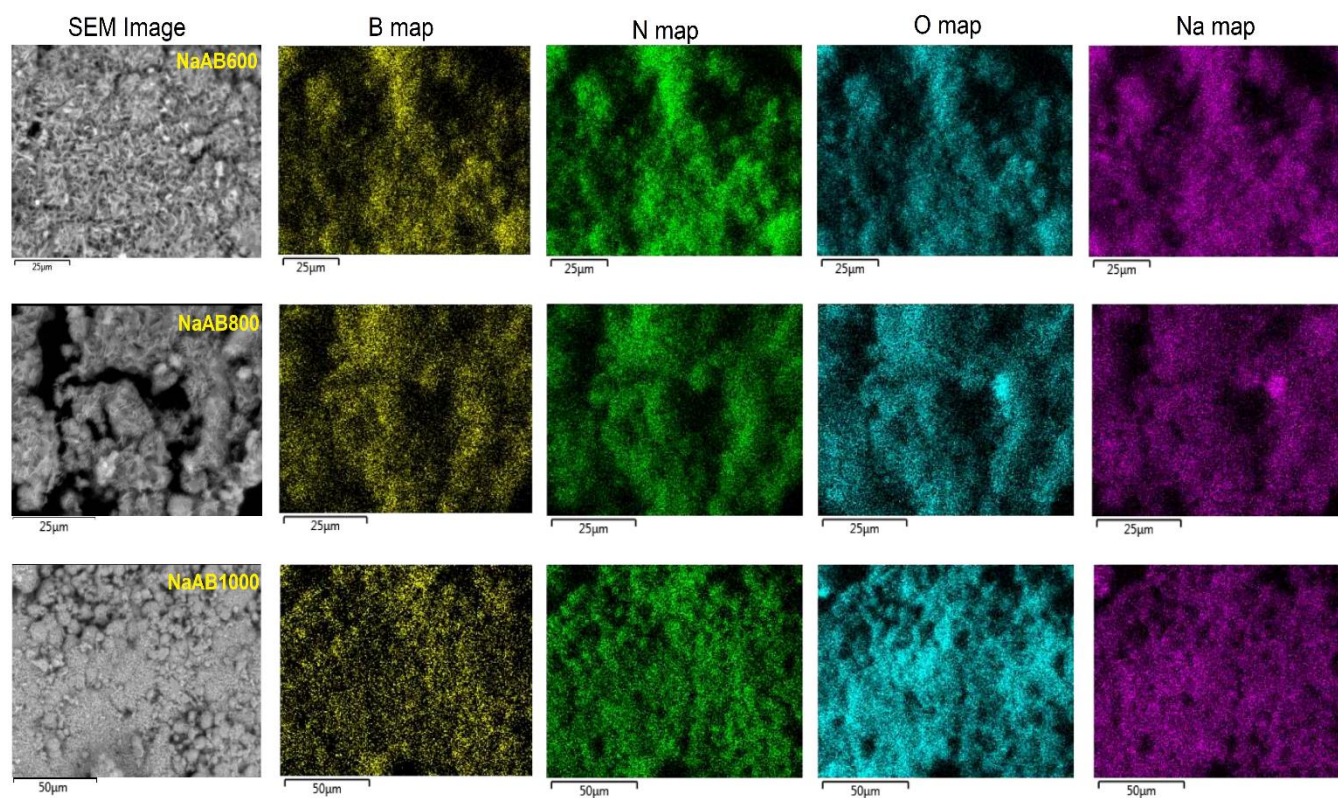


Figure A 8. SEM images and EDX elemental maps of NaAB600, NaAB800 and NaAB1000.

**Powder X-Ray Diffraction comparison from samples (AB, LiAB, NaAB) pyrolyzed at 1000°C**

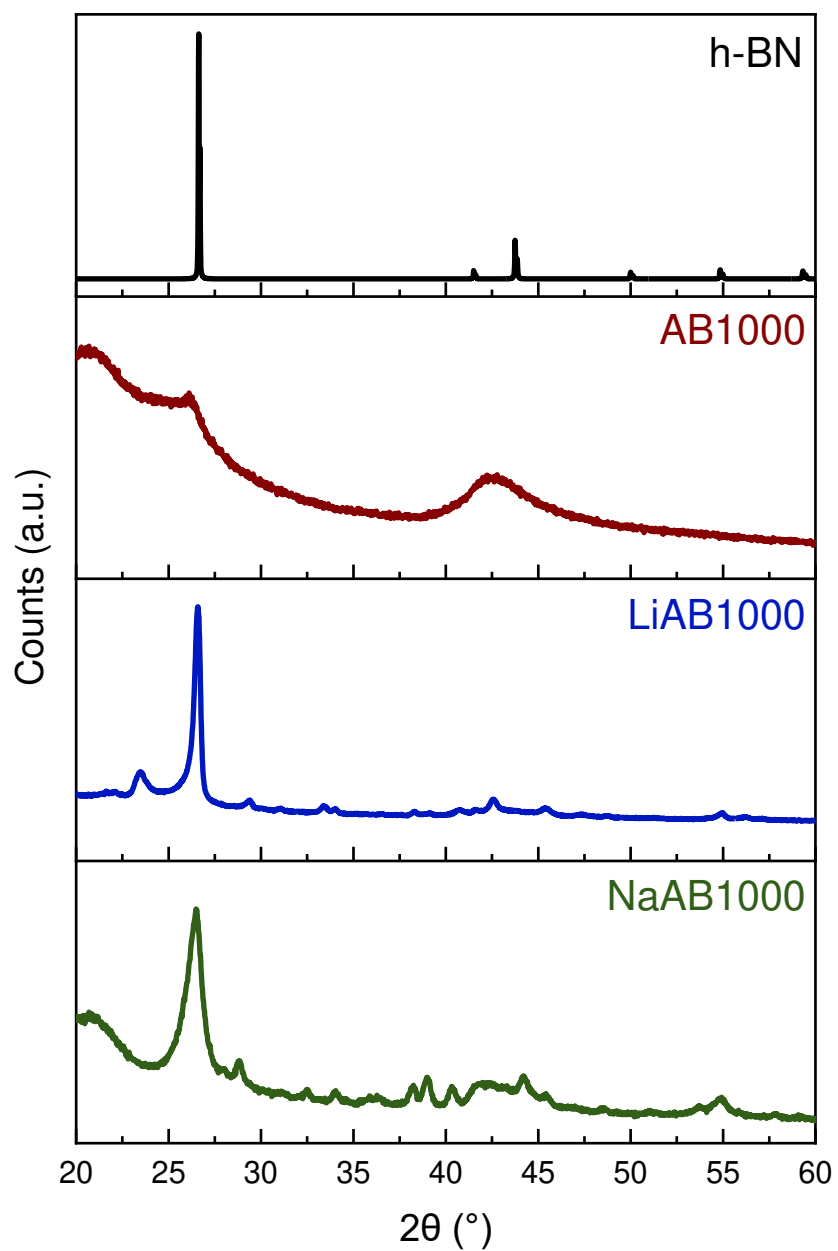
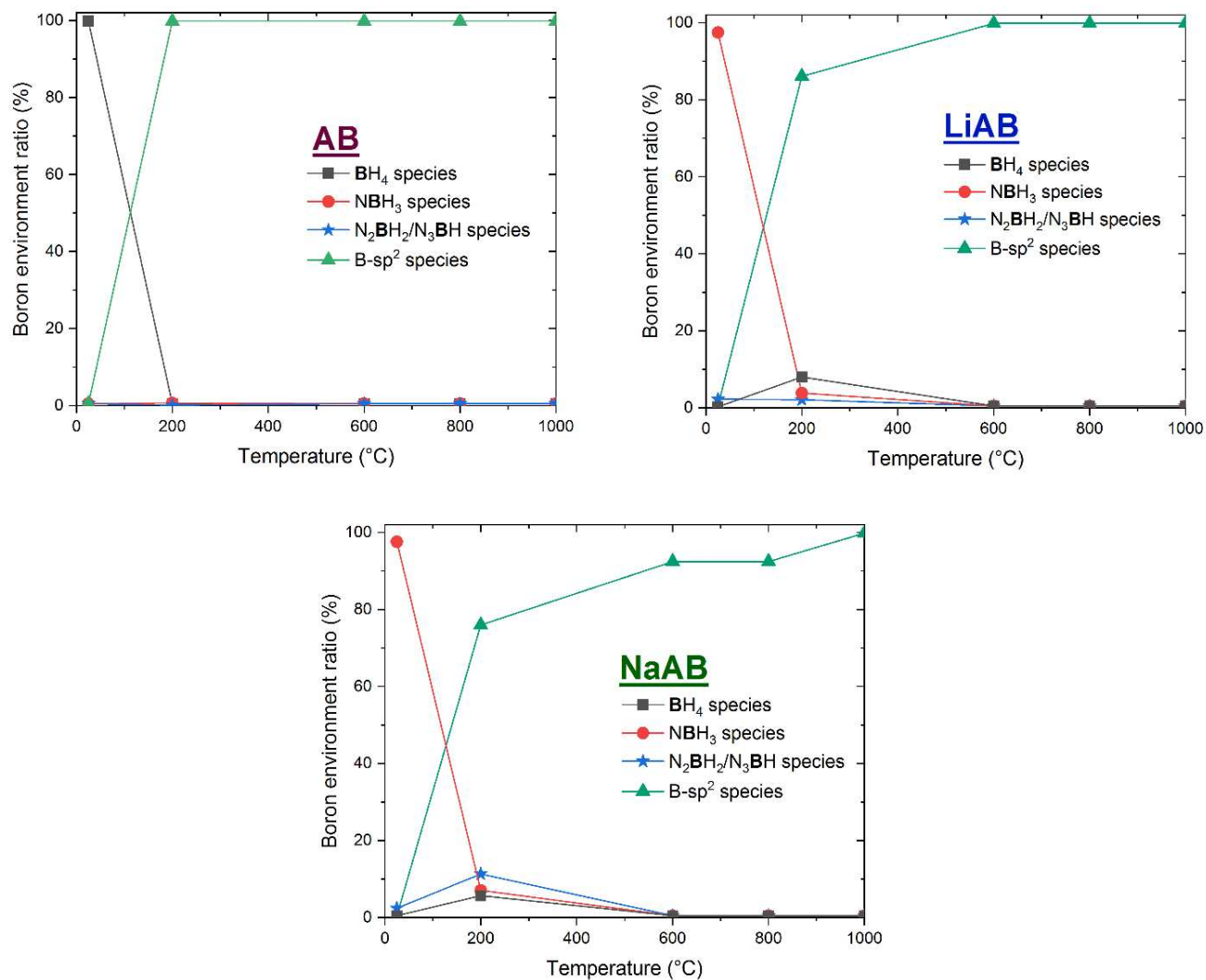


Figure A 9. Comparison between the PXRD patterns of the samples treated at 1000°C and h-BN.

## Evolution of boron species determined by $^{11}\text{B}$ MAS NMR from the pyrolyzed samples (AB, LiAB, NaAB)

The peak areas of the  $\text{BH}_4$ ,  $\text{NBH}_3$ ,  $\text{N}_2\text{BH}_2/\text{N}_3\text{BH}$  and the  $\text{sp}^2$ -hybridized boron environments were integrated in the 100 to -100 ppm range and plotted in function of the temperature.



**Figure A 10.** Peaks area ratios of boron species ( $\text{BH}_4$ ,  $\text{NBH}_3$ ,  $\text{N}_2\text{BH}_2/\text{N}_3\text{BH}$  and the  $\text{sp}^2$ -hybridized B) as a function of the temperature up to  $1000^\circ\text{C}$ . The  $\text{N}_2\text{BH}_2$  and  $\text{N}_3\text{BH}$  signals were summed up.

## XPS survey spectra of the samples derived from AB, LiAB and NaAB

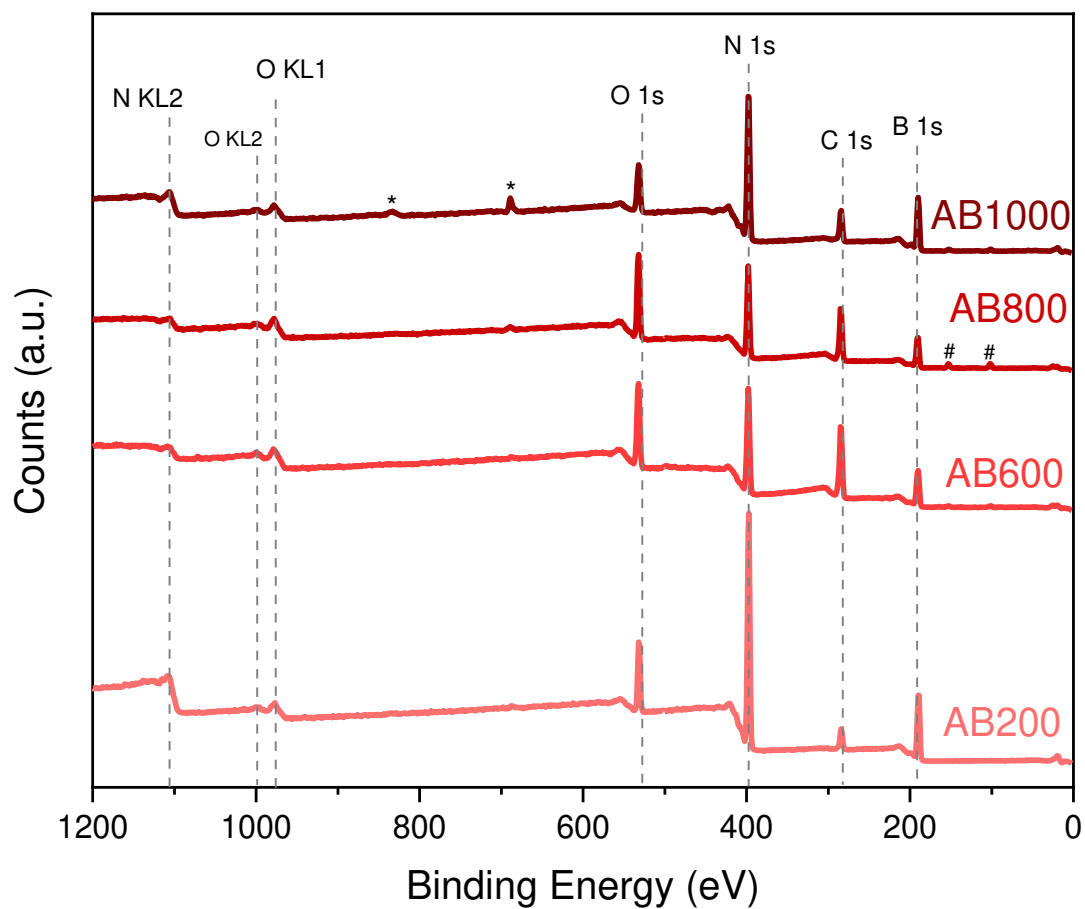


**Figure A 11.** XPS survey spectra of the AB-derived materials pyrolyzed at 200, 600, 800 and 1000°C. Some impurities peaks were detected and are indicated by a \* for F and by # for Si.

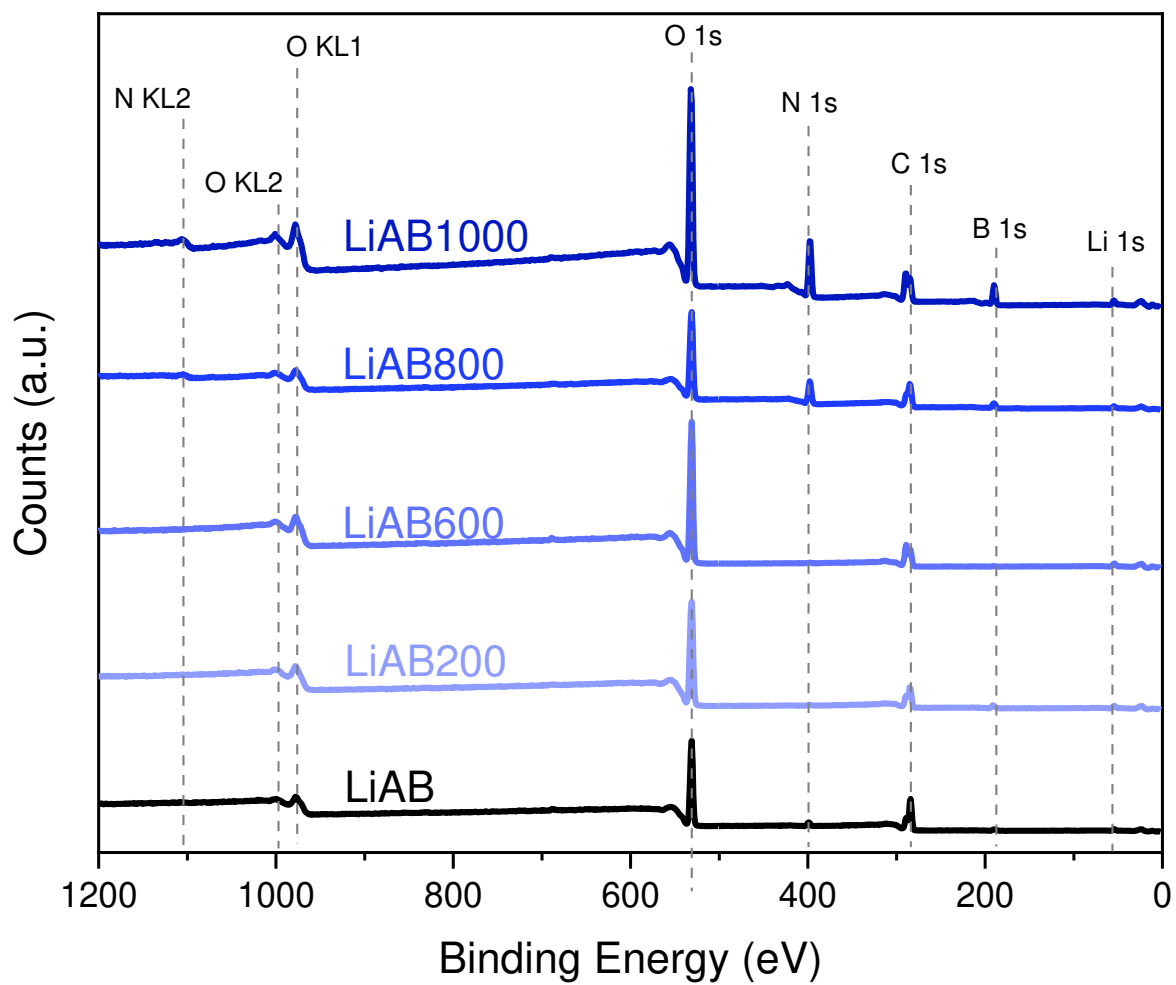


Figure A 12. XPS survey spectra of LiAB and the LiAB-derived materials pyrolyzed at 200, 600, 800 and 1000°C.

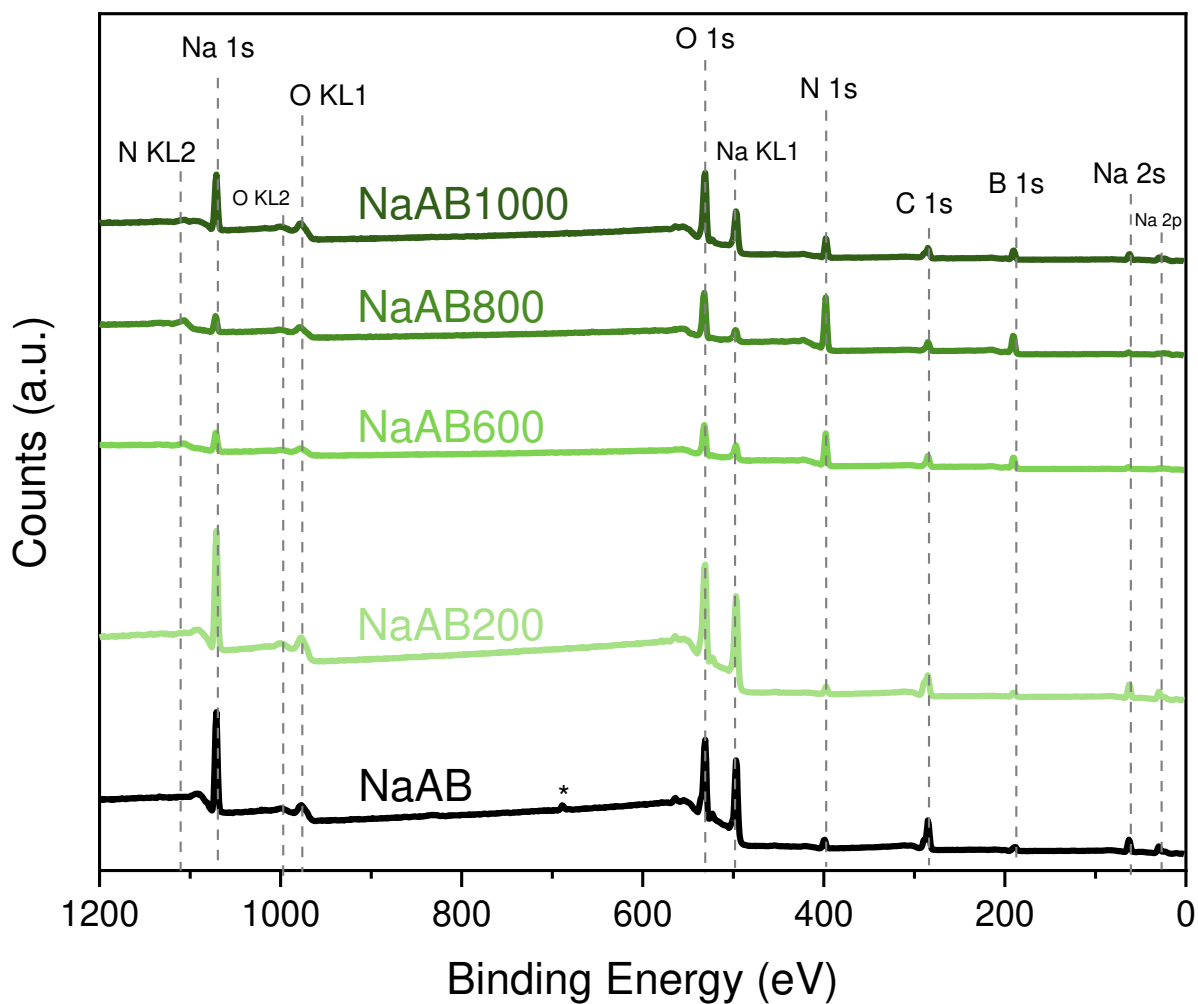


Figure A 13. XPS survey spectra of NaAB and the NaAB-derived materials pyrolyzed at 200, 600, 800 and 1000°C. Some impurities peaks were detected and are indicated by a \* for F.

## CO<sub>2</sub> uptake by the pyrolyzed samples of AB, LiAB and NaAB

**Table A 1.** CO<sub>2</sub> sorption capacity by the pyrolyzed samples of AB, LiAB and NaAB at 1.5 bar and 30°C.

Sample	mg g <sup>-1</sup>	mmol g <sup>-1</sup>	cm <sup>3</sup> g <sup>-1</sup>
AB200	15.9	0.4	8.0
LiAB200	8.7	0.2	4.4
NaAB200	7.5	0.2	3.8
AB600	46.4	1.0	23.6
LiAB600	6.1	0.1	3.1
NaAB600	32.9	0.7	16.7
AB800	30.1	0.7	15.2
LiAB800	8.8	0.2	4.5
NaAB800	15.7	0.3	8.0
AB1000	37.1	0.8	18.9
LiAB1000	7.3	0.2	3.8
NaAB1000	14.9	0.4	7.6